Amsterdam quays under pressure

Modelling and testing of historic canal walls

Hemel, M.

DOI
10.4233/uuid:102edff8-8960-4633-830c-369aef8e279f

Publication date
2023

Document Version
Final published version

Citation (APA)
Hemel, M. (2023). *Amsterdam quays under pressure: Modelling and testing of historic canal walls* . [Dissertation (TU Delft), Delft University of Technology]. https://doi.org/10.4233/uuid:102edff8-8960-4633-830c-369aef8e279f

Amsterdam quays under pressure Mart-Jan Hemel

Amsterdam quays under pressure

Modelling and testing of historic canal walls

Mart-Jan Hemel

Amsterdam quays under pressure

Modelling and testing of historic canal walls

Proefschrift

ter verkrijging van de graad van doctor
aan de Technische Universiteit Delft,
op gezag van de Rector Magnificus prof.dr.ir. T.H.J.J. van der Hagen,
voorzitter van het College voor Promoties,
in het openbaar te verdedigen op
donderdag 30 november 2023 om 10:00 uur

door

Mart-Jan HEMEL
Civiel Ingenieur, Technische Universiteit Delft, Nederland
Geboren te Utrecht, Nederland

Dit proefschrift is goedgekeurd door de promotoren.

Samenstelling promotiecommissie bestaat uit:

Rector Magnificus,	voorzitter
Prof. Dr. ir. S.N. Jonkman	Technische Universiteit Delft, promotor
Dr. ir. D.J. Peters	Technische Universiteit Delft, copromotor
Dr. ir. M. Korff	Technische Universiteit Delft, copromotor

Onafhankelijke leden:

Prof. dr. K.G. Gavin	Technische Universiteit Delft
Prof. dr. A.J. Whittle	Massachusetts Institute of Technology, Verenigde Staten
Prof. dr. ir. J.W.G. van de Kuilen	Technische Universiteit Delft Technische Universität München, Duitsland
Dr. ir. S. Bork	Gemeente Amsterdam
Prof. dr. ir. W.S.J. Uijttewaal	Technische Universiteit Delft, reservelid

The Delft University of Technology has conducted this research with the valuable support of the Amsterdam Institute for Advanced Metropolitan Solutions and the Municipality of Amsterdam.

ISBN: 978-94-6469-656-1

Cover design: Mart-Jan Hemel

Printed by: www.proefschriftmaken.nl
An electronic version of this dissertation is available at repository TU Delft:
https://doi.org/10.4233/uuid:102edff8-8960-4633-830c-369aef8e279f

“Amsterdam, die groote stad, die staat op honderd palen.
En als die stad eens ommevalt, wie zal dat betalen?”

Johannes van Vloten, 1894

Propositions

accompanying the dissertation

Amsterdam quays under pressure

by

Mart-Jan Hemel

1. When performing bending capacity checks on historic timber foundation piles, one should use an effective diameter instead of an external diameter, whereas for geotechnical calculations an external diameter should be employed. (*chapter 3 & 4*)
2. For historical pile foundations, pile group effects such as in-line effects and side-by-side effects are not as relevant, as variations in strength are primarily caused by natural variability and biological deterioration of the timber piles. Consequently, the focus shifts towards the behavior of an average pile when analyzing pile groups. (*chapter 4*)
3. Historic quay walls can be best modelled using an analytical model instead of finite element software. (*chapter 5*)
4. Observations on past performance of quays should be included in the reliability analysis using Bayesian updating and this will prevent unnecessary replacements. (*chapter 7*)
5. The current practise of a highly detailed analysis of an unknown quay wall geometry essentially leads to reliable fiction.
6. New inner-city quays should preferably be constructed with a timber pile foundation.
7. Those who understand historic quay walls have a comprehensive understanding of civil engineering.
8. "*One good test is worth a thousand expert opinions*" (Wernher Von Braun, 1940)
9. Technical optimism is dangerous.
10. The efforts and investments in extending the lifespan and constructing new quay walls are futile. In a hundred years Amsterdam will be flooded.
11. There is no place to learn as quickly as on a construction site.

These propositions are regarded as opposable and defendable, and have been approved as such by the promotor Prof.dr.ir. S.N. Jonkman, co-promotor dr.ir. D.J. Peters and co-promotor dr.ir. M.Korff.

Stellingen

behorende bij het proefschrift

Amsterdamse kades onder druk

door

Mart-Jan Hemel

1 Bij het uitvoeren van toetsingen van de momentencapaciteit van historische houten paalfunderingen moet men een effectieve diameter gebruiken in plaats van een externe diameter, terwijl voor geotechnische berekeningen een externe diameter moet worden gebruikt. (*hoofdstuk 3 & 4*)

2 Voor historische paalfunderingen zijn paalgroepseffecten, zoals in-lijn-effecten en zij-aan-zij-effecten, niet zo relevant, omdat variaties in sterkte voornamelijk worden veroorzaakt door natuurlijke variabiliteit en biologische achteruitgang van de houten palen. Hierdoor verlegt de focus bij het analyseren van paalgroepen zich naar het gedrag van een gemiddelde paal. (*hoofdstuk 4*)

3 Historische kademuren kunnen het beste worden gemodelleerd met een analytisch model in plaats van met eindige elementen software. (*hoofdstuk 5*)

4 Observaties van succesvolle prestaties van kades uit het verleden moeten worden opgenomen in de betrouwbaarheidsanalyse met behulp van Bayesiaanse updating. Dit zal onnodige vervangingen zal voorkomen. (*hoofdstuk 7*)

5 De huidige werkwijze van een zeer gedetailleerde analyse van een kademuur met een onbekende geometrie leidt tot een betrouwbare fictie.

6 Nieuwe binnenstedelijke kades dienen bij voorkeur gebouwd te worden met een houten paalfundering.

7 Degenen die historische kademuren begrijpen, hebben een veelomvattend begrip van civiele techniek.

8 *"Eén goed experiment is meer waard dan duizend deskundige meningen*" (Wernher Von Braun, 1940)

9 Technisch optimisme is gevaarlijk.

10 De inspanningen en investeringen in het verlengen van de levensduur en nieuwe kademuren te bouwen zijn tevergeefs. Over honderd jaar zal Amsterdam overstroomd zijn.

11 Er is geen plek waar je zo snel kunt leren als op een bouwplaats.

Deze stellingen worden opponeerbaar en verdedigbaar geacht, en zijn als zodanig goedgekeurd door de promotor Prof.dr.ir. S.N. Jonkman, copromotor dr.ir. D.J. Peters en copromotor dr.ir. M. Korff.

Summary

Amsterdam faces the challenge of maintaining a domain of 200 km historic quay walls, which is a vital part of the city's historical landscape. Many quays are currently in poor condition and require renovation or replacement in the near future, significantly impacting the city. The quay walls can be up to 300 years old and their structure consists of a masonry cantilever wall on top of a timber floor, which is supported by headstocks founded on multiple vertical timber pile rows. In recent years, quay walls have shown signs of damage, partial collapse, and early warnings of such events. The most recent and severe incident was the collapse of the Grimburgwal in 2020, where approximately 20 meters of quay wall suddenly collapsed, plunging into the canal within a matter of seconds. Consequently, it is important to be able to predict the resistance of these structures and understand their potential failure mechanisms.

The most common and severe failure mechanism observed in Amsterdam's city centre is the lateral failure of the pile foundation, visualized in the figure below. Calculating the resistance against this mechanism with existing models, leads to estimates of insufficient strength and safety. It seems that these models are too conservative, because in reality, the majority of the existing structures that proof unsafe on paper is performing quite well in practice. The discrepancy between the models and reality arises from uncertainties in the working principles of historic quay walls, geometrical unknowns, as well as uncertainties in soil and structural properties.

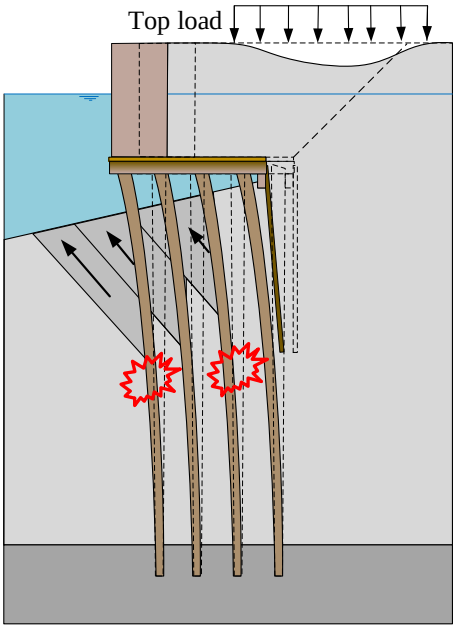

Failure mechanism 'lateral failure of the quay wall foundation'.

This thesis provides a comprehensive understanding of the lateral failure of the pile foundation by full-scale quay wall experiments and it proposes a computational model to predict the resistance against this failure mechanism.

To gain a comprehensive understanding of the lateral failure mechanism, an unique and extensive experimental program has been conducted on an existing historic quay wall, founded on timber piles. The quay is located at Amsterdam Overamstel and dates back to 1905. Experiments have been conducted at three different system levels. At level 1, four-point bending experiments have been performed on individual piles to obtain the bending material properties. At level 2, lateral pile group experiments have been conducted on two 3x4 pile groups to study the pile-soil-pile interactions. At level 3, proof load experiments have been carried out on entire full scale quay wall sections, to study the overall behaviour of the quay. As part of the experimental program, an extensive geotechnical site investigation has been performed. The experimental approach chosen enables a stepwise validation and calibration for computational quay wall models.

Through the experimental program, it is demonstrated that among all potential failure mechanisms, the lateral failure mechanism is most likely to occur when a quay wall is subjected to large surface loading at its backside. Examples of such loads in practice are parked or moving cars, heavy vehicles or goods. The mechanism is triggered by an increase in soil stresses at the backside of the quay, which pushes the foundation towards the water. This, in turn, results in the bending of the timber piles, accompanied by the development of bending stresses. State-of-the-art models (ABAQUS, PLAXIS and spring models) were used to predict the failure surface load of the Overamstel quay, with an estimated value of approximately 20kPa. However, in reality, the quay demonstrated significantly greater strength, as failure was not observed even for loads as high as 55kPa. While part of this underprediction can be attributed to experiment-specific effects not considered in the prediction analysis, the substantial underprediction of the failure load still emphasizes the conservatism in current modelling approaches.

Clear indicators of the lateral failure mechanism include the inclined position of the top of the piles, broken piles, settlements at the backside of the quay, and lateral deflection of the foundation. These indicators can effectively be monitored, as demonstrated by the employed monitoring plan in the experiments. Elements of this plan, such as inclination sensors mounted on the pile caps, can be implemented in Amsterdam's city centre to detect signs of lateral failure.

The foundation piles experience fracture when they reach a state of full yielding, which occurs when the bending stresses in the timber surpass the modulus of rupture across the entire cross-section of the pile. Bending experiments conducted on timber piles indicate a substantial variance in both the modulus of rupture (variation coefficient of 0.26) and the modulus of elasticity (variation coefficient of 0.3). Consequently, the piles exhibit a wide range of flexural stiffnesses and bending moment capacities. These discrepancies stem from natural variability and biological degradation of the timber, which lead to the formation of a weakened outer layer or "soft shell" starting at the perimeter of the piles, going inward. The soft shell thickness is approximately 10% of the external pile diameter and it does not contribute to the structural strength of the piles.

The substantial variations in load carrying capacities within a timber pile group can be primarily attributed to the variations in pile stiffness and bending capacity. Surprisingly, typical pile group effects such as in-line, side-by-side, pile free height, and pile diameters do not have a large contribution to the variations in individual lateral pile resistances found. When multiple piles are considered together, significant variations between individual piles compensate each other, leading to a group resistance that was almost identical in the two pile group experiments. This finding is advantageous from a computational modelling and risk assessment standpoint.

Within the tested pile groups at the Overamstel site, with 200-300 mm diameter piles, partial yielding starts at approximately 100 mm of group deflection. The first pile breakages are expected to initiate at 140 mm of deformation; however, due to the redistribution of lateral loads among the piles, it does not directly result in group failure. Nevertheless, when deformations exceed 200 mm, a majority of the piles will break, leading to group failure. It is vital to emphasize that the transition from the initial onset of yielding to group failure requires merely a slight additional lateral load of 15%.

An analytical quay wall model has been developed to predict the resistance against lateral failure of historic quay walls. This model comprises a framework of elastic beams embedded in an elastic foundation, which is externally loaded by a linear elastic soil model based on Flamant's theory. The framework is made up of multiple Euler-Bernoulli beams, connected to each other by boundary and interface conditions. The stiffness of the connection between piles and headstock is described by a pile-headstock interface model. The elastic foundation is represented by a series of independent p-y springs, approximated with a bilinear elastic-perfect-plastic model. A method is developed to include the pile-soil-pile interaction and the influence of a sloping surface by adjusting the plastic branch of the p-y springs. This method has been validated through multiple experiments documented in literature in which steel piles were used, eliminating material property uncertainties.

The analytical quay wall model has been validated and calibrated with the Overamstel quay wall experiments, employing the stepwise approach. In the first step, the bending properties of the timber piles were obtained from the level 1 bending experiments. Subsequently, in the second step, the model's capability to describe laterally loaded pile groups was validated through the level 2 pile group experiments. Finally, the Flamant soil model and the model's ability to describe a historic quay were validated using the level 3 quay experiments. As a final step, the model was compared with finite element computations, demonstrating a good agreement in displacements and forces.

The analytical quay wall model accurately predicts lateral displacement, pile bending moments, and bending stresses at various depths, allowing for the assessment of pile fracture under specific surface loads. Its key advantages over state-of-the-art finite element modelling software include robustness, computational speed, feedback loops (e.g. force and displacement-dependent pile-headstock connection stiffnesses), minimal input requirements, and no numerical stability issues at large deformations. The model is highly suitable for trend analysis, sensitivity studies, and probabilistic analysis due to its short computational time in seconds, compared to complex three-dimensional FEM software that takes minutes to hours. The effectiveness and potential of the validated analytical quay wall model have been demonstrated in two "follow up" studies, described below.

In the first study, the quay model has been employed to investigate the failure of the Grimburgwal. With the model it was demonstrated that bending stresses in the timber piles exceeded the modulus of rupture as a consequence of local deepening of the canal in front of the quay. It therefore provides valuable insights for Amsterdam's historical centre. The analyses have served as an additional validation step for the analytical quay wall model developed in this thesis, specifically for applications to the quay walls of Amsterdam's historical centre.

In the second study the quay model has been used to effectively showcase the potential of Bayesian updating by incorporating evidence of survived loading situations and corresponding deformations. This approach enables refinement of the reliability predictions

and parameter distribution uncertainties, leading to a more accurate prediction of the resistance against the lateral failure mechanism of quay wall foundation piles. Depending on the type of evidence, an a-priori reliability prediction for a quay wall that fails to meet safety standards can be updated to any of the three consequence classes (CC3, CC2, and CC1b) outlined in NEN8700. In a fictive case study, a quay wall with an a-priori reliability of β = 1.5 has been increased to β = 3.2 by including evidence of an extreme survived load of 10 kN/m^2 that resulted in displacements of less than 4mm. This is a decrease in failure probability by two orders of magnitude, showing the potential impact of using observational information in combination with Bayesian updating

The main practical implication of this thesis has been the improvement in modelling accuracy, as a result of the Overamstel experiments. The revised "gain" in modelling accuracy for bending moments and deflection was 43% and 37% respectively. This improvement can be attributed to advancements in modelling techniques, such as accurately simulating pile-soil-pile interaction and modelling the pile-headstock connection, as well as utilizing precise location-specific geotechnical and structural material properties as model input. The improved modelling accuracy results in a less conservative evaluation of the quay walls, leading to a reduction in the number of unnecessarily rejected quay walls for the Amsterdam quay wall domain.

The most practical recommendations for Amsterdam are: a) to develop accurate techniques for mapping quay wall configurations, b) to implement comprehensive quay wall monitoring systems in the city centre, c) to utilize the analytical model in future studies and assessments, d) prioritize geotechnical site investigations before making model predictions, and e) perform non-destructive tests in the city centre and incorporate this information in the assessment.

The methods and insights developed in this dissertation enhance the understanding of the lateral failure of historic quay walls and enable more precise predictions of their resistance against such failures. The developed model can be effectively used to support decisions regarding the safe usage, remaining service life, and the necessity of replacement of urban quay walls.

Samenvatting

Amsterdam staat voor de uitdaging om een historisch kademuur areaal van 200 km te onderhouden, hetgeen een essentieel onderdeel vormt van het straatbeeld in de stad. Veel kades verkeren momenteel in slechte staat en vereisen renovatie of vervanging in de nabije toekomst, wat een aanzienlijke impact op de stad heeft. De kademuren kunnen tot 300 jaar oud zijn en de constructie bestaat uit een gemetselde gewichtsmuur bovenop een houten vloer, die wordt ondersteund door kespen op meerdere houten loodpalen. In de afgelopen jaren hebben de kademuren tekenen van schade, gedeeltelijke instorting en waarschuwingssignalen van dergelijke gebeurtenissen ervaren. Het meest recente en ernstige incident was de instorting van de Grimburgwal in 2020, waarbij ongeveer 20 meter kademuur plotseling instortte en binnen enkele seconden in het kanaal stortte. Het is daarom belangrijk om de weerstand van deze constructies te kunnen voorspellen en hun potentiële faalmechanismen te begrijpen.

Het meest voorkomende en ernstigste faalmechanisme dat wordt waargenomen in het centrum van Amsterdam is het laterale falen van de paalfundering, geïllustreerd in de onderstaande figuur. Berekeningen van de weerstand tegen dit mechanisme met bestaande modellen geven onvoldoende sterkte en veiligheid weer. Het lijkt erop dat deze modellen te conservatief zijn, omdat in werkelijkheid de meeste bestaande constructies die op papier onveilig lijken, in de praktijk vrij goed presteren. Het verschil tussen de modellen en de werkelijkheid komt door onzekerheden in de werking van historische kademuren, onzekerheden in de geometrie en in het geotechnisch en constructief materiaalgedrag.

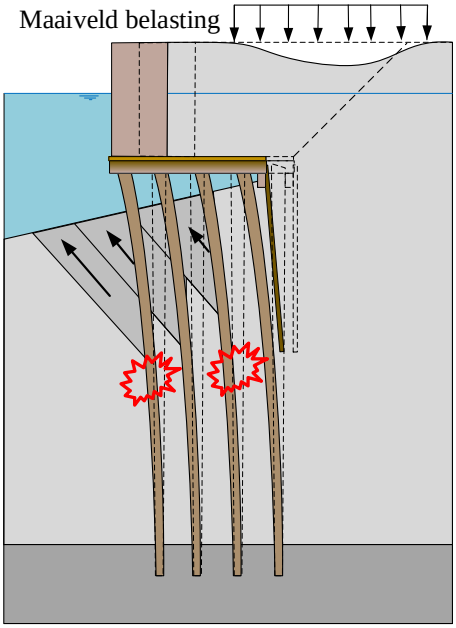

Faal mechanisme ‘lateraal bezwijken van de paalfundering’ van een kade.

Dit proefschrift biedt een grondig inzicht in het lateraal falen van de paalfundering doormiddel van grootschalige kademuur-experimenten en het stelt een rekenkundig kademuurmodel voor om de weerstand tegen dit faalmechanisme te voorspellen.

Om een uitgebreid begrip van het laterale bezwijkmechanisme te krijgen, is er een uniek en uitgebreid experimenteel programma uitgevoerd op een bestaande historische kademuur die gefundeerd is op houten palen. De kade is gelegen in Amsterdam Overamstel en dateert uit 1905. Er zijn experimenten uitgevoerd op drie verschillende systeemniveaus. Op niveau 1 zijn vier-punts-buigproeven uitgevoerd op individuele palen om de buigeigenschappen van het materiaal te verkrijgen. Op niveau 2 zijn laterale paalgroep experimenten uitgevoerd op een 3x4 paalgroep om de paal-grond-paal interactie te bestuderen. Op niveau 3 zijn proefbelastingen uitgevoerd op kademuursecties op ware grootte om het algehele gedrag van de kademuur te bestuderen. Als onderdeel van het experimentele programma is een uitgebreid geotechnisch bodemonderzoek uitgevoerd. De gekozen experimentele aanpak maakt een stapsgewijze validatie en kalibratie mogelijk voor rekenmodellen van de kademuur op de drie systeemniveaus.

Met behulp van het experimentele programma is aangetoond dat het laterale faalmechanisme het meest waarschijnlijk optreedt wanneer een kademuur aan de achterzijde op het maaiveld wordt belast. Voorbeelden van dergelijke belastingen in de praktijk zijn geparkeerde of rijdende auto's, zware voertuigen of goederen/bouwmaterialen. Het mechanisme wordt getriggerd door een toename van de effectieve grondspanning aan de achterzijde van de kademuur, die vervolgens de fundering naar het water duwt. Dit resulteert op zijn beurt in het buigen van de palen, hetgeen gepaard gaat met de ontwikkeling van buigspanningen in het hout. Bestaande modellen (ABAQUS, PLAXIS en veermodellen) werden gebruikt om de kritieke maaiveldbelasting te bepalen waarbij de kade zou falen, met een geschatte waarde van 20 kPa. In werkelijkheid vertoonde de kade echter veel grotere sterkte, aangezien er zelfs bij belastingen tot 55 kPa geen falen werd waargenomen. Hoewel een deel van deze onderschatting kan worden toegeschreven aan experiment-specifieke effecten die niet in de predictie analyse werden meegenomen, benadrukt de aanzienlijke onderschatting het conservatisme in de huidige modelleringswijze.

Duidelijke indicatoren van het lateraal faal mechanisme zijn negatief schoorstaande palen, gebroken palen, zettingen aan de achterzijde van de kademuur en laterale vervorming van de fundering. Deze indicatoren kunnen effectief worden gemonitord, zoals is aangetoond door het gebruikte monitoringplan in de experimenten. Elementen van dit plan, zoals scheefstand-sensoren op de paalkoppen, kunnen worden geïmplementeerd in het stadscentrum van Amsterdam om tekenen van lateraal falen te detecteren.

De funderingspalen breken wanneer de vezels in het hout volledig plastisch vervormen, hetgeen optreedt wanneer de buigspanningen in het hout de buigtreksterkte van het hout overschrijden over de gehele doorsnede van de paal. Buigproeven op houten palen laten een aanzienlijke variatie zien in zowel de buigtreksterkte (variatie coëfficiënt van 0.26) als elasticiteitsmodulus (variatie coëfficiënt van 0.30). Als gevolg hiervan hebben de palen een breed scala aan buigstijfheden en buigende momentcapaciteiten. Deze spreiding is het gevolg van natuurlijke variabiliteit en biologische degradatie van het hout, wat leidt tot de verzwakking van de buitenste laag, ook wel bekend als de "zachte schil", die zich vanaf de buitenkant van de palen naar binnen toe verspreidt. De zachte schil heeft een dikte die ongeveer gelijk is aan 10% van de externe paaldiameter en draagt niet bij aan de constructieve sterkte van de palen.

De aanzienlijke variaties in lateraal draagvermogen die worden waargenomen in lateraal belaste paalgroepen kunnen voornamelijk worden toegeschreven aan variaties in de paal stijfheid en momenten capaciteit van de palen. Opvallend genoeg dragen typische effecten die we kennen bij lateraal belaste paalgroepen, zoals in-line, side-by-side, de vrije hoogte van de palen en paaldiameters, niet sterk bij aan de gevonden variaties tussen

individuele palen. Wanneer meerdere palen samen worden beschouwd, middelen variaties in individuelen palen elkaar uit. Deze bevinding is gunstig vanuit een modellerings- en risicobeoordelingsperspectief.

Voor de geteste paalgroepen op de Overamstel-locatie, met palen van 200-300 mm diameter, begint hout plastisch gedrag te vertonen bij groepsvervormingen van ongeveer 100 mm. De eerste paalbreuken worden verwacht bij 140 mm vervorming; echter, vanwege de herverdeling tussen de palen in de groep, leidt dit niet direct tot groeps-falen. Desalniettemin, wanneer de vervormingen de 200 mm overschrijden, zullen de meeste palen breken, wat leidt tot groeps-falen. Het is van essentieel belang om te benadrukken dat de overgang van het initiële begin van plastische vervormingen tot aan groeps-falen slechts een additionele laterale belasting van 15% vereist.

Er is een analytisch rekenkundig kademuurmodel ontwikkeld om de weerstand tegen lateraal bezwijken van historische kademuren te voorspellen. Dit model bestaat uit een raamwerk van elastische balken ingebed in een elastische fundering, dat extern wordt belast door een lineair-elastisch grondmodel gebaseerd op de theorie van Flamant. Het raamwerk bestaat uit meerdere Euler-Bernoulli balken, die met elkaar verbonden zijn door rand- en overgangsvoorwaarden. De stijfheid van de verbinding tussen palen en de kesp is beschreven door middel van een paal-kesp interface model. De elastische fundering bestaat uit een reeks onafhankelijke p-y-veren, benaderd met een elastisch-perfect-plastisch model. Er is een methode ontwikkeld om de paal-grond-paal interactie en de invloed van een talud op te nemen door de plastische tak van de p-y-veren aan te passen. Deze methode is gevalideerd aan de hand van meerdere experimenten gedocumenteerd in de literatuur waarin stalen palen werden gebruikt, waardoor onzekerheden in materiaaleigenschappen zijn geëlimineerd.

Het analytische model van de kademuur is vervolgens gevalideerd en gekalibreerd met behulp van de Overamstel kademuur-experimenten, waarbij de stapsgewijze methodiek werd toegepast. In de eerste stap werden de buigeigenschappen van de houten palen verkregen uit de niveau 1 buig experimenten. Vervolgens is de paal-grond-paal interactie van het model gevalideerd met de niveau 2 paalgroep experimenten. Ten slotte is het grondmodel en het vermogen van het model om een historische kademuur te beschrijven gevalideerd met behulp van de niveau 3 kademuur-experimenten. Als laatste stap is het model vergeleken met eindige-elementen berekeningen, waarbij een goede overeenstemming werd aangetoond in verplaatsingen en krachten.

Het analytische model van de kademuur voorspelt nauwkeurig laterale verplaatsingen, buigende momenten in de palen en bijbehorende buigspanningen, waardoor een beoordeling van lateraal falen mogelijk is voor verschillende kademuur geometrieën en verschillende belastingen op het maaiveld. De belangrijkste voordelen ten opzichte van geavanceerde eindige-elementen (EEM) programma's zijn robuustheid, rekenkracht, feedback loops (bijv. kracht- en verplaatsingsafhankelijke paal-kesp connectiestijfheden), minimale invoervereisten en geen numerieke stabiliteitsproblemen bij grote vervormingen. Het model is zeer geschikt voor trendanalyses, gevoeligheidsstudies en probabilistische analyses vanwege de korte rekentijd in seconden, in tegenstelling tot complexe driedimensionale EEM-software die minuten tot uren in beslag neemt. De effectiviteit en potentie van het gevalideerde analytische kademuurmodel is aangetoond in twee "vervolgstudies", hieronder beschreven.

In de eerste studie is het kademuurmodel gebruikt om het falen van de Grimburgwal te onderzoeken. Met behulp van het model is aangetoond dat de buigspanningen in de houten palen de buigtreksterkte overschreden als gevolg van een lokale verdieping in het kanaal voor

de kademuur. Het levert daarmee waardevolle inzichten op voor de gemeente Amsterdam. De analyses dienden tevens als een aanvullende validatiestap voor het ontwikkelde kademuurmodel, specifiek voor toepassingen op de kademuren in het historische centrum van Amsterdam.

In de tweede studie is het kademuurmodel gebruikt om het potentieel van bewezen sterkte aan te tonen door bewijs van overleefde belastingsituaties en bijbehorende vervormingen mee te nemen in de beoordeling. Deze aanpak maak het mogelijk om faalkansen aan te scherpen en parameteronzekerheden te verkleinen. Dit leidt tot een nauwkeurigere voorspelling van de weerstand tegen het laterale faalmechanisme van de kademuur. Afhankelijk van het soort bewijs kan een a-priori betrouwbaarheidsanalyse voor een kademuur die niet voldoet aan de veiligheidsnormen worden bijgesteld naar een van de drie gevolg klassen (CC3, CC2 en CC1b) zoals beschreven in NEN8700. In een fictieve casestudy is de betrouwbaarheid van een kademuur, die aanvankelijk $\beta = 1.5$ was, verhoogd naar $\beta = 3.2$ door bewijs van een extreme overleefde belasting van 10 kPa, met bijbehorende verplaatsingen van minder dan 4 mm, mee te nemen in de beoordeling. Dit komt neer op een afname van de faalkans met twee ordes van grootte, wat het potentieel aantoont van het gebruik van observatie-informatie in combinatie met Bayesian updating.

De belangrijkste praktische implicatie van dit proefschrift is de verbetering van de modellering van binnenstedelijke kademuren, als gevolg van de Overamstel-experimenten. De “winst” in nauwkeurigheid voor het bepalen van buigende momenten en vervormingen in de paalfundering is respectievelijk 43% en 37%. Deze verbetering komt door verbeterde modelleringstechnieken, zoals het correct simuleren van paal-grond-paal interactie en het modelleren van de paal-kespverbinding, evenals het gebruik van precieze locatie-specifieke geotechnische- en constructieve materiaaleigenschappen als modelinvoer. De verbeterde modellering resulteert in een minder conservatieve evaluatie van de kademuren, wat leidt tot een vermindering van het aantal onnodig afgekeurde kademuren voor het Amsterdams kademuren areaal.

De meest praktische aanbevelingen voor Amsterdam zijn: a) het ontwikkelen van nauwkeurige technieken om kademuur geometrieën in kaart te brengen, b) het implementeren van uitgebreide monitoringssystemen voor kademuren in het stadscentrum, c) het gebruik van het analytische model in toekomstige studies en beoordelingen, d) het uitvoeren van geotechnisch onderzoek voordat model berekeningen worden gedaan, en e) het uitvoeren van niet-destructieve testen in het stadscentrum en deze informatie meenemen in de beoordeling.

De methodieken en inzichten die in dit proefschrift zijn ontwikkeld, vergroten het begrip van het lateraal bezwijk mechanisme van binnenstedelijke kademuren en stellen ons in staat om nauwkeurigere voorspellingen te doen van hun weerstand tegen falen. Het ontwikkelde model kan effectief worden gebruikt om beslissingen met betrekking tot het veilige gebruik, de resterende levensduur en de noodzaak van vervanging van binnenstedelijke kademuren te ondersteunen.

List of symbols and abbreviations

1[ ]	The indicator function
1V:2H	One Vertical - Two Horizontal (slope inclination)
BEF	Beam on Elastic Foundation
BH	Bore Hole
CPT	Cone Penetration Test
CPTu	Cone Penetration Test with pore pressure measurement
cpw	Corrected passive wedge
CV	Coefficient of variation
Eq.	Equation
FC	Fragility curve
FEM	Finite Element Modelling
FO	Fibre Optic
FORM	First Order Reliability Method
FRP	Fibre Reinforced Polymer
FS	Failure Slice
IML	Non destructive micro drilling
IPI	In-Placed-Inclinometer
MC	Monte Carlo method
MEMS	Micro Electro-Mechanical System
MOE	Modulus Of Elasticity
MOR	Modulus Of Rupture
NAP	Normaal Amsterdams Peil
PBK	Programma Bruggen en Kademuren
PDF	Probability Density Function
PS	Phreatic Sensor
RTS	Robotic Total Station
SAAF	Shape Accel Array Field
SCPT	Seismic Cone Penetration Test
SW	Strain Wedge
UC	Unity Check
WPS	Water Pressure Sensor

Latin

a	[m]	Depth of maximal moment
A		Coefficient matrix
a_i		Sensitivity factors
c	[kN/m^2]	Cohesion soil
C		Integration constant / vector containing integration constants
c'	[kN/m^2]	Effective cohesion soil
D	[m]	Diameter of the pile
D_F	[m]	Diameter of the pile centre line of loading
D_l	[m]	Diameter of the pile at local reference system ($x = 0$)
dx	[m]	Grid width of failure slice cell
dy	[m]	Grid length of failure slice cell
dz	[m]	Grid height of failure slice cell

E_b	[MPa]	Young's bending modulus (for timbers often referred to as MOE)
$E_{b,mean}$	[MPa]	Mean young's bending modulus parallel to the fibre
E_c	[MPa]	Young's compression modulus
e	[m]	Eccentricity
EI	[kNm^2]	Flexural stiffness pile
EI_d	[kNm^2]	Flexural stiffness headstock
$\widetilde{EI}$	[kNm^2]	Flexural stiffness pile obtained from four point bending tests
F	[kN]	Arbitrary load
f		Failure
F_1	[kN]	First point load in four-point bending test
F_2	[kN]	Second point load in four-point bending test
F_{cap}	[kN]	Measured lateral cap force
$F_{container}$	[kN]	Pile averaged vertical container load (in quay experiments A,B,C,D)
F_{fill}	[kN]	Resultant horizontal load on the top structure per unit width
F_{group}	[kN]	Lateral group resistance
F_h	[kN]	Active soil force
F_k	[kN]	Euler buckling force
$F_{lateral}$	[kN]	Average lateral pile resistance (in pile group experiments F)
f_m	[N/mm^2]	Bending strength parallel to the fibre
f_m	[N/mm^2]	Compression strength parallel to the fibre
$f_{m,k}$	[N/mm^2]	Characteristic bending strength parallel to the fibre
f_s	[MPa]	Sleeve friction from CPTu
F_s	[kN]	Force from sheet pile on transverse beam per unit width
$f_{\underline{X}}$		Common probability density function of $\underline{X}$
F_τ	[kN]	Total segmental friction force per unit width
g		Performance function
G		β-q curve (fragility curve)
G_w	[kN]	Weight of the gravity wall per unit width
G_η		β-q observation curve (fragility curve for observation)
H	[m]	Effective pile diameter
h_d	[m]	Transverse beam height
h_{EW}	[m]	The centre-to-centre distance between East and West fibre
h_{NW}	[m]	The centre-to-centre distance between North and South fibre
h_p	[m]	Pin height
h_w	[m]	Wedge depth
I	[m^4]	Moment of inertia piles
I_d	[m^4]	Moment of inertia transverse beam
k	[kN/m^2]	Spring stiffness
K_a		Active soil pressure coefficient
K_c		Lateral earth pressure coefficient for cohesion
k_h	[kN/m^3]	The modulus of horizontal subgrade reaction
K_p		Passive soil pressure coefficient
K_q		Lateral earth pressure coefficient
L	[m]	Length of pile
L_1	[m]	Location of first point load in four-point bending test
L_2	[m]	Location of second point load in four-point bending test
L_b	[m]	Pile breakage depth with respect to loading centre line
L_f	[m]	Free pile length (part of the pile which is not embedded in soil)

L_k	[m]	Buckling length
L_s	[m]	Sheet pile length
$L_{s,eff}$	[m]	Embedded sheet pile length
M	[kNm]	Bending moment
m		Number of failure slice cells
M^*		Normalized moment by first yield moment
M_0	[kNm]	First yield moment
M_{con}	[kNm]	Bending moment obtained with constant pile diameter.
$M_{d,l}$	[kNm]	Bending moment left of the pile-transverse beam connection
$M_{d,r}$	[kNm]	Bending moment right of the pile-transverse beam connection
M_e	[kNm]	Eccentric moment
MOR	[N/mm^2]	Modulus of rupture in bending
M_{pin}	[kNm]	Pin moment
M_{rot}	[kNm]	Pile cap moment
N	[kN]	Axial load / Normal force
n		Number of unique soil layers
n		Total number of simulations
$N_{d,l}$	[kN]	Normal force left of the pile-transverse beam connection
$N_{d,r}$	[kN]	Normal force right of the pile-transverse beam connection
n_f		Number of failed simulations
N_p	[kN]	Axial force on the pile cap
O		Exceedance observation function
p	[kN/m^2]	The soil reaction of the pile
P_f		Probability of failure
$P_{f,p}$		Posterior probability of failure
$P_{f,p;FC,\eta 1}$		Posterior probability of failure with FC and evidence $\eta 1$
$P_{f,p;MC,\eta 1}$		Posterior probability of failure with MC and evidence $\eta 1$
$P_{f,p;MC,\eta 2}$		Posterior probability of failure with MC and evidence $\eta 2$
P_s		Probability of survival
P_w	[m]	Polynomial fit trough prism measurements
q	[kN/m^2]	Arbitrary distributed load
Q		Force vector
q_c	[MPa]	Cone resistance from CPTu
q_c	[kN/m^2]	Critical surface load
$q_{c,\eta}$	[kN/m^2]	Critical surface load during observation
q_d	[kN/m]	Load representing the soil on the quay floor per unit width
$q_{d,G}$	[kN/m]	Load representing the gravity wall on the quay floor per unit width
q_f	[kN/m]	Horizontal effective stress along imaginary boundary per unit width
q_G	[kN/m]	Horizontal load on the gravity wall per unit width
q_h	[kN/m]	Horizontal effective stress along the sheet pile per unit width
q_s	[kN/m]	Horizontal distributed load from sheet pile on piles per unit width
q_η	[kN/m^2]	Survived extreme surface load
R		Resistance of the structure
R_{int}		Interface strength
r	[m]	Distance between F and point of interest in the stress field
R^2		R-squared
S		Load on a structure

s		Loading variable
s_c		Critical load
s_u	[kN/m^2]	Undrained shear strength
u		Realization of a standard normal random variable
u_0	[MPa]	In-situ hydrostatic stress
u_2	[MPa]	Pore pressure from CPTu
V	[kN]	Shear force
v	[m]	Lateral deflection of the piles within the quay framework
$V_{d,l}$	[kN]	Shear force left of the pile-transverse beam connection
$V_{d,r}$	[kN]	Shear force right of the pile-transverse beam connection
v_f		Amplification factor Euler buckling
V_p	[kN]	Transverse force on the pile cap
W	[kN]	Total weight of a failure slice
w	[m]	Vertical deflection of transverse beams within the quay framework
W_{cpw}	[kN]	Corrected failure slice weight
w_d	[m]	Transverse beam width
w_p	[m]	Pin width
W_s	[m]	Width of quay wall segment
w_η	[m]	Observed mean deformation
$w_{\eta,max}$	[m]	Upper bound of the observed displacements
$w_{\eta,min}$	[m]	Lower bound of the observed displacements
X	[m]	Distance between pile and start slope
$\underline{X}$		Vector of random variables
x_{Fi}	[m]	x-location of the centre of the pile within a pile group
$\underline{X}_\eta$		Vector of all random variables at the time of observed survival
y	[m]	Pile displacement
y_{Fi}	[m]	y-location of the centre of the pile within a pile group
z	[m]	Depth
Z		Limit state function

Greek

Δ		Difference between observation and reliability prediction
a	[m/m]	Tapering of pile
a_F	[-]	Load ratio between two point loads in a four-point bending test.
β_i		Load fraction parameter for sheet pile onto the piles
β		Reliability index
β_m	[deg]	Mobilized base angle
β_p		Posterior reliability index
β_s	[deg]	Wedge angle of the active soil volume
γ	[kN/m^3]	Soil weight
γ'	[kN/m^3]	Effective soil weight
δ	[deg]	Friction angle coefficient
ε		Material strain
ε_E		Measured strains in the East fibre
ε_N		Measured strains in the North fibre
ε_S		Measured strains in the South fibre
ε_W		Measured strains in the West fibre

η		Evidence
η_1		Evidence of a survived extreme surface load
η_2		Evidence of a survived extreme surface load with deformation measurements.
θ	[rad]	Gradient of between F and point of interest in the stress field
θ_1	[rad]	First gradient of between q and point of interest in the stress field
θ_2	[rad]	Second gradient of between q and point of interest in the stress field
κ	[m^{-1}]	Curvature
κ^*		Normalized curvature by first yield curvature
κ_0	[m^{-1}]	First yield curvature
κ_{EW}	[m^{-1}]	Curvature in East-West direction
κ_{NS}	[m^{-1}]	Curvature in North-South direction
κ_t	[m^{-1}]	Total curvature in plane of bending
ρ		Correlation coefficient
ρ_t	[kg/m^3]	Density of timber pile
σ	[N/mm^2]	Bending stress
σ_{outer}	[N/mm^2]	Bending stress in the most outer fibre
σ_p	[kN/m^2]	Pressure per unit front area of pile
σ_{pc}	[kN/m^2]	Corrected pressure per unit front area of the pile
σ_v'	[kN/m^2]	Effective overburden pressure
σ_{xz}	[kN/m]	Effective shear stress
σ_{zz}	[kN/m]	Vertical effective stress per unit width
τ	[kN]	Total friction of a failure plane
τ_{cpw}	[kN]	Corrected failure plane friction
τ_s	[kN]	Friction force at one side of the quay wall segment
φ	[rad]	Pile rotation
φ	[deg]	Internal friction angle
Φ		Cumulative normal distribution
Φ_{EI}		Linear scaler parameter for flexural bending stiffness
φ_m	[deg]	Wedge fan angle
φ_r	[rad]	Deviation between fibre orientational plane and the plane of actual bending
Φ_{soil}		Soil scalar parameter for lateral load and bending moment.
Φ_w		Segmental friction coefficient
Ψ_c		Correction factor for the cohesion
Ψ_γ		Correction factor for the overburden pressure
Ω	[%]	Micro drilling drill resistance
Ω_f	[%]	Micro drilling feed resistance

Contents

1 Introduction

Photograph by the author

1.1 Historic inner-city quay walls

1.1.1 History of inner-city quay walls

Because of the poor soil conditions in the Northwestern part of Europe, houses, public buildings and infrastructures were founded on timber piles. Also the historical inner-city quay walls which can be found along the canals in the historic hearts of many Northwestern European cities like Hamburg, Copenhagen and Amsterdam. The specific application in this thesis relates to the strength of historic quay walls in the city centre of Amsterdam. The historical quay walls of Amsterdam have been integral to the city's waterway system for centuries, providing docking, shelter, unloading, and loading services for local smaller ships[1]. Up until the early 20th century, the loads on the quay walls comprised of goods, horses, and carriages. In addition, the canals serve a vital purpose of regulating the flow of water in and out of Amsterdam, ensuring the city's continued prosperity. A painting showing the quay walls as part of the unique golden age (17th century) cityscape is presented in Figure 1.1. Bridges were present for crossing the canals, with their abutments founded on timber piles that were similar to the foundations of quay walls.

Figure 1.1, Painting of the Nieuwezijds Voorburgwal near the Bloemmarkt by Gerrit Berckheyde ca.1675. (Archive of Amsterdam)

The development of Amsterdam over the past millennium has shaped the city's structure and its quay walls. It is important to highlight the historical background of quay walls in order to better understand the present-day issues. In the distant past, every house owner of Amsterdam was responsible for the quay and its revetment in front of their house. This led to unsustainable situations such as illegal land reclamations and irregular construction works until the fourteenth century. In response, a provision was made in April 22, 1399, mandating

[1] Larger vessels anchored outside the city centre on the river 'IJ' (North-West of Amsterdam) and transferred their cargo to smaller ships for unloading. The largest ships (used for the United East Indian Company), could not enter the 'Zuiderzee' and were moored at the Reede of Texel.

that the facade of the house must be at least 3.7 meters away from the waterfront, and the rear of the house at least 2.8 meters away from the waterfront (Tussenbroek, 2012). This reveals the width of the quays and shows that the waterfront with the embankment was a reference point for the buildings along the street. The development of Amsterdam within the 'Singel gracht' area in sixteenth and seventeenth century is presented in Figure 1.2. The Singel Gracht is a waterway that encompasses the entire Amsterdam centre. In the past, the canal and the ramparts on the city side served as the outer fortifications of the city.

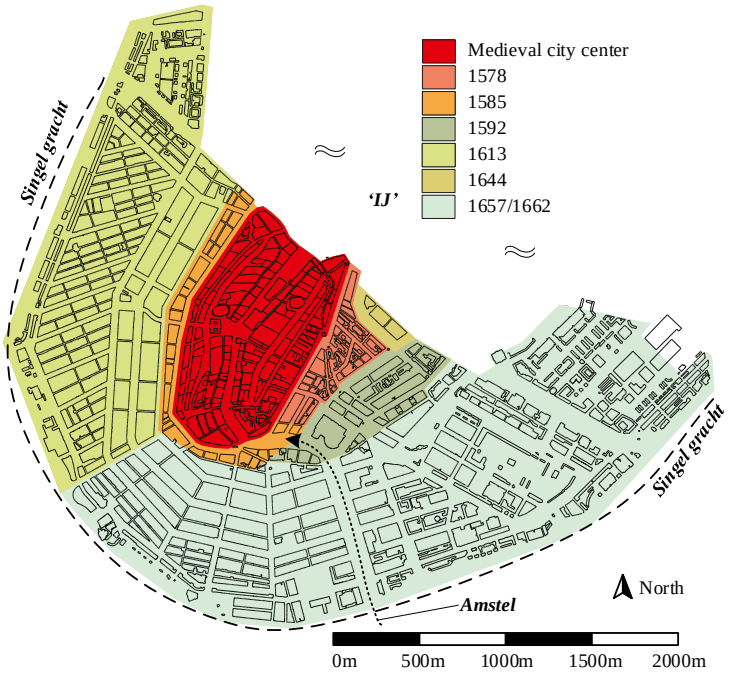

Figure 1.2, Development of Amsterdam within the 'Singel gracht'. Edited version, original from (Tussenbroek, 2012).

Around the year 1550, the city had around 13,000 inhabitants of which the majority lived in the medieval city centre. In 1578, the year of the 'Aliteratie', the mayors of Amsterdam decided that the city needed to expand because of military-defensive and economical reasons. The first of eventually four consecutive phases of expansion lasted until 1586. Even before the first expansion was completed, a much more ambitious plan was carried out, partly due to the increasing pressure from the Spanish troops. Four artificial islands were created, Marken, Uilenburg, Rapenburg and Vlooienburg, of which the last three were used to accommodate the growing shipbuilding industry. The second expansion was soon a fact and between 1578 and 1596 the total city area was almost doubled. New canals were dug, which were connected to the existing network of before 1578 and provided direct access to the river Amstel or the IJ. Nevertheless, even after this extraordinary urban achievement, the city still did not have enough space to accommodate the continuous stream of newcomers. In 1610, another decision was made to extend the city. In comparison to previous expansions, this expansion mostly involved extending towards – until that moment – undeveloped land and bringing it within city limits of Amsterdam. Many new canals, quay walls, bridges, and especially new houses and streets were built. The third expansion was a fact, and the three

most famous canals since then were dug: the Herengracht, Keizersgracht and Prinsengracht (see Figure 1.3). This time, the work was done on a much larger scale than for the older, narrower canals. The canals were broad and bounded by high quay walls. The canals were popular among the wealthier citizens, who often purchased double lots and built houses with beautiful façades and many tall windows that provided views to the water. The larger canals were connected to smaller cross-canals, and in 1652, the fourth and final expansion of the city (and its canal system) began. This expansion was an indirect result of a national conflict in 1650, which led to a period where the regents of Amsterdam and other major cities held power, and the succession of the late Prince of Orange, Willem II, was postponed. The fourth expansion was needed because of a wave of immigrants and a lack of space caused by the flourishing trade, similar to the preceding decades. In just under 120 years, the population of Amsterdam grew from 13,000 inhabitants to more than 160,000, a twelve-fold increase.

Figure 1.3, View along the Prinsengracht near the Reesluis in a northern direction. Approximately 1717-1735. (Archive of Amsterdam)

Between 1650 and 1730, the population of the city continued to grow until it reached around 240,000 citizens, making it the third largest city in Europe after London and Paris. In the 30's of the 18th century this growth comes to a stop. The city was no longer able to create the vast number of job opportunities and other economic possibilities that had made it a European economic power. As a result, the Amsterdam economy declined and a lacklustre, culturally uninspired climate emerged. In 1815, the population of Amsterdam declined to 180,000 and the city, which had taken its definitive shape after the fourth major expansion, began to show signs of decay. Many houses were abandoned and some neighbourhoods became slums. The quay walls and bridges were also subject to significant deterioration. With the construction of the 'Noordzee kanaal' in 1876 Amsterdam became ones again an important seaport. Because of the industrialization and better living conditions and healthcare, the population of Amsterdam grew from 240,000 in 1860 to 500,000 in 1900. This growth was accompanied by the expansion of the city outside the Singel Gracht. In 1877, plans were devised to construct the 19th century "Grachten gordel" (Canal belt) in Amsterdam. This development

involved the construction of new housing and quay walls, which were also built on timber piles. At this point, the purpose of the quay walls had drastically changed. Rather than serving as a place for loading and unloading cargo, the quay walls in Amsterdam had become a roadway, a cultural landscape, and a place for public recreation. The majority of quays fell under the jurisdiction of the municipality instead of private owners. The historic centre of Amsterdam remained untouched throughout the two World Wars. As of 2023, Amsterdam has seen an increase in population due to modern expansion, bringing its total number of inhabitants to 870,000.

1.1.2 Present day issues

In 2023, the municipality of Amsterdam faces the immense task of maintaining a quay wall area that spans over 200km throughout the city. In many places, the quays are part of the historic cityscape and represent historical value. The quay walls and canals of Amsterdam are part of the national heritage and are an UNESCO monument. Many of the quays are over a hundred years old and come in a variety of configurations, which are intensively used by road traffic, often also by heavy vehicles. In recent years, quay walls have experienced signs of damage, partial collapse, and premonitory warnings of such events. Examples of recently collapsed quay walls in the period 2017-2020 include: the Entrepotdok[1], Marnixstraat[2], the Nassaukade[3] and the Grimburgwal[4]. After research by an external commission in 2019 (Cloo, 2019), a bridges and quay wall program 'Programma Bruggen en Kademuren' was set-up (Amsterdam, 2020b). The program focuses on three parallel areas of work: research, safety measures and renovation or replacement.

Research: In collaboration with various knowledge institutes, the municipality works on improving the knowledge of historical quay walls to gain a better insight in the structural state. Research on the topic includes a range of diverse methods and studies, such as divers inspections (Pagella et al., 2021), seismic survey methods (Balestrini et al., 2021), satellite monitoring (Venmans et al., 2020), lab-experiments on timber piles (van de Kuilen et al., 2021) and masonry (Sharma et al., 2023), axial bearing capacity of timber piles (Honardar, 2020), the recently started NWA Urbiquay program (4 million euros) (NWO, 2022), and lastly this study.

Safety measures: Not all quay walls can be replaced at once. For quay walls that show early signs of failure, traffic restrictions or even temporary stabilizing sheet pile structures are employed. Bridges and quay walls in the highest risk category are monitored frequently.

Renovation and replacement: As part of an innovation partnership (IPK) (Amsterdam, 2019), the municipality of Amsterdam is collaborating with market partners to develop smart, innovative, and durable quay walls. In this partnership, some quay walls are completely replaced or provided with a new foundation. This is done both in a planned and systematic way, as well as on an ad hoc basis, in the event that the quay wall exhibits unexpected signs of damage or collapse. In 2021, the average cost of replacing 1km of quay wall was 35M euros (Kruyswijk, 2021). With a total length of 200 kilometres, the total cost of renovation today can be roughly estimated to be more than seven billion euros.

[1] ("Ravage door sinkhole in Amsterdam," 2017)
[2] ("Sinkhole Marnixstraat zorgt nog langer voor hinder," 2017)
[3] ("Kademuur bij Nassaukade ingestort; lek waterleiding weer gedicht ", 2018)
[4] ("Instorten Amsterdamse kademuur deels veroorzaakt door boten," 2020)

1.2 Working principles of historic quay walls

1.2.1 Quay wall configuration

An edited photograph taken at the present time, exposing the historical quay wall construction, can be seen in Figure 1.4. A historic technical drawing, containing the terminology of quay wall components, is presented in Figure 1.5. The quay wall construction consists of a masonry cantilever wall on top of a timber floor, which is supported by headstocks situated on three to six timber pile rows. In many cases, these piles are founded on a downward sloping canal bed. Behind the gravity wall, a layer of fill is present, upon which roads, parking lots, pedestrian paths, and even trees are located. To prevent soil from moving towards the canal, a timber sheet pile wall is present of which the location can vary with respect to the headstock. The masonry wall is held firmly in place by its own weight and the addition of lateral side wood, which are secured by locking blocks.

Technical drawings, stored in the Archive of Amsterdam show that quay walls up until the 1920s were built with timber piles and timber decking. In the 1940s, concrete became an important component in the top structure of inner-city quay walls, but the foundation still relied on timber piles. Timber piles were used for quay wall foundations until the late 1980s, after which reinforced concrete piles were introduced. The use of inclined piles (raking piles) in Amsterdam began around 1900, which provided greater horizontal stability.

Figure 1.4, Cutaway drawing of historical quay wall structure. Photograph taken at Reguliersgracht, Amsterdam (Mart-Jan Hemel, 23 December 2021).

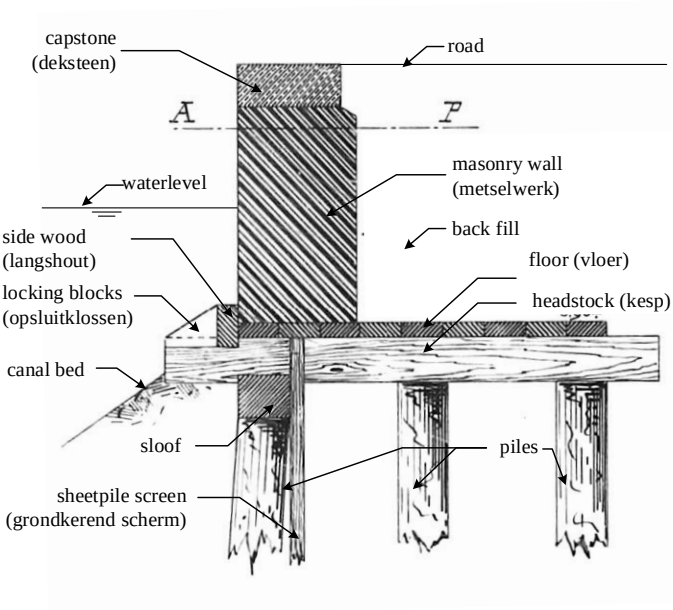

Figure 1.5, Cross-section of historical quay wall structure with terminology. (Lijnbaansgracht, tussen Palmgracht en perceelno. 14, Archive of Amsterdam)

1.2.2 Failure mechanisms

When modelling quay walls to assess their safety, it is essential to discern the various failure mechanisms and evaluate each one separately. Historical quay walls may be subjected to a variety of identified failure mechanisms, such as global stability, overturning or sliding of the masonry wall, axial bearing capacity failure of pile(s), failure of the headstocks and/or floor, lateral failure of the pile foundation, and failure of connections between headstocks and piles or sheet pile (Heming, 2019). The failure mechanisms are visualized in Figure 1.6.

Among the listed failure mechanisms, the lateral failure of the pile foundation is regarded as the most critical. In this mechanism, the soil pressure at the backside of the quay wall pushes the quay wall towards the canal side. The passive resistance against this active horizontal force is generated by the lateral resistance of the pile foundation. In fact, the quay wall acts as a soil retaining structure. In the event that the active horizontal force becomes larger than the horizontal resistance of the pile group, lateral failure of the pile foundation is expected. The pile group can experience lateral failure due to either local geotechnical failure of the pile foundation or bending capacity failure of the piles, or a combination of them. That this mechanism is considered most critical is supported by assessment reports (Neijzing et al., 2023) as well as practical observations. Early signs of this mechanism, which are most commonly observed throughout the city centre, include leaning or bulging of the quay wall towards the waterfront, surface settlements on top and behind the quay, inclined piles, or even indications of broken piles. When this type of failure occurs, the consequences can be significant, as the entire quay and its foundation may collapse into the canal. Moreover, this mechanism is the least understood. Although computational models predict failure, in reality, the quay remains stable.

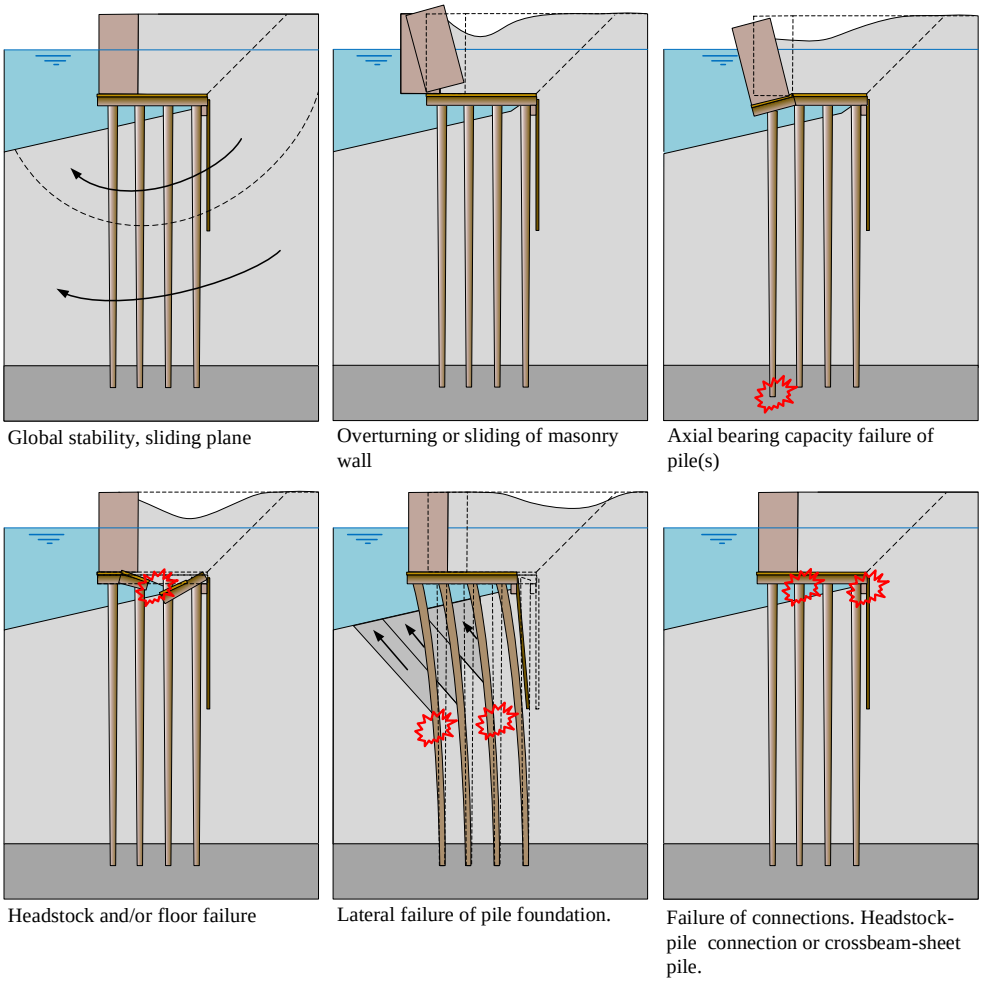

Figure 1.6, Historical quay wall failure mechanisms (not all encompassing).

1.2.3 Knowledge gaps

Although much research has been conducted on the strength of quay walls in large ports outside urban centres (De Gijt, 2010; Ichii, 2004; Roubos et al., 2014; Roubos et al., 2020), less is known about historic quay walls. Specific knowledge gaps with respect to the failure mechanism 'lateral failure of the pile foundation' are summed.

1. Frequently, the geometry of quay walls, including the number of piles, the length of the foundation, and the corresponding dimensions, are not well-documented or may be unknown. Seismic survey methods for quay walls are studied but it remains hard to identify structural elements (Balestrini et al., 2021). Studies on hydrographic inspections on historic quays using multibeam echosounder and acoustic cameras are performed by (Karamitopoulos, 2022). The method shows promise in mapping canal bottom profiles and detecting piles, but currently it is only effective for detecting piles in the first row.

2. Timber piles are subjected to bacterial deterioration (Harmsen et al., 1965; Varossieau, 1949) influencing the strength and stiffness properties of the timber. Historic timber bridge foundation piles were researched by (Pagella et al., 2021; van de Kuilen et al., 2021). In these studies, the axial strength, 'soft shell' and stiffness properties were examined. However, bending characteristics for historic pile foundations are still unknown.
3. The foundation of historic quay walls consists of closely spaced piles, inducing lateral pile-soil-pile group effects (Han et al., 1992). Many research on lateral pile has been conducted, both experimentally (Reese et al., 1975; Snyder, 2004), as modelling (Ashour et al., 2004; Hansen et al., 1960; Norris, 1986) in which mainly steel, concrete or new timber piles are considered. However, the lateral pile-soil-pile interaction of old closely-spaced timber piles in cohesive soils is not fully understood.
4. There is a significant degree of uncertainty associated with the geotechnical model input data for quay walls. The first 6-7 meters of the Amsterdam subsurface typically consist of soft clay and peat layers, for which the geotechnical strength and stiffness properties are not well defined.
5. It is not known how the soil medium behind the quay transfers its self-weight and any additional surface loads as a horizontal load onto the pile foundation. The fill medium behind the quay wall typically consists of 'man-made soil', which often includes tree roots (Amsterdam, 2020a) (possibly armouring the soil), utility lines and cable infrastructure. (Ophof, 2021) studied the influence of quay wall deformations on utility leakage, as well as the reverse relationship between leakage and quay wall failure.
6. The pile foundation of a quay wall is subject to various time-dependent effects, such as soil creep (Neukirchner, 1987) and timber creep (Van de Kuilen et al., 2011), whose impact on the force distribution within the structure is not well understood. To address this issue, Spannenburg (2020) conducted a theoretical modelling study on the effects of timber creep on forces in timber pile foundations of historic quay walls in Amsterdam (Spannenburg, 2020).
7. The three-dimensional redistribution effects of the masonry gravity wall on the overall stability of a quay wall are not yet fully understood. Several researchers have conducted theoretical modelling studies on this topic (Heming, 2019; Sharma et al., 2023; van Hulten, 2021). Currently, the city of Amsterdam and Delft University of Technology are collaborating on testing pieces of masonry to determine the material properties.

The seven knowledge gaps outlined above pose a significant challenge in demonstrating the structural safety of historic quay walls in Amsterdam through a computational assessments. Even with current models and insights, it is difficult to prove the stability without the use of a safety margin. It can be stated that an overarching 8th knowledge gap is the difficulty in assessing the lateral failure mechanism as a whole and that the current calculations exhibit a significant amount of conservatism. Because a significant portion of these knowledge gaps is associated with uncertainties in the working principles of historic quay walls, as well as uncertainties in soil and structural properties, there is clear potential for improving the analysis methods of the old quay walls to prevent that these have to be replaced on a large scale and within a short period of time.

1.3 Scope and objective

Specifically, this thesis examines the 'traditional' Amsterdam quay wall configuration, as depicted in Figure 1.5, other configurations are not directly considered. The scope of this research is limited to the lateral failure of the timber pile foundation. This failure mechanism is considered to be the most critical (as discussed in section 1.2.2). In addition to research conducted in Amsterdam, existing experimental data, research experience, and models developed from other areas of the world are utilized to create a model suitable for Amsterdam's soil and structural conditions. Masonry (gap 6) and time dependent processes such as timber creep and soil creep (gap 7) are not part of the scope.

The first objective of this study is to gain a comprehensive understanding of the quay wall failure mechanism known as 'lateral failure of the pile foundation'. A second and equally important objective in this thesis is to develop a reliable computational quay wall model (excluding conservatism) for predicting the resistance against this failure mechanism. The research aims to reduce the uncertainties associated with this particular failure mechanism and to gain further insight into its causes and effects. As failure mechanisms are often interdependent (such as the strength of timber influencing overall stability), insights gained from studying one mechanism can be applied to understanding and improving others as well. The findings of this study are not only relevant to the Amsterdam quay wall area, but also to other cities with historic timber-founded structures, as well as contemporary structures with horizontally loaded piles.

1.4 Research questions

Based on the objective stated in the previous section, the central research question of this thesis can be formulated.

How can the lateral failure of the pile foundation of historic inner-city quay walls be understood and predicted with computational models?

The central research question is addressed through a series of six key questions.

- **I.** How can an experimental program be designed to enhance our understanding of the lateral failure of historic quay walls, and to validate and calibrate computational quay wall models ? ***(Chapter 2)***
- **II.** What are the bending properties of centuries old timber quay wall foundation piles? **(*Chapter 3*)**
- **III.** How can the lateral pile group interaction of historic foundation piles be modelled and validated through testing? **(*Chapter 4*)**
- **IV.** How can the lateral failure of the pile foundation of historic quay walls be modelled and validated through testing? **(*Chapter 5*)**
- **V.** How can the analytical quay wall model be utilized to understand the collapsed Grimburgwal? **(*Chapter 6*)**

VI. How can Bayesian[1] updating be applied to reduce uncertainties in failure probabilities and refine geotechnical and structural parameter distributions associated with the lateral failure mechanism of historic quay walls? **(*Chapter 7*)**

1.5 General approach

The heart of this thesis is the development of a new computational model, which follows a stepwise approach involving three levels. These levels correspond to different levels of detail in the structural quay wall system. Level 1 focuses on the bending of timber piles, level 2 considers the lateral behaviour of timber pile groups, and level 3 addresses the lateral behaviour of historic quay walls. These levels have been chosen to isolate the major uncertainties in the lateral behaviour of historic quay walls, specifically the bending properties of individual timber piles (gap 2), the soil-pile-soil interaction of laterally loaded timber piles (gap 3), and the external loading on the pile foundation caused by the soil medium behind the quay wall (gap 5).

To address the uncertainties associated with each level, a full-scale proof load testing program is conducted. This unique experimental program takes place on a historic quay wall at Overamstel, Amsterdam, and is dedicated to testing historic quay walls in a manner that has never been done before. The experimental program comprises the three levels. Level 1 involves conducting four-point bending experiments on timber piles. Level 2 consists of lateral pile group experiments. Finally, level 3 entails performing proof load experiments on quay wall segments. Each computational model development step consists of the same cycle, a problem, an hypothesis, a predictive model, experiments to test the hypothesis, an interpretation and model validation. Together, the three steps result in a stepwise validated and calibrated model which is visualized in Figure 1.7.

As mentioned in the scope, knowledge gaps 6 (time-dependent effects) and 7 (redistribution effects of the masonry gravity wall) are not within the scope of this study. Given that the quay wall at Amsterdam Overamstel features raking piles that provided horizontal stability to the quay during its lifetime before the test, the impact of time-dependent effects such as timber creep and soil creep on the lateral movement of the timber pile foundation can be considered negligible, effectively eliminating knowledge gap 6. Note that for the experiments, the raking piles will be removed to obtain a geometry more like the inner city canal walls. Additionally, the quay wall will be loaded in a two-dimensional configuration by dividing the quay into independent segments. This approach eliminates knowledge gap 7, which pertains to the redistribution effect of the masonry gravity wall in the longitudinal direction.

[1] Bayesian updating, used for reducing modelling uncertainties and enhancing structural safety assessment, involves information from monitoring, direct observations, or past performance of engineering systems (Straub, 2011). Bayesian updating, requires fast computational time (Ehre et al., 2018) due to the many simulations needed. The modelling of both modern and historic quay walls is most often conducted through finite element programs (Alyami et al., 2009; Iai et al., 1993; Roubos et al., 2020; Wolters et al., 2014) because of the complex issue of pile-soil-pile interaction and the soil body behind the quay, which necessitates a considerable computation effort, making the process of reliability updating impractical.

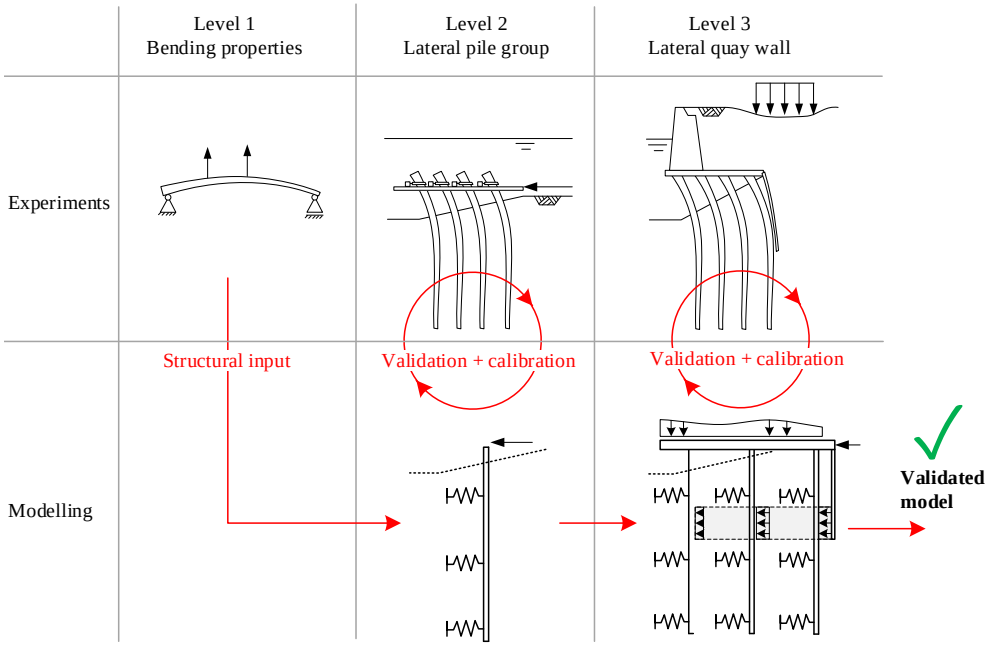

Figure 1.7, Stepwise validation and calibration approach following three levels.

1.6 Thesis outline

The chapters in this thesis are linked to the key questions by I-chapter 2, II-chapter 3, III-chapter 4, IV-chapter 5, V-chapter 6 and VI-chapter 7. The outline of the thesis can be found in Figure 1.8.

Chapter 2 provides an overview of the full-scale proof load experimental program that was established and conducted in the first half of 2022 at Amsterdam Overamstel. The chapter outlines the details about the Overamstel site, such as its quay wall configuration, geotechnical site conditions, and the experimental program. The methods and outcomes of the individual experiments are not discussed in this chapter but in chapter 3, 4 and 5. These chapters form the heart of the thesis in which the computational quay wall model is developed according to the stepwise approach.

In **chapter 3**, multiple bending experiments on timber piles are performed and analysed in order to get a better understanding of the bending properties of the timber piles. This chapter corresponds to level 1, indicated in Figure 1.7. The obtained bending properties such as the modulus of rupture, flexural stiffness and soft shell information are used as model input in chapter 4 and 5.

In **chapter 4**, an analytical pile group model is developed and validated with field experiments from literature and the lateral pile group experiments from the Overamstel test program. This chapter corresponds to level 2, indicated in Figure 1.7. The analytical pile group model is the fundament of the subsequently developed analytical quay wall model.

In **chapter 5**, the analytical quay wall model is developed which elaborates further on the analytical pile group model. The quay wall model is validated with quay wall field experiments from the Overamstel test program. This chapter corresponds to level 3, indicated in Figure 1.7.

In **chapter 6**, the analytical quay wall model is used to investigate the collapse of the Grimburgwal using a forensic engineering approach. This chapter can be seen as an extra validation of the quay wall model on a real life failure case.

In **chapter 7** the analytical quay wall model is used to demonstrate the potential of Bayesian updating for historical inner city quay walls.

A conclusive **chapter 8** answers the research questions and reflects on the previous chapters and describes how all findings result in a better understanding and modelling approach of lateral pile foundation failure of historic inner-city quay walls.

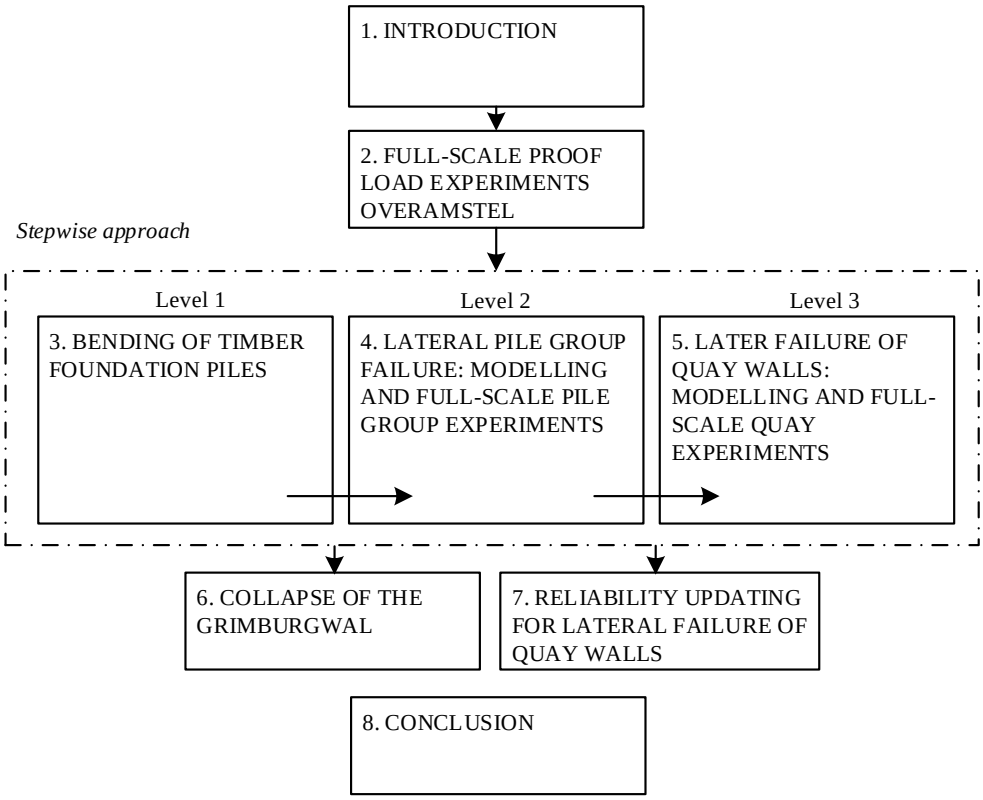

Figure 1.8, Thesis outline.

1.7 Project organization and cooperation

This PhD study is part of a research project in cooperation with the municipality of Amsterdam, Technische Universiteit Delft (TU Delft) and Advanced Metropolitan Solutions institute (AMS). This collaboration resulted from a large-scale program which was set-up in 2019 by the municipality of Amsterdam (Amsterdam, 2020b). This program was initiated to map the quality of the quay walls and bridges, discover risks and take measures to prevent unexpected events, such as the collapse of the Grimburgwal.

The academic heart of the AMS institute is formed by Technische Universiteit Delft, Wageningen University & Research (WUR) and the Massachusetts Institute of Technology (MIT). The three universities are working closely together on research tasks, offering education and establishing a data platform. The mission of AMS Institute is formulated as understanding the city, designing solutions for its challenges and implementing them in Amsterdam. Understanding the issues of the quay walls and designing solutions for them fit perfectly into this mission. It is the ambition of AMS to look at this issue more broadly than just the question of structural safety and to include social, durability and other aspects.


deKlerk
deKlerk

2

Full-scale proof load experiment Overamstel

To expand the understanding of relevant parameters and failure mechanisms, as well as to refine computational models of quay walls, a comprehensive full-scale proof load experimental program was planned and executed during the first half of 2022. The experimental program took place on a timber founded quay wall located at a small inlet harbour at Amsterdam Overamstel which dates back from 1905. This chapter provides background information on the Overamstel test site, the overall experimental program and geotechnical conditions. Detailed information on the individual experiments are reported in the corresponding chapters, namely chapter 3 the bending of timber foundation piles, chapter 4 covering lateral pile group failure, and chapter 5 addressing the later failure of quay walls.

Drone footage by CRUX Engineering BV

2.1 Introduction

In the introduction chapter 1 several knowledge gaps were highlighted that contribute to our limited understanding of the lateral behaviour of historic quay walls. A summary of the gaps that are within the scope of this this thesis is as follows:

1 The **geometry** of quay walls is often unknown.
2 **Bending properties** of bacterial deteriorated timber piles are unknown.
3 The lateral **pile-soil-pile interaction** of old closely-spaced timber piles in cohesive soils is not fully understood.
4 There is a significant degree of uncertainty associated with the **geotechnical model input** data for quay walls.
5 It is not known how the **soil medium behind the quay** transfers its self weight and any additional surface loads as a horizontal load onto the pile foundation.

A significant portion of these knowledge gaps is associated with uncertainties in the working principles of historic quay walls, as well as uncertainties in soil and structural properties, including the homogeneity of material properties. A commonly used approach to reduce uncertainties in engineering is to conduct full-scale experiments (Briançon et al., 2012; Duffy et al., 2022; Manna et al., 2009; Nimityongskul et al., 2018; Peters et al., 2015). By doing so, engineers gain a better understanding of the behaviour and strength of structures and have the possibility to validate computational models with the obtained experimental results. To validate quay wall models and gain more insight in the typical behaviour of a historical quay wall, a full-scale load test on a quay wall section is of paramount importance. However, no full-scale experiments have been conducted on historic timber founded inner-city quays.

The objective of this chapter is to design and describe a test program for a historic quay wall, aiming to address and reduce knowledge gaps 2, 3 and 5 (see above), ultimately improving our understanding of the behaviour of lateral failing quay walls. The test program is designed to isolate the main uncertainties associated with these knowledge gaps, enabling a stepwise approach for accurate validation and calibration of computational models. The objective of this chapter is reflected in the following key research question:

"How can an experimental program be designed to enhance our understanding of the lateral failure of historic quay walls, and to validate and calibrate computational quay wall models?"

The experimental program is conducted on a timber quay wall situated in a small inlet harbour at Amsterdam Overamstel. This particular quay wall, dating back to 1905, has become redundant due to a city housing project. This well-documented and regularly inspected quay wall provides a known geometry, thereby reducing geometric uncertainties (associated with knowledge gap 1). To tackle knowledge gap 4, which pertains to geotechnical model input, a geotechnical site investigation was performed. The findings and analysis of this investigation are presented in a separate report titled "Overamstel Project - Geotechnical Base report of Overamstel Project." (Choosrithong et al., 2023). The report includes laboratory and in-situ test results, subsoil schematizations, and an assessment of the key parameters for constitutive modelling of the subsoil conditions at the Overamstel site. A summary of the subsoil conditions and the most relevant modelling parameters is provided in section 2.3 of this thesis.

The outline of the chapter is as follows. First the Overamstel test site and quay wall configuration is considered in section 2.2. Accordingly, a brief summary of geotechnical site conditions is provided in section 2.3 which includes the subsurface layering and an overview of suggested geotechnical modelling parameters. Finally the testing program and experimental choices are elaborated in section 2.4.

2.2 Amsterdam Overamstel site

2.2.1 Overamstel test site

The Overamstel test site location is situated in Amsterdam-Oost, in the new district of Amstelkwartier, which is located between Spaklerweg and Duivendrechtsevaart indicated in Figure 2.1. The district is being developed in three phases, with a total of approximately 3,300 new homes planned for the Amstelkwartier. The aerial photograph shows the completed first phase the housing development and the preparation for construction in the second phase. As part of the district's construction, the quay walls of the inlet harbour will be redundant, providing an opportunity to test the strength of existing quay walls through "destructive testing". The specific quay wall chosen for testing is located in the South-West section of the inlet harbour and is highlighted in yellow. Figure 2.2 showcases the 90-meter long quay that will be subject to testing.

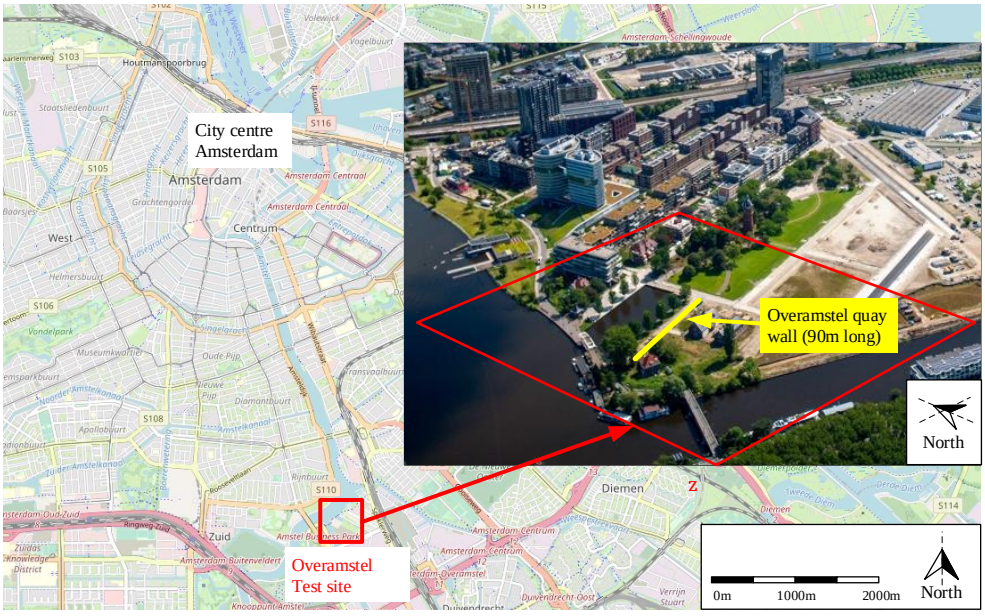

Figure 2.1, Location of Overamstel test site including an aerial photo of former industrial estate Overamstel, currently under development into a new residential and working area. In the photograph, indicated with yellow, the quay wall is present. Photo by Gemeente Amsterdam, 2016.

Figure 2.2, Photograph of Overamstel quay wall site to be tested.

2.2.2 Quay wall configuration Overamstel

The construction of the quay wall in the inlet harbour took place in 1905 with the purpose of unloading coal from vessels onto a train destined for the gas factory known as Zuidergasfabriek. A photograph of this historic setting is presented in Figure 2.3, where both the portal crane and the train were positioned directly on top of the quay.

Figure 2.3, Historic photograph of Overamstel inlet port at the 'Zuidergasfabriek' terrain. Approximately 1905-1920. (Archive of Amsterdam)

A historic technical drawing is depicted in Figure 2.4. The top view and pile plan of the Overamstel inlet harbour can be found in Appendix A, specifically in Figure A.1 and Figure A.2. The quay's top structure consists of a reinforced concrete gravity wall, covered with basalt blocks at the front. The gravity wall has a height of 1.90m, with a top thickness of 0.5m and a bottom thickness of 1.0m. At the crest of the quay wall, located at Normaal

Amsterdams Peil (NAP) +0.7m (NAP being the Dutch national reference level), there is a visible cap stone.

The gravity structure is supported by a timber foundation below the waterline, which maintains a minimum varying height of NAP-0.47m. A timber beam, designed for shear resistance, connects the gravity structure to the foundation. The foundation consists of four rows of vertical piles and a single row of raking piles. The piles are tapered and have an average cap diameter of 0.24m. The pile tip is placed in the first sand layer at approximately NAP -12.5m. The piles are positioned with a longitudinal spacing of 1.0m and a perpendicular row spacing of 0.85m. The soil level in front of the piles ranges from NAP -2.5m to NAP -3.5m, while the slope of the soil beneath the quay wall varies along its length, ranging from 1V:3H to 2V:3H.

On top of the piles, timber headstocks known as “kespen” are placed, with a length of 2.9m, height of 0.2m and a width of 0.23m. These headstocks provide support for a longitudinal timber plank-based relief floor. The front of the floor is situated at an elevation of NAP-1.2m, inclined at a ratio of 1V:10H. The floor itself has a thickness of approximately 0.06m and a width of around 0.2m. To prevent soil erosion, a timber sheet pile seepage barrier with a length of 5m is installed at the rear of the floor.

The depicted mooring bollards shown in the drawing are no longer in use and have been removed prior to the test. Similarly, the chain connecting the bollard to a separate anchorage screen, installed away from the quay structure, has also been removed. It is possible that the anchorage screen itself may still be present in the ground behind the quay wall.

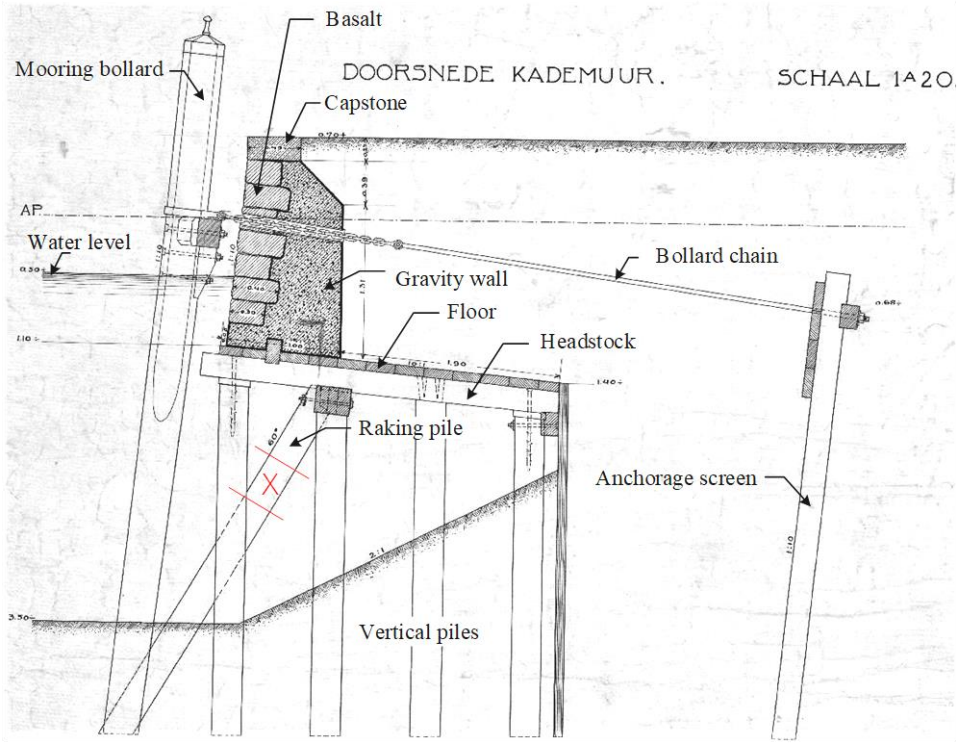

Figure 2.4, Cross-sectional technical drawing on Overamstel quay wall obtained from Archive of Gemeente Amsterdam. Terminology of structural elements is provided.

The Overamstel quay wall shares many similarities with the historic quay walls found in the city centre of Amsterdam, shown in Figure 1.5. However, there are also differences between this type of quay wall and the inner-city quay walls. The main design difference is the presence of a row of raking piles in the Overamstel quay wall, which is typically not found in the city centre. Conducting tests with raking piles is undesirable because the main failure mechanism under investigation assumes that the piles are horizontally loaded (in bending) and transfer their load as a pile group to the ground. Another difference is that the water depth near the quay is slightly greater here: NAP-3.5m compared to approximately – NAP-2m in the city centre. Consequently, the pile free height is larger than in the city centre. Additionally, the floor is inclined, which contributes to the stability of the gravity wall. Since the failure of the gravity wall is no objective in this study, this difference is considered irrelevant. Although there are differences between the Overamstel quay and the inner-city quays, these disparities can be effectively mitigated through adjustments to the experimental setup and analysis. Specifically, the raking piles are intentionally disabled by omitting 0.5m of pile along the 90m quay wall length. This modification is made to accurately replicate the structural characteristics of historic quay walls found in Amsterdam's city centre, which predominantly feature vertical piles. Furthermore, trees and their roots were removed.

Thereby, the insights of this experimental program and the models derived will also be applicable to the inner city quays.

2.3 Summary of geotechnical site investigation for Overamstel[1]

2.3.1 Site investigation and in-situ tests

Two site investigations were conducted in the South-West region. The initial investigation was carried out prior to site preparation and involved 11 cone penetration tests (CPT) with pore pressure measurements (CPTu), as well as six boreholes (BH). Additionally, two Seismic CPTs (SCPTu) were performed. After the segmentation process, 20 additional CPTs were conducted to study soil heterogeneity after site preparation. Figure 2.5 presents the locations of CPTu, SCPTu, and BH. Furthermore, the location of the various experimental sites, referred to as ‘segments’ are visualized. The purpose of each segment is explained in section 2.4.

Figure 2.6 shows the profiles of the measured cone resistance q_c[Mpa], sleeve friction f_s[Mpa] and pore pressure u_2[Mpa]. In the pore pressure diagram, the in-situ hydrostatic stress u_0[Mpa] is provided. The cone resistance plays a role in determining the modulus of horizontal subgrade reaction, which is utilized to compute the elastic branch of individual pile-soil springs. A detailed explanation of this concept can be found in chapter 4 and Appendix G.

[1] This section provides a summary of the geotechnical site investigation conducted by K. Choosrithong and M. Korff (Choosrithong et al., 2023). The geotechnical report presents a comprehensive analysis of the subsoil conditions at the Overamstel site. The main objective of the report is to establish appropriate parameters for constitutive modeling through a combination of laboratory and in-situ tests. The summary in this chapter focuses on the parts that are relevant to this thesis, considering their direct implications and contributions to the research topic.

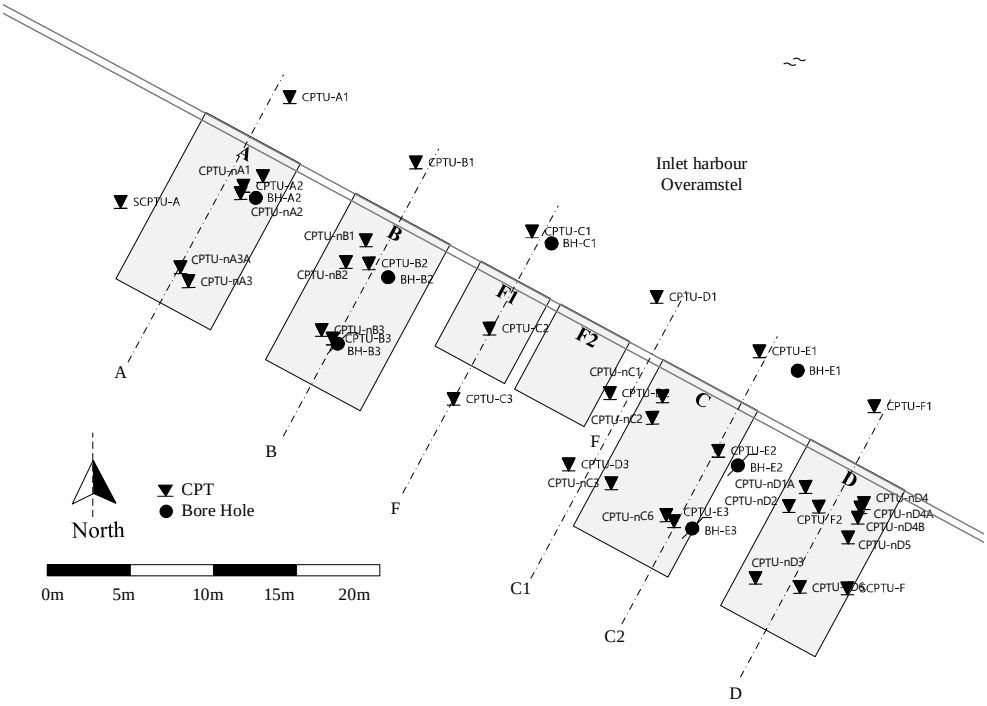

Figure 2.5, Plan view for in-situ tests CPTUs, SCPTUs and BH taken on land and in the water. Label CPTU-XX refers to the CPTs conducted prior to site preparation, while CPTU-nXX refers to the CPTs performed after site preparation. The location of experiment segments is provided.

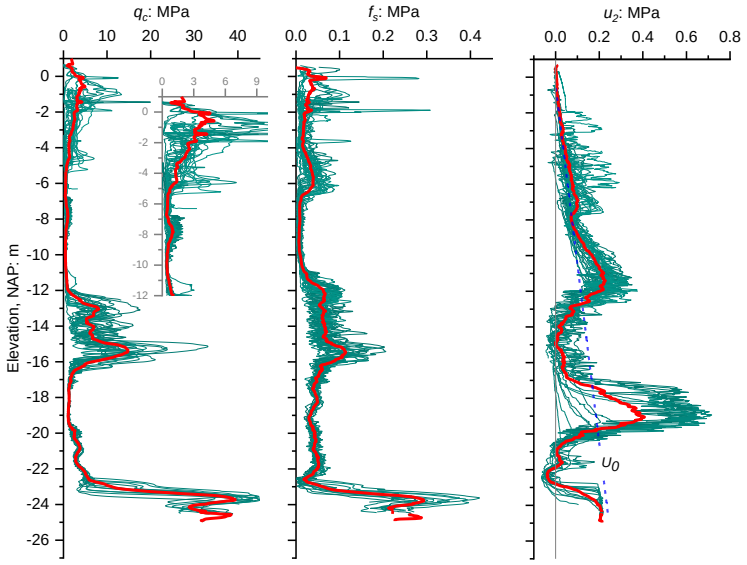

Figure 2.6, CPTu and SCPTu data; q_c cone tip resistance, f_s sleeve friction, u_2 pore pressure measurement. The red line is the average of the data (Choosrithong et al., 2023).

2.3.2 Subsoil conditions

Based on the CPT and borehole data, a cross-sectional soil layering profile has been identified at the centre (see Figure 2.5) of each segment. For segment A, the cross-sectional soil layering profile can be observed in Figure 2.7 and for segment D in Figure 2.8. The soil layering of other segments (e.g. B,C and F) can be found in Appendix A.2. The soil profile at the Overamstel site consists of several layers. Starting from the surface (at NAP+0.7m), there is a man-made anthropogenic fill layer (Ophooglaag, zand), followed by a layer of soft clay (Geulopvulling, slappe klei) and a peat layer (Hollandveen). Below the peat layer, there is another layer of soft clay (Oude Zee klei), and beneath that, a thin layer of sand (Wadzand) is present. Next, there is a layer of Hydrobia clay (Hydrobiaklei) followed by Basal peat (Basisveen). Beneath all these Holocene soft soil layers, the first sand layer (Eerste zandlaag) is found between NAP-12.0 m and NAP-14.0 m. This sand layer serves as the foundation for most of the piled foundations in the inner city of Amsterdam, including the majority of the quay walls. Below this first sand layer, a silty/sandy layer known as the Allerod is present. At a depth of NAP-16m, the second sand layer (Tweede zandlaag) is encountered, followed by a very stiff Eemclay (Eemklei) layer.

Varied layer thicknesses are observed between the surface level and the first sand layer, especially in the shallower layers, creating significant spatial heterogeneity. The man-made sandy fill layer behind the Overamstel quay wall exhibits considerable variation due to construction and soil remediation. From segment A to D, there is a gradual increase in the thickness of the man-made sand fill, resulting in improved stability.

In each segment, a water pressure sensor (WPS) is installed in the Wadsand layer at NAP-8m, measuring average pore pressures of 76kPa. Additionally, a phreatic level tube sensor (PS) is installed in each segment at NAP-2.5m in the man-made soil, measuring a mean pore pressure of 22kPa. The water level in the inlet port was monitored at a minimal varying level of NAP-0.47m.

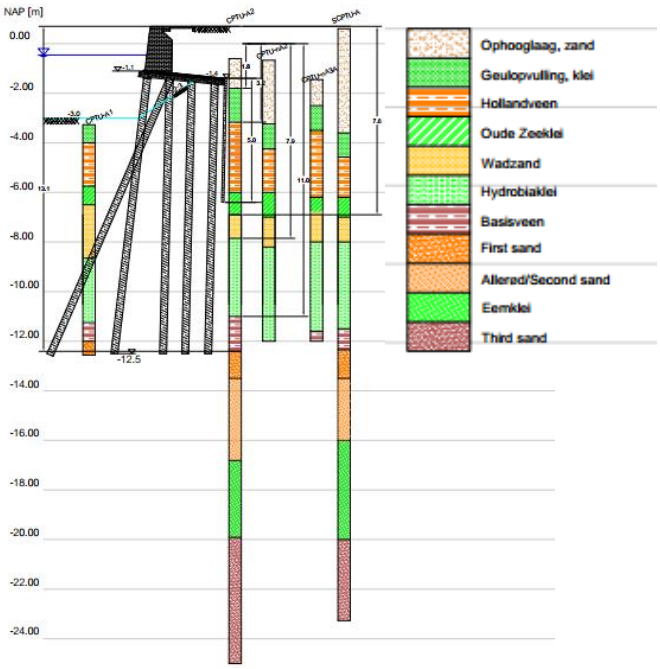

Figure 2.7, Cross-sectional geotechnical conditions for segment A (Choosrithong et al., 2023).

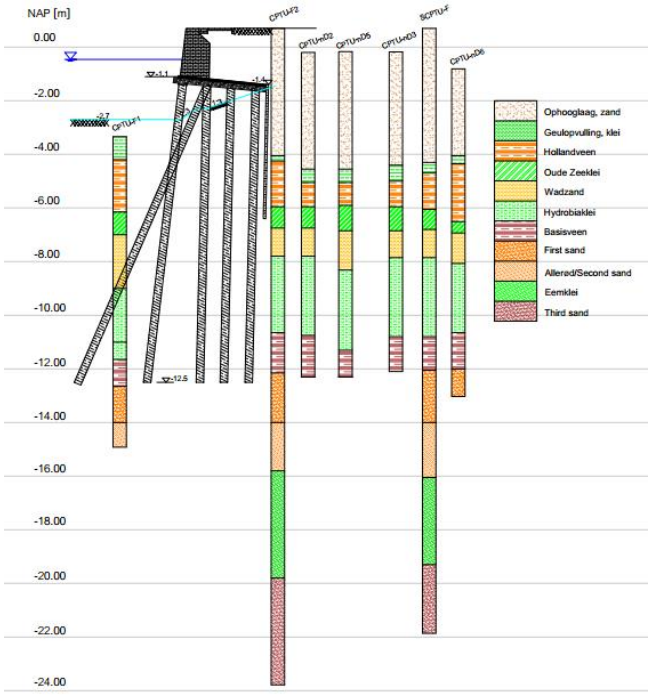

Figure 2.8, Cross-sectional geotechnical conditions for segment D (Choosrithong et al., 2023).

Table 2.1 presents a selection of geotechnical modeling parameters relevant to this study. These parameters include the dry unit soil weight γ_{dry} [kN/m^3], saturated unit soil weight γ_{sat} [kN/m^3], effective friction angle φ' [deg], and effective cohesion c' [kN/m^2]. These parameters are used in the determination of the plastic limit of individual soil springs with Brinch Hanssen's theory and in the determination of the lateral load on the pile foundations.

Table 2.1, Table with relevant geotechnical modelling parameters (Choosrithong et al., 2023).

Soil type/ Parameters	(in Dutch)	γ_{dry} [kN/m^3]	γ_{sat} [kN/m^3]	φ' [deg]	c' [kN/m^2]
Sand fill	Ophooglaag, zand	15.0	19.0	38	0
Clay	Geulopvulling slappe klei	14.0	16.9	30	1
Peat	Hollandveen	2.0	10.1	33	3
Sea Clay	Oude zeeklei	12.2	16.5	28	3
Sand deposit	Wad deposit	13.3	18.5	35	3
Clay	Hydrobiaklei	9.0	14.5	27	4
Peat	Basisveen	2.0	11.7	26	6
First sand layer	Eerste zandlaag	19.0	29.0	33	3
Allerod/second sand layer	Allrod/tweede zandlaag	15.0	19.0	33	0
Clay	Eemklei	11.3	16.8	28	15
Third sand layer	Derde zandlaag	19.0	19.0	35	5

In drained layers, the ultimate soil resistance is determined using the Brinch Hanssen method, considering the parameters c and φ. However, in undrained cohesive layers, the undrained shear strength s_u[kN/m^2] is used, and the friction angle is assumed to be 0. The undrained

shear strength and effective friction angle are plotted in Figure 2.9, with an average value provided in red.

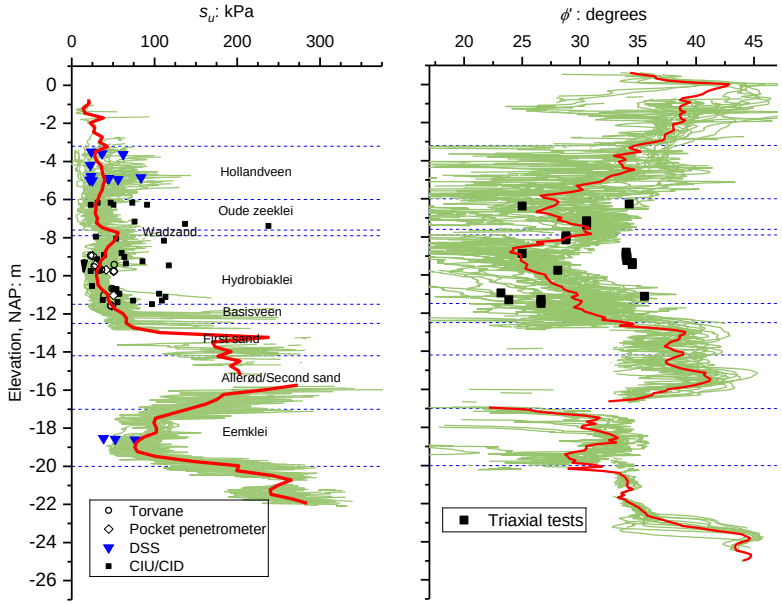

Figure 2.9, Interpretation of undrained shear strength and friction angle from CPTUs. From CPTUs in green, from lab tests in markers and mean line in red (Choosrithong et al., 2023).

2.4 Overview of experimental program

2.4.1 Overamstel test program

Performing just one full-scale proof load would lead to accumulation of uncertainties – such as the bending properties of timber piles, the pile-soil interaction and the soil medium behind the quay. To avoid mixing of uncertainties from varies sources three types of experiments are performed. These are: Four-point bending tests on timber piles, lateral pile group experiments and proof load experiments on quay wall segments. For each test, the number of tests, structural detail level, and targeted knowledge gap are provided in Table 2.2. The chosen levels correspond to different levels of detail in the structural quay wall system. Level 1 focuses on the bending of timber piles, level 2 considers the lateral behaviour of timber pile groups, and level 3 addresses the lateral behaviour of historic quay walls. With the chosen levels, a stepwise validation and calibration for computational quay wall models is possible.

Table 2.2, Overamstel experiments and their knowledge gaps.

Experiment	# tests	Level	Addressed knowledge gap
Four-point bending experiments	6	1	2: Bending properties of bacterial deteriorated timber piles are unknown.
Lateral pile group experiments	2	2	3: The lateral pile-soil-pile interaction of old pile foundations is not fully understood.
Quay wall proof load experiments	5	3	5: The transfer mechanism of soil loads behind the quay onto the pile foundation is unknown.

To accommodate multiple experiments on a 90m long continuous quay wall, a segmental approach is adopted. This approach involves dividing the quay wall into several independent parts, allowing for separate testing and analysis. This 'segmental approach' is chosen for two reasons: first, to simulate a two-dimensional quay wall failure and reduce any potential three-dimensional effects; second, to make optimal use of the quay wall by performing multiple experiments. In those experiments the quay wall geometry, loading, and geotechnical conditions can be varied. Performing more-or-less identical experiments decreases uncertainties in spreading. Figure 2.10 provides a top view of the South-West quay wall, including the arrangement of the quay wall segments. Segment F1 and F2 are utilized for the lateral pile group experiments, while segments A, B, C, and D are dedicated to the quay wall experiments. Bending tests take place on land. An overview table (Table 2.3) provides a comprehensive summary of all the experiments conducted, along with their corresponding segments. The experiments are described in 2.4.2.

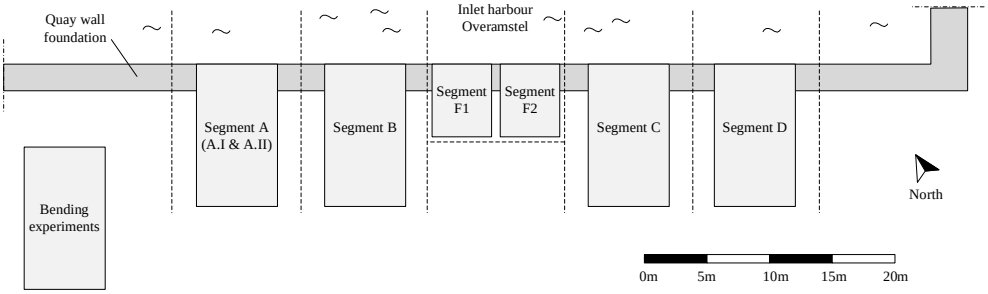

Figure 2.10, Plan view of the South-West quay wall of the Overamstel inlet harbour including segmental layout.

Table 2.3, Overview of the experiments performed at the Overamstel site. Piles indicated with red are installed with fibre optical wires to measure bending strains over the full pile length.

Four-Point bending experiments	Lateral pile group experiments	Quay wall experiments
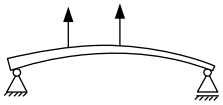	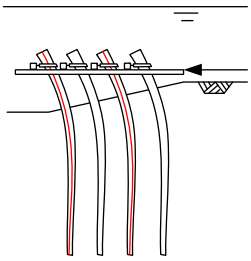	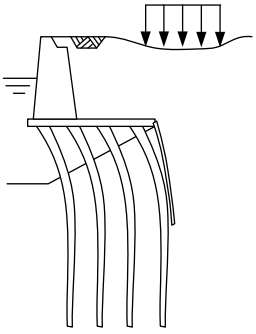
Location: Main land *Number of experiments:* 4	*Location:* Segment F1 *Number of experiments:* 1	*Location:* Segment A.I and B *Number of experiments:* 2
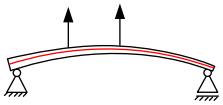	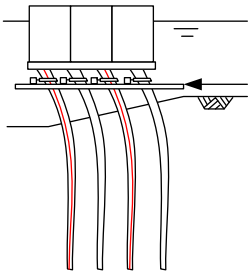	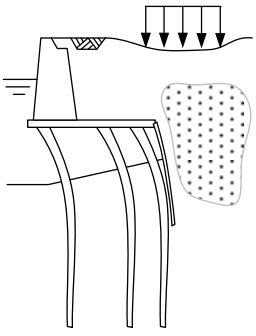
Location: Main land *Number of experiments:* 2	*Location:* Segment F2 *Number of experiments:* 1	*Location:* Segment C and D *Number of experiments:* 2
		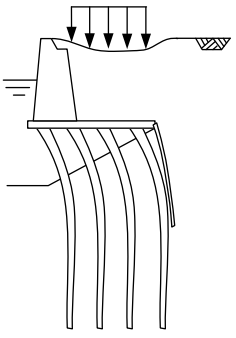
		Location: Segment A.II *Number of experiments:* 1

2.4.2 Experiment description

Four-Point Bending Experiments: A photograph of this experiment is provided in Figure 2.11. These experiments focus primarily on determining the bending modulus of rupture and modulus of elasticity for the historic timber piles. A total of six experiments are conducted, with two piles equipped with fibre-optics (FO) to validate the monitoring technique. This technique is subsequently implemented in the lateral pile group experiments to measure pile strains. The bacterial deterioration of the timber piles is examined with micro drilling. The bending experiments are elaborated on in chapter 3

Lateral pile group experiments: A photograph of this experiment is provided in Figure 2.12. These experiments focus on the resistance of a laterally loaded 3x4 pile group. In experiment F1, the pile group is laterally loaded without a top load. In experiment F2, the pile group is laterally loaded with a top load which is equivalent to the weight of the original top structure of the quay wall including soil. This helps to identify the effect of the top load on the lateral response of the pile foundation. FO instrumentation in a selection of piles is used to measure in-ground strain measurements. Furthermore, cap forces, pile deflections, and pile rotations are monitored during loading. The lateral pile group experiments are elaborated on in chapter 4.

Quay wall experiments: A photograph of this experiment is provided in Figure 2.13. These experiments are conducted on quay wall segments with a width of 6.5m each, studying a quay wall subjected to a excessive surface load. In Segment A and B, the quay is loaded directly behind the earth retaining screen. In experiments C and D, the second pile row is disabled to weaken the quay, mainly due to the presence of a thicker sand layer behind the quay wall that provides greater stability to the applied top load and increases the overall stability of the quay. Experiment A.II is conducted after the already executed experiment A.I, where a top load is placed directly on top of the pile foundation to study second-order effects of an already deformed quay wall. The quay wall segments are instrumented to measure the cross-sectional motion of the quay wall, including the surrounding soil body, and water pressures in specified layers. Quay wall experiments are elaborated on in chapter 5.

Figure 2.11, Four-point bending experiment on timber quay wall foundation pile.

Figure 2.12, Lateral pile group experiment (3x4 pile group) with top load.

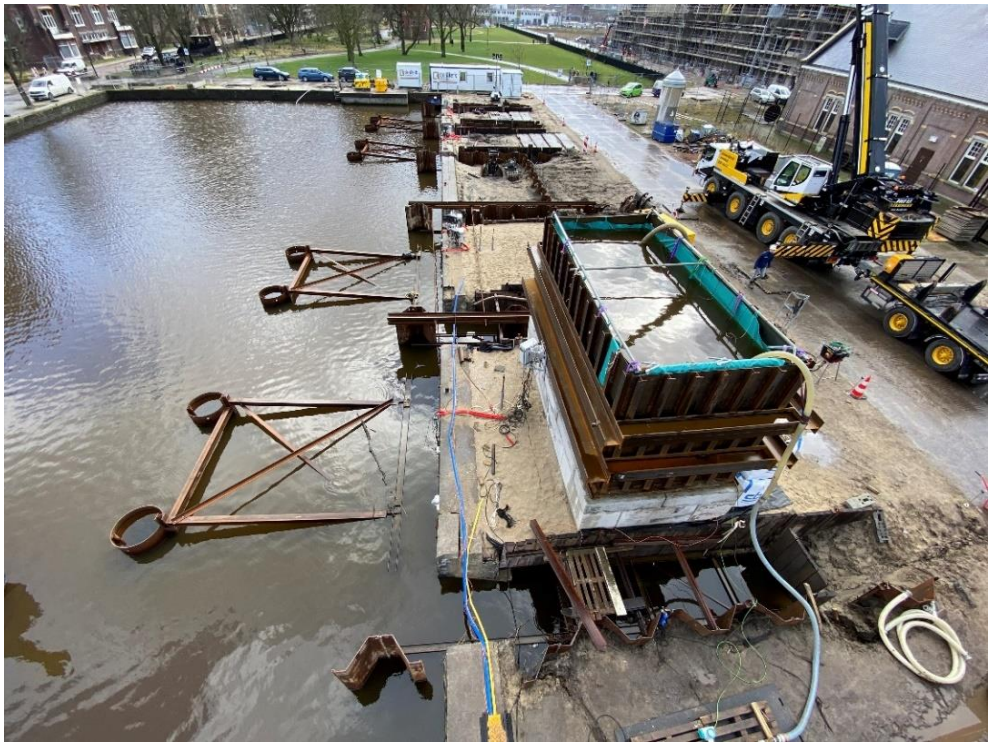

Figure 2.13, Proof load experiment on quay wall segment.

2.4.3 Timeline of experiments

The timeline of all experiments is provided in Table 2.4 in chronological order.

Table 2.4, Timeline of experiments

Experiment	Timeline
Quay wall experiments	
Segment A.I	22-02-2022 – 25-02-2022
Segment B	28-02-2022 – 04-03-2022
Segment C	09-03-2022 – 16-03-2022
Segment D	17-03-2022 – 22-03-2022
Segment A.II	24-03-2022 – 28-03-2022
Four-point bending experiments	
Pile 1	13-04-2022
Pile 2	13-04-2022
Pile 3	14-04-2022
Pile 4	14-04-2022
Pile 5	11-05-2022
Pile 6	11-05-2022
Lateral pile Group experiments	
Segment F1	11-05-2022 and 17-05-2022.
Segment F2	02-06-2022

2.4.4 Challenges encountered

During the construction and execution of the experiments, several challenges were encountered. Here is a brief description of the most important challenges is provided:

- One of the challenges faced was cutting the raking piles. The compression within these piles caused saw blades to get stuck. Furthermore, ensuring the safety of divers during the cutting process was essential. To overcome this challenge, a special bracing structure was designed and installed at 5 meters from the pile foundation. This bracing structure helped stabilize the quay and allowed for the dismantling of the raking piles without disruption of interaction between the piles and the soil.
- Ensuring continuous and controlled loading of the quay wall was crucial for the experiments. Additionally, it was necessary to enable quick and safe reduction of the load in case of an unstable situation. To achieve this, water was used that could be released quickly.
- Looking for a reliable way of creating a uniform pressure (of e.g. 30 kPa) over a defined surface area the water head was applied via a membrane, rather than in a stiff box that would be able to redistribute forces and possibly 'respond' to local soil deformation by resting on high ground. A hollow container with a infill membrane was selected as a form of loading that is able to adopt to the soil surface, during the experiment
- Installing multiple monitoring sensors in a small, poorly visible space posed a significant challenge for the divers. The compact field of piles beneath the quay made it difficult to manoeuvre, and there was a risk of damaging the already installed sensors.
- Reducing friction on the vertical boundary surfaces between the different segments proved to be challenging. To address this, a special construction, explained in detail in chapter 5, was designed specifically for this purpose.
- Installing the fibre optic wires in the biological degraded piles presented a challenge. An even greater challenge was driving these piles, with the fibres, into the ground without damaging them. The fibre optic wires also protruded from the pile head. To prevent damage, a separate wooden sleeve was created to cover the pile head and protect the protruding fibre optic cables.
- Extracting the historical piles was challenging as a simple vibratory clamp was insufficient. Instead, a customized 3-meter long steel gripping clamp, designed specifically for timber piles in Amsterdam, was used.
- The lateral pile group experiments took place entirely underwater without visibility. This required strict communication between the divers and the operators on land. During the tests, decisions had to be based solely on data without any physical visual input. If something went wrong during the experiment, it was not immediately visible. For example, in the lateral pile test, a jack slipped out of its position.
- During the installation of steel sheet piles to create the segmental divides, liquefaction occurred in segment C. This resulted in the formation of sinkholes behind the gravity wall due to small openings in the timber floor. To address this issue, the problem was resolved by excavating the soil up to the floor level and restoring the floor to be soil-tight using a combination of a foil and dragline mats.

2.4.5 Organisation and execution of experiments

The initiative for this test program arose from discussions between the municipality of Amsterdam and TU Delft in 2019. In 2020, a research plan was formulated (Kuiper et al., 2020), and a concrete project plan was developed based on which the Bridges and Quays Program (PBK) allocated a budget to conduct this research. To make optimal use of available knowledge, a construction team consisting of TU Delft/AMS, a measurement company, and a contractor to build the test setup was assembled, with the municipality of Amsterdam as the client. In early 2021, the tender process was organized to select the construction team partners. The construction team consists of the following parties:

TU Delft/AMS provided research leadership for the testing program. They were responsible for designing the experiments and the overall test setup. During the construction phase, TU Delft/AMS, provided research related guidance to the construction team. During the execution of the experiments, this team determined when to start the tests, the loading increments, the loading rate based on monitoring, real-time assessment, and evaluation of the duration of testing during the day. They also decided when to end the tests. After the test program was executed, TU Delft/AMS was responsible for interpreting the results.

The Municipality of Amsterdam was the client of the testing program and therefore the financer of the experiment. The Municipality of Amsterdam took on the responsibility of contracting the construction partners and coordinating the construction team throughout the construction and testing phases. During the testing phase, they had the authority to make final decisions regarding the start/stop of the tests and the working hours.

Engineering firm IV-infra was responsible for the monitoring of all experiments. The monitoring plan was developed in collaboration with TU Delft/AMS. IV-infra was responsible for the detailed design of the sensor plan and its installation during the construction phase. During the experiments, IV-infra presented the monitoring data in real-time, enabling the control of the experiments. They were also responsible for data storage, online data presentation, and reconfiguring sensors during the setup and dismantling of the experiments. After the completion of the experiments, IV-infra corrected any measurement errors or deviations and delivered the data, along with a measurement report, to the Municipality of Amsterdam.

Construction company De Klerk, Werkendam was responsible for the final construction design of the experiments and their detailing. This included temporary structures, loading structures, the construction and dismantling of structures, and related on-site activities. During the experiments, De Klerk was responsible for ensuring safety and health at the construction site. They also provided the following services during the experiments:

- Providing electricity, site facilities (such as a temporary office), toilets, and water
- Setting up and dismantling the water container
- Operating the pump (filling and emptying) or hydraulic jacks
- Operating the emergency hose
- Observing stability during the experiment and reporting any concerns
- Setting up and dismantling concrete blocks and gravel.

The installation and measurement of the fibre optics for the four-point bending experiments and the lateral pile group experiments were performed by the **Municipality of Rotterdam**. However, they were not part of the construction team.

The total cost of the full-scale experimental program Overamstel was 2.5 million euros.

2.4.6 Datasets per experiment

For each experiment, the datasets are published on 4tu.nl. The DOI for each experiment is provided in Table 2.5. The three data-sets are compiled in a collection with DOI: https://doi.org/10.4121/d2d001b5-ec3f-4518-a90c-8461c1ff9ff3.

Table 2.5, Datasets of Overamstel experiments.

Experiment	Location of dataset (DOI)
Four-point bending experiments	
1) Forces and deflection data 2) Micro drilling data 3) Fibre optic data (pile 5 and pile 6)	https://doi.org/10.4121/86c74fa5-1bcf-49f0-8396-c14f9a45eeef
Lateral pile Group experiments	
1) Cap forces, cap rotations, group deflections 2) Fibre optic data (F1P2, F1P8, F2P2, F2P8)	https://doi.org/10.4121/2f3d53fd-d4aa-4cad-9757-626cecb785a6
Quay wall experiments	
1) Movement of structural components, container load and soil movement.	https://doi.org/10.4121/0e224b88-8d6b-4622-ab2d-c818f0f266e7

3

Bending of timber foundation piles

The understanding of historic timber foundation piles subjected to bending is crucial for gaining insight into the lateral failure of quay wall foundations. This chapter examines the bending experiments conducted on six foundation piles from the Overamstel site. By extracting the 115-year-old timber foundation piles and performing bending experiments, it is possible to explore their bending material properties in detail.

Photograph by the author

3.1 Introduction

3.1.1 Timber piles in Amsterdam

The usage of piles in order to improve the bearing capacity of the soil goes back roughly two millennia when Romains used pile foundations below bridges and houses. Between 1300 and 1600, the foundation was built on many shallow piles, named 'slieten', which relied on sleeve friction (Winsen et al., 2015). In Amsterdam, driving of long timber piles into the first load-bearing layer of sand to support houses, bridges and quay walls began at the end of the 16th century (Klaassen et al., 2012). Figures depicting the development of wooden pile foundations from the Middle Ages to the 20th century, based on Amsterdam's experiences, can be found in (Amsterdam, 1975). Large-scale expansion projects utilizing timber piles were already underway in the 17th and 18th centuries, eventually culminating in the late 19th and early 20th century, when many Dutch cities saw substantial growth (Klaassen, 2008). For the timber piles, mostly spruce wood was used, retrieved from Scandinavia (van Tussenbroek, 2012). Alternately pine trees were also used but to a lesser extent. Timber piles were driven into place by manual labour using a 'tipi' type of structure as visualized in Figure 3.1. With this equipment a falling height of 2-3 meters could be reached and the weight of the driving block ranged between 400 and 1,000 kg (De Gijt, 2010). Around 50 people gathered to lift the massive weight, singing in unison as they did so. The singing did not only contribute to a pleasant work environment but most of all, it helped coordinating the work (Wennekes et al., 2002).

Figure 3.1, Dutch pile driving equipment in 17th century. (Photo from Rijksmuseum Amsterdam)

Pile foundations used in different parts of the world have on average a cap diameter of 300 to 500mm and at the toe, a diameter of 120 to 230mm (Das, 2010). Piles in Amsterdam are considerably smaller with on average a pile cap diameter of 200-300mm and a toe diameter of 100-150mm. The tapering of the piles is roughly 5 to 10mm per meter. For bridges, public buildings, and houses, timber piles are mostly loaded axially, with the loads typically being absorbed by the soil with shaft friction and toe resistance. The toe of the piles is often located

at a depth of NAP[1]-12 to NAP-14m, where the First Sand layer is present. Quay walls, however, are soil-retaining structures used to load goods onto vessels and enable people to walk or drive on them. As such, quay wall foundation piles are not only loaded axially, but also laterally, introducing significant bending moments in the piles. To model and assess the lateral bending of timber pile foundations, a proper estimate of the bending properties is essential. The objective of this study on historic foundation piles is to gain the most comprehensive and thorough insights into their material bending properties. The objective of this chapter is reflected in the following key research question:

"What are the bending properties of centuries old timber quay wall foundation piles?"

The chapter outline is as follows. In section 3.1, an introduction on the bending of timber piles is provided which includes a brief literature overview, developed theories and design ideas. Accordingly, the methodology of the bending test is explained in section 3.2. In here, the test set-up, instrumentation, pile dimensions and loading procedures are provided. Subsequently the bending test results are presented in section 3.3. The chapter ends with a conclusion in section 3.4.

3.1.2 Importance of bending properties and use in practice

In the modelling and assessment of timber piles an important bending property is the bending modulus of elasticity E_b[Mpa]. This modulus is defined as the ratio of stress to strain in the linear domain and is a measure of a member's stiffness when subjected to bending moments. When modelling piles, the modulus of elasticity is usually combined with the moment of inertial I[m^4] resulting in the flexural stiffness EI[kNm^2] to obtain the bending stresses σ_b[N/mm^2]. The bending strength of timber material is characterized by the modulus of rupture MOR[N/mm^2]. When stresses in timber exceed the modulus of rupture, the fibres are permanently damaged, resulting in plastic behaviour. The MOR is often referred to as bending strength f_m[N/mm^2]. Currently, timber piles are assessed using the Unity Check (UC) equation: UC = $\sigma_{b,d}$ / $f_{m,d}$ < 1, where subscript d refers to the 'design value'. In the current assessment of quay walls, C24 timber class is used according to the 'CROW / CUR – Recommendation 124 Structural safety of existing bridges and viaducts for local authorities'. Characteristic values are the mean modulus of elasticity parallel to the fibres $E_{b,mean}$ = 11,000MPa and characteristic bending strength parallel to the fibres $f_{m,k}$ = 24N/mm^2.

3.1.3 Literature on bending of timber piles

One way to obtain the bending properties is through bending experiments of which a brief overview is given. The usage of bending tests is widely applied in a variety of research fields such as wear of asphalt pavements (Pais et al., 2012), timber beams (Lim et al., 2013), ultimate flexural resistance in concrete (Yin et al., 2019) or even in medical (Kemper et al., 2007) and ecology applications where trees are tested on their strength (Van Casteren et al., 2012). Executing bending tests gives insights in the stress-strain response of a material and therewith information on the modulus of elasticity, bending stresses and bending strains ε[mm/mm]. Besides that, bending tests provide insight in the ultimate bending strength, often referred to as modulus of rupture for structural timbers (Cline et al., 1912), and have been used for centuries to demonstrate the strength of wood (Thurston, 1879). For timber, the modulus of elasticity is often referred to as MOE[Mpa]. Two types of bending experiments

[1] NAP stands for "Normaal Amsterdams Peil," which is a Dutch term that translates to "Normal Amsterdam Datum." It is a reference level used for measuring elevations and depths in the Netherlands.

are commonly used, three-point bending tests and four-point bending tests. The fundamental difference between the two tests is having bending with shear (three-point bending) and pure bending without shear (four-point bending). Another difference, which is of importance for this particular application, is the location of the maximal bending stress (Chitchumnong et al., 1989). In three-point bending, the maximum stress occurs directly at the load. In contrast, four-point bending tests produce a wider distribution of maximum bending stresses that extend between the two applied loads. This distribution increases the likelihood that a larger portion of the tested material will be exposed to the maximum stress, which in turn raises the probability of encountering a weak spot within the sample. As a result, four-point bending tests may provide more comprehensive insights into the structural properties and failure mechanisms of the material being tested. Both testing methods result in slightly different outcomes in strength parameters such as E_b and *MOR* and their use is evaluated by a number of researchers (Hein et al., 2018; Mujika, 2006).

For round timber members, many bending test studies have been performed in the past. A brief overview is given below. A study was performed by (Ranta-Maunus et al., 2011) in which more than 6,000 specimens of dry spruce and pine grown in several European countries were tested by destructive and non-destructive methods. The average *MOR* was 40.2N/mm^2 and E_b was 11,200Mpa. Wilkinson conducted four-point bending- and compression experiments on southern pine, red oak and douglas-fir tapered members to determine the strength properties (Wilkinson, 1968). For southern pine, E_b for the piles was 9,238MPa and *MOR* 12.5 N/mm^2 respectively. The relation between timber densities and the modulus of rupture was studied by (COWN et al., 1983). Small-diameter ponderosa pine logs were tested in three-point bending by (Larson et al., 2004) resulting in E_b = 11,307Mpa and *MOR* = 64 N/mm^2 at the pile cap and E_b = 9,790MPa and *MOR* =42N/mm^2 at the pile tip. Chilean radiata pine piles were subjected to bending tests and evaluated by (Cerda et al., 2003) and an average E_b of 10,500MPa was found. The test set-up used by Cerda was rather different from a standard three-point bending test. The 12m piles were bended in the horizontal plane with a cable, 0.6m from the pile cap. The load was delivered by means of a truck. Lopez-Anido investigated the effect of a composite Fibre Reinforced Polymer (FRP) shield to repair broken piles by performing three-point bending tests (Lopez-Anido et al., 2003). (Wolfe et al., 2005a, 2005b)compared the load capacity of small timber tapered round pile members with sawn timber members. The influence of the moister content on the bending strength properties of round timber piles was researched by (Ido et al., 2013). To do so, bending and compression tests were conducted that showed that the average strength of air-dried round timber was higher than that of green round timber.

As stated before, one of the advantages of a four-point bending test is the ability to have a constant outer fibre bending stress between the two loading points. This forces the member to fail at the most critical cross section. For members that have a large longitudinal variation in material properties, finding the most critical section is of paramount importance. For tapered piles, a constant bending stress between the loading points can only be obtained by maintaining a certain load ratio. The load ratio is defined as $a_F=F_1/F_2$ in which F_1[kN] is the first point load and F_2[kN] is the second point load. (Wilkinson, 1968) stated that the force ratio a_F between the two loads should be proportional to the section modulus ratio between the two load points. This rule of thumb does not take into account the self-weight of the pile.

The E_b can also be determined by a number of non-destructive methods. (Green et al., 2006) determined the E_b by transverse vibration. (Morales-Conde et al., 2017) used stress waves to determine the E_b. (Christoforo et al., 2012) performed non-destructive three-point

bending experiments on Pinus Caribaea round structural timber beams to obtain the E_b in which the mid-span deflection was limited to L/200 and L/300.

3.1.4 Literature on bacterial decay of timber piles

The described bending test studies in the previous paragraphs were executed on round timber members that have had no, or a neglectable service life time. Historical timber quay wall foundation piles can be up to 300 years old. After hundreds of years in service, load carrying capacities of timber piles may be affected by load effects but also biological degradation (van de Kuilen et al., 2021). One of the first fundamental studies on the degradation of timber piles was carried out by (Varossieau, 1949) and (Harmsen et al., 1965). During the past years, more and more research has been done on the biological decay of historic pile foundations. A study by (Huisman et al., 2008) examined the relationship between timber degradation caused by erosion bacteria and the physicochemical properties of foundations with timber piles from sites in the Netherlands, Germany and Italy. (Klaassen et al., 2012) gave a survey of the behaviour of timber foundations over time. Research of (Ceccato, 2013) on the effect of wood degradation and soil creep on the behaviour of timber pile foundations below historical buildings in Venice. An integrated finite element analyses was made by coupling wood decay and soil creep. In a study of (Björdal et al., 2021) nine timber foundation piles of spruce and pine in Gothenburg were examined for fungal and bacterial degradation on a microscopic level. This study stated that two parameters have a significant impact on the bacterial decay; time and pile diameter. Other correlations between decay and spatial parameters could not be found. The most severe decay was present in the outermost layers of the piles with a thickness of 1- 3 cm. Thereafter the decay generally decreased and stopped at varying depths. A study on 125 year old timber piles below a building in Ljubljana was performed by (Humar et al., 2021). (Pagella et al.) made a characterization and assessment of the compressive mechanical properties of spruce foundation piles obtained from bridges in Amsterdam. In this study, full-scale compression experiments on head, middle and tip parts of 12 foundation piles were performed. The ‘soft shell’ was investigated by micro-drilling. It was concluded that micro-drilling gives promising results to predict the level of decay and make clear distinctions between healthy core wood and a decayed soft shell. Pagella also studied the influence of knots and density distribution on the compressive strength of timber foundation piles. It was concluded that compression failure occurred in more than 70% of the cases in sections with the highest density of knots (G Pagella et al., 2022).

3.1.5 Conclusion of literature study and objectives

The modulus of rupture (*MOR*) and modulus of elasticity (E_b) are critical parameters when modelling and evaluating timber pile foundations subjected to bending. Biological decay can significantly affect the bending properties of timber and create a soft shell around the healthy core wood. While bending experiments have been conducted on various timber pile species, no research has yet investigated the bending properties of historical timber foundation piles.

To address this gap in knowledge, this study aims to determine the bending properties of spruce foundation piles from the Overamstel quay wall by conducting six four-point bending tests. Since variations in material properties are expected due to different diameters, the presence of knots, and bacterial decay, a four-point bending test is preferred because it can provide information on the flexural modulus of elasticity, the modulus of rupture, and the stress-strain behaviour of the foundation piles over the full pile length. To account for the soft shell due to biological decay, non-destructive micro drillings are

performed on all six piles. In addition to obtaining the material properties, the four-point bending test also serves as a validation and calibration tool for the fibre optic technique used in the two lateral pile group experiments described in chapter 4.

3.2 Methodology bending tests

3.2.1 Bending test set-up

To test the structural response of old timber foundation piles, four-point bending tests were performed of which a front view of the test set-up can be seen in Figure 3.2A and a side view in Figure 3.2B. The principle of this bending test set-up is based on the principle of tensioning a bow. The pile with length L[m] is held in place at the outer ends ($x = 0$ and $x = L$) with support slings and tensioned by hoist slings attached to chain hoists in the middle ($x = L_1$[m] and $x = L_2$[m]). With chain hoists, it is possible to lift large loads with high precision which results in a displacement controlled four-point bending test. The test set-up is designed in such a way that it is possible to vary with the span, the location of loading and the amount of loading per hoist.

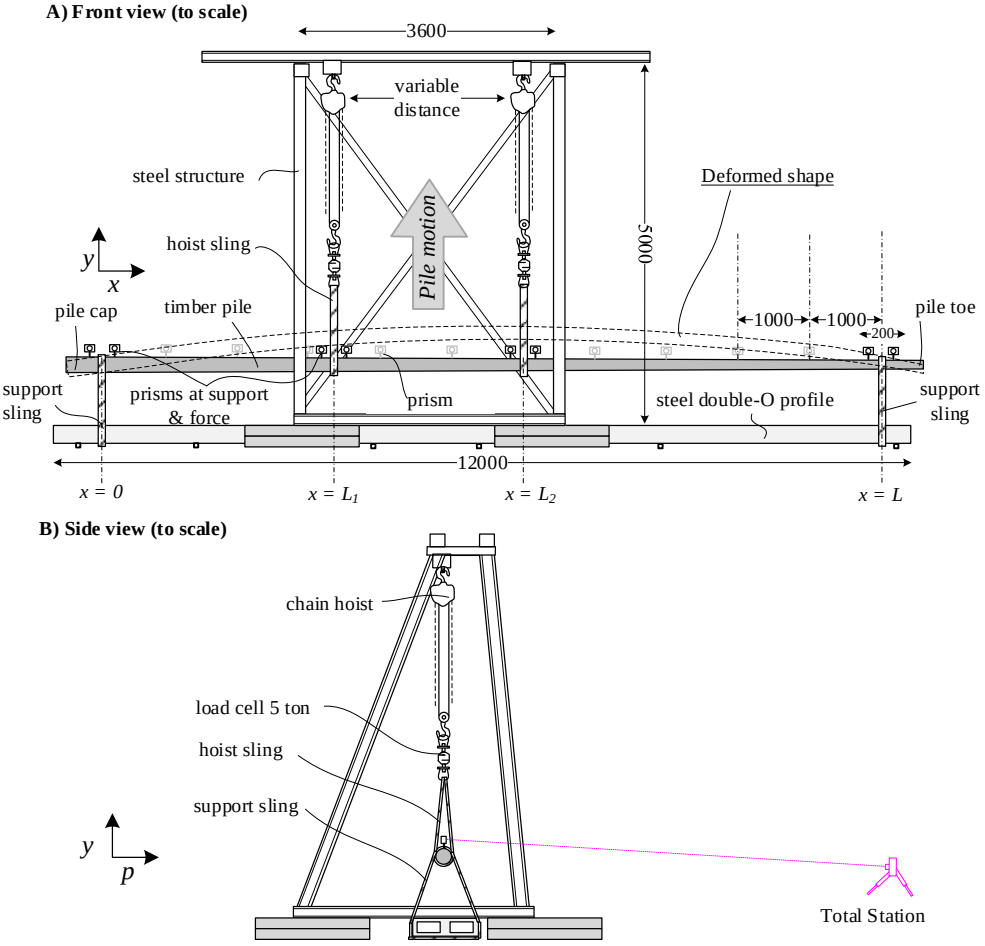

Figure 3.2, Technical drawing on the experimental set-up for the four-point bending experiment. A) presents the front view of the bending experiment and B) the side view of the experiment.

First, the piles are suspended by the two hoist slings without attaching the support slings at the ends. Due to its own weight, the pile deforms in an arch shape. Accordingly, the support slings at both ends of the pile are attached and the hoist chains are pulled until tension starts to develop at the support slings. This situation is considered the 'zero situation'. It should be noted that at this moment, the pile is already subjected to bending stresses. The test starts and the pile is loaded by two point loads, applied by pulling the hoist chains step by step, increasing the bending stresses in the pile. A photograph during the bending test can be seen in Figure 3.3. The force ratio between the two applied point loads with the hoist slings is kept constant from the start of the test till breaking of the pile with the aim of having a constant outer-fibre stress between the loading points. The force ratio is defined as $a_F=F_1/F_2$ in which F_1 is the load at L_1 and F_2 is the load at L_2. This force ratio depends on the pile dimensions and loading configuration and is elaborated for each pile in section B.1. The experiment is however displacement controlled and a schedule of displacement targets is pursued. In total six piles have been subjected to the four-point bending test.

3.2.2 Pile extraction and dimensions

In total, ten piles have been extracted from the Overamstel quay wall site. The extraction was performed with a vibrating customized steel pneumatic clamp of 3m long in order to avoid pile breakage or damage. The extraction device with timber foundation pile can be seen in Figure 3.4. Four piles were extracted from segment F. The remaining six piles were extracted from segment B, after the quay wall test (chapter 5) was performed. The piles were visually inspected and no plastic deformations (broken timber fibres) as a consequence of the quay wall experiment were observed. From the ten piles, the six piles in the best condition were equipped with fibre optic (FO) wires and four piles were left unchanged. In the bending experiment, two FO piles and four untreated piles were tested. The remaining four FO piles were used in the lateral pile group experiments which are presented in chapter 4. The piles were stored fully submerged to ensure that the timber did not dry out and the moisture content remained the same prior to extraction. A schematic visualization of the six piles that were used for the bending test is given in Figure 3.5. The length of the piles varied between 11m and 13m. During the extraction process, some piles were damaged. The head of pile 1 and pile 4 was damaged severely and therefore removed from the pile before tested. Pile 4 was cracked at 9m depth during extraction, which made it necessary to remove the lower part of the pile. Furthermore, the toe of pile 3 was broken and left behind in the ground. In addition to the broken toe, the soft shell of the cap was partly damaged due to the extraction clamp with which high tensile forces were exerted on the timber. Pile 2, 5 and 6 had no significant damage. Furthermore, knots were observed on the surface of all timber piles.

For all the six piles tested, the pile diameter D[m] as function of the pile length is plotted in Figure 3.6. Three diameters per pile are plotted, measured vertically, horizontally and computed from the circumference. For trendlines, an average of the three diameters is used. The values of the tapering a[m/m] and density ρ_t[kg/m^3] can be found in Table 3.1. Furthermore, the diameter at $\bar{x} = 0$ is provided, indicated with D_L[m]. Because the dimensions and length vary a lot between the piles, a unique loading configuration for each pile is made which can be seen in Figure 3.5. A global reference system, located at the original pile cap is indicated with (x,p) and for each pile, a local reference system $(\bar{x},\bar{p})$ is provided. The support slings are connected to the pile at $\bar{x} = 0$ and $\bar{x} = L$. The hoists are connected to the pile at $\bar{x} = L_1$ and $\bar{x} = L_2$. The values of L, L_1 and L_2 can be found in Table 3.1 and are determined so that that the maximal stresses are present at around $\bar{x} = L/3$ of the

pile length. For lateral loaded piles embedded in soil, this is the depth at which bending moments are expected to be maximal. Another important factor in the determination of L, L_1 and L_2 is the force ratio. This ratio should not be greater than 5 in order to assure the workability of the hoist cranes.

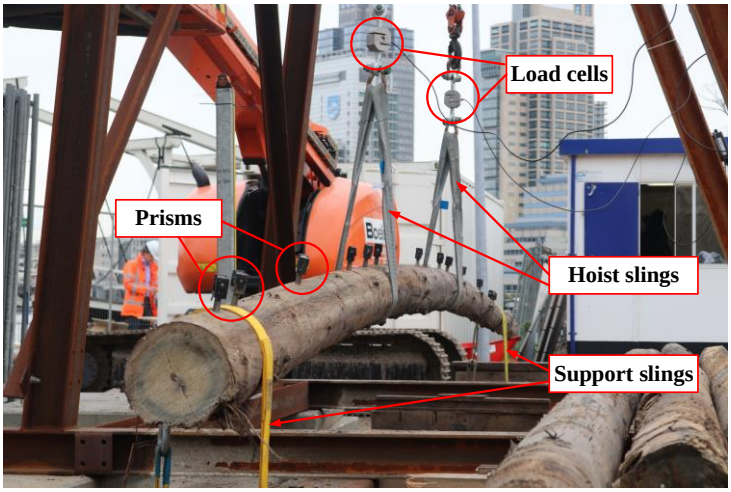

Figure 3.3, Photograph of pile bending test set-up during loading.

Figure 3.4, Extraction of timber foundation pile with steel pneumatic clamp under vibration.

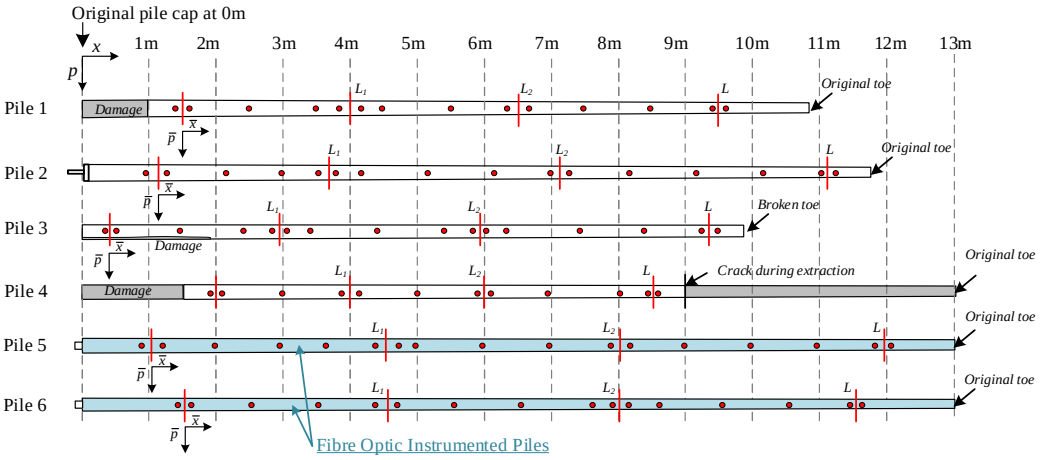

Figure 3.5, Piles that are used for the four-point bending test. Grey area represents a part of the pile that is removed. A red dot represents a measuring prism and a red stripe represents a support or hoist point. FO installed piles are indicated in blue.

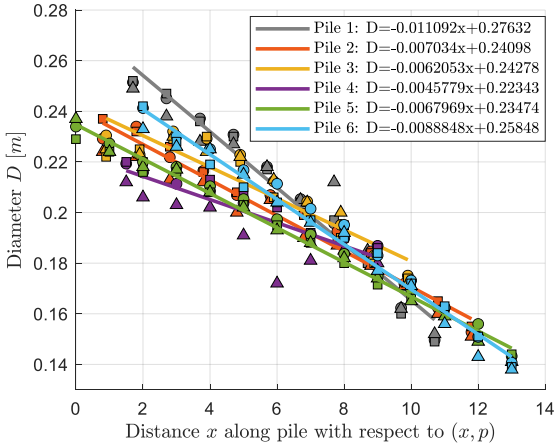

Figure 3.6, Pile diameter at multiple locations along the pile length with respect to global reference system (*x*,*p*). Scatter legend: ○ – D from circumference measurement, □ - D from horizontal measurement, Δ - D from vertical measurement.

Table 3.1, Pile properties and their loading dimensions with respect to their local reference ($\bar{x}$,$\bar{p}$).

Pile [#]	Taper a [m/m]	ρ_t [kN/m^3]	($\bar{x}$,$\bar{p}$) [m]	D_l [m]	L_1 [m]	L_2 [m]	L_3 [m]
1	0.01109	7.10	1.5	0.259	2.5	5.0	8.0
2	0.00703	6.58	1.1	0.233	2.5	6.0	10.0
3	0.00620	7.59	0.4	0.240	2.5	5.5	8.9
4	0.00578	7.15	2.0	0.214	2.0	4.0	6.5
5	0.00679	7.20	1.0	0.228	3.5	7.0	11.0
6	0.00884	7.18	1.5	0.245	3.0	6.5	10.0

3.2.3 Force ratio

The mechanical scheme for the four-point bending test on tapered piles can be seen in Figure 3.7. While performing the four-point bending test, it is important that stress in the most outer fibre σ_{outer}[N/mm^2] remains constant between the two loads F_1 and F_2. A constant stress between L_1 and L_2 forces the beam member to break at the most critical cross section. For a member that has a constant flexural modulus (EI) over the full pile length and a symmetrical loading scheme, a constant outer-fibre stress between the loads is reached with a force ratio a_F=F_1/F_2 of 1. For tapered piles where the self-weight is included, it is theoretically not possible to create a perfectly constant outer-fibre stress between the two loads because both the self-weight and the modulus are varying over the pile length. It is however possible to find a solution for the F_1/F_2 ratio in which σ_{outer} at L_1 is equal to σ_{outer} at L_2, resulting in a more or less constant outer-fibre stress profile between L_1 and L_2 (see bending stress diagram in Figure 3.7). The ratio for obtaining a semi-constant σ_{outer} between L_1 and L_2 stress is determined analytically. An important assumption in the derivation of the force ratio is that the timber has a constant modulus of elasticity E_b and is an isotropic and homogeneous material. As E_b can not be measured, this is the best assumption possible. Force ratios can be found in Table 3.2. The analytical derivation of bending moment formulas and of the force ratios for pile 1-6 can be found in appendix B.1.

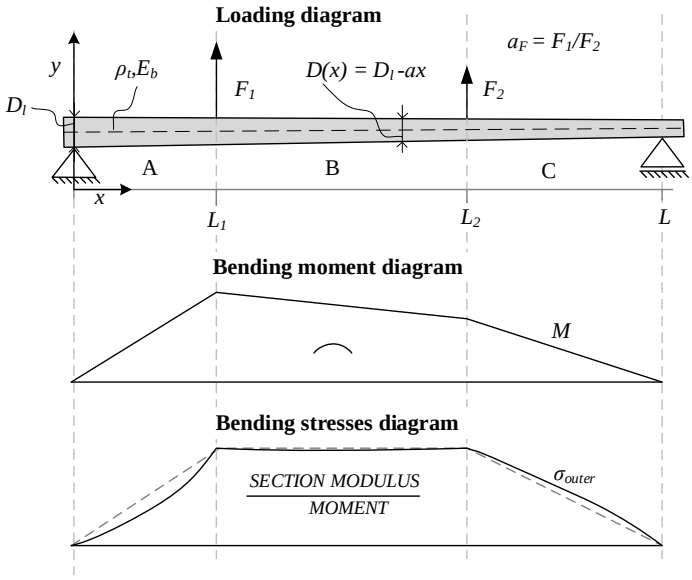

Figure 3.7, Mechanical scheme four-point bending test on tapered pile. Trapezoidal dashed shape in bending stress diagram is provided to show non-linearity in bending stresses. Moment is indicated with *M*.

Table 3.2, Force ratios for each individual pile during the bending experiment.

Pile [#]	a_F [-]
1	4.2
2	4.3
3	2.8
4	2.2
5	3.7
6	4.4

3.2.4 Instrumentation

The deflection of each pile is determined by an array of prisms for tachymetry with a spacing of 1m across the entire pile length. At the location of hoist-and support slings, prisms are placed at both sides of the sling which can be seen in Figure 3.5. The prisms are screwed in the timber with a depth of approximately 1cm. Between each load step, the location of all prisms is measured with a total station. From the displacement measurements across the pile length, the curvature κ[m^{-1}] of the pile in the *xy*-plane can be determined. In order to do so, a fourth order polynomial function is fitted through the displacement measurements to create a continuous deflection as function of the pile length. Using the kinematic bending relation expressed in eq. 3.1, the curvature as function of the pile length can be determined.

$$\kappa = -\frac{d^2y}{dx^2} \qquad \textbf{eq. 3.1}$$

To determine the load in the hoist slings, two 50kN S-load cells are used with a frequency of 1Hz. By measuring every second, it is possible to maintain a constant force ratio while operating the hoist cranes which is of paramount importance to keep the outer-fibre stress constant between the point loads during the entire experiment. The load cells and prisms can be observed in Figure 3.3.

3.2.5 Fibre optic technique

Besides the instrumentation described in the previous section, two piles - pile 5 and 6 - are equipped with fibre-optical[1] wires to obtain the bending strains, curvatures and deformations. To validate the FO technique, measurements obtained from the prisms are used. While prism measurements may not be entirely free from error, they can still be considered accurate with a monitoring error of 1mm. The application of FO-installed-piles is used in the lateral pile group experiments in order to monitor the in-depth strains and pile deformations.

Per FO instrumented pile, two wires are glued inside the pile along the entire pile length. Each wire covers two perpendicular sides of the pile, starting from the pile cap towards the pile toe. Accordingly, the wire is pierced towards the other side of the pile and brought back to the cap. In this manner, the wires are installed in quadrant orientation which can be observed in Figure 3.8. The two wires are labelled North-South and East-West. The centre-to-centre distance between North and South is indicated with h_{NS}[m] and perpendicular to that, the East-West distance with h_{EW}[m]. Values for h_{NS} and h_{EW} can be found in appendix F.1. A quadratic orientation is essential, as with two fibres the curvature can only be determined in one plane, N-S or E-W. Any deviations φ_r[rad] between the fibre orientational plane and the plane of actual bending, shown in Figure 3.9, would result in an underestimation of curvature and thus displacement. By installing the fibres in four main directions the curvatures κ_{NW}[m^{-1}] and κ_{EW}[m^{-1}], in N-W and E-W direction, can be computed from the strain measurements along the pile length according to eq. 3.2. In this equation, ε_N, ε_S, ε_E and ε_W [mm/mm] are the measured strains in the North, South, East and West fibres. Since the curvature is a vector, the total curvature in the plane of bending κ_t[m^{-1}] can be computed using eq. 3.3. The fibres have a spatial resolution of 0.25m.

$$\kappa_{NS} = \frac{\varepsilon_N - \varepsilon_S}{h_{NS}} \qquad \kappa_{EW} = \frac{\varepsilon_E - \varepsilon_W}{h_{EW}} \qquad \textbf{eq. 3.2}$$

$$\kappa_t = \sqrt{K_{NS}^2 + K_{EW}^2} \qquad \textbf{eq. 3.3}$$

Since the grooves in the timber are sawn manually and this remains a practical exercise, it is not guaranteed that the North-South direction and East-West direction are perfectly perpendicular towards each other. From the resultant curvature κ_t across the pile length, illustrated in Figure 3.9, the deflections y[m] can be obtained according to eq. 3.4. The derivation this equation can be found in appendix B.4.1. Given that the curvature has a spatial resolution of 0.25m, eq. 3.4 is discretized.

$$y(x) = -\frac{\left(\int_0^L (1-x)\kappa_t(x)dx\right)x - L\left(x\left(\int_0^x \kappa_t(x)dx\right) - \left(\int_0^x x\kappa_t(x)dx\right)\right)}{L} \qquad \textbf{eq. 3.4}$$

[1] The application of fibre optical wires in timber foundation piles or structural members is not new. In 2020, axial loading experiments were performed in new timber foundation piles (Honardar, 2020). To monitor the axial response of the timber pile, fibre optical wires were installed likewise the explained orientation in Figure 3.8. Fibre optical wires are also used in study where laminated timber is subjected to a four-point bending test (Goodwin et al., 2022) in order to assess the structural behaviour. Variations are made with multiple strain wires with respect to the neutral axis to study the compression and tension side of the laminated timber member. Installing fibre optical wires in 115 year old timber foundation piles, to understand the bending response, is unique and as far as known never been done before.

Please note that eq. 3.4 is derived for a member on two supports, which makes it suitable for the piles in the bending test configuration. Other mechanical schemes, like a pile embedded in soil, have a different mechanical scheme and therefore their own curvature-displacement relation.

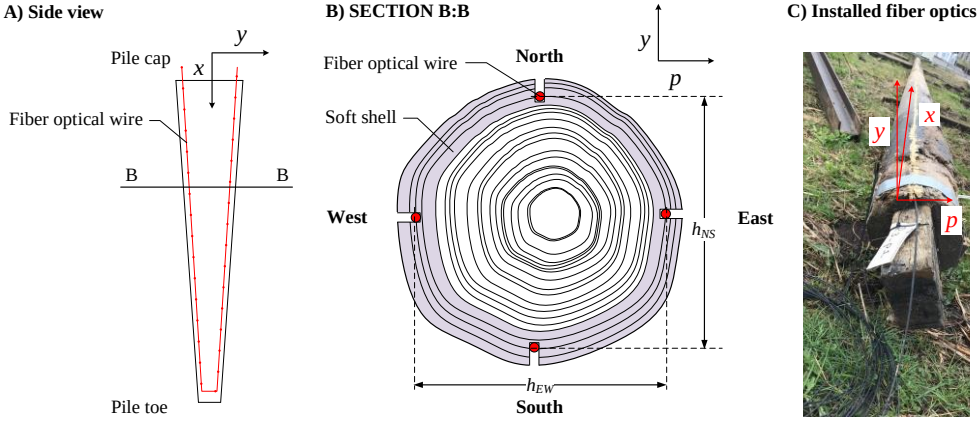

Figure 3.8, Fibre optic wire orientation. A) Side view on pile with fibre optical W-E wire. B) Sectional view on the quadratic orientation of the fibres. C) Fibre optical wires installed in the timber pile and groove is filled and finished with glue.

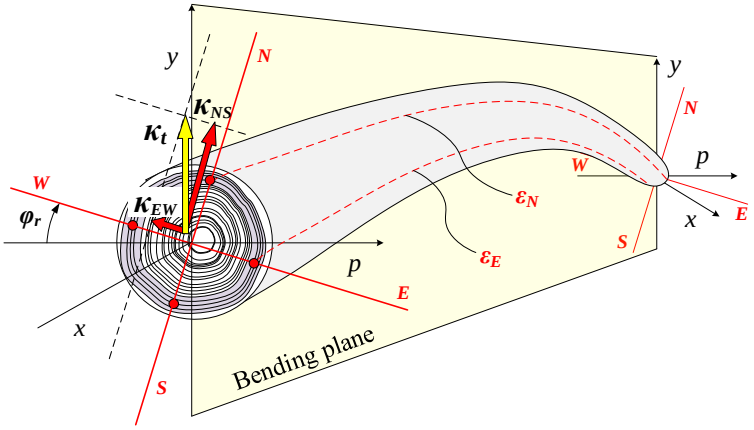

Figure 3.9, Schematic illustration of a pile subjected to bending. The pile reference system is indicated with (*x,y,p)* in which *x* is in the direction of the axis and *y* the direction of bending. The bending plane *x-y,* is indicated in yellow. The orientation of the fibre-optic reference system is indicated by (N-S,E-W). The fibre-optic reference system is rotated with φ_r with respect to the bending reference system.

3.2.6 Micro drilling measurements to determine soft shell

For this bending experiment, it is essential to determine the thickness of the soft shell in order to make an effective diameter estimate. The effective diameter is indicated with *h*[m]. It is important to exclude the soft shell from the strength analysis of the timber pile since the soft shell has hardly any structural strength. Including the soft shell instead of using an effective diameter underestimates the modulus of elasticity E_b and the modulus of rupture *MOR* of the

heartwood. It should be noted that when performing bending capacity checks of timber piles, this also needs to be done with an effective diameter instead of an external diameter.

A non-destructive method to determine the soft shell of the timber piles is micro-drilling (van de Kuilen et al., 2021). In order to make an estimate of the soft shell, the micro-drilling method with IML-RESI PD is used which can be observed in Figure 3.10. This method is widely used for timber in general and currently an IML-Resi is in trial stage for underwater use in the historic centre of Amsterdam. An extensive analysis of the micro drilling resistance, the positive and negative aspects of the IML technology has been carried out by (Gard et al., 2018). The method is briefly elaborated here. The IML RESI PD has a drilling tip of 3mm at the tip which converges to a shaft of 1.5mm. The drill is pushed, while drilling, with a constant feed through the timber. Two parameters are important while drilling, the feed resistance Ω_f [%] and the drill resistance Ω [%]. Both resistances are measured and an example as function of the drilling depth can be found in Figure 3.11. Large densities, for example knots, can be identified as large amplitude peaks. Furthermore, year rings can be identified by high frequency wiggles. Low resistance amplitudes can indicate cavities, low quality timber or degraded timber. At the location of each prism, a micro-drill has been performed (in the *y*-direction). For pile 2,3 and 4 also micro-drills have been performed in the *p*-direction direction. An overview of drillings per pile can be found in Table 3.3. All drillings have been performed after the bending tests.

Figure 3.10, IML micro drilling performed on all piles after the bending experiment was executed.

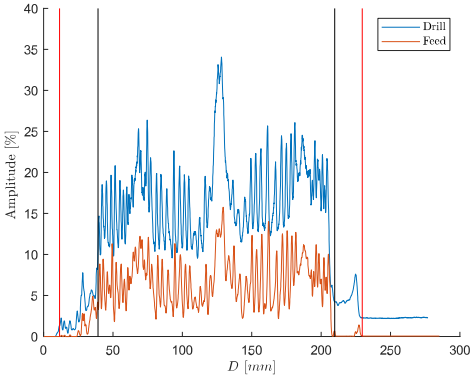

Figure 3.11, Drilling resistance profile obtained from micro drill test data. Area between vertical red lines represents the cross section of the pile. Area between vertical black lines represents the estimated effective diameter *h* of the timber pile. Distance between black and red lines is the estimated soft shell.

Table 3.3, Overview of number of IML measurements per pile.

Pile [#]	IML *y-direction*	IML *p-direction*
1	18	-
2	11	11
3	15	15
4	12	12
5	17	-
6	15	-

3.3 Results and interpretations

3.3.1 Moment curvature diagrams

To obtain the κ-M (curvature-moment) diagrams, first the curvature and bending moment diagrams need to be constructed. For illustration purposes, pile 5 is considered. In Figure 3.12A, the deflection of the pile during different load steps can be seen. Note that not all load steps are visualized in order to keep the figures clear. Through the prism measurements, fourth order polynomial functions $P_w(x)$[m] are fitted, describing the deflection as function of x. From the deflections, the curvature along the pile length is determined by $\kappa = -d^2P_w(x)/(dx^2)$ according to eq. 3.1. The curvature for each load step can be seen in Figure 3.12B. Since the curvature is obtained from the second derivative of a polynomial fit through discretized prisms, small errors are expected. Especially at the supports errors can be observed where in theory curvatures should be zero, but clearly are not always. An interval along the x-axis is chosen within which the curvature is considered useful for analysis, indicated with dashed vertical lines at $x = 2$ and $x = 9$. The corresponding bending moments for each load step, determined by eq. B.4, can be observed in Figure 3.12C. The same figure as Figure 3.12, but for pile 1-4 and 6 can be found in appendix B.2.

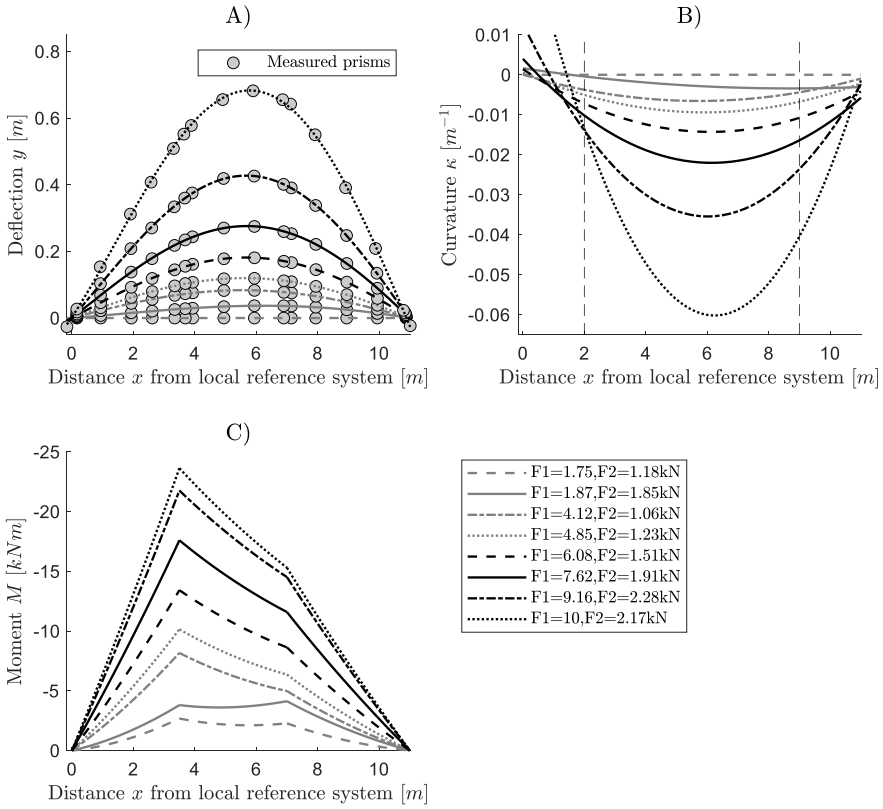

Figure 3.12, Bending test results pile 5. Note that not all load steps are visualized. A) Displacement obtained by measuring prisms, indicated with grey dots. Through the prism measurements, fourth order polynomial functions $P_w(x)$ are fitted, describing the deflection as function of x. B) Curvature obtained from $P_w(x)$ C) Bending moment obtained by load cells.

Now the bending moment and curvature along the *x*-axis of the pile are known for each load step, it is possible to construct the *κ-M* diagram at different cross sections of the pile. In Figure 3.13, the *κ-M* for different cross sections along the *x*-axis for pile 5 is given. The same figure as Figure 3.13, but for pile 1-4 and 6 can be found in appendix B.3.

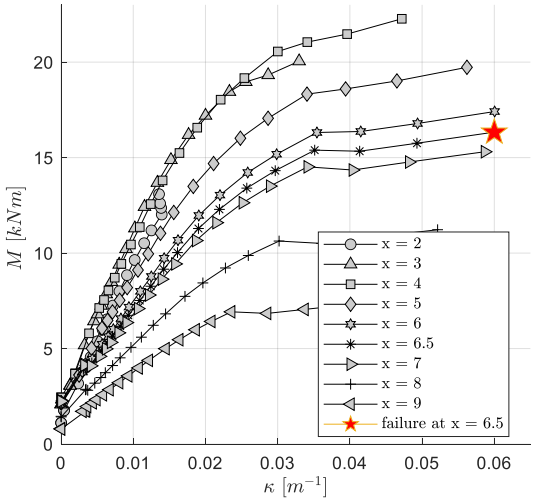

Figure 3.13, *κ-M* diagram of pile 5 for different cross sections along the *x*-axis.

As can be observed, the *κ-M* diagrams follow a linear trajectory that transitions into an elastic-plastic behaviour. The gradient of the linear trajectory is associated with the flexural stiffness *EI* of the pile and is, according to the measurements, largest at the cap of the pile (*x*=2) and smallest at tip of the pile (x=9). This is expected since the piles are tapered, having a larger pile diameter at the cap than at the tip. The pile breaks at *x* = 6.5m which is indicated with a red star in the diagram. From Figure 3.13 it can be seen that bending moments already occurred while the curvature in the pile is zero. This has to do with the fact that the prisms are initially measured when the pile bends on its own weight in the hoist slings. It is therefore essential to shift the *κ-M* curves along the *κ*-axis so that the slope of the linear part passes exactly through the origin. This correction of the *κ-M* diagram is done after the comparison with fibre-optical data in order to have a proper validation.

3.3.2 Validation of deflections with fibre optic strain measurements

In this section, the fibre-optical technique is validated with the prims measurements. For pile 5, the measured strains in the North-South direction are presented in Figure 3.14. The North-South direction is placed in the direction of bending. The horizontal axis indicates the wire length and on the vertical axis, the macrostrain $\mu\varepsilon$ is situated. Figure 3.14 is explained from left to right. Between 101.176m and 113.173m, the wire is in the open air and enters the pile cap until the local reference system at the cap-support sling at *x = 0*. The wiggles are caused by temperature influences. From 113.173m to 124.403m, the North strain is measured between the two support slings. Between 124.403m and 126.445, the wire goes to the pile tip and back to the support at *x=L*. From 126.445m to 137.675m, the South strain is measured between the two support slings. From 127.675m to 157.584m, the wire leaves the pile and is in the open air, again the wiggles are due to temperature influences. Only the measured strain in the North-fibre and South-fibre are relevant and therefore indicated in colour, the rest is

left grey. The fibre breaks directly after the loading step F_1 = 9.16, F_2 = 2.28kN with a maximal strain of 2800$\mu\varepsilon$ which is in an earlier stage than the breakage of the pile itself.

It can be seen that the strain in the North-fibre and South-fibre are not symmetrical, especially for the larger loads. The strain at the North fibre has a trapezoidal profile which corresponds to the intended stress profile from Figure 3.7. However, for the South fibre, this is clearly not the case. Large peaks appear in the measured strain at loading step F_1 = 7.09, F_2 = 1.8kN and the strain profile narrows. Peaks start to form at a strain of around 1550$\mu\varepsilon$ in the South fibre, no significant peaks are observed in the North fibre. Nevertheless, the maximal strain in the North fibre is more or less equal to the maximal strain in the South fibre. Likewise the North-South direction, the measured strains in the East-West direction are presented in Figure 3.15. It can be seen that the bending strains are considerably lower than measured in the North-East fibre which is a sign that the orientation of the North-South direction was placed in good alignment with the plane of bending. No large peaks are observed since the measured strains are low (<800$\mu\varepsilon$).

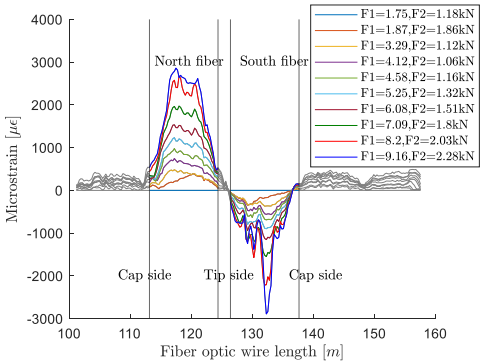

Figure 3.14, Measured strain in pile 5. North-South direction.

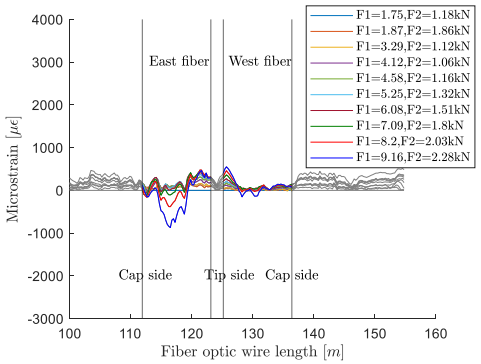

Figure 3.15, Measured strain in pile 5. East-West direction.

The measured strains in the North, South, East and West are used to compute the curvature according to eq. 3.2 and eq. 3.3. The curvature of pile 5 can be found in Figure 3.16. Besides the curvature obtained from the fibre optical measurements, the prisms obtained curvature $P_w(x)$ is presented as well. It can be observed that the FO-curvatures match the prism curvatures in good correspondence until load step F_1 = 9.16, F_2 = 2.28kN. After that, computed curvatures from FO measurements become poor. At x = 6.5m, a small bump is present which increases in size for an increasing load. This is the location at which the pile ultimately breaks. Based on the methodology explained in section 3.2.5, the curvature profile is converted into a deflection along the pile length, visualized in Figure 3.17. Besides the deflections obtained from the fibre optics, the prism measurements are added, which are considered accurate due to their measuring error of 1mm. Deflection computations over the full pile length with fibre optics are in very good correspondence with the measured deflections by prisms until load step F_1 = 8.2, F_2 = 2.03kN. From this load step and onwards, deflections are underpredicted by FO, followed by the breakage of the fibre optical wire.

The strain measurements and validation of pile 6 can be found in appendix F.2.1 and appendix F.2.2, here a brief summery is given. Contradictory to pile 5, the stress distribution of the North fibre and South fibre are symmetrical and have a trapezoidal shape as intended. The fibre breaks with a maximal strain of 2500$\mu\varepsilon$ which is slightly less compared to pile 5

which broke at 2800$\mu\varepsilon$. Large peaks and deep troughs start to appear, mainly in the South fibre, when loads increase and strains approach 1600$\mu\varepsilon$. Curvatures and thus displacements are well predicted until this load stage. After 1600$\mu\varepsilon$ predictions become poor due to the disturbed strain signal, which is comparable to pile 5 in which predictions became poor at 1550$\mu\varepsilon$.

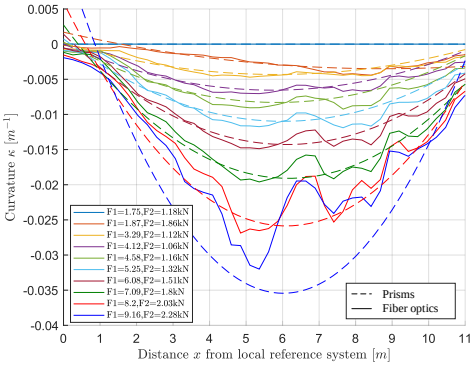

Figure 3.16, Curvature of pile 5 obtained from fibre strains.

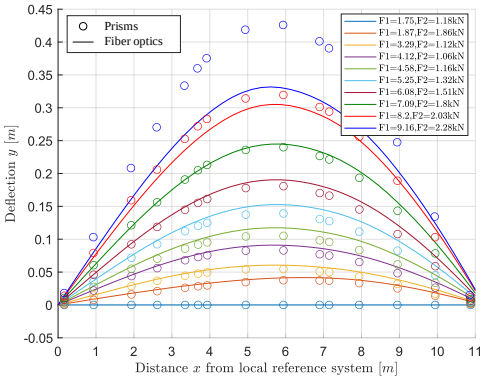

Figure 3.17, Deflection of pile 5 obtained from curvature profile.

For both piles 5 and 6, it is concluded that curvature and displacement predictions are accurate for strains below 1600$\mu\varepsilon$. With higher strains, the strain measurement becomes disturbed and large peaks and troughs start to form in the strain profile, mainly in the compression zone of the pile. However, the fibre remains operational until roughly 2500-3000$\mu\varepsilon$ after which the fibre wire breaks. A discussion with recommendations is provided in section 3.4.

3.3.3 Flexural stiffness across pile length

The flexural stiffness of each pile is determined using its moment curvature diagrams. For each location along the pile x-axis, the moment-curvature diagram is constructed, as demonstrated in Figure 3.13. Accordingly, the gradient of the linear section of the moment-curvature diagrams is determined for the various locations along the x-axis. This process is repeated for all six piles, resulting in a plot of flexural stiffness along the x-axis of each pile, as shown in Figure 3.18. On the horizontal axis, the distance along the pile length is shown with respect to the location of the original pile cap (or general reference system). It is clear that, for all piles, the flexural stiffness is largest at the pile cap and smallest at the pile toe. In between, a slight non-linear convex gradient can be observed. According to the same methodology as discussed in section 3.3.1, the flexural stiffness is determined with the fibre optical measurements. It can be seen that the flexural stiffness determined with the fibre-optics technique is in good alignment with the flexural stiffness obtained from the prism measurements. A linear trendline is added which is a weighted average of the prism obtained stiffnesses. This trendline is considered a mean flexural stiffness for Overamstel timber foundation piles and will be used in chapter 4 and chapter 5 when performing pile group averaged computations.

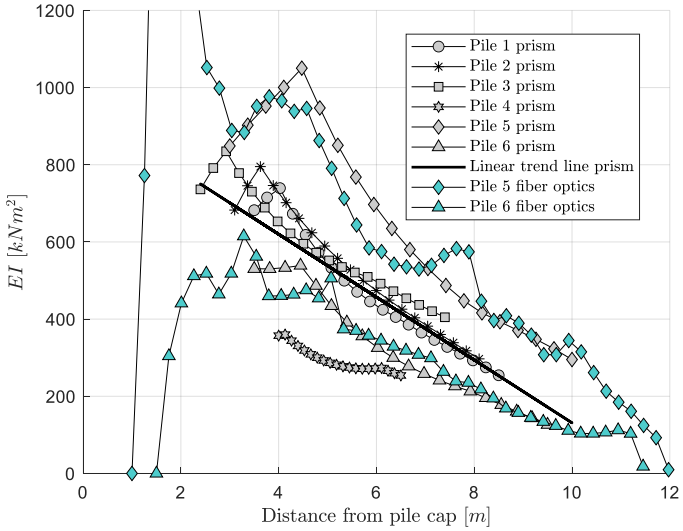

Figure 3.18, Flexural stiffness of pile 1-6 across pile length obtained by prism method. For pile 5 and pile 6, the flexural stiffness obtained with fibre optics is presented for validation purposes. A linear trendline is provided based on the prism method *EI(x)* = -81.46*x* + 945.77.

In the determination of the flexural stiffness, only a certain range of the pile length is taken into account. This has two reasons. The first reason is that the support slings are not connected to the outermost ends of the pile resulting in the absence of bending information at those extreme parts. The second reason has to do with the uncertainty in the curvature and bending moment measurements close to the sling supports. Since both the curvature and the moment approach zero at the location of the supports, errors become infinitely large at $x = 0$ and $x = L$. Close to the supports, the determination of the flexural stiffness is considered unreliable and therefore excluded from Figure 3.18.

3.3.4 Estimate of effective diameter by IML measurements

In the determination of the modulus of elasticity and the modulus of rupture, the effective pile-cross section is of significant importance. As described in section 3.2.6, IML measurements are performed in order to make an estimate of the soft shell and thus the effective diameter *h*. Drilling resistance profiles for each individual pile, obtained from micro drill tests, can be found in appendix E.1. During the bending experiments, the appearance of the soft shell became visible. An example can be seen in Figure 3.19 where the soft shell 'cracks open' from the healthy heartwood. During this process, the measured forces in the pile were hardly influenced, indicating that the soft shell has a neglectable influence on the bending of the pile. For all six piles, it was observed that the soft shell moved like a sleeve around the heartwood without a significant contribution to the bending resistance. The estimated soft shell for pile 3, based on IML measurements, can be found in Figure 3.21. It can be observed that the thickness of the soft shell is less than 10mm at the pile cap but 2m away from the cap, the softshell increases to 20-35mm. The spatial variability of the thickness is significant. The thickness of the soft shell of the other piles can be found in appendix E.2. No correlation between pile diameter and soft shell thickness was present and also no correlation between soft shell and longitudinal pile location was found, indicating that the

biological decay of timber piles has a large arbitrary spatial variety. Figures on the correlation between soft shell thickness and pile location or pile diameter can be found in appendix E.2.

Figure 3.19, Soft shell visible during loading of pile 4 at load step 14 of 26. Soft shell 'cracks open'.

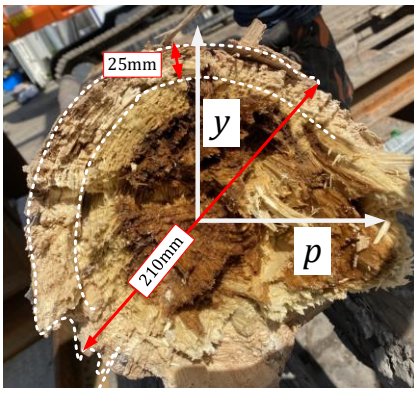

Figure 3.20, Photograph of bending failure cross section of pile 3. Softshell can be identified by colour and structure of the timber fibres. Shell in positive *y*-direction is estimated to be 20mm by visual inspection.

In Figure 3.20, a cross-sectional photograph of pile 3 is presented directly after the breakage. The soft shell is indicated with a dashed white line and it can be seen that the texture of the timber shell looks different from the heartwood. The soft shell fibres seem to have a more open and brittle structure than the core wood. Figure 3.20 was taken at 5m from original pile cap and in the positive *y*-direction, the soft shell at this location was estimated to be 25mm. This is in good correspondence to IML drillings, in which a soft shell of around 20-25mm was determined, seen in Figure 3.21. The average soft shell thickness of the tested pile population (see Figure 3.22) was 21mm with a 95% characteristic value of 36mm.

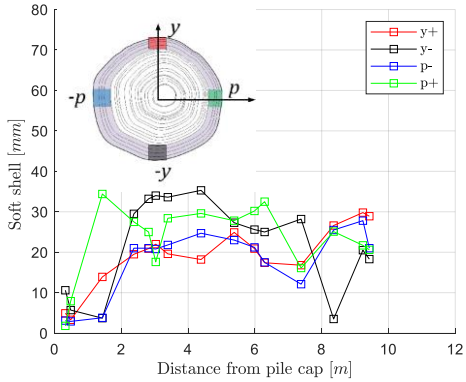

Figure 3.21, Soft shell estimate of pile 3.

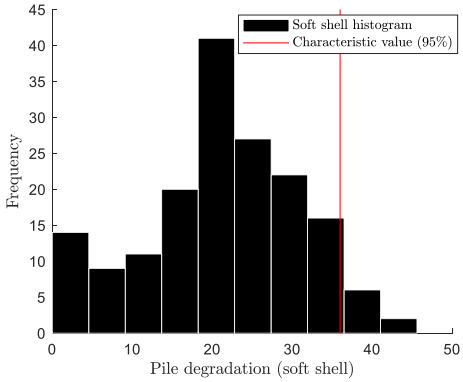

Figure 3.22, Histogram on pile degradation for all IML measurements.

3.3.5 Modulus of elasticity and modulus of rupture

The flexural stiffness of a pile is composed of two quantities: the modulus of elasticity E_b and the moment of inertia I. The moment of inertia is dependent on the pile's cross-sectional shape, which vary along its length, while the modulus of elasticity may not be constant throughout the pile's length (Larson et al., 2004). To calculate the moment of inertia, an effective diameter is used, resulting in $I = 1/64\pi h^4$. The modulus of elasticity can be computed by dividing the determined flexural stiffness $\widetilde{EI}$ by the by the moment of inertia, presented in eq. 3.5. To avoid confusion with E_b denoted on both sides of the equation, the flexural stiffness is indicated with a tilde to emphasize that it should be considered a single parameter.

$$E_b = \frac{\widetilde{EI}\ 64}{\pi h^4} \qquad \textbf{eq. 3.5}$$

The effective diameter h is determined at each IML drill location so only at these points the modulus of elasticity is determined. The elastic modulus as function of the pile length can be found in Figure 3.23. Note that measurements close to the sling supports are excluded due to measuring uncertainties as explained in section 3.3.3.

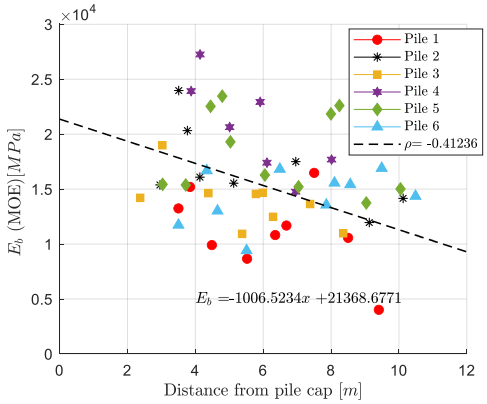

Figure 3.23, Modulus of elasticity as function of the pile length.

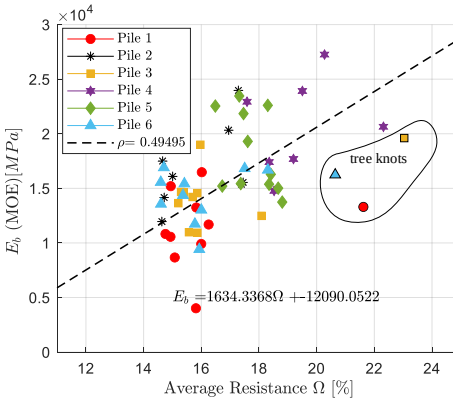

Figure 3.24, Modulus of elasticity as function of the average IML drilling resistance. Because of their high Ω, tree knots are excluded from linear regression.

A large spread of the modulus of elasticity can be observed. Even given the large spread, a trend between the pile location and modulus of elasticity is found. E_b seem to be roughly two times higher at the cap than at the toe. The observed phenomenon can be attributed to the growth pattern of the tree, where the pile cap, which is the bottom of the tree, experiences greater pre-loading compared to the top when the tree is alive. While the correlation coefficient for all measurements is ρ = -0.41, the correlation of individual piles is, in order of the pile number, ρ = -0.64, -0.75, -0.62, -0.81, -0.14 and 0.40. The correlation within a specific pile is higher than for the entire population, except for pile 5, which again underlines the large spread between and within the different piles. The average modulus of elastic found is 16.5GPa.

In order to make an estimate of the modulus of elasticity based on IML drillings, the modulus of elasticity is plotted as function of the average drill resistance Ω. The relation between E_b and Ω is visualized in Figure 3.24. It can be observed that the drilling resistance

and modulus of elasticity are moderate correlated (ρ = 0.50). The larger the drill resistance, the larger the modulus of elasticity.

In order to determine the modulus of rupture, the moment-curvature outcomes from the experiment are compared with the theoretical moment-curvature relation for a circular cross-section containing elastic-perfect plastic material properties. To do so, the moment M[kNm] and curvature κ are normalized according to their first yield values M_0[kNm] and κ_0[m^{-1}], resulting in $M^*=M/M_0$ and $\kappa^*= \kappa/\kappa_0$. The normalized theoretical curvature-moment diagram, including normalized experimental data, can be found in Figure 3.25A. Please note that only experimental data is used for which the yielding was observed. Mathematical expressions for the theoretical normalized moment-curvature of a circular cross-section can be found in eq. 3.6 and eq. 3.7, where $\sin(a^*)=1/\kappa^*$ (Pandit et al., 2022). The stress-strain diagram of an elastic-perfect plastic material can be found in Figure 3.25B. Figure 3.25 is explained briefly. For $0<\kappa<\kappa_0$, the diagram is linear and associated with the linear-elastic phase. All cross-sectional stresses remain below the modulus of rupture. For $\kappa > \kappa_0$, the outer fibre stress becomes larger than the modulus of rupture, associated with the elastic-plastic phase. The limit value which the bending moment reaches, is found when the curvature becomes infinitely large. At this point, all fibres are fully plastified with a stress equal to the *MOR*. It can be seen from Figure 3.25A that the timber piles follow the theoretical elastic-perfect plastic trajectory in good correspondence. Only for pile 4, significant hardening behaviour is observed when curvatures become more than twice the elastic curvature κ_0.

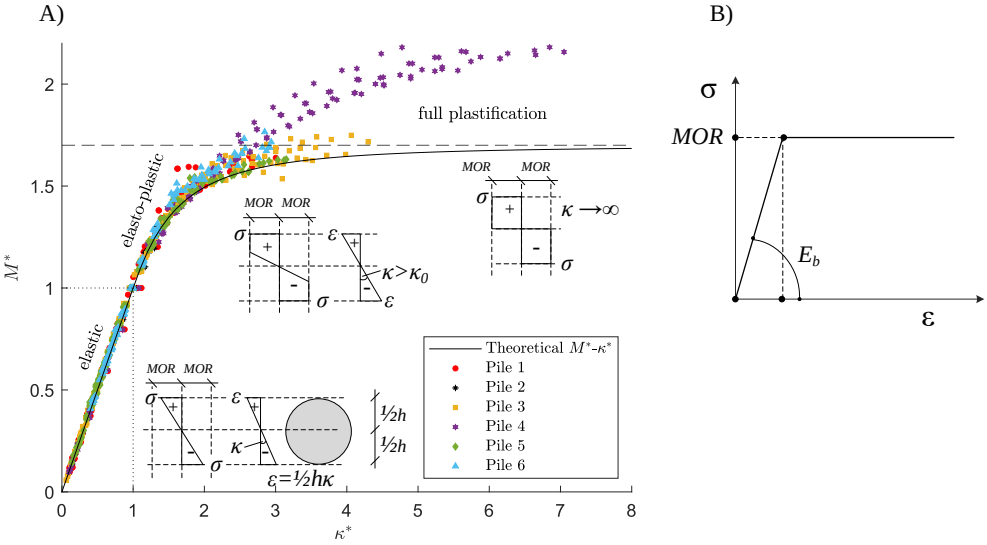

Figure 3.25, A) Normalized moment-curvature diagram based on a circular cross section with bi-linear stress-stain behaviour. Measurements are normalized according to $M^*=M/M_0$ and $\kappa^*= \kappa/\kappa_0$. B) Bi-linear stress-strain diagram.

$$\kappa^* \leq 1 \qquad M^* = \kappa^* \qquad \textbf{eq. 3.6}$$

$$\kappa^* > 1 \qquad M^* = \frac{16}{3\pi}\left(1-\frac{1}{\kappa^{*2}}\right)^{3/2} + \frac{2\kappa^*}{\pi}\left(a^* - \frac{\sin(4a^*)}{2}\right) \qquad \textbf{eq. 3.7}$$

The timber is assumed to behave as an elastic-perfect plastic material due to the strong correlation observed between the measurements and the bi-linear theory. By describing the timber material as an elastic-perfect plastic material, it is possible to determine the stress-

strain relationship and thus the modulus of rupture of the timber material. Relations between bending stress and bending strain are provided for the elastic phase in eq. 3.8 and elastic-plastic phase in eq. 3.9. Because the modulus of elasticity E_b, strain ($\varepsilon = \kappa h/2$), bending moment M, and the effective diameter h are known, it is possible to determine σ and construct the stress-strain diagram. The derivation of eq. 3.9 can be found in appendix B.4.2.

$\kappa^* \leq 1 \quad \sigma = \varepsilon E_b$ **eq. 3.8**

$\kappa^* > 1$

$$M = \frac{h^3\left(\left(\frac{8}{3}E_b^2\varepsilon^2\sigma - \frac{8}{3}\sigma^3\right)\sqrt{\frac{E_b^2\varepsilon^2 - \sigma^2}{E_b^2\varepsilon^2}} + E_b^3\varepsilon^3\left(\arcsin\left(\frac{\sigma}{E_b\varepsilon}\right) - \frac{\sin\left(4\arcsin\left(\frac{\sigma}{E_b\varepsilon}\right)\right)}{4}\right)\right)}{16E_b^2\varepsilon^2} \quad \textbf{eq. 3.9}$$

The stress-strain diagrams for all six tested piles in bending are provided in Figure 3.26. Multiple lines are plotted for each pile, representing yielding positions along the length of the pile at the same spots where IML drillings were conducted. The slope of the linear trajectory is defined by E_b and the plastic limit by *MOR*. Pile 4 shows hardening behaviour while the other piles have a more or less constant plastic limit with an increasing strain. On the left side of Figure 3.26, a histogram of the *MOR* is presented with 90% confidence interval. The mean modulus of rupture found is 23.16N/mm^2 with a standard deviation of 6.9N/mm^2.

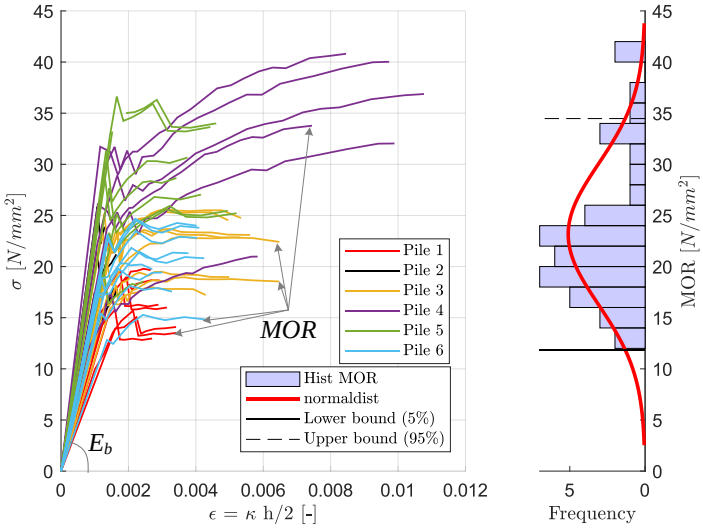

Figure 3.26, Stress-strain behaviour timber piles in bending. Horizontal part of bilinear curve is defined as modulus of rupture *MOR* and linear trajectory is defined as modulus of elasticity E_b.

From Figure 3.26 it is apparent that a large spread in the modulus of rupture is present, varying from 13N/mm^2 to 40 N/mm^2. The spread within each pile is smaller but still significant. In Figure 3.27, the *MOR* as function of the location along the pile axis is plotted. An average modulus of rupture of around 20-25 N/mm^2 was found with a very poor correlation between *MOR* and location along the pile axis. The relation between the IML drill resistance and the *MOR* is provided in Figure 3.28. Here a moderate correlation of $\rho = 0.65$ is found, which reads that a higher drill resistance corresponds to a higher modulus of rupture.

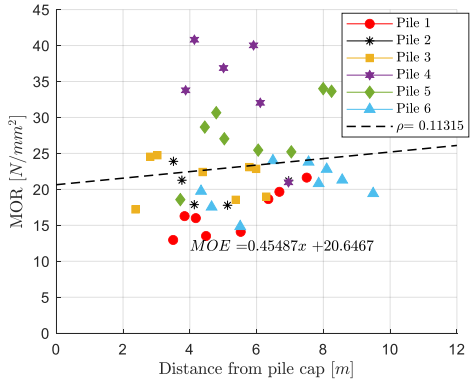

Figure 3.27, Modulus of rupture as function of the pile length.

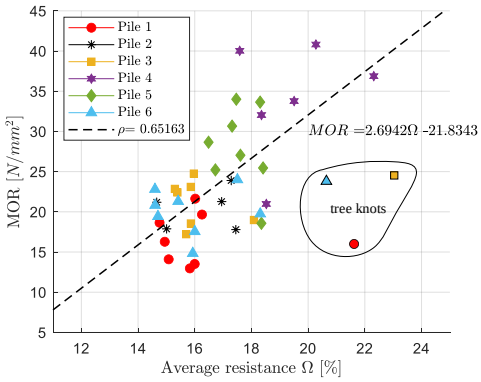

Figure 3.28, Modulus of rupture as function of the average IML drilling resistance. Tree knots are excluded from linear regression.

To illustrate the effect of using an effective diameter *h* in the determination of the modulus of elasticity and modulus of rupture, Figure 3.29 is provided. In here, E_b is plotted against *MOR*. In red, the determination of strength parameters is done with an external diameter *D*. In black dots, strength parameters are computed with an effective diameter *h*, subtracting the soft shell from the external diameter. Including or excluding the soft shell has hence a large impact on the outcome of the modulus of rupture and modulus of elasticity. It can be seen that the modulus of rupture and the modulus of elasticity are strongly correlated (ρ = 0.83).

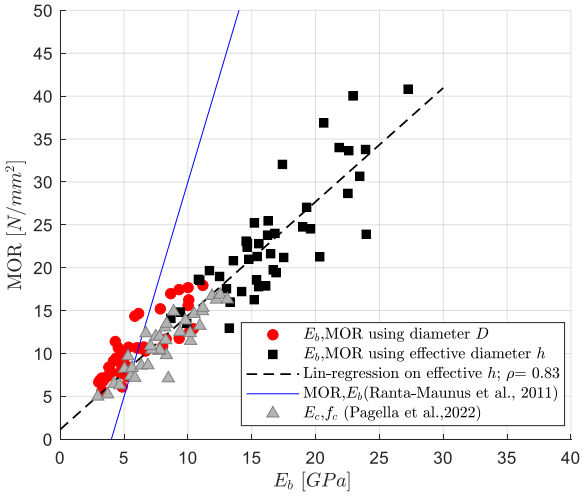

Figure 3.29, Modulus of rupture plotted versus the modulus of elasticity. In red, the determination of strength parameters is done with the measured outer diameter *D*. In black dots, strength parameters are computed with an effective diameter *h* which is based on IML measurements. For the datapoints based with effective diameter, a regression line is presented. From literature, a trendline on spruce bending tests (Ranta-Maunus et al., 2011) and compressions strengths of (Giorgio Pagella et al., 2022) are provided, discussed in section 3.3.6.

3.3.6 Comparisons with literature

A study was performed by (Ranta-Maunus et al., 2011) in which more than 6000 specimens of dry spruce and pine grown in several European countries were tested by destructive and non-destructive methods. The results of this study are presented in Table 3.4. Added to the table are the results of this study and of a study on historic foundation bride piles by (Giorgio Pagella et al., 2022). In their research, spruce timber foundation piles were tested in compression while fully saturated. The piles were extracted from foundations of two demolished historical bridges in Amsterdam. Experimental results from (Ranta-Maunus et al., 2011) and (Giorgio Pagella et al., 2022) are included in Figure 3.29. Because Ranta-Maunus et al. corrected the *MOR* value for a wide 150mm sample and a modification factor needs to be applied because the timber is dry, the match is probably better than the graph suggests.

One major difference between Amsterdam piles and new European spruce piles is their density. Amsterdam piles have a higher density due to saturation. Additionally, the mean modulus of rupture (*MOR*) for new piles is significantly higher (a factor of 1.73) than for historical piles. In this study, the mean modulus of elasticity (E_b) for Amsterdam piles was found to be 1.48 times higher than for new dry spruce piles. The gradient of the E_b-*MOR* diagram for new piles is more than twice as steep as for the piles in this study, but it is comparable to the gradient found by Pagella. However, the compression strength and stiffness obtained by Pagella are smaller than those found in this study, which also used an effective cross-section. This difference can be explained by the fact that reducing the diameter of a pile by subtracting the soft shell has a much greater impact on bending strength compared to compression strength. This is because in bending, $MOR \sim M/h^3$, while in compression, $f_c \sim N/h^2$, where N[kN] is the compression force.

Table 3.4, Overview of bending properties for spruce timber in Europe (Ranta-Maunus et al., 2011), compared with results from Overamstel four-point bending experiments and Amsterdam compression experiments (Giorgio Pagella et al., 2022).

Spruce in bending	*MOR* [N/mm^2] mean	E_b[MPa] mean	ρ_t [kN/m^3] mean	samples
(Ranta-Maunus et al., 2011)				
Sweden	42.5	11,300	4.35 dry	210
Poland	38.5	11,400	4.40 dry	433
Slovenia	43.7	12,000	4.45 dry	1162
France	42.9	11,900	4.40 dry	118
Slovakia	34.8	10,200	4.15 dry	213
Romania	35.5	9,600	3.87 dry	321
Ukraine	36.2	10,000	3.89 dry	204
All above	40.2	11,200	4.28 dry	2776
Amsterdam Overamstel				
With diameter *D*	10.6	5,992	7.13 wet	44
With effective diameter *h*	23.2	16,590	7.13 wet	44
Spruce in compression				
Amsterdam city centre	f_c [N/mm^2]	E_c[MPa]		
Pagella et al (2022)	11.2	8,090	7.36 wet	36

3.4 Conclusion

The mechanical properties of existing spruce foundation piles, retrieved from a historic quay wall at Overamstel in Amsterdam, were studied. The main aim of this study was to investigate the stress strain behaviour of the historic timber foundation piles in bending in which the *MOR* and E_b were of most interest. To better understand the material properties of historic foundation piles in bending, a series of 6 four-point bending experiments were conducted. An adjustable bending test setup was used in which timber piles were bent by hoist and support slings. The forces were adjusted such that the outer fibre stress between the two forces was consistent, leading to a failure at the weakest cross-section. Measurements of the curvature and force distribution were taken along the pile length during loading. In addition, biological decay in the outer layer of the timber piles, also referred to as 'soft shell', was identified with IML micro-drillings. Internal strains were measured by gluing fibre optical wires inside the soft shell of the timber piles. From this study, the following conclusions were drawn:

- The average flexural stiffness of the tested pile population is given by EI[kNm^2] = $-81.46x + 945.77$ where x[m] is the distance along the pile starting from the pile cap.
- The mean value of E_b was found to be 16.5GPa with variation coefficient 0.30, while the *MOR* had a mean value of 23.2N/mm^2 with variation coefficient of 0.26. There was a significant variation in both E_b and *MOR* values between the different piles. When analysing a single pile at multiple locations along its length, the spread in values was smaller, but still significant. Despite the spread between individual piles, a strong correlation of 0.83 was observed between the modulus of elasticity and the modulus of rupture.
- For five piles, a bi-linear elastic-perfect-plastic material behaviour was observed in which the plastic limit was reached at 1800 micro strain. One of the piles showed considerable hardening behaviour.
- Micro-drilling is a promising technique for estimating bending strength parameters and determining the soft shell. The correlations between IML micro-drill resistance and the modulus of elasticity and modulus of rupture were found to be 0.65 and 0.5, respectively.
- Bacterial deterioration appears to be independent of both the outer pile diameters and the location along the timber pile. An in situ IML drill at the pile cap on a pile foundation does not provide a comprehensive assessment of the deeper parts of the same pile. On average, a soft shell of 21mm was found, with maximum values reaching up to 45mm.
- The insertion of fibre optic techniques into historic foundation piles to measure bending strains is an effective instrumentation tool, as it can measure up to a value of 1600-2000 micro strain. However, when larger strains are present, the accuracy of the measurements becomes compromised, as strain peaks appear in the measured signal, eventually followed by breaking of the FO wires. The failure of FO wires can be attributed to their connection with the timber fibres, which undergo permanent deformation at approximately 1800 micro strain. This deformation causes stress concentration in the FO wires, ultimately leading to their failure.
- A comparison of historical deteriorated spruce foundation piles with new, dry spruce piles reveals that the historical piles have a lower modulus of rupture by a factor of 1.73 and a higher modulus of elasticity by a factor of 1.48 when strength determination is based on an effective diameter h.

When performing bending capacity checks of timber piles, it is recommended to use an effective diameter instead of an external diameter. For geotechnical computations, it is advised to use an external diameter, including the soft shell. To conclude, time effects such as timber creep are not studied but can be of significant importance when assessing timber foundations in bending over al long time span.


EVERYDAY
A NEW
#CHALLENGE
1216
deKlerk

4

Lateral pile group failure:
Modelling and pile group experiments[1]

The modelling of the lateral pile-soil interaction of old timber foundation piles in cohesive soils forms a large part of the challenges in the assessment of historic quay walls. Historic inner-city quay walls often have a closely spaced pile field in which centre-to-centre distances can be less than five pile diameters, introducing significant group effects. In this chapter, an analytical pile group model is developed which is validated with experiments from both literature and the Overamstel experiments. The timber pile bending properties obtained in chapter 3 were used in the validation with the Overamstel lateral pile group experiments. Geotechnical model input was used according to chapter 2.

[1] Section 4.1, 4.2 and 4.3 are part of the publication "Analytical model for laterally loaded pile groups in layered sloping soil" published in Marine Structures (Hemel, Korff, et al., 2022)

Photograph by the author

4.1 Introduction to modelling of laterally loaded piles

4.1.1 Lateral loaded pile foundations below quay walls in Amsterdam

Piled structures are often subjected to significant lateral loads. Examples of such loading situations can be found in a variety of structures (Selby et al., 1991). In offshore structures, waves on platforms, berthing vessels on jetties, floating ice on piers (Dong et al., 2012) and in onshore structures, strong winds on high rise buildings or break and acceleration forces on bridge abutments, earth pressures in soil retaining structures and earthquakes can cause high horizontal forces on pile foundations. In historic structures, the use of inclined piles was not common and lateral loads were resisted by installing a matrix of vertical piles. When the intermediate distance between piles becomes smaller than ten diameters, group effects, generally referred to as pile-soil-pile interaction become significantly relevant (Han et al., 1992).

Laterally loaded pile groups are often found below quay walls. The specific application in this thesis relates to historic quay walls in the city centre of Amsterdam. In Amsterdam, the driving of long timber piles (around 12m) to support quay walls started at the end of the 16th century (Klaassen et al., 2012). Large expansion projects with timber piles were already under development in the 17th and 18th centuries culminating in the late 19th and early 20th century when many Dutch cities expanded (Klaassen, 2008). An old poster with cross-sectional drawings of historical quay wall structures can be seen in Figure 4.1. The quay wall construction consists of a brick cantilever wall on a timber deck supported by three to six timber pile rows. In many cases, the piles are founded on a downwards sloping canal bed. On top of the timber deck, behind the gravity wall, a layer of fill is present on which roads, parking lots, pedestrian paths and even trees are located. Recently a quay wall in Rotterdam, which has a similar configuration as the quay walls in Amsterdam, was removed and excavated until the timber deck level which can be seen in Figure 4.2. The pile rows plus support beams of the deck can be observed as well as the start of the slope in which the piles are located. Horizontal earth pressures from behind the quay wall cause a lateral load on the pile caps.

Not surprisingly, these very old quay walls are in a poor condition and may have reached the end of their service life. The structural behaviour of these structures remains largely unexplored, making it challenging to prove their safety or stability using state-of-the-art models. The knowledge gaps (see chapter 1) contributing to our limited understanding of the lateral behaviour of historic timber pile foundations can be summarized as follows: 1) Uncertainty in pile group geometry, encompassing factors like the number of piles, foundation length, and corresponding dimensions. 2) Bacterial deterioration impacts the strength and stiffness properties of timber piles (Pagella et al., 2021; van de Kuilen et al., 2021). 3) The foundation of historic quay walls consists of closely spaced piles, leading to lateral pile-soil-pile group effects (Han et al., 1992). However, the understanding of lateral pile-soil-pile interaction for old closely spaced timber piles in cohesive soils remains limited. 4) Uncertainties are associated with the geotechnical model input data for quay walls, particularly concerning the first 6-7 meters of the Amsterdam subsurface, characterized by soft clay and peat layers with undefined geotechnical strength and stiffness properties. 6) Time-dependent effects, including soil creep (Neukirchner, 1987) and timber creep (Van de Kuilen et al., 2011), affect the pile foundation of quay walls.

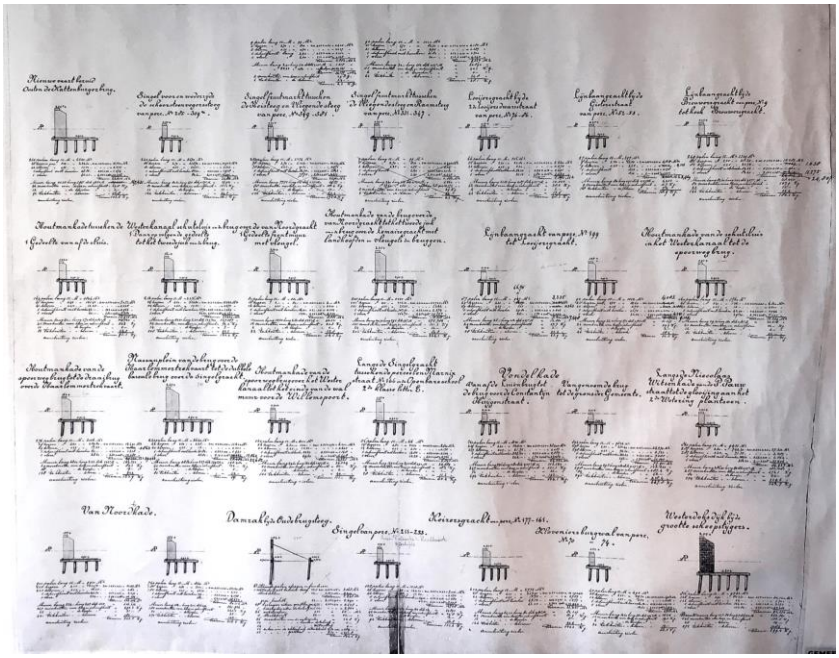

Figure 4.1, Documentation of historical quay walls in the city centre of Amsterdam. This is cropped part of a large poster which contains many historical technical drawings. Source: Archive of Gemeente Amsterdam.

Figure 4.2, Excavated historical quay wall, 'Maaskade' in Rotterdam. Left of the pile foundation, the water is situated and right the hinterland used to be present. Photograph: Julianus, Eric. "Exposed timber pile foundation of the Maaskade". 2019. Havenbedrijf Rotterdam.

Because an important part of the uncertainty lies in soil and structural properties, there is a clear potential for improving the analysis methods of the old quay walls to prevent these have to be replaced on a large scale and within a short period of time. One commonly used approach to reduce uncertainties in engineering is to conduct full-scale experiments (Duffy et al., 2022; Peters et al., 2015). By doing so, engineers gain a better understanding of the behaviour of structures.

This chapter has two objectives. The first objective is to develop a fast, yet accurate method for modelling the response of laterally loaded pile groups of quay walls, with a focus on applicability to historical quay walls in Amsterdam. The second objective is to study the lateral behaviour of historic laterally loaded pile groups found below historic quay walls in Amsterdam through a full-scale lateral pile group experiment, which also functions as validation and calibration dataset for the developed lateral pile group model. The two objectives are reflected in the following key research question:

"How can the lateral pile group interaction of historic foundation piles be modelled and validated through testing?"

The chapter is outlined is discussed, of which a flowchart can be found in Figure 4.3. Firstly, in section 4.1, a literature overview is presented on methods to model lateral loaded piles and lateral pile experiments. Then, the (analytical) pile group model for describing laterally loaded pile groups in layered sloping soil is elaborated in section 4.2. The pile group model is calibrated and validated using three field experiments from literature in section 4.3. These experiments are: 1) a full-scale lateral load test of a 3x5 pile group in soft clays and silts, 2) a full-scale lateral load test of a single pile located on a slope in layered soils, and 3) a small-scale lateral load test of a single pile located near a slope in sand. Next, the focus shifts towards historic quay walls with the performance of two lateral 3x4 pile group experiments on the timber pile foundation of an historic quay wall at Amsterdam Overamstel. In-depth information on the Overamstel site and geotechnical conditions can be found in chapter 2. The methodology of the lateral pile group experiments is presented in section 4.4, and the results of the experiments are discussed in section 4.5, followed by an interpretation in section 4.6. The analytical model is then validated and calibrated once more with the field experiments on the Overamstel quay foundation in section 4.7. Finally, in section 4.8, a discussion and conclusion of the analytical model and the Overamstel test results is provided.

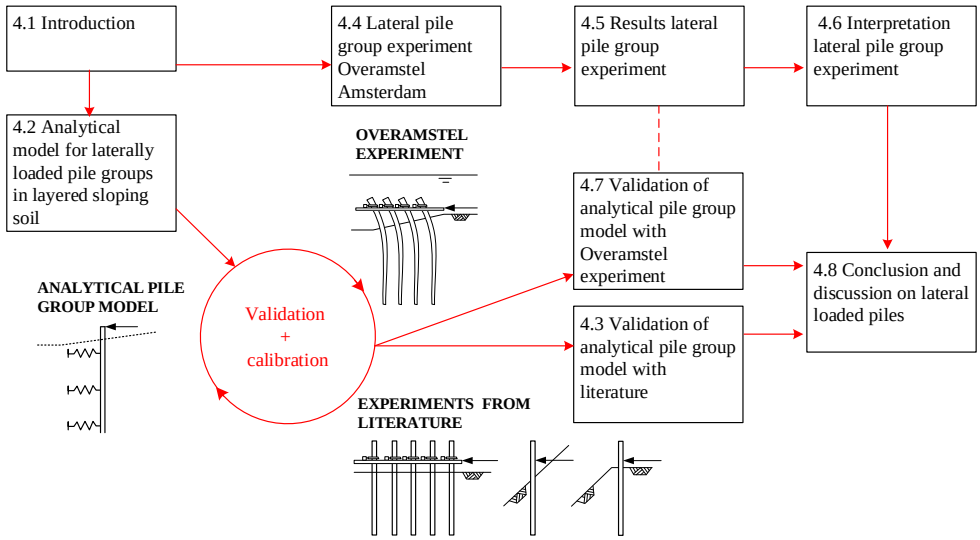

Figure 4.3, Flowchart on the outline of chapter 4.

4.1.2 Literature on modelling and testing of lateral loaded piles

The response of a laterally loaded single pile is a complicated soil-structure interaction problem for which reliable methods, to capture the lateral response, have been developed in the past decades. One of the first methods to analyse laterally loaded piles is the ultimate lateral resistance model of Blum (Blum, 1932) in which passive soil resistance is used to find an equilibrium of the pile. This ultimate strength method was improved by Brinch Hansen (Hansen, 1961) who made it possible to analyse piles in layered cohesive and granular soils. These ultimate limit state methods fail to predict the deformation and force distributions of the pile. Various methods to predict bending moments, deflections and soil stresses are developed over time. In most of these methods, the pile is modelled as a beam on elastic foundation (BEF). There are many approaches to describe the soil behaviour but for the majority, globally two types can be identified; spring models and continuum models (Sun, 1994).

In the first type of models, the soil behaviour is represented by a series of independent (non)linear springs. The method of Brom (Broms, 1964) used the theory of subgrade reaction to compute the lateral deflections, the ultimate lateral resistance and moment distributions. Matlock (Matlock, 1970) proposed the *p-y* curve method which can conveniently take nonlinear behaviour and non-homogeneity property of soil into account. In a *p-y* curve, p[kN/m^2] is the soil reaction per unit length of the pile and y[m] is the corresponding relative pile-soil displacement. The many *p-y* curves that are developed over time are based on empirical curve fitting from full-scale experiments (Abdelhalim et al., 2020; Mirzoyan, 2007; Reese et al., 1975), centrifuge model tests (Jeanjean, 2009) and finite element modelling (Bransby, 1999). To address the problem of group effects, Brown, Morrison and Reese (Brown et al., 1988) was the first to modify the single pile *p-y* curve by introducing a constant reduction factor or p-multiplier. The magnitude of the p-multiplier is always a function of the lateral load or deflection, pile stiffness, pile spacing and soil type (McVay et al., 1995; Rollins et al., 1998) and is mostly obtained from full-scale field tests on pile groups. Examples of full-scale pile group experiments are (Rollins et al., 2005; Rollins, Olsen, Jensen, et al., 2006; Rollins et al., 1998; Snyder, 2004). Many p-multiplier methods have been developed over

time (Duncan et al., 2005; McVay et al., 1995; McVay et al., 1998; Ruesta et al., 1997). It should be noted that the *p-y* relationship is not a soil property, but rather a pile-soil property. The strain wedge (SW) model initially developed by Norris (Norris, 1986) was introduced to relate stress-strain-strength behaviour in terms of three-dimensional soil-pile interaction, to a one dimensional BEF problem. The SW model has been improved and modified for layered soil (Ashour et al., 1998) and sloping ground (Gabr et al., 1990; Peng et al., 2019; Xu et al., 2013). Ashour et al. (Ashour et al., 2004) modified the SW model approach to make it applicable for pile groups in layered soils by correcting for the overlap of shear zones, both parallel and normal to the loading direction, among the piles in the group at various depths. The method of Brinch Hansen is often combined with a BEF. The software D-Sheet Piling (for single piles) by Deltares is an example of such a combination wherein the reaction-deformation relationship of the discrete springs is linear elastic with a plastic limit described by the ultimate soil resistance of Brinch Hansen. Typical *p-y* programs are PyPile for single piles and D-Pile Group for group piles. Please note that the above-described pile group methods are group equivalent pile procedures, that are based on a subgrade reaction method.

In the second type of models, the soil is represented by an elastic continuum. Poulos (Poulos, 1971) described the pile as an infinitely thin linearly elastic strip embedded in an elastic media and approximated the solution numerically. Poulos extended his previous analyses to investigate the influence of a slope on the behaviour of single laterally loaded piles (Poulos, 1976). Apart from single piles, Poulos et al. (Poulos et al., 1980) used their previous work on single piles to describe closely spaced lateral loaded pile groups. The application of the principle of minimum potential energy has been applied by Salgado et al. (Salgado et al., 2014) to obtain the response of a laterally loaded pile group in layered elastic soil. Banerjee et al. (Banerjee et al., 1978) used the boundary element method to solve the problem of elastic continuum by using two elastic half spaces. Nowadays, 3D FEM (Finite Element Modelling) programs are widely used to solve complex pile-soil-pile interaction problems. Because of the three-dimensional nature of the problem and the high degree of nonlinearity, two-dimensional finite element modelling of laterally loaded piles is fundamentally incorrect. Throughout time, a significant amount of research with 3D FEM modelling for lateral loaded single piles has been carried out. Brown et al. (Brown et al., 1990b) modelled laterally loaded single piles with a numerical three-dimensional finite element model. Other 3D FEM examples are studies that investigate the effect of pile and soil properties (Fan et al., 2005), the effect of sloping ground (Ng et al., 2001) and oil-contaminated slopes (Abdelhalim et al., 2020). (Brown et al., 1990a; Selby et al., 1991) analysed pile groups subjected to lateral loading using n three-dimensional FEM. The effect of a sloping surface on a laterally loaded pile group was researched by (Chae et al., 2004) using 3D FEM modelling. FEM models require enormous computational effort, which is not proposed for routine design and therefore also certainly not considered suitable for Bayesian updating (performed in chapter 7).

4.1.3 Approach in this chapter

A hybrid method is proposed which strikes a balance between computational speed and modelling accuracy. In this chapter, a semi-analytical model for laterally loaded pile groups in layered sloping soil is developed. In the proposed method, the piles are described by a beam on elastic foundation in which the soil behaviour is represented by a series of independent *p-y* springs, idealized with a bilinear elastic-perfect-plastic approximation. The modulus of horizontal subgrade reaction is determined according to the theory of Ménard (Ménard et al., 1971) and the plastic limit is computed with the ultimate soil resistance method of Brinch Hansen (Hansen, 1961). These models, e.g. D-Sheet Piling for single piles,

work well for single piles with mild slopes but predictions fail when piles are closely spaced and slope gradients increase. To maintain the advantage of such models, a modification is made by correcting the earth pressure coefficients of Brinch Hansen for each depth. The correction is based on the reduction of the passive soil wedge due to the overlap of shear zones between group piles and the presence of a downward sloping surface. Hereto a new SW model is introduced to construct a three-dimensional soil wedge in layered soil. This proposed SW model takes into consideration the relative sliding of the failure slices within a three-dimensional strain wedge, which is innovative compared to previous studies (Ashour et al., 1998; Ashour et al., 2004; Gabr et al., 1990; Peng et al., 2019; Yang et al., 2019) in which the strain wedge was considered as a whole. Another difference in this study compared to previous work is the way the strain wedge model is used. While in existing SW studies, the strain wedge model is used to obtain the nonlinear *p-y* relations by including the stress-strain-strength relationship into the strain wedge model, in this study the developed wedge model is used as a geometrical tool to obtain correction factors for Brinch Hansen's ultimate soil resistance. The proposed method is therefore an extension of an existing proven pile method making the application widely applicable and computationally fast which is required for use in reliability updating. Furthermore, the method can easily be incorporated in a quay wall model that consists of a framework of elastic beam elements. This model would be suitable to describe failure mechanisms of quay walls concerning lateral pile behaviour both covering structural and geotechnical aspects.

The proposed method is validated in two ways, by experiments from literature and by two full-scale lateral pile group experiments on a historic timber pile foundation at Amsterdam Overamstel. Experiments from literature typically use new steel or concrete piles, resulting in minimal uncertainties in pile material properties and dimensions. Consequently, these experiments are an excellent tool to accurately validate the methodology of the developed pile group model. The model is therefor validated with laterally loaded pile groups in layered soil (Snyder, 2004), lateral loaded single piles in layered sloping soil (Mirzoyan, 2007) and lateral loaded single pile at various distances near a slope crest in sand (Abdelhalim et al., 2020).

However, to validate and calibrate the model's applicability in modelling laterally loaded historic pile foundations, a lateral pile group experiment on a historic foundation in Amsterdam is essential due to the unique challenges posed by deterioration, uneven diameters, varying material properties, and the presence of a "soft shell". As no such experiments have been conducted, two lateral 3x4 pile group experiments are performed on the timber pile foundation of the Overamstel quay wall.

4.2 Analytical model for laterally loaded pile groups in layered sloping soil

4.2.1 Beam on elastic foundation using a bilinear approximation

Figure 4.4a schematically demonstrates the beam on elastic foundation model (BEF), where the lateral bearing soil-pile interactions are modelled by a series of independent lateral springs (*p-y* spring). Each individual spring has its own *p-y* curve which is dependent on the soil properties, depth and pile dimensions. While the actual *p-y* curve of foundation soil has a non-linear elastic-plastic character it can, according to API code (American Petroleum, 1989), be idealized with a bilinear elastic-perfect-plastic approximation. The non-linear and bilinear *p-y* curves are schematized in Figure 4.4b in black. The gradient of the elastic branch is the modulus of horizontal subgrade reaction, indicated by k_h[kN/m^3]. In this study, the horizontal subgrade reaction is determined according to semi-empirical formulas derived by Baguelin et al. (Baguelin et al., 1972) in which correlations between geotechnical characteristics of the soil, including the pile dimension, and the Ménard-pressuremeter stiffness were found. These formulas are suitable for soft soils which can be found in the shallow subsurface of Amsterdam. The method developed by Baguelin et al. is one of the many proposed successful methods in which pressuremeter data is used for the design of laterally loaded piles (Baguelin, 1982; Briaud et al., 1983; Robertson et al., 1985). The Ménard stiffness is calculated from the slope of pseudo-elastic pressure-displacement curves and obtained by a series of pressuremeter tests in which a uniform pressure in a cylindrical borehole is gradually increased through an expandable cylindrical probe while measuring the radial expansion. The first stage of the pressure test is recompression followed by a pseudo-elastic soil response which finally becomes plastic. The Ménard stiffness corresponds to the pseudo-elastic soil response. The semi-empirical formulas to obtain the modulus of horizontal subgrade reaction per unit length pile can be found in appendix G.1. This subgrade reaction must be multiplied by the width of the pile D[m] in order to use it as a spring stiffness (k[kN/m^2] = k_hD) in BEF computations. Furthermore, empirical relations between cone resistance and the Ménard stiffness are provided which can be used in an early design stage. Using a pseudo-elastic soil response over the full pile length is often applied in engineering models (Baguelin et al., 1972; Briaud, 2013), neglecting that at great pile depths a fully elastic soil response may be a better approach. Despite the absence of a recompression stiffness in the deeper layers, the method is widely used and also incorporated in engineering guidelines like Fascicule 62, A.P.I. and P.H.R.I. (Maouche). The plastic limit is determined with the ultimate soil resistance theory of Brinch Hansen which is further elaborated in section 4.2.3. To correct for the pile group interaction and the presence of a sloping surface, the plastic limit of individual *p-y* springs is corrected, which can be observed in Figure 4.4b with a red solid line. The correction is based on the reduction of the passive soil wedge due to the overlap of shear zones between group piles and the presence of a downward sloping surface. The geometrical shape of the passive soil wedges is modelled with a new proposed strain wedge model for layered soils. It is well established that group interaction effects affect both the ultimate soil resistance and the pile-soil interaction stiffness during the loading trajectory prior to failure. This method does not take into account a change in horizontal subgrade reaction as a consequence of neighbouring piles and or the presence of a downward directed slope during the loading trajectory. However, as soon as slices of the soil wedges interfere with neighbouring piles a group effect is accounted for in the method. Since the application of this chapter is on Bayesian updating, the ultimate resistance of pile group foundations is of main interest. The lateral failure of pile foundations occurs on average for larger pile group displacements, making this simplification justifiable.

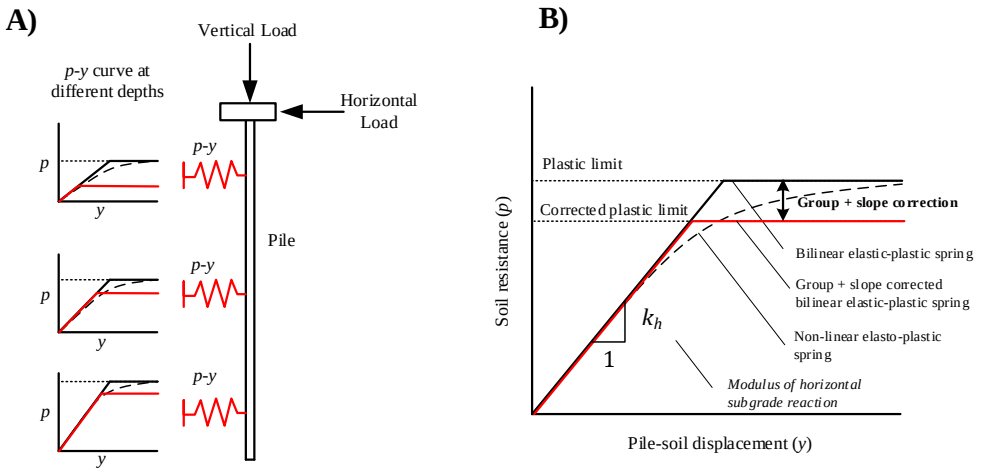

Figure 4.4, Schematic representation of proposed BEF method. Pile horizontally supported by p-y springs (a). Enlargement of a p-y ¬diagram (b). Black dashed line represents a non-linear elastic-plastic p-y curve. Black line represents a bilinear p-y curve with plastic limit. Red line represents a bilinear elastic p-y curve with corrected plastic limit due to pile group and slope surface correction.

4.2.2 Proposed strain wedge model

To have consistency between the method of correction and the plastic limit of individual springs, the strain wedge model must be based on the same underlying theory that Brinch Hansen is based on. This theory is the passive Rankine state, developed by Rankine (Rankine, 1857). Rankine's earth pressure assumes a finite amount of failure planes, or as Rankine called planes of rupture, according to the circle of Mohr which is sufficiently correct for reasonably small depths. At greater depths plane case of failure happens horizontally (Hansen et al., 1960). The strip of soil that is bounded by two failure planes is named a failure slice. A side view of failure slices in front of a laterally loaded pile, located in homogenous soil, is shown in Figure 4.5a. For layers that reach their plastic limit, passive failure slices develop towards the surface with mobilized base angle β_m[deg] with respect to the vertical, creating a passive wedge in front of the pile. Rankine's theory was developed for an infinite long deflected wall which makes the theory suitable for two-dimensional cases. However, in the situation of a deflected pile, the failure slices which are developed, should be analysed in three dimensions. According to Ashour (Ashour et al., 2004), the passive wedge spreads out with wedge fan angle φ_m.. The relation between the mobilized fanning angle and mobilized base angle is formulated in eq. 4.1 (Ashour et al., 1998).

$$\beta_m = 45 + \frac{\varphi_m}{2} \qquad \textbf{eq. 4.1}$$

The shape of the three-dimensional wedge in homogeneous soil is straightforward and evaluated by multiple researchers (Blum, 1932; Norris, 1986; Reese, 1986). For layered soil, this chapter proposes each plastic layer have its own mobilized base angle β_m and wedge fan angle φ_m. A side view of the development of failure slices in layered soil is illustrated in Figure 4.5b. Together the failure slices in layered soil form a passive wedge in front of the pile.

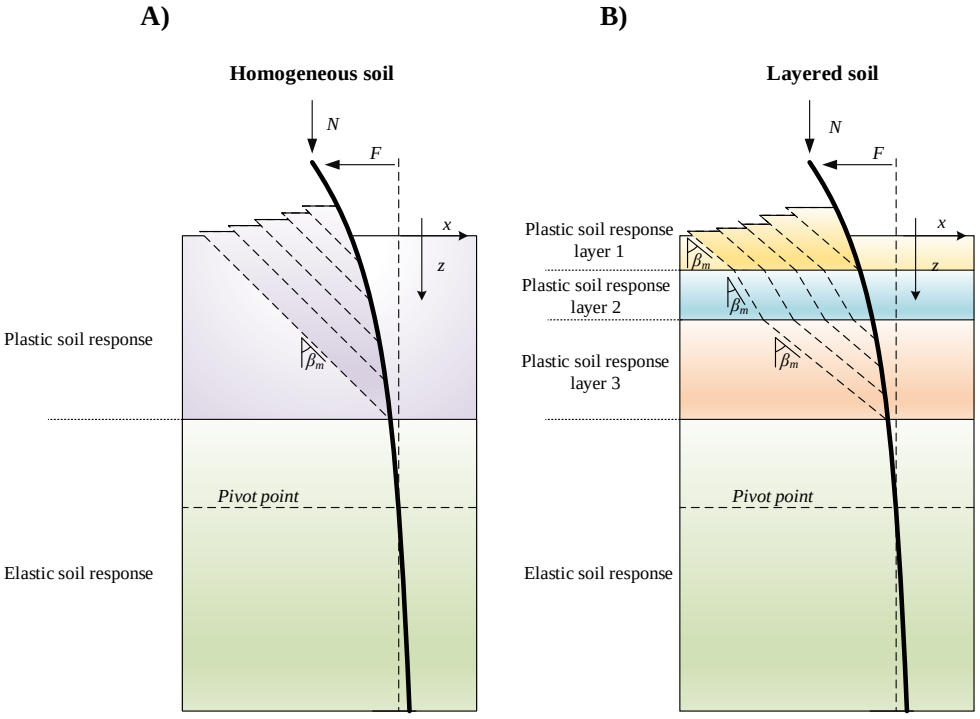

Figure 4.5, Development of failure planes for lateral loaded piles in homogeneous (a) and layered (b) soil.

The geometrical shape of the three-dimensional passive wedge in layered soil is more complex than for homogeneous soil and can be found in Figure 4.6. The proposed geometry of the passive wedge is based on the three-dimensional development of failure planes that originate at the axis of the pile at various depths. Because of the complexity of the three-dimensional problem, a discretized approach is applied. The pile is discretised in parts that have a constant height dz[m]. At each discretised depth z[m] of the pile, a failure plane is constructed which develops towards the free surface, intersecting different plastic layers, with a layer dependent mobilized base angle β_m and mobilized fan angle φ_m. In Figure 4.6 indicated in grey, an arbitrary failure slice, bounded by two failure planes, is shown. Each failure slice consists of a number of failure slice cells (FS-cells) of which one is visualized in red in Figure 4.6. A fully discretised wedge of an illustrative case can be found in Figure 4.9 in which the same colour indication is used as in Figure 4.6. The FS-cells are constructed by connecting two superimposed failure planes at each discretized depth. FS-cells therefore have a grid height of $2dz$, width of dx[m] and length of dy[m].

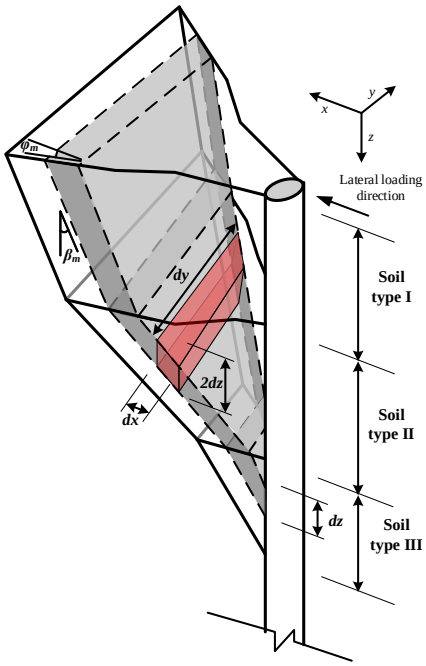

Figure 4.6, Proposed three dimensional geometry of passive wedge in layered soil.

Applying this procedure for all failure slices creates a fully discretised wedge which has a stepped structure of cells, e.g. the first failure slice consists of m=1 failure slice cell, the second failure slice consist of m=2 failure slice cells and so on to the deepest plastic failure slice. If for example a laterally loaded pile has a plastic soil response for the first 2.5m, which is typically found for timber quay wall foundation piles, a total of 25 failure slices is used to describe the wedge in case dz = 0.1. The total number of failure slice cells in this particular case is 1+2+3+…+25 =325. The FS-cells are used to compute the volumetric weight of failure slices W[kN] and the friction between failure slices τ[kN] at the location of a failure plane. The reduction of both quantities, due to the overlap of shear zones between group piles and the presence of a downward sloping surface, are used to correct the plastic limit of individual *p-y* springs. The volumetric weight of failure slices can be computed with eq. 4.2. The friction between failure slices depends on the cohesion of the soil layer and the corresponding surface area of the failure plane and can be computed with eq. 4.3.

$$W(z) = \sum_{j=1}^{m} dz_j \times dx_j \times dy_j \times \gamma_j' \qquad \textbf{eq. 4.2}$$

$$\tau(z) = \sum_{j=1}^{m} \frac{dz_j}{\cos(\beta_{m,j})} dy_j \times c_j' \qquad \textbf{eq. 4.3}$$

where

W = total weight of a failure slice, developed at depth z [kN]
τ = total friction of a failure plane, developed at depth z [kN]
j = 1,2..m where m is the amount of FS-cells per failure slice, developed at depth z
γ' = effective weight of FS-cell at depth z [kN/m^3]
c' = cohesion of FS-cell at depth z [kN/m^2]
β_m = mobilized base angle at depth z [deg]

The integration of equations eq. 4.2 and eq. 4.3 takes place over the length of the plastic zone, from the first slice until the last slice, which is equal to the length of the plastic zone divided by grid height *dz*. A balance needs to be found between the grid height and the accuracy of the model outcome. Decreasing the value of *dz* increases the number of failure planes and increases the accuracy of computations on failure plane surface areas and failure slice volumes. However, a fine grid height increases the total number of cells which increases computational effort. As a rule of thumb, halving the grid size *dz* quadruples the total number of failure slice cells needed. To show the impact of the grid height *dz*, a sensitivity study is provided in section 4.3.1. Based on this study it can be concluded that for piles with a length in the order of L[m] = 12m, an appropriate grid height is 0.1m. Assuming that in practice the plastic zone does not become larger than roughly 6m for 12m long driven piles, the total amount of grid cells varies globally between 0 and 2000.

Values of the wedge fan angle φ_m have been determined from model tests with a small flat plate in sand. Bowman (Bowman, 1958) stated from these model tests that the fan angle is probability a function of the void ratio of the sand, with values ranging from $\varphi'/3$ to $\varphi'/2$ for loose sand to φ' for dense sand in which φ[deg] is the internal friction angle. For cohesive soils, assumed to be in an undrained-condition, the value of the internal friction angle φ' is equal to zero and thus the value of the mobilized friction angle φ_m is zero too (Hansen, 1961; Reese et al., 1975; Stacul et al., 2018). The result is an earth wedge that has a width equal to the width of the pile (Matlock, 1970). This theory is still used by many researchers (Lin et al., 2016; Stacul et al., 2018; Yang et al., 2019). Field tests of Gabr et al.(Gabr et al., 1990) show that the developed soil wedge in clay is in practice wider than the width of the pile and therefore, the volume of this proposed SW model in cohesive soils, according to Reese, could be underestimated. A non-zero fanning angle, to construct the geometrical shape of the passive wedge in undrained cohesive soils, is often applied. Ashour (Ashour et al., 1998; Ashour et al., 2004) assumes a stress-dependent wedge fan angle, according to the Mohr failure criterium. For sand, with a Poisson ratio vary from 0.1 at very small strain to 0.5 or larger (due to dilatancy) at failure, the fanning angle varies from $\varphi_m = 0$ for $\epsilon = 0$ to for say φ_m =40deg at failure. In clay soil with a Poisson's ratio assumed to be 0.5 (undrained behaviour), the fanning angle varies from $\varphi_m = 0$ for $\epsilon = 0$ to for say φ_m =25deg at failure. Kim et al (Kim et al., 2011) found a best fit fanning angle of $\varphi'/5$ in cohesive undrained soils based on the comparison between tests results and theoretical force equilibrium.

4.2.3 Plastic limit reduction

The Brinch Hansen ultimate soil resistance for a laterally loaded single pile, without correction, is given by eq. 4.4. This method includes three-dimensional effects, is suitable for layered granular and cohesive soils and is validated with experiments by Christensen (Christensen, 1961). Further elaboration of the mathematical expressions for earth pressure coefficients K_q and K_c in eq. 4.4 are given in appendix G.2.

$$\sigma_p = K_q \sigma'_v + K_c c \qquad \textbf{eq. 4.4}$$

where

σ_p = pressure per unit front area at depth z [kN/m^2]
σ_v' = effective overburden pressure at depth z [kN/m^2]
K_q = lateral earth pressure coefficient [-]
K_c = lateral earth pressure coefficient for cohesion [-]
c = cohesion [kN/m^2]

The resultant earth pressure σ_p[kN/m^2], which is the passive minus the active pressure, at depth z is based on the passive Rankine case, in which force equilibrium is found between a resultant pressure force in front of the pile surface area and a friction force of failure slices. The friction force considers the friction between the surface areas of the failure planes (cohesion) and the weight of a failure slices (vertical overburden pressure). The two quantities are multiplied with their corresponding depth depending earth pressure coefficients K_q and K_c to obtain the ultimate soil resistance at depth z. However, these coefficients are based on freely developing failure planes, i.e. freely developed passive wedge, not taking into account surrounding piles or a sloping surface.

Decreasing the spacing between the piles reduces the lateral soil resistance because the soil wedges of the pile group start to interfere (Wright, 1982). According to Reese et al. (Reese et al., 2010), the interaction can be distinguished into effects of in-line piles and side-by-side piles. Both interaction effects are due to closely spaced piles, but the type of interaction is different due to the direction of the load. The in-line effects, based on the proposed passive wedge geometry, can be observed in Figure 4.7a where the rear pile is located in the 'shadow' zone of the leading pile. The passive wedge in front of the leading pile overlaps with the passive wedge of the rear pile. The mobilized soil of the front pile cannot act as a passive wedge for the rear pile under the assumption that the soil cannot be mobilized twice. Therefore, the overlap between the pile wedges is cut off from the passive wedge of the rear pile. This is indicated in Figure 4.7a with a red dashed line. For the side-by-side interaction effect, the piles are organized parallel to the loading direction which is illustrated in Figure 4.7b. Again, each pile develops a passive soil wedge and if the pile's wedges overlap, the piles share the same mobilized soil. Under the assumption that the mobilized soil cannot be used twice and that the piles develop the same passive soil wedge, the mobilized soil is divided equally between the piles. The reduction of the middle pile passive wedge is indicated with two red dashed lines.

Piles placed on a downward sloping surface have a smaller resistance compared to piles located in a flat surface because there is less soil available in front of the piles to generate a passive earth wedge (Mezazigh et al., 1998). The effect of a sloping surface on a developed passive wedge is visualized in Figure 4.7c. The reduction of the passive wedge is indicated with a red dashed line.

To incorporate the effects of closely spaced piles and a downward sloping surface, two depth dependent correction factors are introduced in the Brinch Hansen ultimate soil resistance equation which can be found in eq. 4.5, resulting in the corrected pressure σ_{pc} [kN/m^2] per unit front area of the pile.

$$\sigma_{pc} = K_q \Psi_\gamma \sigma'_v + K_c \Psi_c c \qquad \textbf{eq. 4.5}$$

where
Ψ_γ = correction factor for the overburden pressure
Ψ_c = correction factor for the cohesion

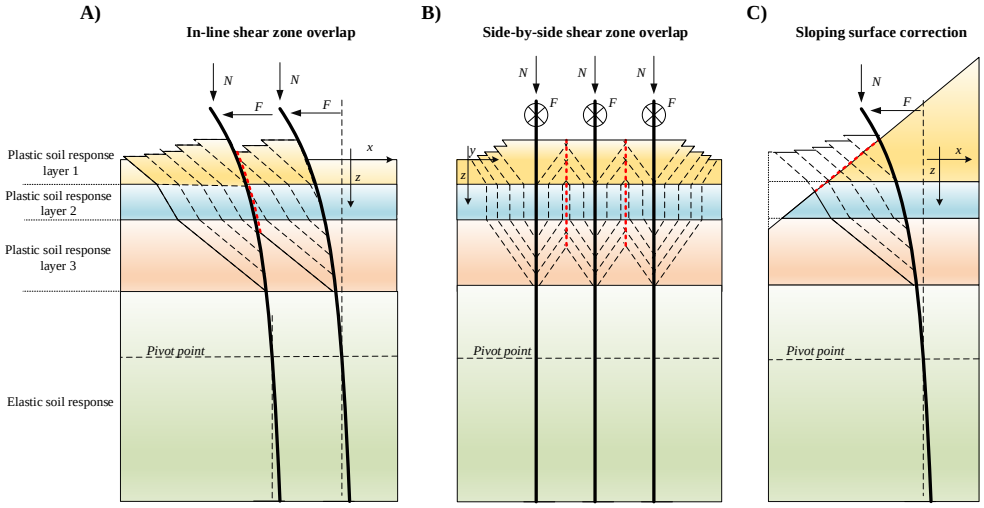

Figure 4.7, Correction on the passive wedge based on; in-line shear zone overlap (a), side-by-side shear zone overlap (b), sloping surface correction (c).

The correction factors Ψ_γ and Ψ_c are based on the comparison between a free developing passive wedge with horizontal surface and a corrected passive wedge which takes into account closely spaced piles and a sloping surface. The corrected failure slice weight W_{cpw}[kN] and corrected failure plane friction τ_{cpw}[kN] are expressed as a fraction of the failure plane weight W and failure plane friction τ of a free developed passive wedge with horizontal surface. These correction factors are depth dependent and can be computed with eq. 4.6 and eq. 4.7. In these equations, the subscript *cpw* stands for 'corrected passive wedge', which is the trimmed volumetric shape of a passive single pile wedge due to the presents of closely spaced piles and or a sloping surface.

$$\Psi_\gamma(z) = 1 - \frac{W - W_{cpw}}{W} = \frac{W_{cpw}}{W} \qquad \textbf{eq. 4.6}$$

$$\Psi_c(z) = 1 - \frac{\tau - \tau_{cpw}}{\tau} = \frac{\tau_{cpw}}{\tau} \qquad \textbf{eq. 4.7}$$

The weight W_{cpw} and friction τ_{cpw} of a corrected passive wedge are computed with eq. 4.2 and eq. 4.3 which is the same procedure as for a free developed passive wedge. However, FS-cells can be narrowed in width, separated into two parts or completely removed from the passive wedge due to; in-line effects, side-by-side effects, a sloping surface or a combination of the three. The three-dimensional geometrical shape of a corrected passive wedge in layered soil can be found in Figure 4.8. The passive wedge is similar to the wedge illustrated in Figure 4.6. However, this illustrative Figure 4.8 shows the in-line effect on the rear pile wedge. In green, an FS-cell within a failure plane is shown which is separated into two parts. In case of a separated cell, an effective length for *dy* is used which is the sum of two cell parts with length *dy/2*. The correction on the pressure coefficient for cohesion is assumed to be proportional to the friction reduction between failure slices within the passive wedge.

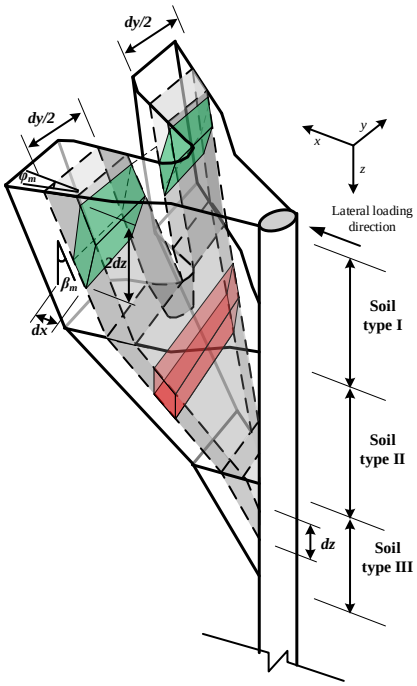

Figure 4.8, Geometry of passive wedge after correction for in-line shear zone overlap. The leading pile and its passive wedge causes a 'cut-out' in the passive wedge of the rear pile.

4.2.4 Computational example plastic limit reduction

To illustrate the method which is used to correct the plastic limit of bilinear springs, a brief example is given. This example shows the in-line, side-by-side and sloping surface effect on the plastic limit of *p-y* springs. Let us consider a laterally loaded pile with length L = 12m and typical diameter D = 0.324m. It is assumed that the first 2m of soil exceeds the plastic strain limit, due to lateral deformations, and hence a passive wedge, with wedge depth h_w = 2m, is formed in front of the pile. Three soil layers are present of which the properties are summarized in Table 1. For demonstrative purposes, the fanning angle φ_m is taken equal to the internal friction angle φ' for each layer.

Table 4.1, Layer properties illustrative example

Layer	Depth [m]	φ' [deg]	c' [kN/m^2]	γ' [kN/m^3]
1	0.0-0.4	20	0	18
2	0.4-0.8	0	20	17
3	0.8- 10	40	0	18

First, the free developed passive wedge is constructed. The geometry is presented in Figure 4.9 in which Figure 4.9a shows the side view of the passive wedge and Figure 4.9b the three-dimensional development of the passive wedge. For visualization purposes, this geometrical shape is constructed with a grid height of dz = 0.2m. At each discretised depth of the pile, a failure plane is constructed towards the surface with mobilized base angle β_m. FS-cells are constructed by connecting all superimposed failure planes at each discretised depth. At a larger distance from the pile, the cell length dy increases due to the wedge fan angle φ_m.

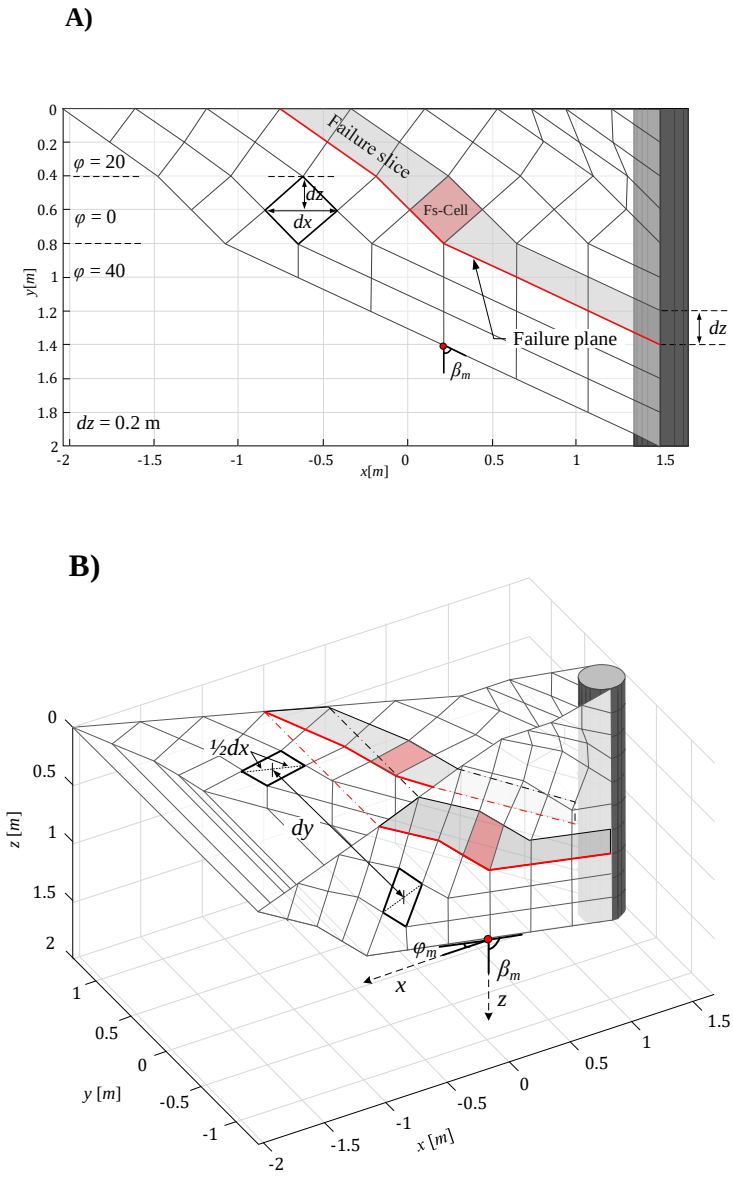

Figure 4.9, Geometrical shape of passive wedge in illustrative example. Side view (a) and three-dimensional view (b).

Further computations are done with a refined grid height dz = 0.05m to make computations more accurate. The passive wedge, containing all developed failure slices, is visualized in Figure 4.10a. To illustrate the correction method the following cases are addressed.

A) In-line effect; leading pile with similar pile wedge is located 1.5m in front of the rear pile.
B) Side-by-side effect; neighbour piles with similar pile wedges are located 1.0m next to the middle pile.
C) Sloping surface effect; a slope inclination of 3H:1V is considered.

The corrected three-dimensional geometrical shape of each case is visualized in Figure 4.10b,c,d. Comparing the freely developed passive wedge from Figure 4.10a with the corrected passive wedges in Figure 4.10b,c,d results in a corrected Brinch Hansen ultimate resistance, which is used as a plastic limit to the *p-y* springs in the BEF method. For each case, the plastic limit and its correction are plotted for each discretized depth in Figure 4.11. Please note that only the first 2m of the pile is plotted because this part exceeds the plastic limit. For all plastified soil layers a 3rd degree polynomial fit $f(z)$ is made which is used to describe the corrected plastic limit as a continuous function of depth. These continuous functions are used to analytically solve the BEF problem of which the solution method is given in section 4.2.5. As can be seen in Figure 4.11a, the failure slices up to 1m depth, are not affected by the presence of the leading pile wedge. This corresponds also to Figure 4.10b. At a depth greater than 1m, the failure slices are reduced in volume because of the presence of the leading pile passive wedge. The effect is the reduction of ultimate soil resistance for the failure slices which are formed at the lowest part of the passive wedge. Because the passive wedge of the leading pile has a kinked shape, a kink can be observed in the plot at around 1.4m. For the side-by-side effect case, which can be observed in Figure 4.11b, the reduction of the ultimate soil resistance starts at depths larger than 1.2m. Like the previous case, the volume of the deeper failure slices is reduced due to the presence of the passive wedges of the neighbouring piles. In the last case, the effect of the slope is discussed. As can be seen in Figure 4.11c, the ultimate soil resistance is reduced for the top and bottom layers. However, the middle layer is not affected by the presence of the slope. According to Brinch Hansen, the cohesive layer only has passive resistance due to cohesion between the failure slices which in this case are not affected by the slope geometry. As a result, the cohesive FS-cells from failure planes that developed in the cohesive layer, weren't affected or cropped out. This causes the ultimate soil resistance by Brinch Hansen not to be reduced for the middle layer. In case the cohesive layer was the top layer, a noticeable effect would be observed.

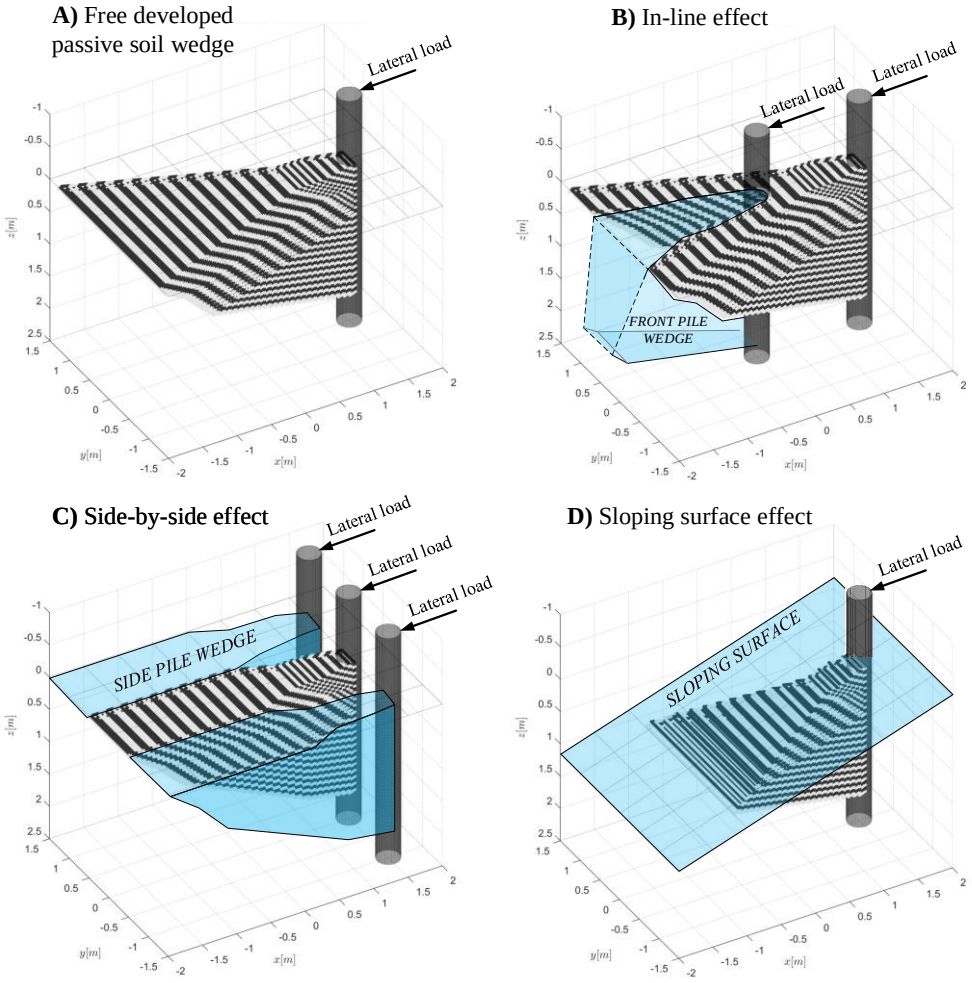

Figure 4.10, Three-dimensional geometrical shape of passive wedge in which failure planes are indicated with a black-white pattern (a). Correction of the passive soil wedge due to in-line shear zone overlap (b), due to side-by-side shear zone overlap (c), and due to a sloping surface (d). Loading on the pile is slope downward directed.

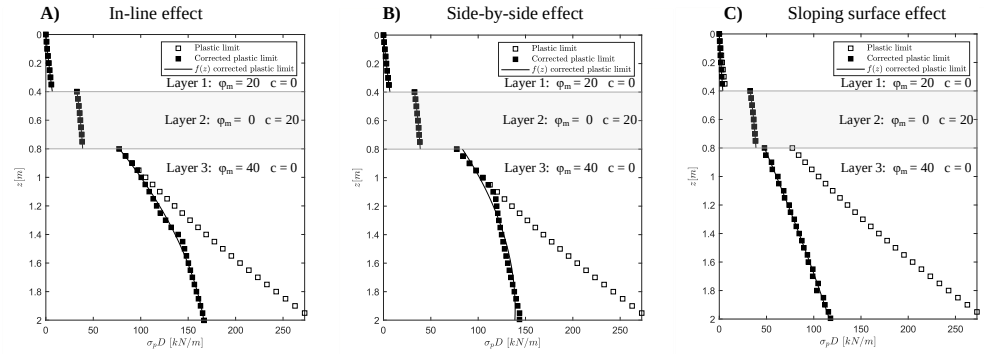

Figure 4.11, Correction plastic limit due to in-line shear zone overlap (a), due to side-by-side shear zone overlap (b), and due to a sloping surface (c).

4

4.2.5 Analytical solution BEF problem

The differential equation of a single beam on elastic Winkler foundation is presented in eq. 4.8 (Winkler, 1867) and its solution and application for laterally loaded piles has been discussed by a number of authors (Gleser, 1953; Reese, 1956) and is still widely used. In eq. 4.8, x[m] is the displacement, EI[kNm^2] *is* the flexural rigidity of the beam, k[kN/m^2] is the stiffness of the elastic foundation and q[kN/m] is an arbitrary distributed load that is dependent on the depth z.

$$EI\frac{d^4x(z)}{dz^4} + kx(z) = q(z) \qquad \textbf{eq. 4.8}$$

Each layer of soil has its own modulus of subgrade reaction k of which the plastic limit is varying with depth. A soil layer that reaches the plastic limit becomes independent of the lateral pile displacement and can therefore be modelled as a constant distributed load. A distinction between plastic and elastic layers must be made in order to solve the BEF problem analytically. An analytical solution is preferred because it reduces the computational time and provides a good insight into the fundamentals of the problem. The bending of a pile in layered soil, subjected to a lateral load F[kN], is described by multiple beams on elastic foundation, of which the general form can be found in eq. 4.9. Here, i = 1,2..n where n represents the number of unique soil layers, i.e. if the subsurface around the pile consists of a sand layer and a clay layer of which part of that clay layer reaches the plastic limit, three unique soil layers are present. Please note that an extra term is added to eq. 4.9 which includes the effect of the axial load on the bending of the pile. A schematic parameter visualization is provided in Figure 4.12. The top of the pile is indicated by z_1 and the tip of the pile is indicated by z_{n+1}. The depth at which interfaces between unique soil layers are present is indicated by z_2, z_3.. z_n. The depth of unique soil layers, and thus also the thickness of each layer, is taken as a multiple of the grid height dz in order to avoid coupling problems between the proposed strain wedge method and the BEF method.

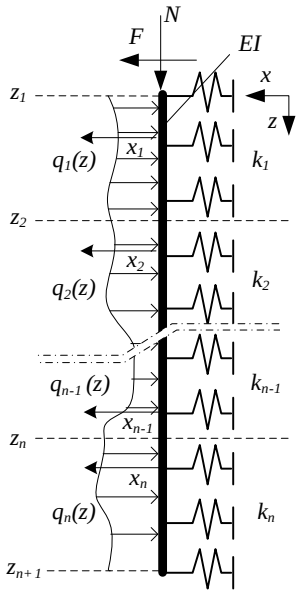

Figure 4.12, Parameter overview of BEM method.

$$EI\frac{d^4x_i(z)}{dz^4} + N\frac{d^2x_i(z)}{dz^2} + k_i x_i(z) = q_i(z) \quad i = 1,2..n \qquad \textbf{eq. 4.9}$$

In eq. 4.9, x is the lateral pile displacement, EI the flexural rigidity of the pile, N the axial load, z the depth, $k = k_h D$, the stiffness of the elastic foundation and $q(z)$ the depth dependent distributed load to describe fully plastified layers. For the depth dependent distributed load, the corrected plastic limit is used so that $q_i(z) = f_i(z) = a_i z^3 + b_i z^2 + c_i z + d_i$. Here, $f(z)$ is the polynomial function that describes the corrected plastic limit $\sigma_{pc} D$ as function of depth which is elaborated in section 4.2.4. The polynomial function is chosen to the third order which makes it possible to find a simple particular solution in the form q/k for the general differential equation presented in eq. 4.9. With higher orders, particular solutions become more complex for this problem (Simone, 2007). For $N < 2\sqrt{kEI}$, the general solution to eq. 4.9, for each unique soil layer i, is formulated in eq. 4.10. The solution is written with natural exponential functions which gives computational advantages over trigonometric functions.

eq. 4.10

$$\begin{aligned} x_i(z) = {} & C_{(4i-3)} e^{\frac{z\sqrt{\left(-\frac{\sqrt{N^2-4\,EI\,k_i}}{EI}-\frac{N}{EI}\right)}}{\sqrt{2}}} + C_{(4i-2)} e^{-\frac{z\sqrt{\left(-\frac{\sqrt{N^2-4\,EI\,k_i}}{EI}-\frac{N}{EI}\right)}}{\sqrt{2}}} \\ & + C_{(4i-1)} e^{\frac{z\sqrt{\left(\frac{\sqrt{N^2-4\,EI\,k_i}}{EI}-\frac{N}{EI}\right)}}{\sqrt{2}}} + C_{4i} e^{-\frac{z\sqrt{\left(\frac{\sqrt{N^2-4\,EI\,k_i}}{EI}-\frac{N}{EI}\right)}}{\sqrt{2}}} \\ & + \frac{6\,N\,a_i\,z}{{k_i}^2} + \frac{2\,N\,b_i}{{k_i}^2} - \frac{a_i z^3}{k_i} - \frac{b_i z^2}{k_i} - \frac{c_i z}{k_i} - \frac{d_i}{k_i} \quad ; i = 1,2..n \end{aligned}$$

Where $C_1, C_2, \ldots C_{4n-1}, C_{4n}$ are the integration constants to be determined from the boundary and interface conditions. In total $4 \cdot n$ integration constants need to be solved. It should be

noted that for an existent mathematical solution *N* needs to be smaller than $2\sqrt{kEI}$ and thus *k* needs to be given a non-zero value, even for fully plastified soil layers. When elaborating the boundary and interface conditions the following relations are used, presented in eq. 4.11. Here, φ is the pile rotation, *M* the moment and *V* the shear force.

$$\varphi = -\frac{dx(z)}{dz}, \qquad M = -EI\frac{d^2x(z)}{dz^2}, \qquad V = -EI\frac{d^3x(z)}{dz^3} \quad \textbf{eq. 4.11}$$

The four boundary conditions, two at the top and two at the bottom of the pile, are denoted in eq. 4.12 to eq. 4.15. It should be noted that the boundary conditions at the top of the pile, can be adapted in case a displacement or external moment is imposed. For now, a lateral load is considered. The horizontal component of the axial load needs to be included in the shear boundary condition. Especially with large deflections, this second order effect works progressive and cannot be neglected.

$$M(z = z_1) = -EI\frac{d^2x_1(z_1)}{dz^2} = 0 \quad \textbf{eq. 4.12}$$

$$V(z = z_1) = -EI\frac{d^3x_1(z_1)}{dz^3} = F - \frac{dx_1(z_1)}{dz}N \quad \textbf{eq. 4.13}$$

$$M(z = z_{n+1}) = -EI\frac{d^2x_n(z_{n+1})}{dz^2} = 0 \quad \textbf{eq. 4.14}$$

$$V(z = z_{n+1}) = -EI\frac{d^3x_n(z_{n+1})}{dz^3} = 0 \quad \textbf{eq. 4.15}$$

In case the pile has a constant flexural rigidity *EI* over the full pile length, the interface conditions between the different unique layers can be written as follows in eq. 4.16 to eq. 4.19. The interface conditions are based on the continuity of displacement, slope, moment and shear force.

$$x_{i-1}(z_i) = x_i(z_i) \quad \textbf{eq. 4.16}$$

$$\frac{dx_{i-1}(z_i)}{dz} = \frac{dx_i(z_i)}{dz} \quad \textbf{eq. 4.17}$$

$$\frac{d^2x_{i-1}(z_i)}{dz^2} = \frac{d^2x_i(z_i)}{dz^2} \quad \textbf{eq. 4.18}$$

$$\frac{d^3x_{i-1}(z_i)}{dz^3} = \frac{d^3x_i(z_i)}{dz^3} \quad \textbf{eq. 4.19}$$

The general solution described in eq. 4.10 is substituted into the boundary and interface conditions which gives a linear system of equations. Aligning the coefficients of each integration constant in columns results in a coefficient matrix A. The matrix of variables, which is a vector containing all unknown integration constants, is constructed and named C. The remaining terms, i.e. terms that do not contain integration constants, are used to form a force vector Q. Solving the linear system AC = Q, shown in eq. 4.20, returns the value of all integration constants. Substituting the integration constants back into the general solution, presented in eq. 4.10, results in the displacement distribution *x(z)* of the entire laterally loaded pile.

$$AC = Q \text{ where } A = \begin{bmatrix} A_{1,1} & A_{1,2} & \cdots & A_{1,4n} \\ A_{2,1} & A_{2,2} & \cdots & A_{2,4n} \\ \vdots & \vdots & \ddots & \vdots \\ A_{4n,1} & A_{4n,2} & \cdots & A_{4n,4n} \end{bmatrix}, \quad Q = \begin{bmatrix} Q_1 \\ Q_2 \\ .. \\ Q_{4n} \end{bmatrix}, \quad C = \begin{bmatrix} C_1 \\ C_2 \\ .. \\ C_{4n} \end{bmatrix} \quad \textbf{eq. 4.20}$$

In practice it is not known in advance which soil layers develop full plasticity because this depends on the deflection of the pile, which is unknown prior to the calculation. Therefore, an iterative process is required in which equilibrium is sought between the lateral load on the pile cap and the resistance that elastic and fully plastic soil layers cause. A flow chart of this iterative process is given in Figure 4.13. First, a fully elastic computation without plastic *p-y* branch is performed which results in the displacement of the pile. At each discretized depth *dz*, the displacement is multiplied with its elastic spring stiffness to obtain the elastic pressures. At each discretized depth *dz*, plastic and elastic soil responses are identified. Accordingly, a new 'unique layering' distribution is made with elastic and plastic layers which is used for a new BEF computation. This iterative process is repeated until the layering distribution does not change or becomes repetitive. Since the thickness of each unique layer is chosen to be a multiple of the grid height *dz* fewer iteration steps are needed with larger grid size. The downside is a decrease in modelling accuracy, which is elaborated in section 4.3.1. Once equilibrium is found, the rotation, moment and shear force distributions of the laterally loaded pile can be obtained with eq. 4.11.

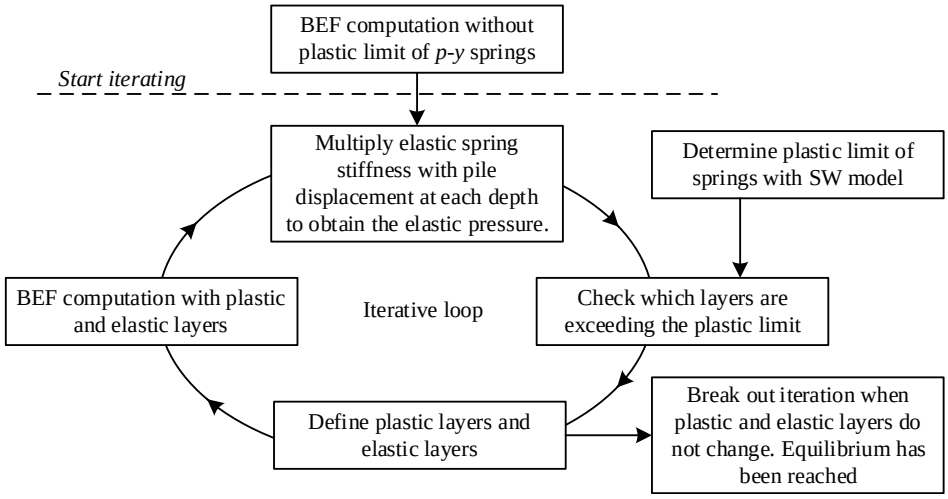

Figure 4.13, Flowchart of iterative solution to solve the non-linear BEF problem.

The analytical model and its corresponding iterative approach, as illustrated in Figure 4.13, have been successfully implemented in a MATLAB computer program. This program aims to effectively solve the challenging problem of a laterally loaded pile within a pile group situated in layered sloping soil. The full analytical quay wall MATLAB computer program (containing the methods described in this chapter) is open source and available for download at: https://doi.org/10.4121/4fd90d71-ffd9-4db2-a358-8576f5b19a32. A manual is included.

4.3 Validation of analytical pile group model with literature

To demonstrate the capability of the model, a comparison of field test results versus model results is made. Three field experiments from literature are considered of which an overview is provided in Table 4.2. The field tests have their own characteristic set-up and different soil and pile properties, making it possible to validate the model for various cases and applications.

Table 4.2, Overview of field experiments from literature to be used for model validation.

Experiment	Laterally loaded pile group. (Snyder, 2004)	Laterally loaded single pile on slope. (Mirzoyan, 2007)	Lateral loaded single pile near a slope. (Abdelhalim et al., 2020)
Set-up	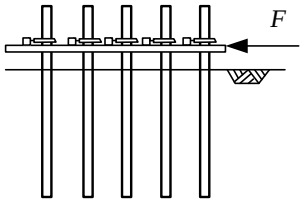 A full-scale pile 3x5 steel pile group in soft clays and silts is laterally loaded and a single pile experiment for reference have been executed. Bending moments, deflections, cap rotations and cap forces are measured.	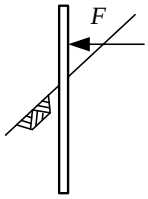 A full-scale single steel pile was loaded on a horizontal and sloping surface in sand / clay soils. Bending moments, deflections, cap forces and cap rotations are measured.	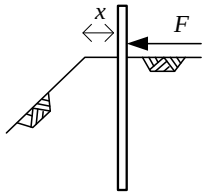 A small-scale single steel pile was loaded at various distances *x* near a slope. Soil composition was sand. Cap forces and deflections were measured.
Validation application	Experiment is applied to validate in-line and side-by-side pile group interaction effects.	Experiment is applied to validate the effect of a sloping surface on lateral loaded pile.	Experiment is applied to validate the effect of a nearby sloping surface on a lateral loaded pile.

4.3.1 Full-scale lateral-load tests of a 3x5 pile group in soft clays and silts (Snyder, 2004).
Snyder conducted a series of static lateral load tests on a group of fifteen piles arranged in a 3x5 pattern. The side-by-side spacing was 1.07m and the in-line spacing was 1.27m. The piles with diameter D = 0.324m, pile length L = 12m and row average flexural rigidity EI = 25,000 kNm^2 were loaded at z = -0.5m. An isolated single pile test was executed for comparison purposes. The flexural rigidity of the single pile is EI = 28,600kNm^2. Cohesive layers are normally consolidated giving $c = su$ and $\varphi = 0$ (su[kN/m^2] is the undrained shear strength). As an initial estimate, the wedge fan angle φ_m is assumed to be equal to the friction angle which results in a wedge fan angle of zero for all clay layers. The model is calibrated on the single pile and on the pile group load test. The layers and their engineering properties are summed in Table 4.3.

Table 4.3, Engineering properties full scale 3x5 pile group experiment (Snyder, 2004).

Depth [m]	γ' [kN/m^3]	Sort [-]	q_c [kPa]	su [kN/m^2]	φ [deg]
0 – 1.2	9.05	clay	1000	20	0
1.2 - 2.1	9.05	clay	1000	35	0
2.1 - 3.0	9.05	clay	1000	20	0
3.0 - 4.8	8.14	sand	15000	0	38
4.8 - 5.3	9.05	clay	5000	56.9	0
5.3 - 5.9	9.05	clay	1000	25	0
5.9 - 6.4	9.0	clay	4000	54	0
6.4 - 20	8.14	sand	10000	0	33

In Figure 4.14, the bending moment distribution of the lateral loaded single pile is plotted for a range of imposed pile displacements. The maximum moment for 4, 6 and 13mm is slightly underestimated. For the other imposed displacements, the predicted moment distribution fits the measured results very well. The depth of the predicted moment occurs at progressively deeper depths with increased deflections, corresponding to the measurements. For all deflections, the depth of the zero-moment crossing is on average 0.5m lower than in the measurements. In Figure 4.15 the moment distributions for the leading pile row and trailing pile rows are plotted. Because the in-line and side-by side effects for all trailing pile rows is the same, model predictions for pile rows 2-5 have identical force distributions. The measurements for the second pile row are used to validate the model predictions on the rear pile rows. The maximum moment of all pile rows is underestimated for the deflections 6 and 13mm. For the largest deflection (89mm), the model overpredicts the moment by 10%. For all other deflections, the moment prediction is very accurate. The zero-moment crossing corresponds to the measured data. For deflections larger than 38mm, the model predicts larger maximum moments for the leading pile row compared to the maximum moments in the rear pile rows. This is in accordance with the measured results. The shape of the moment distributions is predicted well, the trailing pile row moment distributions stretch out more into the depth compared to the leading pile row.

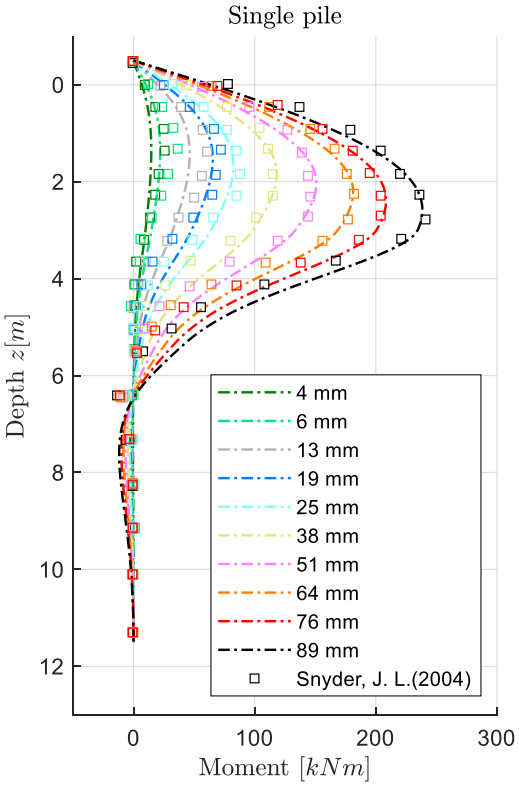

Figure 4.14, Comparative analysis of bending moment distribution in a laterally loaded single pile for varying imposed pile deflections as a function of depth. The figure illustrates the comparison between model predictions (dashed lines) and measurements obtained from the Snyder experiment (square markers).

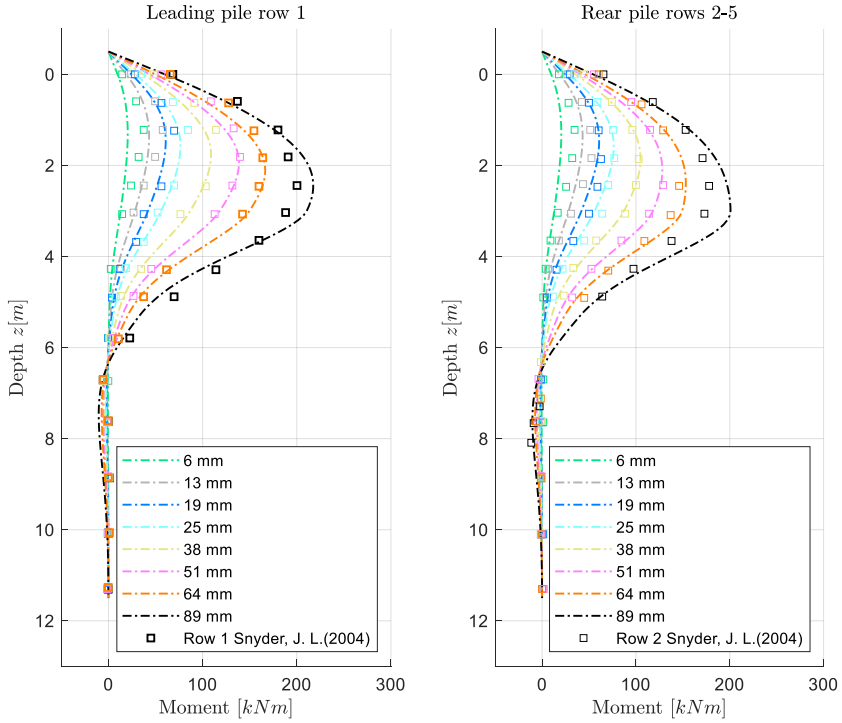

Figure 4.15, Comparative analysis of bending moment distribution of lateral loaded 3x5 pile group for imposed pile deflections as function of depth. Left plot considers leading pile row, right plot considers the trailing pile rows 2-5. Model predictions (dashed lines) and measurements (square markers). To validate the trailing pile rows, field data of pile row 2 is used.

In Figure 4.16, the average leading and trailing pile rows loads are plotted as function of the pile group deflection. In Figure 4.17, the maximum moment of the leading and trailing pile is plotted as function of the pile group deflection. In both figures, single pile model predictions and measured data is provided. The wedge fan angle φ_m for cohesive layers is calibrated on the lateral load and bending moment data which results in the best fit for a wedge fan angle of 15 degrees. To show the sensitivity of the fanning angle, an upper and lower limit of 10 degrees is presented which results in a bandwidth of 5-25 degrees for the cohesive layers. The chosen bandwidth corresponds to the theoretical limit which was found by Ashour, described in section 4.2.2. It can be observed that the wedge fan angle has much more impact on the trailing rows than the leading rows which is logical since the leading piles do not have in-line interactions. The initial estimate, in which the wedge fan angle φ_m is assumed to be equal to the friction angle, overestimates (especially for larger deflections) the lateral loads and moments by roughly 10-20% for the trailing pile rows. Because the first 3m of soil is cohesive with a wedge fan angle of zero, in-line and side-by-side pile interactions are small causing an underestimated reduction of the plastic limit. To increase the interaction effects, a non-zero wedge fan angle is assigned to the cohesive layers. A non-zero wedge fan angle corresponds to the shear cracks that appeared in the cohesive top layers during the field experiment.

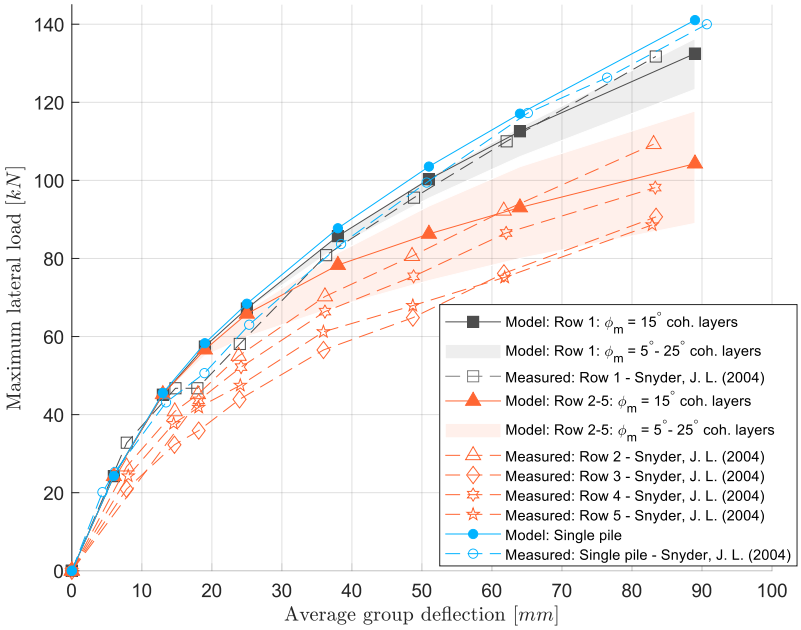

Figure 4.16, Comparison of average pile row load vs. applied group deflection. Pile group is computed with $\varphi_m = \varphi$ for granular layers and φ_m = 15 deg. for cohesive layers with a bandwidth of ± 10 deg. Filled markers are model predictions and open markers are measurements.

First, the force-displacement predictions in Figure 4.16 are discussed. The model prediction for the single pile fits the measured data perfectly. Also, the leading pile row prediction is very accurate. The force-displacement curve of the leading pile row is predicted slightly lower than the curve of the single pile due to side-by-side interaction. This is also in good agreement with the measurements. Because the in-line and side-by side effects for all trailing pile rows is the same, model predictions for pile rows 2-5 have identical force distributions. However, in the experiment, the force-displacement curves of all pile rows are presented. The spread of these curves is quite large, row 2 and 4 have a steeper curve than row 3 and 5. As mentioned before, the model is not capable of making distinctions between the different trailing pile rows.

In the first stage of loading, group deflections are underestimated. For large lateral group loads, near geotechnical failure, group deflections are overestimated (e.g. a steeper force-displacement curve in the first stage of loading and more gentle force-displacement curve at the final loading stage). This effect can be explained. Passive wedges start to grow as function of the pile deflection and start to interfere with each other at a certain displacement. According to this method, it is not possible to have group interaction for small displacements since the passive wedges are still small in volume at that moment of time. Also, the compacting of soil between the piles in case of large pile group deflections is not taken into account. The compacted soil cannot escape between the piles creating a higher stiffness of the soil. Despite these two effects, the model is capable of predicting the average lateral load of the trailing rows, especially for the larger displacements, quite well.

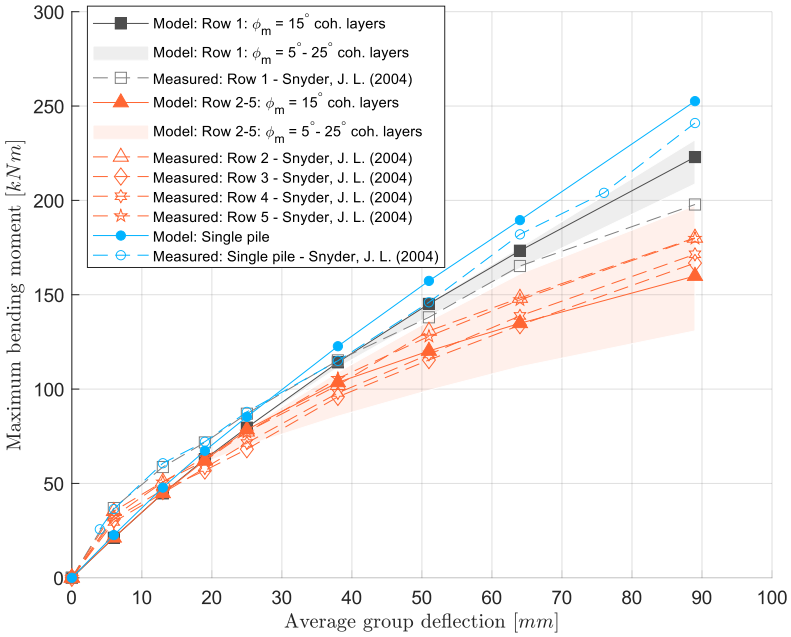

Figure 4.17, Comparison of maximum bending moment vs. average group deflection. Pile group is computed with $\varphi_m = \varphi$ for granular layers and φ_m = 15 deg. for cohesive layers with a bandwidth of ± 10 deg. Filled markers are model predictions and open markers are measurements.

Subsequently, the moment-displacement prediction in Figure 4.17 is discussed. The model prediction for the single pile fits the measured data perfectly. Also, the leading pile row prediction is accurate, only for the largest deflection of 89mm an error of approximately 10% is made. It should be noted that this measured moment is an outlier in the dataset of Snyder. Again, the moment-displacement curve of the leading pile row is predicted slightly lower that the curve of the single pile due to side-by-side interaction. Because the in-line and side-by side effects for all rear pile rows is the same, model predictions for pile rows 2-5 have identical moment distributions. The spread in maximum measured moment of the trailing pile rows is less compared to the spread found in the force-displacement measurements. The maximum moment prediction by the model is very accurate and pretty much the average of the trailing pile row measurements. Also, the pile group displacement at which group interaction start to take place is predicted perfectly.

Computations in this section are performed with a grid height of dz = 0.05m. To illustrate the effect of the grid height dz on the accuracy on the model outcome, the maximal bending moment and lateral load at the pile cap are plotted as function of dz for three different imposed pile cap displacements 13mm, 38mm and 89mm. The results can be found in Figure 4.18. It can be observed that for smaller grid sizes than dz = 0.1m, the model outcome does not change and accuracy doesn't improve further. An appropriate pile height to grid height ratio, without losing accuracy, in this validation is L/dz = 120.

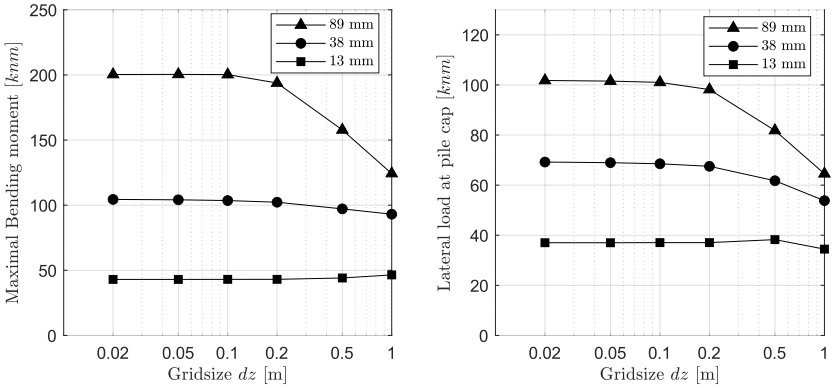

Figure 4.18, Sensitivity of grid height dz on model outcome. Left figure indicates bending moment predictions for three imposed deflections as function of dz. Right figure indicates the lateral load at the pile cap for three imposed deflections as function of dz.

From the calibration with the Snyder experiment it can be concluded that our model is able to predict lateral loads and bending moment magnitudes at all levels for the leading and the trailing piles in the pile group very accurately, which is a sign that the soil pressure distributions applied in the model are correct.

4.3.2 Lateral resistance of piles at the crest of slopes in sand (Mirzoyan, A. D. 2007).
Mirzoyan conducted a series of static lateral load tests on a single pile in layered horizontal and in sloping soil. The slope in the field test has an inclination of 1V:1.75H which is rather steep for underwater slopes but still in the range of application for canal bed slopes in Amsterdam. The field tests are executed at the same location as the field test of Snyder. The piles have a diameter D = 0.324m, pile length L = 13.5m flexural rigidity EI = 28,600 kN·m^2 and are loaded at z = -0.5m. The layers and their engineering properties are summarized in Table 4.4. Cohesive layers are normally consolidated giving $c = su$ and $\varphi = 0$.

Table 4.4, Engineering properties full scale lateral single pile test (Mirzoyan, 2007).

Depth [m]	γ' [kN/m^3]	Sort [-]	q_c [kPa]	su [kN/m^2]	φ [deg]
0.0 – 1.8	17.0	sand	15000	6	45
1.8 – 2.7	6.9	sand	7500	6	45
2.7 – 3.0	9.13	clay	2000	40	0
3.0 – 3.6	9.13	clay	2000	50	0
3.6 – 4.8	9.13	clay	2000	40	0
4.8 – 6.3	8.3	sand	15000	0	38
6.3 – 6.8	9.13	clay	2000	56	0
6.8 – 7.5	9.13	clay	2000	25	0
7.5 – 7.9	9.13	clay	2000	54	0
7.9 – 20	9.13	sand	15000	0	47

In Figure 4.19, force-displacement diagrams are shown for the single pile in layered horizontal and sloping soil. In Figure 4.20, the maximum bending moment as function of the lateral load is presented.

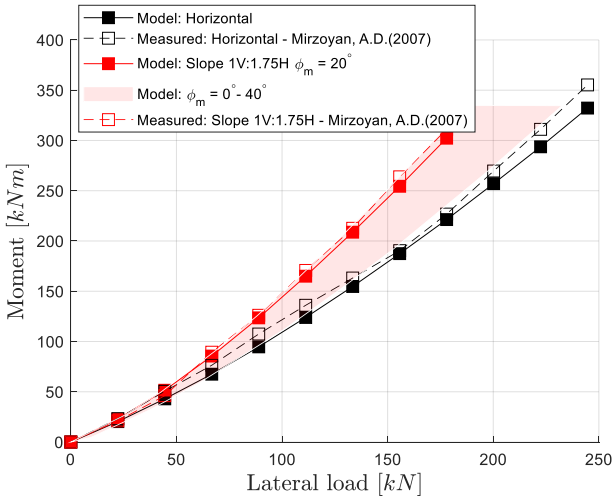

Figure 4.19, Comparison of maximal bending moment vs applied load for a single pile in horizontal and sloping ground. Filled markers are model predictions and open markers are measurements.

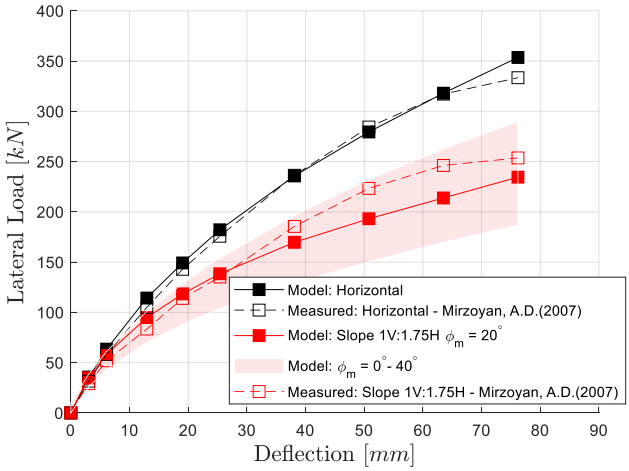

Figure 4.20, Comparison of pile load vs applied pile deflection for a single pile in horizontal and sloping ground. Filled markers are model predictions and open markers are measurements.

The first 3m of soil is classified as sand with slight cohesion in which a passive wedge develops. The wedge fan angle φ_m is calibrated on the lateral load and bending moment data which results in a best fit for a wedge fan angle of 20 degrees. According to Bowman (Bowman, 1958), the wedge fan angle in sand varies with values ranging from $\varphi'/3$ to $\varphi'/2$ for loose sand up to φ' for dense sand. The calibrated wedge fan angle of 20 degrees corresponds to a value of $\varphi'/2$ which can be classified as moderated loose to slightly dense sand. During the field experiment, shear cracks appeared at the surface, with an angle of 22 degrees with respect to the loading direction. The best fit wedge fan angle of 20 degrees is in very good agreement with the angle of shear cracks found in the field experiment. The force-displacement model prediction of the pile with a horizontal soil surface matches the measurements very well. For the pile in sloping soil, above 150kN lateral load, the model

predicts larger displacements than measured. The bending moment prediction fits the measured data for both horizontal and sloping surface very well. To show the sensitivity of the fanning angle on the lateral resistance and bending moment, an upper and lower limit of 20 degrees is presented which results in a bandwidth of 0-40 degrees. The chosen bandwidth corresponds to the theoretical limits found by Ashour (Ashour et al., 1998) and the maximum wedge fan angle in dense sand according to Bowman (Bowman, 1958). Increasing the wedge fan angle causes larger reductions of the plastic limit of *p-y* springs which decreases the lateral loads resistance and thus bending moments. Reducing the wedge fan angle has an opposite effect, smaller plastic limit reductions cause larger lateral resistance and larger bending moments.

The theoretical lower limit, a zero wedge fan angle, found by Ashour (Ashour et al., 1998) is only valid for cases with no strain. Therefore, a wedge fan angle of zero at failure in sand is impossible and meaningless. Small wedge fan angles can underpredict the plastic limit reduction and lead to an overprediction of the lateral resistance of piles in sloping soil. However, with large fanning angles, bending moments can be underestimated.

From the calibration on the Mirzoyan experiment it can be concluded that our model is able to predict lateral loads and bending moment magnitudes at all levels for piles in sloping soil with high accuracy. The correct match of the bending moment indicates that the lateral soil resistance prediction is correct. The less accurate match of the displacement means that there might be an underestimated effect in the model of the reduced soil stiffness in the case of sloping soils.

4.3.3 Experimental and numerical studies of laterally loaded piles located near oil-contaminated sand slope (Abdelhalim et al., 2020).

Abdelhalim et al. performed small scale experiments on a laterally loaded pile in sandy soil near the crest of a slope. The following model parameters were used; pile diameter D = 0.021m, pile length L = 0.4m, loading point z = -0.05m, slope = 1V:2H, flexural rigidity EI = 183 kNm^2. In the experiment, the distance X near the slope is varied from 'at the crest' to 8D from the crest. First, the model is calibrated on the X = 8D force-displacement data which most closely resembles a pile loaded in horizontal surface. The engineering properties are summarized in Table 4.5.

Table 4.5, Soil properties small scale pile near slope experiment.

Depth [m]	γ' [kN/m^3]	Sort [-]	q_c [kPa]	su [kN/m^2]	φ [deg]
0 – 1.0	17	sand	350	1.2	37

For the X=8D case, the plastic limit correction due to the slope is small and therefore, the magnitude of the wedge fan angle has a limited impact on the lateral resistance of the pile. For the case in which the pile is located on the crest of the slope, plastic limit corrections are the largest and therefore, the wedge fan angle φ_m is calibrated on the X = 'at crest' force-displacement data. A best fit is found for a wedge fan angle of 21 degrees which, according to Bowman (Bowman, 1958), corresponds to medium to dense sand ($\varphi'/2 < \varphi_m < \varphi'$). The wedge fan angle is estimated to be 20-35 degrees based on shear crack formation during the experiment. The calibrated wedge fan angle is in the same range as the angle of the shear cracks during the experiment. For the cases, X = 8D, 6D, 4D, 2D and 'at the crest' the force-displacement diagram is presented in Figure 4.21. The model predictions are compared with

the measured data. For X = 8D, 6D, 2D and 'at crest' the model predictions match the data very well. For X = 4D, the displacements are overpredicted by approximately 10%. Figure 4.21 visualizes the softening behaviour of the different cases at a distance X near the crest of a slope. For all cases, the model predicts a slightly steeper force-displacement curve between 50N and 170N lateral load.

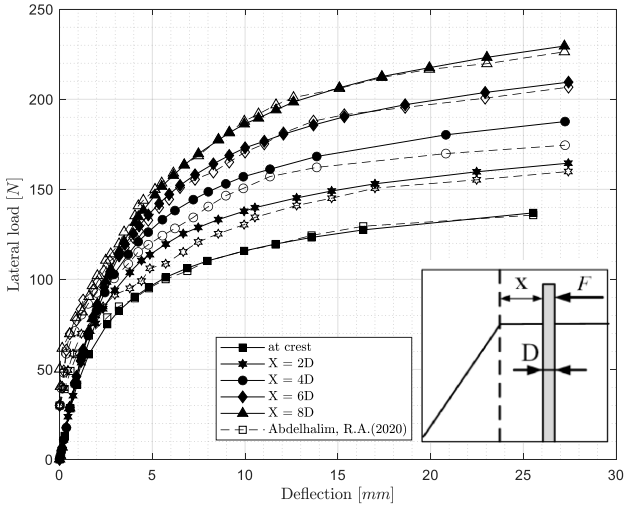

Figure 4.21, Comparison of pile load vs. applied deflection for various distances X with respect to the slope crest. Filled markers are model predictions and open markers are measurements.

From the calibration on the Abdelhalim et al. experiment, it can be concluded that our model is able to predict lateral loads for piles at a distance X near the crest of a sloping soil with high accuracy.

4.3.4 Discussion on validation with literature experiments

The results of the validation provide two significant findings regarding the computation of pile groups. The first finding emphasizes the importance of incorporating a non-zero fanning angle to accurately model the interaction between group piles in undrained cohesive soils. For plastic limit computations with Brinch Hansen, the effective friction angle in undrained cohesive layers needs to be taken zero (Hansen, 1961). Because the effective friction angle and mobilized fanning angle are related to each other, this results in a fanning angle equal to zero. The construction of a passive wedge without fanning angle results in a narrow wedge width and steep base angle causing the passive wedge to be rather small in volume. The side-by-side and in-line overlapping of shear zones becomes small to negligible which gives almost no plastic limit reduction of *p-y* springs. In order to increase the in-line and side-by-side effect of the trailing pile rows in the model, the wedge fanning angle for undrained cohesive layers should be given a non-zero value. Note that the effective friction angle should not be increased as an attempt to increase the wedge fan angle and thus the shear zone overlapping. This would result in an increase of the plastic limit of *p-y* springs and as a result in a decrease of the difference between leading and trailing piles and in an overall larger resistance of the pile group, which are both incorrect.

The second finding reveals that during the initial stage of loading, the computed group deflections tend to be underestimated. For large lateral group loads, near geotechnical failure, group deflections are overestimated (e.g. a steeper force-displacement curve in the first stage of loading and more gentle force-displacement curve at the final loading stage). The same trend, but to a lesser extent, can be observed for the moment prediction. The following phenomena not included in the model may play a role here:

- Passive wedges start to grow as function of the pile deflection and start to interfere with each other at a certain displacement. The moment at which interaction starts to take place has to do with the pile group configuration, strength of piles and the soil characteristics. According to this method, it is not possible to have group interaction for small displacements since the passive wedges are still small in volume at that moment of time. This underestimates the group deflection and therefor also bending moments for small lateral group loads.

- The soil-pile-soil interaction is captured by a volume based passive wedge reduction. However, soils get compacted between the piles when the pile group deflects, causing an increase in soil stiffness and extra loads on piles (e.g. the trailing pile row pushes its soil against the leading pile row). For large group deflections, the soil stiffness could be underestimated. As a result, group deflections due to large lateral loads can be overestimated.

The model seems to work well for sloping surfaces despite the fact that the effect of a slope on the overburden pressure is not taken into account. The overburden pressure σ_p is computed by multiplying the depth with the effective weight of soil layers as if the surface is horizontal. Effective soil pressures below a slope or near the crest of a slope are smaller than effective soil pressures that are computed for a horizontal surface. The result is a stiffer predicted soil pile response, especially for the first stage of loading. This effect can be seen in both slope experiments. This chapter only prescribes a slope correction method for slope downward loaded piles. In the situation of slope inward loaded piles, the wedge failure slices become larger due to the 'extra' soil compared to a flat surface resulting in a higher ultimate soil resistance. Correction factors are now larger than 1 instead of smaller.

The following phenomena are not included in the model and have a limited to negligible effect; Increase of friction between soil and pile, in case of excessive pile deformation, is not evaluated as contributor to lateral resistance and has only a noticeable effect for large diameter piles. Furthermore, the gap behind the pile is not taken into account, which reduces the active pressure in the top layers. Also, soil accumulation in front of piles due to excessive pile deflections, causing an increase of the lateral resistance, is not part of the model.

4.3.5 Conclusion on validation with literature experiments

A semi-analytical model is proposed as analysis tool for laterally loaded pile groups. The model is validated with three different field experiments. The lateral loaded pile, as a part of a pile group in layered sloping soil, is modelled as a BEF. The elastic subgrade reaction of the soil is described by *p-y* springs which have a depth-dependent bilinear elastic-perfect-plastic approximation. The plastic limit is corrected based on the reduction of the passive soil wedge due to the overlap of shear zones with other piles at close proximity and due to the presence of a soil slope, going downward in the direction of the lateral load.

The proposed model is able to predict pile forces and displacements with high accuracy for three different field experiments. However, for pile groups, the maximum bending moments as function of the group displacement in the trailing pile rows could be underestimated, especially when the pile is near geotechnical failure. For piles located in a slope or near the crest of a slope, the model is an accurate and powerful tool to use. The accuracy of the model and its predictive value is affected by an informed choice of parameters, amongst which the fanning angle of the passive wedge, as discussed in the chapter. For each experiment, a best fit fanning angle is calibrated for the top layers in which the passive earth wedge forms. For the Snyder field experiment, a 15 degree fanning angle is found for undrained cohesive clay layers, corresponding to the non-zero fanning angle in undrained cohesive soils found by Ashour et al. (Ashour et al., 1998; Ashour et al., 2004) and Gabr et al. (Gabr et al., 1990). The Mirzoyan field experiment and the Abdelhalim et al. experiment are exectuted in moderate dense sand with slight cohesion and for both experiments, a best fit fanning angle equal to $\varphi'/2$ is found. This dependency on the friction angle correspond to the observed shear cracks at the surface during the experiments and to theoretical values stated by Bowman (Bowman, 1958). Because the fanning angle is very much dependent on the soil characteristics a large variety of fanning angles can be found in literature. This makes it is hard to choose an appropriate estimation without doing any experiments prior to performing computations. It is therefore recommended to perform field tests and geotechnical research in order to calibrate computational models.

For conservative pile design, a large wedge fan angle is recommended in the determination of the lateral pile capacity while for bending moment predictions, a small wedge fan angle is advised. The model has a short computational time, in the order of seconds, compared to complex three-dimensional FEM software, in the order of minutes to hours, which makes it an excellent tool for preliminary pile design and probabilistic analysis. With relatively little input, a proper estimate of the pile behaviour can be made.

4.4 Lateral pile group experiment Overamstel Amsterdam

To test the lateral response of old timber quay wall foundations, two lateral experiments have been carried out on 3x4 pile groups in Overamstel Amsterdam. In one of the experiments, the piles are loaded axially/vertically by means of a top load. The experiment without top load is labelled F1 and the experiment with top load is labelled F2. The set-up, instrumentation and test procedure of both tests is elaborated in this paragraph. Geotechnical information is provided in chapter 2.

4.4.1 Lateral pile group experimental set-up

First, the test set-up of the lateral pile group experiment without top load (F1) is explained of which a side view is presented in Figure 4.22 and a plan view is presented in Figure 4.23. The test is conducted on a pile group in which pile rows are spaced on average 0.85m centre-to-centre in the direction of loading and 1.0m centre-to-centre perpendicular to the direction of loading. The piles have been assigned numbers 1 to 12, starting from the top left (harbour side) and ending at the bottom right (land side). In the F1 experiment, the piles are designated as P1F1, P2F1, ..., P12F1, while in the F2 experiment, they are designated as P1F2, P2F2, ..., P12F2. The entire pile group is located below an almost constant water level which is artificially kept at NAP-0.4m. The piles are situated on a manually dredged sloping harbour bed of which the gradient is approximately 1V:3H.

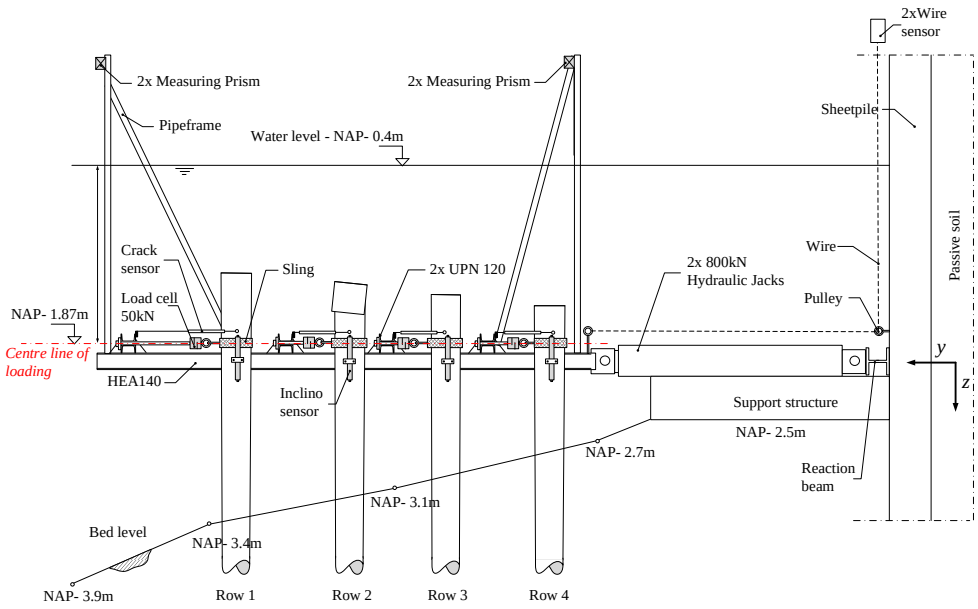

Figure 4.22, Sideview of lateral pile group experiment without top load (F1).

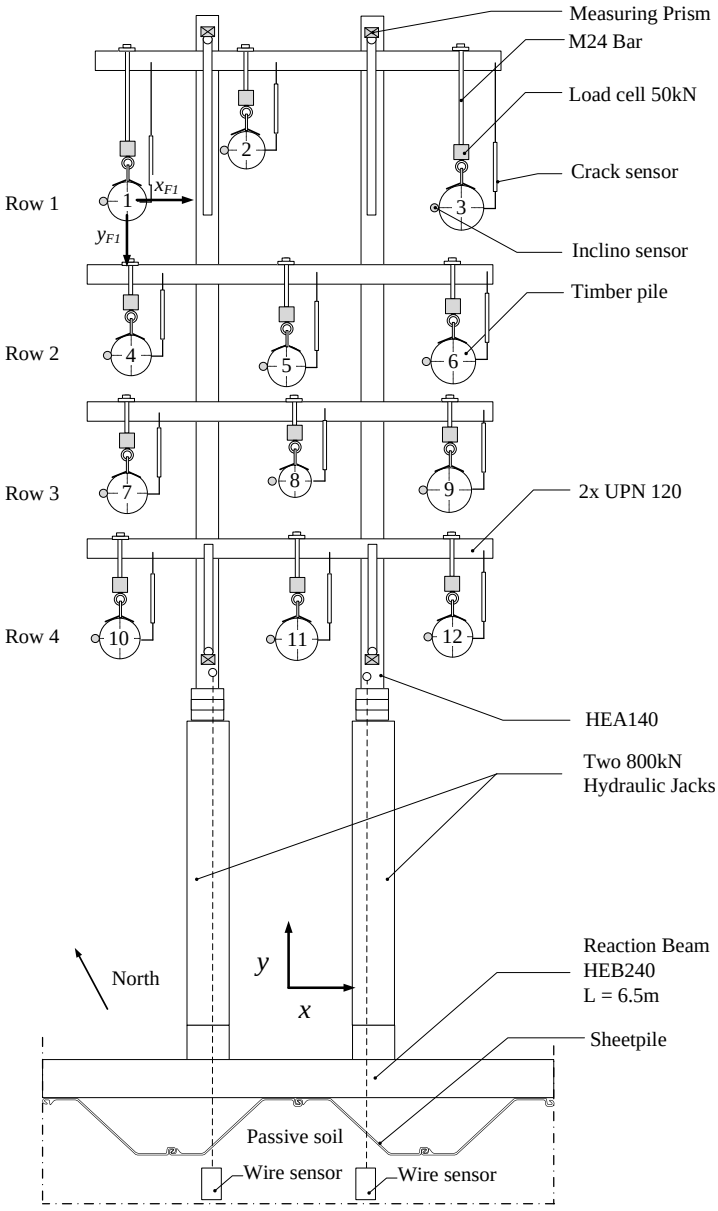

Figure 4.23, Planview of lateral pile group experiment without top load (F1).

The lateral load was applied by two 0.8MN (80 ton) hydraulic jacks, powered by two independent hydraulic pumps with a maximum pressure of 400 bar. The centre line of loading was located at NAP-1.87m (indicated in red in the side view). The jacks were placed 1m apart and installed with a hinged connection between a steel frame, see Figure 4.25, and a reaction beam. The steel frame is lifted in place by rattle slings, connected at the tops of the piles. The reaction beam is horizontally supported by a passive sheet pile wall. The steel frame is connected to the timber piles with tension slings. For illustrational purposes, the

pile-frame connection is reconstructed on land and can be seen in Figure 4.24. Around the pile, a sling is rattled which is connected with a shackle to a loadcell of 50kN. At the end of the loadcell, an M24 bar is present which is guided through a double UPN profile and locked in place with an endplate and M24 nut. Further instrumentation is elaborated in section 4.4.2. Before the test starts, each connection is pre-tensioned with 50N-100N. This procedure is time consuming and highly sensitive because all connections influence each other when adjusting the tension. The advantage of the connection chosen is that no bending moment is transferred to the pile caps.

A lateral pile group experiment F2 is carried out, similar to the F1 experiment, except that this time an additional constant top load is applied by placing large concrete blocks (LEGIO blocks) on the pile foundation. A plan view of the test set-up of the experiment with top load is presented in the appendix in Figure C.1 and a side view is presented in Figure C.2. For this test, the original outermost timber-headstocks are left on the pile foundation. In other words, the headstocks on top of piles 1,4,7,10 and piles 3,6,9,12. The dimensions of the headstocks are W×H×L = 0.23×0.20×3.0m. On both timber headstocks a line load is applied by placing concrete LEGIO blocks with an average unit weight of 24kN. The line load is linear and 33kN/m at the location of the first pile row and 23kN/m at the location of the fourth pile row. The line load is chosen equally to the absent weight of the soil body and masonry wall which are normally located on top of the quay foundation. The weight of the removed masonry wall is 33.8kN/m^2 and the weight of the removed soil is 26kN/m^2. No line load was applied on the middle headstock since it was removed because of installation work. Experiments F1 and F2 are executed in an identical way with the same instrumentation but on different pile groups. A plan view of the pile configuration for test F1 and F2 is provided in Figure 4.26. A separate histogram on the pile diameters is provided in Figure 4.27. In both experiments, pile 2 and 8 are equipped with fibre-optic wires (FO) which is discussed in section 4.4.2. Exact pile group dimensions and pile diameters can be found in Table 4.6.

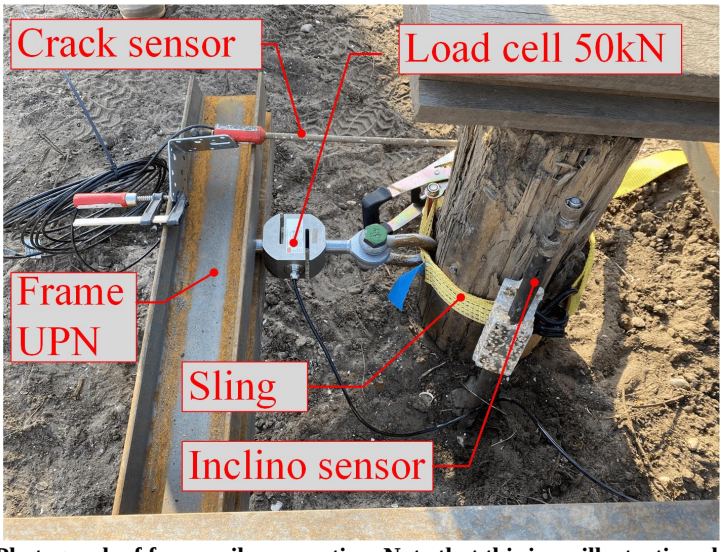

Figure 4.24, Photograph of frame-pile connection. Note that this is an illustrative photograph on land to demonstrate the connection while the actual test took place on a pile group below the water table.

Figure 4.25, Steel frame to be installed underwater and connected with tension slings to the 3x4 pile matrix.

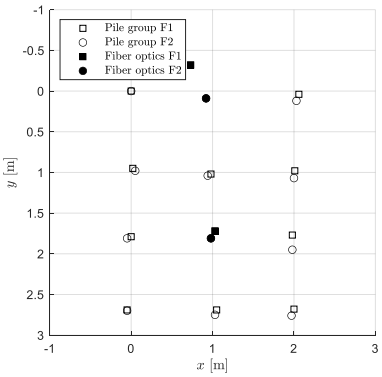

Figure 4.26, Plan view of 3x4 pile configurations F1 and F2. Fibre-optic-installed piles are visualized in black.

Table 4.6, Pile group configuration and dimensions of test F1 and F2. Diameter D_{Fi}[m] is the pile diameter, measured at the centre line of loading. x_{Fi} [m] and y_{Fi} [m] indicate the location of the pile.

Pile [#]	x_{F1} [m]	y_{F1} [m]	D_{F1} [m]	x_{F2} [m]	y_{F2} [m]	D_{F2} [m]
1	0	0	0.242	0	0	0.258
2	0.73	-0.32	0.242	0.92	0.09	0.226
3	2.06	0.04	0.290	2.03	0.12	0.253
4	0.02	0.95	0.261	0.05	0.98	0.258
5	0.98	1.02	0.245	0.94	1.04	0.266
6	2.01	0.98	0.283	2	1.07	0.248
7	0	1.79	0.277	-0.05	1.81	0.240
8	1.03	1.72	0.223	0.98	1.81	0.231
9	1.98	1.77	0.279	1.98	1.95	0.239
10	-0.05	2.69	0.250	-0.05	2.7	0.236
11	1.05	2.69	0.258	1.03	2.75	0.253
12	2	2.68	0.304	1.97	2.76	0.264

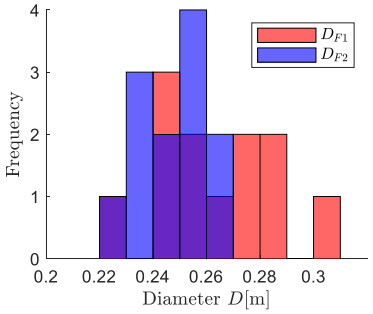

Figure 4.27, Histogram on pile diameters F1 and F2.

4.4.2 Instrumentation

The pile group was instrumented to measure pile cap deflections, rotations and pile cap loads. For a selection of piles, strain measurements along the piles were carried out. For test F1 and F2, the instrumentation is identical. First, the instrumentation at the frame-pile connection is discussed, presented in Figure 4.24. Individual pile cap loads were measured by AE-BM3 50kN S-loadcells. Strains are expected in the sling connection, introducing deformations between pile and frame. This deformation is measured by a J2-vibrating wire crack meter (which measures the spacing). The pile cap rotation is measured by an In-Placed-Inclinometer (IPI) sensor. The sensors are installed at the NAP-1.87m, the same height as where the loads are applied.

The deflection of the pile caps is determined in two ways. The first one is by measuring the extension of the hydraulic jacks by placing wire sensors between the frame and the sheet pile wall. In the second method, the displacement of the pile caps is measured by tachymetry. On the steel pile frame, steel pipes are welded which reach above the water level. On top of the steel pipes, 4 measuring prims are installed. The set-up of the wire sensors

and prisms can be seen in Figure 4.22 and Figure 4.23. With four prisms, the orientation of the pile frame in three dimensions is determined. For both methods, the pile displacement needs to be corrected with the extension of the frame-pile connection, measured with the crack-sensors. The wire sensors were used to steer during the experiment as it is a direct method with a high frequency (1Hz). Displacement data that is obtained with tachymetry (≈1/120Hz) is used in the postprocessing because of the higher accuracy.

In depth strain measurements are performed on pile 2 and pile 8, visualized in the plan view in Figure 4.26. To do so, pile 2 and 8 have been extracted from the pile group and instrumented with fibre optical wires. The fibre optical technique was successfully validated in the bending test, described in section 3.2.5. Per pile, fibre optical wires along the pile length are installed in a quadrant orientation, measuring the in-depth strain in the outer fibres. From the strain measurements along the pile, a resultant curvature profile κ_t[m^{-1}] is obtained. The methodology of this procedure is described in section 3.2.5. From the curvature profile, the bending moments can be obtained according to eq. 4.21. In this equation, $z = 0$ at the pile cap and $z = L$ at the pile tip. Furthermore EI [kNm^2] represents the flexural stiffness of the pile as function of the depth z.

$$M(z) = \kappa_t(z)EI(z) \qquad \textbf{eq. 4.21}$$

For the fibre optical piles, the instrumentation procedure is briefly explained. The extraction was performed with a vibrating customized steel pneumatic clamp of 3m long in order to avoid pile breakage or damage. The extraction device with timber foundation pile can be seen in Figure 3.4. Four piles were extracted at the fibre optical locations presented in Figure 4.26. The remaining six piles were extracted from segment B. From these ten piles, six piles in the best condition were equipped with FO wires. Four FO piles in the best condition were used in the lateral pile group experiments F1 and F2. The remaining two FO piles and four non instrumented piles were used in the bending experiment which is elaborated in chapter 3. The preparation of fibre equipped timber piles took around two weeks. In order to maintain the pile hole and to disturb the soil as little as possible, a temporary new timber pile with similar dimensions was placed directly after the removal of the old timber pile. After the FO piles were ready, the new timber piles were removed and replaced by the FO piles. This procedure can be seen in Figure 4.28. The FO piles were vibrated into the already existing pile hole. To protect the pile cap and the fibre wires, which sticks out of the pile cap, a timber corset was constructed around the pile cap.

4.4.3 Test procedure

In this subsection, the test procedure of the lateral pile group experiments is elaborated. Both lateral pile group experiments are performed in a displacement controlled manner. The displacement steps can be found in Table 4.7. Preparations, and step sizes were determined according to the CUR7 and ASTMD 3966. The step size gradually increases each four displacement steps. The duration of each individual step is based on the time which is needed for the pile group to find equilibrium with the imposed displacement. The pile group is assumed to be in equilibrium when the lateral resistance of the pile group has stabilized over time. The waiting time between the imposed displacements is therefore determined on the basis of the group resistance measured during the experiment.

Because the timber piles differ in diameter and in material properties, it is expected that the lateral resistance of individual piles has a large spread. This causes the resultant lateral group

resistance to be asymmetrical with respect to the two hydraulic jacks. To prevent the frame from warping in the horizontal plane due to this asymmetrical response, the jacks are operated with independent hydraulic pumps. The possibility of unequal loading allows the frame to be "steered". The steering is based on the displacement measurements obtained by the two wire sensors which are monitoring the extension of each hydraulic jack separately. When the lateral resistance drops drastically, the test is stopped. The remaining load is reduced in four steps, 75%, 50% and 25% en 0% accordingly.

Figure 4.28, Temporary new timber pile (right) is removed and directly replaced with fibre-optic-installed pile (left).

Table 4.7, Loading steps for test lateral pile group experiment F1 and F2.

Step [#]	Displacement [mm]	Step size [mm]	Step [#]	Displacement [mm]	Step size [mm]
1	5	+5	11	170	
2	10		12	200	
3	15		13	250	+50
4	20		14	300	
5	35	+15	15	350	
6	50		16	400	
7	65		17	475	+75
8	80		18	550	
9	110	+30	19	625	
10	140		20	700	

4.5 Results lateral pile group experiment

In this section, the results of the lateral pile group experiments are discussed. The order of elaboration for each subsection is: first experiment F2 followed by experiment F1. The reason for this order is due to a sudden technical defect during the F1 experiment. After 8 displacement steps, the reaction beam was pushed out of position resulting in a sudden loss of loading force. The test was interrupted for a week in which the test setup was restored and installation equipment was reinstalled. As a result, experiment F1 has a (initially unintended) unloading step, giving extra complexity in the results when compared to experiment F2.

4.5.1 Load and deflection results

In Figure 4.29, the time series of experiment F2 is presented. The left y-axis indicates the total group load and the right y-axis, the group deflection. The reaction force spikes instantaneously when imposing a new target deflection, followed by a immediate decline towards a consolidated reaction force level over time. This sudden increase in lateral resistance decreases exponentially in time and eventually becomes stable. When displacements become bigger, the spike in reaction force becomes larger too. After 200mm of group deflection, the lateral group load starts to decline rapidly. The pile group fails as a result of a combination of geotechnical failure and pile breakage. The test is proceeded until 450mm deflection. From the time series, the stabilized group loads and corresponding target deflections are marked and visualized in Figure 4.29. These moments in time are considered stabilized load situations and used in further analysis. Displacements larger than 200mm are excluded from further analysis because the pile group F2 has already failed and the analytical pile group model cannot model this.

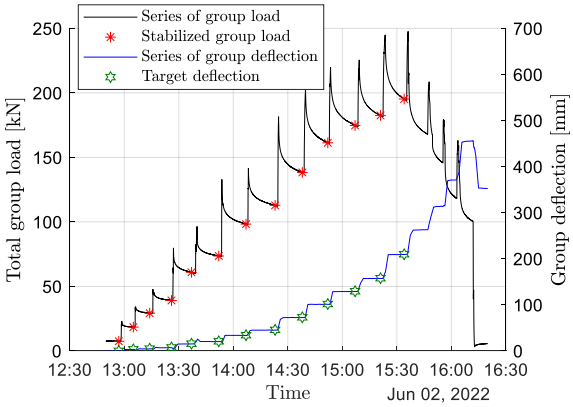

Figure 4.29, Loading time series of test F2. Group load and displacement as function of time are plotted and stabilized load steps are identified.

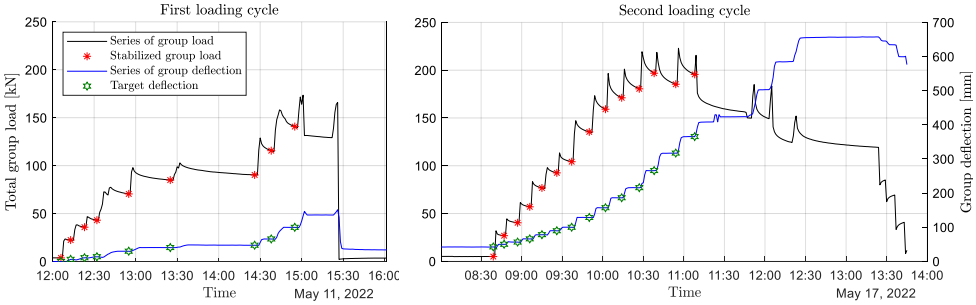

Figure 4.30, Loading time series of test F1 on May 11 and 17, 2022. Group load and displacement as function of time are plotted and stabilized load steps are identified. Note that test F1 has a relaxation step, resulting in a first loading cycle and second loading cycle.

In Figure 4.30, the time series of experiment F1 is presented. The figure is split into two parts, the first loading cycle and the second loading cycle. This has to do with the unloading step due to technical defects during the test as explained in the introduction of this section. The technical defects in the first loading cycle caused irregular waiting times between the loading steps because of consultation and interim adjustments. The response seen in both cycles is similar to that seen in experiment F2. In the first cycle, displacements up to 50mm are reached. In the second cycle, the lateral pile group resistance reaches a maximum at 275mm after which the lateral group resistance remains constant for another 100mm, followed by rapid decrease of resistance. This decrease was due to a combination of geotechnical failure and pile breakage. At 650mm group deflection, the test was stopped. In Figure 4.30, the stabilized group loads and corresponding target deflections are marked. Displacements larger than 350mm are excluded from further analysis because the pile group F1 has already failed.

4.5.2 Correction of deflection measurements

Not all piles have the same deformation with each loading step. This has to do with the extension of the sling connection during loading. For both experiments F1 and F2, the sling extension as function of the pile deflection is presented in the appendix Figure C.4 and Figure C.5. Each sling extends differently due to the variation in lateral resistance by individual piles. Installation imperfections, such as the length of the sling, also contribute to the

variations in sling extension. When individual pile deformations are considered, the individual sling extension is subtracted from the frame displacement. The average group deflection is determined by the displacement of the frame minus the average sling extension.

4.5.3 Load distribution between piles and pile rows

To study and understand the group effects of old timber pile foundations, the load distribution between individual piles and pile rows is of paramount importance. From the load-cells on each pile and the deflection of individual piles, load versus deflection graphs are constructed. Figure 4.31 shows the lateral cap load taken by individual piles of experiment F2. The lateral loads are plotted versus the pile deflection for each row separately. Within a row, piles do not carry identical loads. The ratio between maximal and minimal cap loads of individual piles within a row is in some cases more than two. This is considered a large spread and unequal load distribution within individual pile rows. At 140mm deflection, pile 4 lost half of its lateral resistance, most likely due to pile breakage. Pile breakage of other piles was observed with deflections larger than 206 mm.

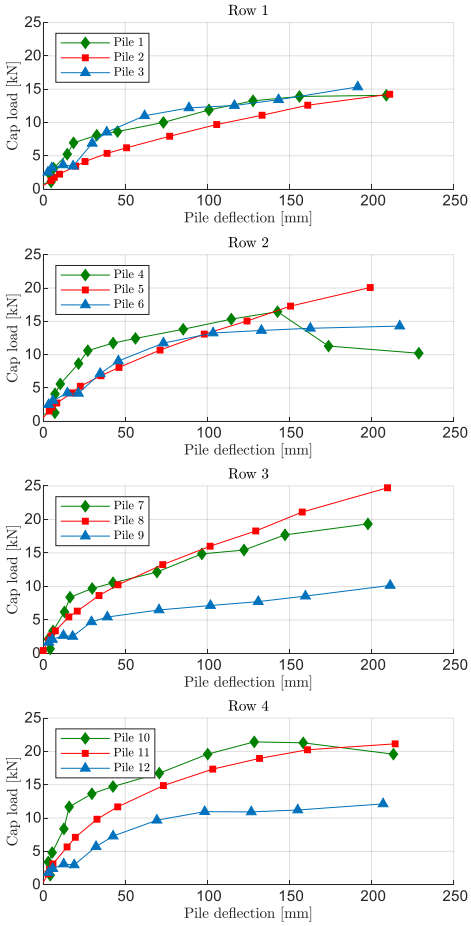

Figure 4.31, Pile cap load versus pile displacements per pile row for test F2.

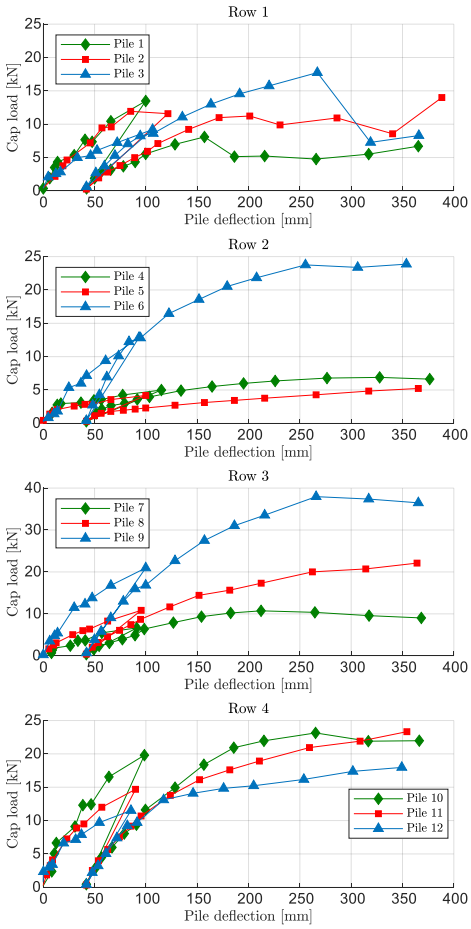

Figure 4.32, Pile cap load versus pile displacements per pile row for test F1.

In Figure 4.33, the row averaged lateral pile resistances are compared. Furthermore, the average group resistance is provided. The variation in lateral resistance between the pile rows was around 10-15% from the group average. The rear pile row, row 4, has the largest lateral resistance. Pile row 2 carries the next largest load followed by row 3. Row 2 and 3 are close to the average cap resistance. The front pile row, row 1 has the least lateral resistance. After 140mm deflection, the load in row 3 starts to become larger than in row 2 due to the breakage of pile 4. Eventually, the third and fourth pile row have the largest and same contribution with deflections greater than 200mm. At 206mm the pile group resistance decays rapidly and the pile group is considered failed. A maximal average lateral resistance of 16.3kN/pile has been reached.

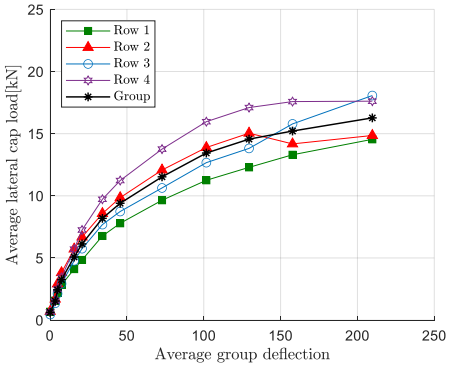

Figure 4.33, Load versus average group deflection graph for experiment F2.

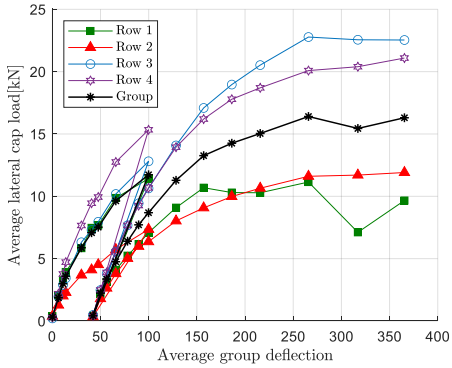

Figure 4.34, Load versus average group deflection graph for experiment F1.

Figure 4.32 shows the lateral cap load taken by individual piles of experiment F1. The lateral loads are plotted versus the pile deflection for each row separately. The relaxation step can clearly be seen and its effect is discussed in section 4.6. The variation between piles within the pile rows is large. Compared to experiment F2, the variation is even larger. A good example is found for pile row 2 in which pile 6 takes up to 25kN and pile 5 hardly 5kN. At 161mm of deflection, pile 1 lost half of its lateral resistance and at 287mm of deflection, pile 3 lost two third of its lateral resistance, most likely due to pile breakage. Pile breakage of other piles was observed for deflections larger than 350mm.

In Figure 4.34, the row averaged lateral pile resistances are compared for test F1. Furthermore, the average group resistance is provided. The variation in lateral resistance between the pile rows was around 25-30% from the group average, which is higher compared to experiment F2. For the first cycle, the rear pile row has the largest lateral resistance. In the first cycle, the first and third pile row behave very similar while pile row 2 has two third of the lateral capacity compared to the group average. After 100mm deflection, the lateral load was suddenly decreased to zero which resulted in a bounce back of the entire pile group with approximately 60mm. In the second cycle, the first and third pile row have a very different trajectory compared to the first cycle. Row 3 tends to follow the rear pile row while pile row 1 follows the second pile row. Eventually, the third pile row has the largest contribution with deflections greater than 150mm. However, the difference with the rear pile row is less than 10%. The first 50mm deflection for the first and second cycle have a similar gradient. When the second cycle has a displacement of 100mm, it has lost 30% of its lateral resistance compared to the first cycle. At 275mm the pile group resistance decays and the pile group is considered to have failed. A maximum average lateral resistance of 16.4kN/pile has been reached.

Finally, the group average pile resistances of experiment F1 and F2 are compared, shown in Figure 4.35. For small deflections, experiment F2 shows a stiffer behaviour compared to experiment F1. For an average cap load of 12kN, the deflection of F1 is 100mm while for F2 this is 70mm. The maximum average cap load was almost the same, 16.3kN/pile for F2 compared to 16.4kN/pile for F1. The deflection at which this maximal lateral load was achieved is different. For experiment F1, this was at 270mm while for experiment F2 this was at 206mm. After the maximal cap load was achieved, a rapid decline for experiment F2 was seen while for experiment F1 a more or less constant behaviour was observed, followed by a rapid decline.

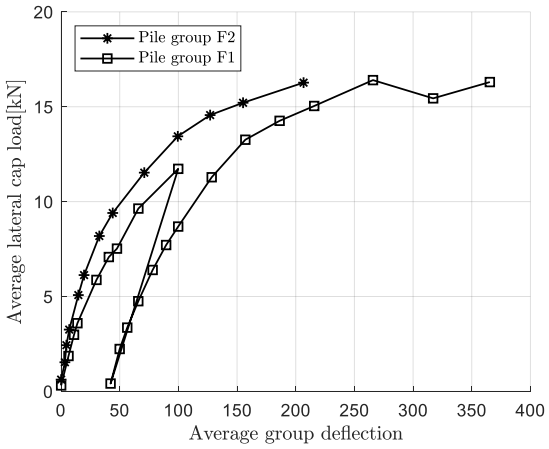

Figure 4.35, Comparison between experiment F1 and F2 for load versus deflection.

4.5.4 Elastic-moment along piles

In this section, FO measurements are employed to obtain bending forces in the piles. However, during experiment F1, the sudden unloading step led to a bounce back effect on the piles, resulting in damage to the fiber optic wires. Consequently, the strain measurements for the second cycle in F1 became unusable. Bending moments are determined for pile P2F2, P8F2, P2F1 and P8F1 according to eq. 4.21. This relation is only valid within the linear elastic behaviour of the timber pile material. It is however not possible to evaluate when the timber cross section enters the elastic-plastic phase since the *MOR* and E_b[MPa] of the timber pile material are unknown and have such a large spread. It is therefore better to refer to κEI or elastic-moment, instead of a bending moment. The interpretation of the elastic moment in section 4.6 presents the bending moments, including the plastic behaviour of the piles.

To determine the elastic moments, the flexural stiffness of the FO piles needs to be determined. Based on four-point bending tests, the average flexural stiffness EI[kN/m^2] for a population of 6 timber piles was determined and presented in eq. 4.22. In this equation, EI is the flexural bending stiffness and z[m] the depth with respect to the pile cap. A linear scalar parameter Φ_{EI} is introduced which takes into account the large variety in flexural stiffnesses found. The scalar parameter Φ_{EI} is calibrated by solving eq. 4.23 for multiple imposed deflections. In this equation, the measured lateral cap force F_{cap}[kN] is set equal to the average FO measured shear force $V(z,\Phi_E)$[kN] in the free pile length L_f[m]. Theoretically, the shear force is constant over L_f. The curvature κ_t is obtained from the fibre optical strain measurements which can be found for all piles in appendix F.2.3. The flexural stiffnesses per pile, and their scalar parameter can be found in Table 4.8. The calibration itself can be found

in appendix C.1.3. The bending moment in the free length of the pile is expected to remain elastic throughout the experiment which makes that eq. 4.23 holds for all imposed deflections.

$$EI(z, \Phi_{\mathrm{EI}}) = \Phi_{\mathrm{EI}}(-81.46z + 945.77) \qquad \textbf{eq. 4.22}$$

$$F_{cap} = \overline{V(z, \Phi_{\mathrm{EI}})} = \frac{\overline{\mathrm{d}\kappa_t(z) EI(z, \Phi_{\mathrm{EI}})}}{\mathrm{d}z} \qquad z[0, L_f] \qquad \textbf{eq. 4.23}$$

The flexural stiffnesses for the four piles are calibrated to be higher than the average flexural stiffness obtained from the bending experiments (e.g. $\Phi_{\mathrm{EI}} > 1$). This finding is explainable since the best four piles in terms of timber quality (based on visual inspection) were selected from a total population of 10. The 6 left over piles were used in the four-point bending experiment.

Table 4.8, Calibrated flexural stiffnesses for FO piles.

Pile	Φ_{EI}	*EI(z)*
P8F2	1.7	1608 - 139 *z*
P2F2	1.1	1040 - 90 *z*
P2F1	1.2	1135 - 98 *z*
P8F1	1.5	1419 - 122 *z*

With the obtained flexural stiffnesses per pile, the elastic moments κEI over the depth for pile P2F2, P8F2, P2F1 and P8F1 are determined, presented in Figure 4.36. For all four FO piles, the depth of the maximal elastic moment occurs at progressively deeper depths with increased deflections. On average, the maximum elastic moment in the first pile row is located between NAP-3.5m – NAP-4.5m. For the third pile row, this is located between NAP-2.5m – NAP-4m. For both piles 2, a linear part can be identified which is due to the relatively large free length of the first pile row. The free length of the third pile row is shorter compared to the front pile row, causing the linear part of the elastic moment distribution in the top to be shorter. Another finding is the depth of the zero moment crossing. Below this point, pile deflections are hardly present. For P2F2, the zero moment crossing due to a deflection of 161.1mm is located at NAP -8m. The zero moment crossing for P8F2 due to a deflection of 172.8mm is located at NAP-7m. Piles P2F1 and P8F1 have similar zero moment crossings compared to piles P2F2 and P8F2 for small imposed deflections. However they cannot be compared for the larger displacements since no data is available for experiment F1.

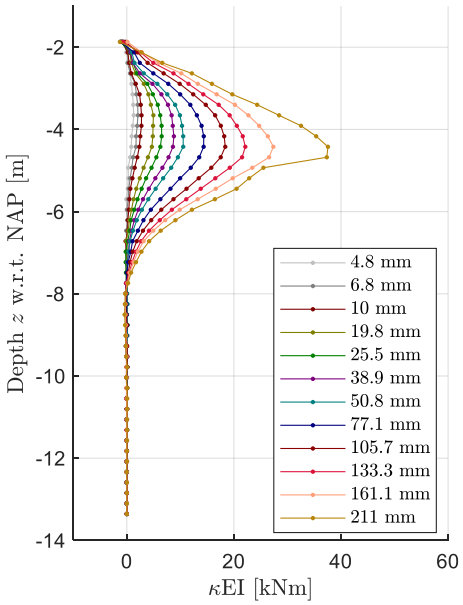

Figure 4.36A, Pile P2F2.

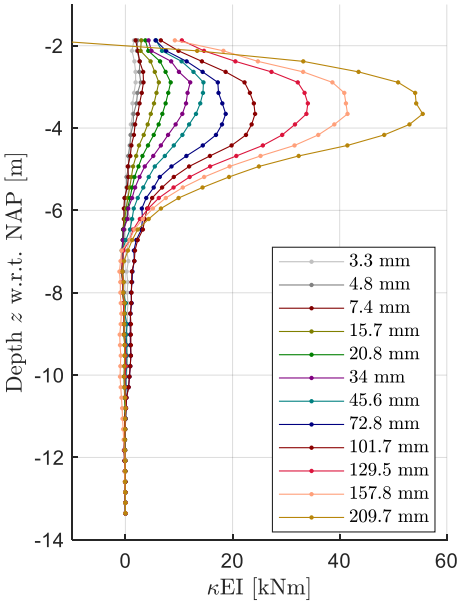

Figure 4.36B, Pile P8F2

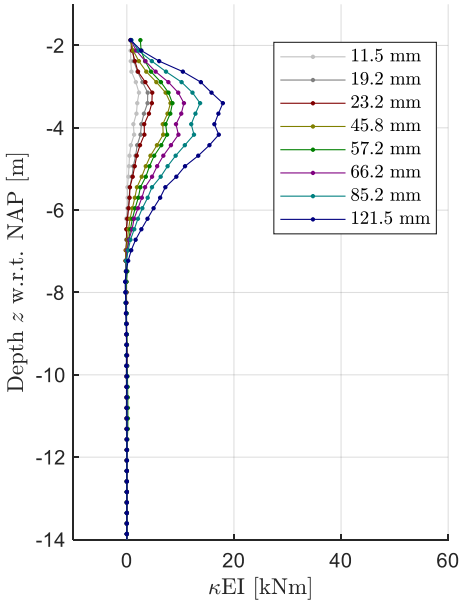

Figure 4.36C, Pile P2F1

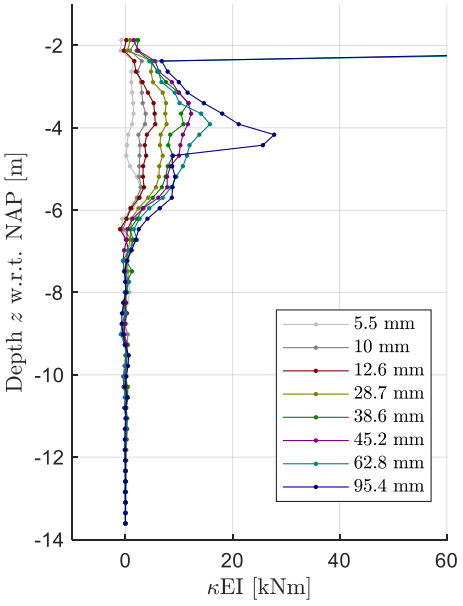

Figure 4.36D, Pile P8F1

Figure 4.36, *κEI* in-depth profile with respect to NAP for multiple imposed deflections. Fibre wires in F1 were severely damaged after unloading step, resulting in unusable data for cycle 2. Note that deflections are not equal due to the variation in sling extension.

In Figure 4.37, the maximum elastic moment κEI is plotted as function of the pile displacement for piles P2F2, P8F2, P2F1 and P8F1. As can be seen, piles 2 have a very similar deflection-κEI diagram. The same can be observed for piles 8, which follow a very similar deflection-κEI diagram. The elastic moments in the third pile row are higher compared to elastic moments in the front pile row. Note that the flattening of the elastic moment curves for larger deflections is not present because elastic-plastic behaviour of the timber pile material is not taken into account. The transition between elastic and plastic bending stresses is discussed in the interpretation in section 4.6.

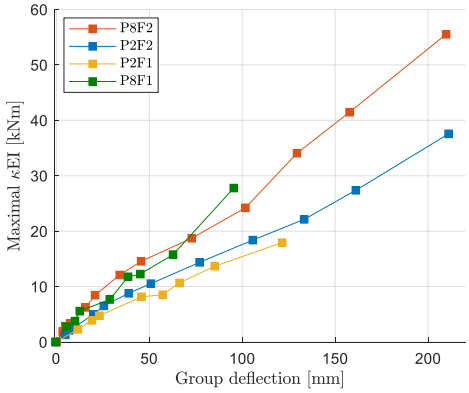

Figure 4.37, Maximum κEI versus pile deflection for piles P2F2, P8F2, P2F1 and P8F1.

Table 4.9, Estimated pile breakage depth with respect to centre line of loading and corresponding deflection for experiment F1 and F2. A broken tilt sensor is indicated by 'X' and no breakage by '-'.

Pile [#]	y F1 [mm]	L_b F1 [m]	y F2 [mm]	L_b F2 [m]
1	161	1.38	206	1.63
2	287	1.99	385	1.95
3	287	2.51	261	2.1
4	-	-	126	1.95
5	465	2.01	291	1.55
6	396	2.91	312	X
7	428	2.24	209	2.55
8	410	2.35	209	2.39
9	369	3.3	260	1.56
10	-	-	209	1.59
11	535	2.53	261	1.7
12	369	2.07	206	1.76

4.5.5 Pile breakage depth

With the measured pile cap rotations and pile deflections, an estimate of the pile breakage depth L_b[m] is made. This is the depth at which piles break with respect to the centre line of loading. The depth is obtained by $L_b = y/\varphi$ in which y[m] is the pile deflection and φ[rad] the pile cap rotation, both at the time of pile breakage. Pile breakage is identified as an instant decrease of significant lateral resistance. The depths at which the piles broke are summarized in Table 4.9. This method assumes the pile to be fully relaxed and straight direct after failure. Furthermore, it is assumed that the horizontal location of the fracture is estimated to be located at the original position of the pile before the experiment started. Both assumptions simplify the problem which introduces errors on the estimated depths. Since the introduced errors are similar for all piles, a comparison between the individual piles and between experiment F1 and F2 can be made.

On average, piles broke deeper and with more deflection for the experiment without top loading compared to the experiment with top loading. The pile group with top loading experienced pile breakage at NAP-3.76m depth (L_b = 1.89m) with an average deflection of 245mm. The pile group without top load experienced the pile breakage at NAP-4.20m depth (L_b = 2.33m) which is 44mm lower than F2 while both slopes and free pile lengths were similar. The breakage depths align well with the depths at which the maximum elastic moments were measured. The breakage of piles for F1 was on average achieved with a deflection of 370mm which is 125mm more than in experiment F2. For both experiments, the deepest pile fractures were found in the middle of the pile field.

4.6 Interpretation lateral pile group experiment

In this section, an interpretation of the Overamstel pile group experiments is provided. First, the lateral load distribution among the piles is explored, followed by an examination of the effect of the top load on this lateral resistance. Next, the elastic moments are interpreted by converting them to elastic-plastic moments, considering the plastic behaviour of the timber. Finally, the effect of the unloading step of experiment F1 is discussed.

4.6.1 Load distribution between piles and pile rows

Experiments F1 and F2 revealed a significant variation in lateral resistance among individual piles, with force ratios reaching up to 5 within pile rows and a variation of 10-30% from the average group load between pile rows. A multi-variable linear regression model was employed to investigate the influence of four significant pile group effects: pile free height, side-by-side effects, in-line effects, and pile diameter on lateral resistance within the pile group. The multi regression analysis can be found in appendix C.1.4. The model was statistically significant, although the resulting R^2 value was low at 0.13, indicating that side by side, free height, in-line, and pile diameter collectively explain only 13% of the variance in lateral pile group resistance. Despite the expectation that larger pile diameters would result in greater lateral resistance, the multi-variable regression reveals that the diameter is insignificant. This is consistent with the bending experiments, which showed a wide range of flexural stiffness, bending strength, and shell thickness with no significant correlation to pile diameter. Furthermore, it was found that the pile free height was dominant over the in-line effect, with the front piles carrying the least amount of load gradually increasing towards the rear pile row. An elaboration of the four effects and corresponding plots can be found in appendix C.1.4.

Hence, the remaining 87% of the variance in lateral pile group resistance can be attributed to various factors not considered in the analysis. These factors include a large variation in pile degradation, flexural stiffnesses and bending strength. Other effects that might play a role are installation effects, and measurement errors.

4.6.2 Effect of top load on lateral resistance

The experiments revealed that the inclusion of a top load led to a stiffer lateral response and a more brittle failure of the pile group (see Figure 4.35), yet the average pile group failure load remained unchanged. Several factors may play a role here:

- With an increase in axial load on the pile, the radial stress experienced by the soil during lateral loading is also increased, improving the soil's shear resistance and ultimately the lateral resistance of the pile. This was also found by previous studies, e.g. (Mu et al., 2015) showed that the presence of a vertical load increases the lateral bearing capacity of piles in sand, as well as reduces their lateral deflection. The same was found by (Al-Baghdadi et al., 2017) by performing large scale tests on lateral axial loaded straight shafted piles and screw piles.
- As lateral deflections increase, second-order effects become more pronounced, resulting in an increase in bending moments (Ding et al., 2017). The significance of the second-order effect is determined by several factors such as the free pile height, clamping depth, horizontal to vertical load ratio, and flexural stiffness. To estimate the second-order effect, one can calculate the amplification factor, $v_f = n/(n\text{-}1)$, where n is determined using the Euler buckling load formula with $n = F_k/N$, where F_k[kN] = $\pi^2 EI/L_k^2$. Following the analogy of a cantilever beam, L_k[m] (buckling

length) can be approximated as 2a, where a[m] is the depth of maximum moment. (Anagnostopoulos et al., 1993) found that applying an axial load on an already laterally loaded single pile resulted in a 4% increase in bending moment. The corresponding amplification factor in their study is v_f = 1.029, while in the Overamstel experiment, v_f = 1.058. Assuming a linear relationship between amplification factors and bending moments, an increase in bending moment due to top load can be expected to be between 5-10%.

- The pile-headstock connection present in experiment F2 provides a cap moment that counteracts the imposed pile cap rotation. The addition of a top load increased the stiffness of this connection, thus enhancing the overall system's stiffness. Figure 4.38 plots the pile cap rotation as a function of pile deflection, with black open dots representing piles 1-12 from experiment F1 and piles 2,5,8,11 from experiment F2, and red dots representing piles 1,3,4,6,7,9,10,12 from experiment F2. Two second-order trendlines are provided (a nonlinear relation is expected), both of which are forced through the origin of the graph. Despite the expectation that piles with a pile-headstock connection would exhibit smaller pile cap rotations compared to free-capped piles for similar deflections, hardly any difference in cap rotations is observed. This indicates that the effect of the pile-cap connection for timber piles/caps is likely to be insignificant, or not possible to accurately identify due to the large variation in cap rotations combined with monitoring accuracy. An assessment on the pile-cross beam connection is performed in chapter 5.

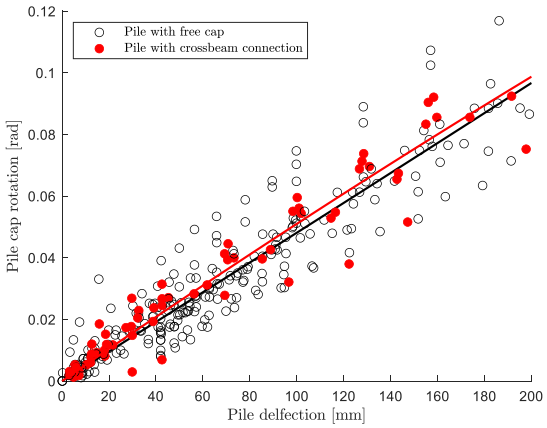

Figure 4.38, Pile cap rotation versus deflection for piles with and without headstock connection.

4.6.3 Elastic moment and elastic-plastic moment

The elastic moment diagram κEI (Figure 4.36) is first interpreted in terms of its shape. It is observed that the zero-moment crossing occurs at a depth of NAP-7m to NAP-8m during larger deflections. At this depth, a 1m thick sand layer known as the 'Wadzand deposit' is present. Throughout the loading process, the zero-moment crossings never exceeded NAP-8m, which suggests that the Wad deposit is the maximum clamping depth for timber piles. The structural resistance of the piles is insufficient to overcome the passive resistance of the Wad deposit. Above the Wad deposit, peat and clay layers are present which have a lower lateral resistance. The elastic moment is equal to the bending moment only when the timber pile material exhibits linear elastic behaviour. However, as the timber pile cross-section begins to exhibit elastic-plastic behaviour, the bending moments are no longer linearly

proportional to κEI. To accurately identify the transition between the elastic moment and the elastic-plastic moment and to make a reliable estimation of the elastic-plastic moments within the pile, an additional procedure is necessary.

The maximum bending moment is located at depth a with respect to the applied cap load, as shown in Figure 4.39A. Following the analogy of a cantilever beam, it is assumed that the cap load and maximal bending moment are proportional, with a moment arm a and a constant factor Φ_{soil} that considers the soil around the pile. The elastic-plastic moment behaviour is expressed as $F_{cap}a\Phi_{soil}$[kNm]. In the linear-elastic region, κEI and $F_{cap}a\Phi_{soil}$ follow the same trajectory. Given the value of a and F_{cap} for each load step, Φ_{soil} can be determined by calibrating the gradient of the $F_{cap}a\Phi_{soil}$ - F_{cap} diagram to the gradient of the κEI -F_{cap} diagram for the first 5 loading steps as these lie within in the elastic region. Beyond a certain load, the elastic moment and elastic-plastic moment start to deviate from each other, resulting in the moment no longer being proportional to κEI. This point is indicated in Figure 4.39A.

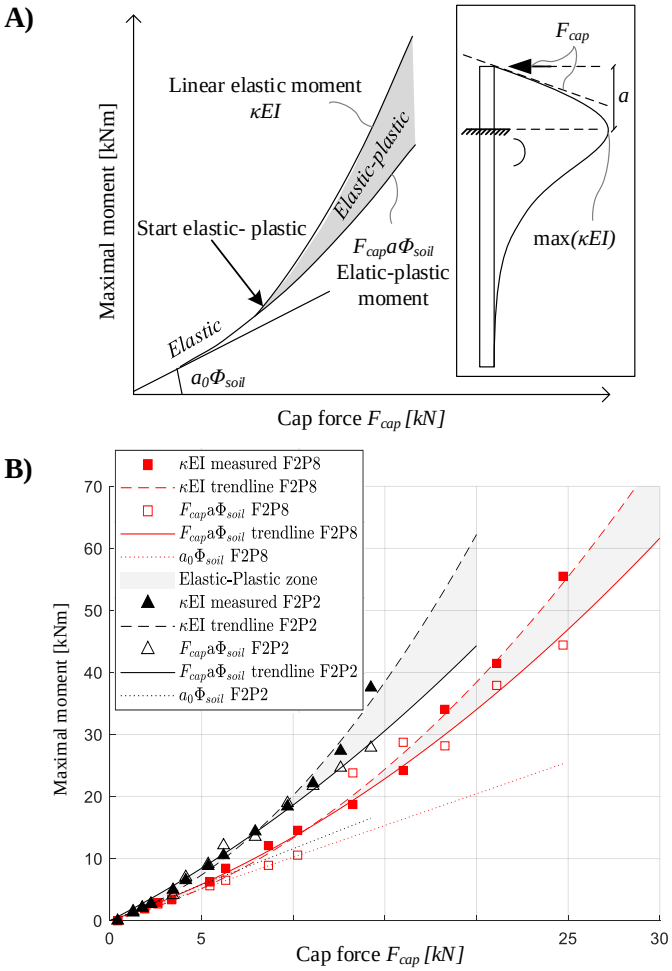

Figure 4.39, Identification of elastic plastic behaviour. A) illustrative figure visualizing elastic moment κEI and elastic-plastic moment $F_{cap}a\Phi_{soil}$. Grey area represents the elastic-plastic zone. B) identification of elastic plastic behaviour for pile F2P2 and F2P8.

The procedure shown in Figure 4.39A is performed for piles P2F2 and P8F2, and the results are depicted in Figure 4.39B. As can be seen, there is a slight scattering of $F_{cap}a\Phi_{soil}$ values due to the discrete 0.25m resolution of the fibre optics, utilized for the calculation of a. To distinguish scatter from the physical non-linear trend, second order trendlines are provided. The elastic-plastic zone for P2F2 begins to form at approximately 10kN, while for P8F2, this zone begins to form at 15kN. For both piles, these cap forces are reached when the deflection is 100mm. Above this level, both piles begin to display elastic-plastic behaviour. Just before yielding, bending moments were 20kNm and 25kNm for P2F2 and P8F2, respectively. Upon failure, these bending moments increased to 30kNm and 45kNm, respectively. Normalizing the bending moments at failure by their first yield moments results in ratios of roughly 1.5 and 1.8, which are comparable to the theoretical normalized ratio of 1.7 for a circular cross-section (Pandit et al., 2022). This indicates that piles break when fully plastified, which is consistent with the results of the four-point bending experiments.

4.6.4 Effect of unloading step

The unloading step (or cyclic loading step) which was present in experiment F1 has an effect on the lateral response of the pile group. In the first cycle, the average cap load at 100mm deflection was 11.72kN, whereas in the second cycle, it reduced by 30% to 8.68kN at the same deflection level. The bounce back was 60% of the imposed deflection. The gradient of the load deflection curve for the first and second cycle were similar for small deflections. The hysteresis loop, which is weakening of the piles by repeated loading (Heidari et al., 2014; Snyder, 2004), can clearly be observed in Figure 4.35. The effect of the cyclic loading step on the outcomes of the experiment are discussed by comparing with previous studies.

The lateral capacity reduction is found by many previous studies in which cyclic single pile and pile group experiments were performed and modelled. Research of (Chandrasekaran et al., 2010) showed that with two-sided cyclic pile group experiments, the lateral capacity reduced by 42% after 50 cycles of loading, with 28% occurring within the first five loading cycles. Additionally, in a closely spaced 3 × 3 pile group, the magnitude of maximum bending moment at 50 cycles of loading was about 50% higher than the static loading and occurred at a depth which was 30% more than the static conditions. (Rollins, Olsen, Egbert, et al., 2006) conducted single-sided cyclic loading tests on pile groups in clay, finding a reduction of 15% in peak load at the same deflection after 15 cycles, with half of this reduction occurring after only one cycle. Furthermore, the same tests showed increases in the maximum bending moment of 14-30% for a given load, with the smallest increases in the leading piles and the largest increases in the trailing row piles. (Nimbalkar et al., 2022) found a lateral reduction of 30% for 100 cycles. The modelling of the hysteresis loops and cyclic loading effects is done by multiple researchers, e.g. with FEM software (Küçükarslan et al., 2003) or *p-y* approach (Leung et al., 1987). The following conclusions can be drawn from experiment F1 and previous studies:

- A 26% reduction in lateral load found after one cycle is comparable (but on the high side) to studies in literature (who give 7.5% - 28%).
- It is likely that the ultimate resistance of experiment F1 has been reduced due to the cyclic loading step.
- The bending moment in the piles is likely to have increased due to the cyclic loading step.
- The depth of the maximum bending moment is likely to have increased due to the cyclic loading step.

Therefor, it can be concluded that if no relaxation step had been present, larger ultimate resistances would have been obtained with pile breakage at shallower depths for larger deflections. Cyclic loading significantly affects the response of lateral loaded timber pile groups, particularly as the number of cycles increases. However, when it comes to quay walls, which are continuously subjected to traffic or other cyclic loads, the impact of cyclic loading is expected to be relatively lower, especially in relation to the bouncing back effect. This has to do with their geometrical layout. The lateral driving force on the quay wall pile foundation is the soil body behind the quay wall. When loads at the surface increase, the soil stress behind the quay, the quay wall and its pile foundation are pushed towards the water. This process is irreversible since the soil wedge behind the quay prevents the pile group to bounce back towards its previous location. The cyclic loading effects for the full quay wall experiments is elaborated on in chapter 5.

4.7 Validation of analytical pile group model with Overamstel experiment

In this section, the results of the lateral pile group experiments conducted at Overamstel are utilized to validate the analytical pile group model. Validation is carried out on the lateral resistance and bending moment of the piles. Finally, a discussion and conclusion are provided.

4.7.1 Analytical pile group model input

The analytical pile group model is used to model individual piles within a pile group and to model pile groups. To validate the model for individual piles, piles P2F2 and P8F2 are used. Individual piles of experiment F1 are not used in the validation since the fibre optical wires were severely damaged during the test. To validate group average computations, experiments F1 and F2 are used. First the structural input parameters are discussed, presented in Table 4.10.

Table 4.10, Structural modelling parameters for pile P2F2, P8F2 and group averaged (F1 & F2)

Input parameter	P2F2	P8F2	Group average (F1 & F2)
EI (at 2m depth)	861.3 kNm^2 (Φ_{EI} = 1.1)	1131.1 kNm^2 (Φ_{EI} = 1.7)	783 kNm^2 (Φ_{EI} = 1.0)
L	12 m	12 m	12 m
D	0.22 m	0.22 m	0.24 m
Level of loading	NAP-1.9m	NAP-1.9m	NAP-1.9m

The pile diameter and the flexural rigidity are modelled constant over the pile length. The values of the constant diameter and flexural rigidity are taken at a depth of 2m below the pile cap. This is the depth at which bending moments are maximal. For the modelling of the piles F2P2 and F2P8, Φ_{EI} is taken as 1.1 and 1.7 respectively (obtained from the calibration in section 4.5.4). For group average computations, Φ_{EI} is taken 1.0 (which is the average flexural stiffness of the tested population). Because the model uses a constant flexural stiffness along the pile length, bending moments are underestimated at the upper part of the pile and overestimated at the lower part of the pile. To correct for the introduced error, the bending moment obtained with the analytical model $M_{con}(z)$ is corrected by the ratio between a depth average flexural stiffness and a constant flexural stiffness chosen at a depth of 2m. The bending corrected bending moment is provided in eq. 4.24.

$$M(z) = M_{con}(z)\frac{EI(z)}{EI(z = 2\text{m})} \qquad \textbf{eq. 4.24}$$

It is assumed that the softshell of the pile is able to withstand the lateral earth pressure and thus contributes to the geotechnical resistance of the pile group. As such, an external diameter, is used in the formulas of Brinch Hansen and Ménard to determine model spring stiffnesses. The soil layers and their engineering properties are summarized in Table 4.11, obtained from the geotechnical soil investigation provided in chapter 2.3. Cohesive layers are consolidated using undrained shear strength *su* and $\varphi = 0$, with a wedge fan angle of $\varphi_m = 15$ degrees as previously validated in section 4.3. The fanning angle for the granular soils is not relevant since the first granular layer is located at NAP-7.0. At this depth, no plastic layers are present which results in the absence of wedge formation. A slope inclination of 1V:3H is used in the model.

Table 4.11, Geotechnical modelling parameters for full scale lateral pile group experiment Overamstel.

Depth -NAP [m]	γ_{sat} [kN/m^3]	γ' [kN/m^3]	Sort [-]	Dutch name [-]	q_c [kPa]	*su* [kN/m^2]	Φ [deg]
2.6 – 4.0	16.9	6.9	clay	Geulopvulling	200	30	0
4.0 – 6.0	10.1	0.1	peat	Holland veen	400	30	0
6.0 – 7.0	19.1	9.1	clay	Oude zeeklei	400	45	0
7.0 – 8.2	18.0	8.0	sand	Wad deposit	1500	0	34
8.2 – 11.6	17.0	7.0	clay	Hydrobiaklei	500	50	0
11.6 – 12.2	11.7	1.7	peat	Basisveen	1500	0	0
12.2 – 14.0	19.0	9.0	sand	Eerste zandlaag	10000	0	33

4.7.2 Validation of analytical model with individual pile measurements

First the bending moment shape is validated with the *κEI* measurements for P2F2 and P8F2. Figure 4.40 displays the plot of moment predictions and measurements for pile P2F2 in subplot A and pile P8F2 in subplot B. For deflections less than ±100mm (which is the elastic zone), the predicted moment and shape of pile P2F2 match the *κEI* results very closely. For very small deflections around 0-20mm, the maximum moment of both piles is slightly underestimated, which was also found in the validation with experiments from literature. For the largest deflections of 161.1 mm and 157.8 mm, the model predicts moments that are 10-15% lower than the measurements taken with *κEI*. This discrepancy is expected, since piles exhibit an elastic-plastic behaviour, which cannot be described by the *κEI* method. Additionally, the maximum bending moment of pile P2F2 is predicted deeper than that of pile P8F2, which is consistent with the measured results. Furthermore, the predicted zero-moment crossing is in agreement with the measured data.

The maximum moment, as a function of pile cap load, is illustrated in Figure 4.41. Measured moments (including elastic-plastic behaviour) are represented by open markers, while predicted bending moments are illustrated by filled markers. As previously mentioned in section 4.6.3, a scatter of $F_{cap}a\Phi_{soil}$ values is present due to the 0.25m resolution of the fibre optics used for the calculation of *a*.

The bending moment prediction is very well for both piles. Despite the fact that the analytical pile group model describes the piles according to the Euler-Bernoulli beam theory, the bending moment predictions fit well for large cap loads. In Figure 4.42, the lateral cap force is plotted as function of the pile deflection. Open markers indicate the measured cap force,

and filled markers represent the predicted cap force. For pile P8F2, the model prediction is accurate up to 150mm, and for P2F2, the model prediction is accurate up to 100mm. However, with larger deflections, the model overpredicts the cap force (5-15%) and underpredicts the bending moment (5-10%).

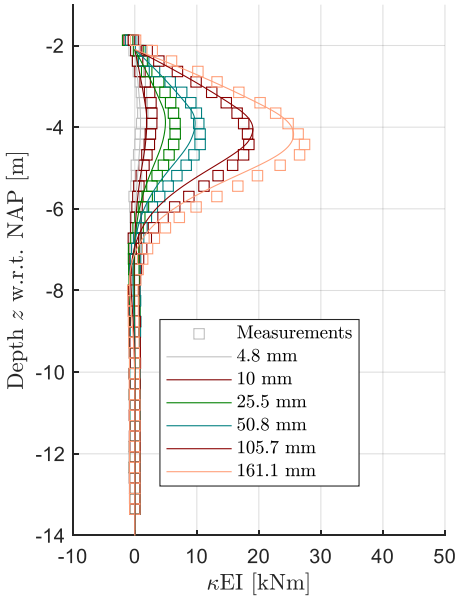

Figure 4.40A, Pile P2F2.

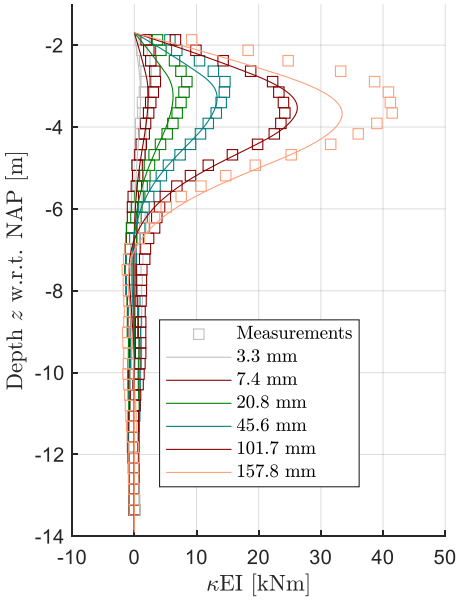

Figure 4.40B, Pile P8F2.

Figure 4.40, *κEI* in-depth profile with respect to NAP for multiple imposed deflections. Square dots represent the measurements and continuous lines represent the model prediction.

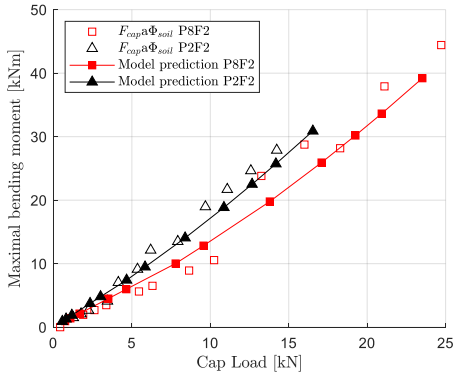

Figure 4.41, Comparison of model predictions with measurements of maximal *κEI* vs applied pile deflection for piles 8 and 2 of experiment F2.

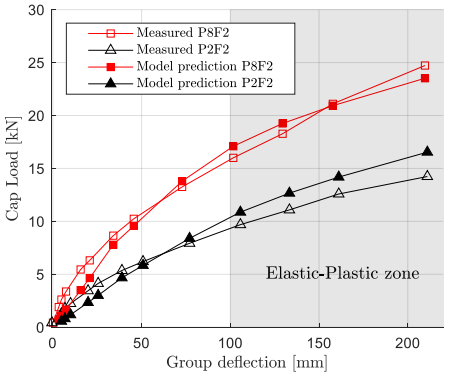

Figure 4.42, Comparison of model predictions with measurements of cap load vs applied pile deflection for piles 8 and 2 of experiment F2.

4.7.3 Validation of analytical model with pile group measurements

To make accurate predictions for individual piles within a pile group, detailed information per pile is crucial. When such specific information is not available, pile-averaged computations can be utilized. This section focuses on further validating the model's ability to perform computations on pile groups, demonstrating its capacity in the absence of detailed per-pile data. To validate the model with experiment F2, the axial forces in the piles due to the presence of a top load and the pile-headstock connection need to be included. Each pile was assigned an axial load of N = 20kN, corresponding to the top load used in the lateral pile group experiment F2. Additionally, each pile cap was loaded with a cap moment M_{rot}[kNm], which simulates the pile-headstock connection. The magnitude of the cap moment is determined with a pile-headstock interface model, which is discussed in section 5.2.3. The necessary inputs for the pile-headstock model are listed in Table 5.1.

In Figure 4.43, the group average cap load is computed and compared with group averaged measured cap load of experiment F1 and F2. For model simulations on F1, it can be seen that for the first 100mm, the force-displacement diagram of the model fits the measurements very well. For simulations on F2 it can be observed that for the first 100mm of displacement, the model prediction displays a stiffer behaviour when compared to the F1 experiment, where no top load and pile-headstock connection is present. This is in good agreement with the field measurements. The stiffer behaviour is slightly under predicted. The underprediction could be due to the absence of an increase in radial stress due to axial loading, improving the soil's shear resistance and ultimately the lateral resistance of the pile. With larger deflections than 100mm, the model overestimates the lateral group load for both experiments. At 200mm, F1 is overpredicted by 13% and F2 by 10%. The overprediction has four main causes:

- The piles are described by linear elastic Euler-Bernoulli beams. The model is not capable of assessing elastic-plastic behaviour and therefore overpredicts the lateral resistance for deflections larger than 100mm. Similar behaviour was found for piles P2F2 and P8F2.
- After 100mm, a cyclic loading step is present which results in higher moments in the piles and smaller ultimate lateral group resistance. The model does not take into account the cyclic loading step, causing an overpredicting with respect to the measured lateral group load.
- Pile breakage was experienced at 161mm which cannot be described by the analytical model.
- The strength properties, amount of degradation, diameter, and installation effects of timber vary greatly in the test pile field as well as in reality, leading to discrepancies between measurements and predictions that are not accounted for in the group-averaged computation.

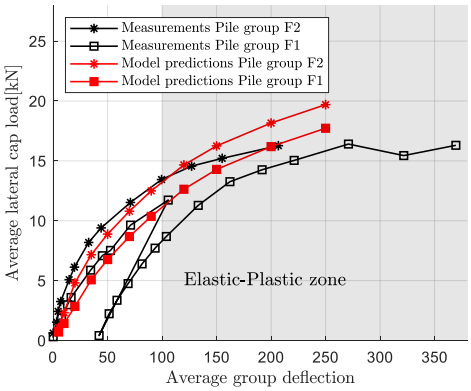

Figure 4.43, Comparison of model predictions with measurements of group average cap load vs applied pile deflections.

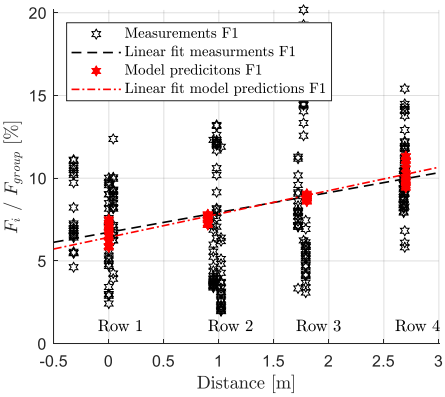

Figure 4.44, Loads taken by individual piles F_i as percentage of the group average pile load F_{group} vs the distance with respect to the first pile row. Model in red filled markers.

In conclusion, it is shown that with pile averaged model input, computations can still be made per pile row. This is highlighted in Figure 4.44 which validates the loads per pile row by presenting model predictions and measurements for experiment F1. The analysis focuses specifically on the loading steps of the first cycle, providing valuable insights into the behaviour of the piles. The model has a small spread compared to the measurements since computations were performed with a group averaged diameter and group averaged flexural stiffness. The model predicts that with pile averaged pile group averaged parameters, the leading pile row takes the smallest lateral load and the rear pile row takes the largest part, which is in accordance with the linear fit through the measurements. Pile group computations are likely to become more accurate with an increasing pile group population, averaging out large variations.

4.7.4 Discussion and conclusion on validation with Overamstel experiment

The presented model is able to predict pile forces and displacements in good correspondence with field experiments for laterally loaded historic timber pile foundations with closely spaced piles in underwater slopes. The model is able to predict lateral loads and bending moment magnitudes along the depth for the leading and the trailing piles in the pile group very accurately, which is a sign that the soil pressure distributions applied in the model are correct. For deflections, greater than 100mm, lateral loads are overpredicted and bending moments underpredicted. These errors arise from the model choice in which pile elements are described as linearly elastic, while in reality they become fully plastic. In the model, flexural stiffnesses and external diameters are taken constant over the pile length and in a second step, bending moments are corrected by a stiffness ratio. This simplification appears to work well and does not introduce significant errors in model predictions. In order to make a proper individual pile computation, detailed pile information is essential. Besides a comprehensive geotechnical dataset, the flexural stiffness of piles (derived from their effective diameter) and the outer diameter (used for geotechnical modelling) are crucial factors that must be considered. When such information is not available for each individual pile, it is still possible to make a group averaged computation which is accurate. Group averaged flexural stiffnesses and diameters can be used to construct a *p-y* curve of the entire pile group. Furthermore, a reliable estimate of the force distribution among different pile

rows can be made when performing group-averaged computations. Bending moments that are computed during group averaged assessments are not representative since variations within the pile group can be very large. The analytical model fails to consider the increase in radial stress caused by axial loading, resulting in a possible underestimation of the lateral resistance of vertical loaded pile groups. Consequently, the model's accuracy could be improved if it were to take this factor into account.

4.8 Conclusion and discussion on lateral loaded piles

An analytical model was developed for modelling the response of laterally loaded pile groups of quay walls, with a focus on applicability to historical quay walls in Amsterdam. In the proposed method, the bending of a pile, which is subjected to a lateral load and axial load, is described by a beam on a Winkler elastic foundation in which the soil behaviour is represented by a series of independent *p-y* springs, idealized with a bilinear elastic-perfect-plastic approximation. The plastic limit was computed with Brinch Hansen ultimate soil resistance and the elastic soil response by the Ménard stiffness. The plastic limit was corrected for each depth, based on the reduction of the passive soil wedge due to pile group effects and the presence of a sloping surface.

First, the analytical model was calibrated and validated with three field experiments from literature. These three studies included a full-scale lateral load test of a 3x5 pile group in soft clays and silts (Snyder, 2004), a full scale lateral load test of a single pile located on a slope in layered soils (Mirzoyan, 2007) and a small scale lateral load test of a single pile located near a slope in sand (Abdelhalim et al, 2020). In all three experiments, precisely installed steel piles were used, eliminating uncertainties such as a variation in pile diameter, pile degradation, variations in material properties and spatial variation of piles in the pile group. It is concluded that the proposed method can adequately predict bending moment distributions and pile deflections and in addition, a good consistency between the analytical model and experimental tests was observed. The method is very fast, making it suitable for probabilistic, Monte Carlo type, simulations and Bayesian updating to determine the probability of failure of quay walls or other structures with horizontally loaded piles.

After performing model validations with literature, the step towards historic quay wall foundations was made by performing two lateral 3x4 pile group experiments on the timber pile foundation of the Overamstel quay wall. In one of the pile group experiments, a top load is placed on top of the original headstocks initiating second order moments in the piles and pile cap moments. The experiments were performed completely submerged, using a steel frame with tension slings, loaded by two hydraulic jacks. The pile group was instrumented to measure pile cap deflections, rotations and pile cap loads. For a selection of piles, in-ground strain measurements were carried out. Based on the experiments the following conclusions are made:

- Within a row, piles do not carry identical loads. The spread in lateral resistance is large with force ratios of up to 5 between the pile carrying the maximum load and the one carrying the minimum load. The variation in lateral resistance between pile rows is approximately 10-30% from the group average. The majority of the variance (87%) in lateral pile group resistance can be attributed to variations in pile degradation, flexural stiffness, bending strength and geotechnical variations. Other minor contributing factors include installation effects and measurement errors. Only

a small proportion (13%) of the variance is accounted for by four typical group effects: “pile free height “, pile diameter, in-line effects, and side-by-side effects.

- For both experiments, an average maximal pile cap load of 16.4kN was found.
- The experiments revealed that the inclusion of a top load led to a stiffer lateral response and a more brittle failure of the pile group, yet the average pile group failure load remained unchanged. Contributing factors are: Increase in radial stresses giving greater lateral resistance, second order moments with increasing deflections and a stiffer system due to pile cap moments.
- Elastic-plastic behaviour is expected to occur at roughly 100mm of group deflection.
- Pile breakage is likely to happen at full plasticity of the timber cross-section.
- Piles are clamped in the Wad deposit at NAP-7m, maximal moments are found at NAP-3m – NAP -4.5m.
- On average, piles broke deeper and with more deflection in the experiment without top loading compared to the experiment with top loading. The deepest pile fractures were found in the middle of the pile field.
- Cyclic loading on timber pile groups has a significant effect on the lateral resistance. A reduction of 26% was found after one loading cycle. Furthermore, cyclic loading increases bending moments, resulting in earlier pile breakage.
- The pile free height (caused by the 1V:3H slope) was dominant over the in-line effect (section 4.6.1).

Finally, the analytical model was validated with the lateral pile group experiments conducted at Overamstel. The analytical model is used to model both the pile group as a whole and individual piles within the group. Geotechnical resistances are computed according to an external pile diameter, while structural resistances are determined based on an internal pile diameter, excluding the soft shell. It is concluded that the proposed model is able to accurately predict pile forces and displacements for lateral loaded timber pile foundations with closely spaced piles on underwater slopes. The model is able to accurately predict the lateral loads and bending moment magnitudes at all depth levels for both the leading and trailing piles in the pile group, indicating that the soil pressure distributions applied in the model are accurate. However, with larger deflections, the model overpredicts the cap force (5-15%) and underpredicts the bending moment (5-10%). This is due to the fact that pile elements are modelled as linearly elastic, while they actually tend to deform plasticly. Even though timber piles are tapered, they can still be modelled as members with constant diameter and constant flexural stiffness using the diameter at a depth of the maximal expected bending moment (found at approximately NAP-3m – NAP -4.5m). In order to ensure the accuracy of the computation, detailed individual pile information is essential. When such information is not available for each pile, it is still possible to make a group averaged computation.

Overall, the analytical model is very suitable for the probabilistic assessment of historic lateral loaded timber pile foundations, as it has a relatively short computational time, in the order of seconds, compared to complex three-dimensional FEM software which typically take minutes to hours. With minimal input, a proper estimate of the pile group behaviour can be obtained.


de Klerk
WERKENDAM
de Klerk
WERKENDAM

5

Lateral failure of quay walls: Modelling and quay experiments

This chapter encompasses two main objectives. The first objective is the development of a new computational model for quay walls that accurately describes the lateral behaviour of historic quay walls in layered sloping soil. The second objective is to conduct a full-scale proof load experiment on a historic quay wall in Amsterdam Overamstel, focusing on investigating the lateral failure of the quay and its pile foundation. The analytical quay wall model is validated and calibrated using these full-scale quay wall experiments.

Photograph by the author

5.1 Introduction to quay wall testing and modelling

5.1.1 Lateral failing quay walls in Amsterdam

The inner city quay walls in Amsterdam are 100-300 years old and serve as soil-retaining structures. They are primarily constructed with masonry on a timber floor that is supported by a matrix of timber piles. A historic technical drawing, containing the terminology of quay wall components, is presented in Figure 5.1. This study considers one of the most dominant yet poorly understood failure mechanisms of historic quay walls, namely lateral failure of the (timber) pile foundation, which is depicted in Figure 5.2. Preliminary stages of this mechanism, such as quay walls that are leaning towards the canal, can be observed throughout the Amsterdam city centre ("Enkele kademuren in Centrum dreigen te bezwijken," 2018). An example of a quay wall that failed as a consequence of lateral pile bending was the Grimburgwal in 2020 (Korff et al., 2021), briefly discussed in chapter 6. In practice, it is difficult to prove that quay walls are safe or even stable with state-of-the-art models. Assessing the lateral failing of the quay foundation is challenging due to various factors (discussed broadly in chapter 1) such as an unknown geometry (due to poor documentation), timber deterioration (Giorgio Pagella et al., 2022; van de Kuilen et al., 2021), complex lateral pile-soil-pile interaction (Hemel, Korff, et al., 2022), uncertainties in geotechnical model input data, uncertainties in the loads imposed by the active soil body on the timber foundation, time-dependent effects like timber creep (Spannenburg, 2020) and the three-dimensional redistribution effects of the masonry gravity wall (van Hulten, 2021). Because an important part of the above mentioned uncertainties lies in geotechnical and structural input data, there is clear potential for improving the analysis methods of the old quay walls by validating with a full scale test. The aim is to decrease uncertainties and consequently to keep quay walls operational for a longer time and avoid having to replace a large number of them on a large scale and within a short period of time.

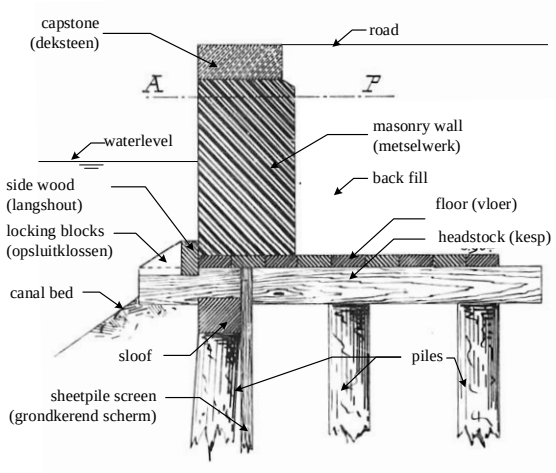

Figure 5.1, Cross-section of historical quay wall structure with terminology. (Lijnbaansgracht, tussen Palmgracht en perceelno. 14, Archive of Amsterdam)

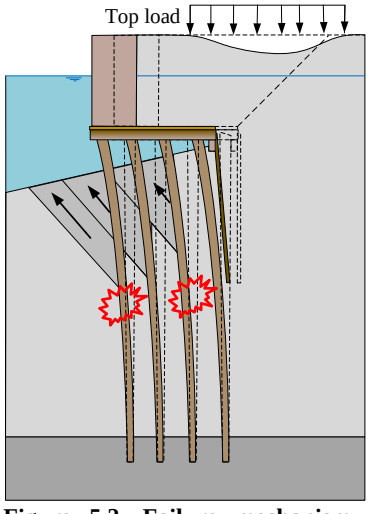

Figure 5.2, Failure mechanism 'Lateral failure of the quay wall foundation'.

5.1.2 Literature on modelling and testing of lateral failing quay walls

One of the ways to reduce uncertainties and to gain a more precise understanding of structural safety of lateral failing quay walls is to conduct physical (lab or field) experiments which can be utilized to validate computational models. There have been a few studies in which experiments on quay walls were conducted in the past. The behaviour of quay walls in earthquakes with dynamic centrifuge model tests was studied by (Zeng et al., 1993). Field tests and numerical analysis on the performance of anchored sheet pile quay walls with a separate pile-supported platform was studied by (Tan et al., 2018). The performance of caisson type of quay walls at the Kobe port was studied by (Inagaki et al., 1996). (Van Alboom et al., 2005) performed a geotechnical characterisation for an L-shaped quay wall in the harbour of Antwerp and monitored the quay wall during its construction. The outcomes were compared with finite element model (FEM) - and analytical model calculations. The stability of two historical gravity quay walls in Antwerp was demonstrated by (Bonte, 2020), by means of full-scale load test for which a finite element calculation clearly fell short. Expensive and time-consuming renovation works were thus avoided and part of the valuable historical heritage could be preserved with minimal intrusive restoration works. However, a study that analyses the lateral failure of quay wall foundations such as present in Amsterdam, by performing (full-scale) experiments, was not found in the literature.

5.1.3 Objective and approach

The primary objective in this study is to develop a calculation model of a quay wall with both high computation speed and accuracy, describing the lateral behaviour of historic quay walls in layered sloping soil. The proposed model is analytical and consists of an elastic beam framework embedded in an elastic foundation, externally loaded by an elastic soil model. A second, equally important objective is to conduct a full-scale proof load experiment on a historic quay wall in Amsterdam to investigate the lateral failure of the pile foundation. The results of this experiment will be used to validate the new analytical quay wall model developed in this study. The objective of this chapter is reflected in the following research question:

"How can the lateral failure of the pile foundation of historic quay walls be modelled and validated through testing? "

The chapter is outlined is discussed, of which a flowchart can be found in Figure 5.3. The analytical quay wall model, describing the lateral behaviour of historic quay walls in layered sloping soil, is explained in section 5.2. Accordingly, the methodology of the Overamstel quay wall experiments is provided in section 5.3. The results of the quay wall experiments are given in section 5.4, followed by an interpretation in section 5.5. In section 5.6, the quay wall model is calibrated and validated with the Overamstel quay experiments. Finally, the results are discussed and conclusions are drawn in section 5.7.

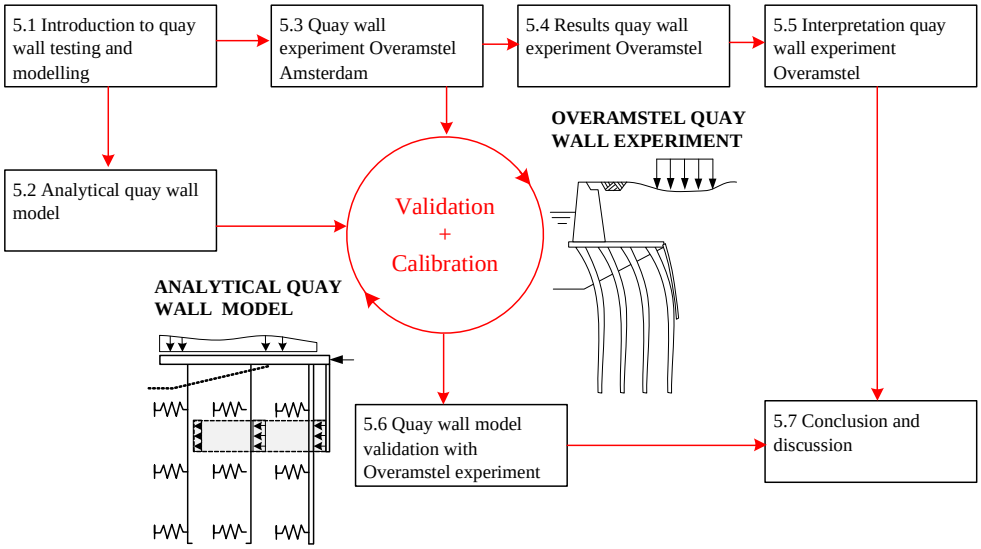

Figure 5.3, Flowchart on the outline of chapter 5.

5.2 Analytical quay wall model

This section discusses the analytical model of the quay wall, focusing on the "lateral failure of the timber pile foundation" failure mechanism. Lateral failure can be caused by either local geotechnical failure of the soil or the bending capacity of the piles, or a combination of both. Local geotechnical failure occurs when the soil's ultimate lateral resistance is insufficient to withstand the applied lateral load on the piles, resulting in significant deformations such as severe tilting of the piles. Bending capacity failure happens when the bending stresses in the piles exceed the strength of the timber ($\sigma_b >$ MOR), leading to pile breakage. The failure mechanisms are interconnected. Large deformations due to geotechnical failure can increase bending moments. Similarly, pile breakage can lead to increased loads on other piles, potentially exceeding the geotechnical capacity and causing severe deformations.

To accurately model the lateral failure of the quay wall, a comprehensive model was developed, taking both geotechnical and structural aspects in consideration. This model calculates local soil pressures acting on the piles and determines bending moments (with corresponding bending stresses), shear forces, displacements, and rotations of the different structural elements (headstocks and piles). The quay wall model was implemented in a MATLAB computer program which is open source and available for download at: https://doi.org/10.4121/4fd90d71-ffd9-4db2-a358-8576f5b19a32. A manual is included.

5.2.1 Elastic beam framework using bilinear spring approximation.

The proposed quay wall model in this chapter consists of a framework of elastic beams embedded in an elastic foundation (BEF) and is externally loaded by a soil model based on the theory of Flamant (1892). The frame model is made up of multiple Euler-Bernoulli flexural members, connected to each other by boundary and interface conditions, as depicted in Figure 5.4a. To model the lateral bearing pile-soil-pile interactions in layered sloping soil, the method developed in chapter 4 is used. The method proposed by the author has been successfully validated through experiments found in literature, as well as experiments

conducted on the timber quay wall foundation of a historic quay wall in Amsterdam Overamstel. This makes it an accurate and efficient tool for describing failure mechanisms of quay walls with regards to lateral pile behaviour, considering both structural and geotechnical aspects.

In this method, the *p-y* springs are described by an elastic-perfect-plastic approximation, presented in detail in Figure 5.4B. In a *p-y* curve, p[kN/m^2] is the soil reaction on the pile and y[m] is the corresponding relative pile-soil displacement. Each individual spring has its own *p-y* curve which is dependent on the soil properties, depth and pile dimensions. The gradient of the elastic branch is the modulus of horizontal subgrade reaction, indicated by k_h[kN/m^3]. This subgrade reaction is determined according to semi-empirical formulas derived by (Baguelin et al., 1972) in which correlations between geotechnical characteristics of the soil, including the pile dimension, and the Ménard-pressuremeter stiffness were found. These semi-empirical formulas to obtain the modulus of horizontal subgrade reaction per unit length pile can be found in appendix E.1. This subgrade reaction must be multiplied by the width of the pile D[m] in order to use it as a spring stiffness (k[kN/m^2] = k_hD) in BEF computations. The plastic limit is determined with the ultimate soil resistance theory of Brinch Hansen (Hansen, 1961) of which the mathematical expressions for earth pressure coefficients K_q and K_c are given in appendix G.2. To correct for the pile group interaction and the presence of a sloping surface, the plastic limit of individual *p-y* springs is corrected, which is indicated in Figure 5.4b with a red solid line. The correction is based on the reduction of the passive soil wedge due to the overlap of shear zones between neighbouring piles and the presence of a downward sloping surface. The reduction depends on the position of the pile in the group.

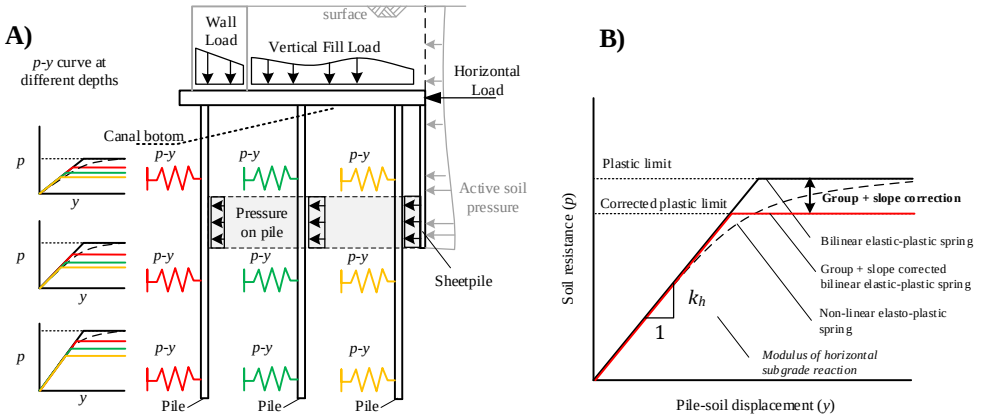

Figure 5.4, (a) Schematic diagram of the proposed BEF quay wall framework is shown. Piles are supported horizontally via *p-y* springs and the external loads by the gravity wall, soil fill and active soil body. (b) Detail of a *p-y* diagram is depicted, with a black dashed line representing a non-linear elastic-plastic *p-y* curve, a black line representing a bilinear *p-y* curve with plastic limit and a red line representing a bilinear elastic *p-y* curve with corrected plastic limit for group effects and slopes.

5.2.2 External forces on beam on elastic foundation framework

In Figure 5.5, a schematic cross-section is provided in which the forces acting on the BEF framework are indicated in red. The forces and their units are listed per unit of width.

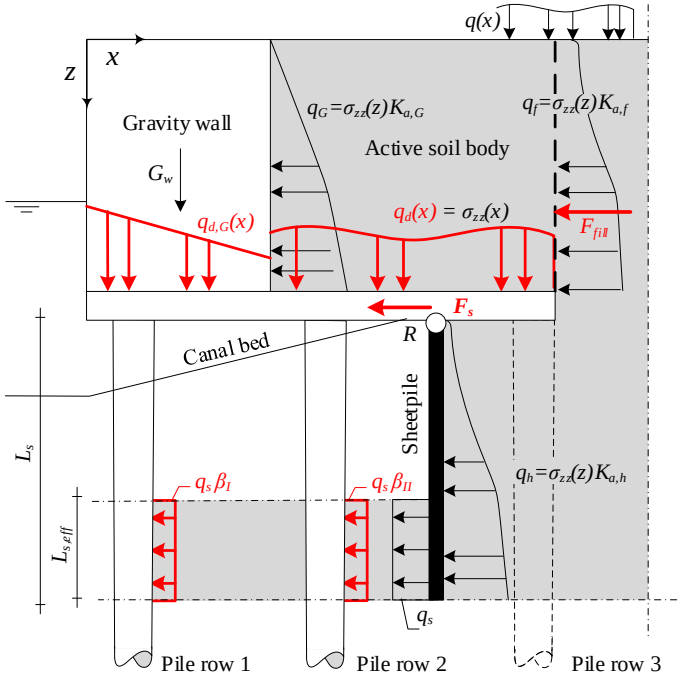

Figure 5.5, Schematic cross-section indicating external forces on the quay wall. Forces to be included in the BEF framework are indicated in red.

The quay wall foundation is subjected to both horizontal and vertical loads from the soil body located on and behind the quay, as well as imposed loads q[kN/m] caused by, for example, cars, trucks, people and goods. The soil body behind and on top of the quay wall is considered an active soil volume due to the lateral movement of the quay foundation and its gravity wall towards the canal. Horizontal effective soil stresses are obtained by multiplying the vertical effective stress σ_{zz}[kN/m] by their corresponding active soil pressure coefficient K_a. To determine the vertical effective soil stresses, a soil model is set-up which is described later on in this section. Formulas to evaluate the active soil pressure coefficients are evaluated in appendix H.1, according to (Coulomb, 1776).

First, the vertical loads on the quay wall floor are discussed. The linear distributed load $q_{d,G}$[kN/m] below the gravity wall is caused by the weight of the gravity wall G_w[kN] and the horizontal load q_G[kN/m]. A detailed analyses of $q_{d,G}$ below the gravity wall can be found in appendix H.4. The distributed load q_d[kN/m] on top of the floor behind the gravity wall is obtained from the vertical effective stress σ_{zz} on the floor surface just above the headstocks.

Second, the horizontal loads on the headstocks and piles are discussed. The top structure of the quay wall (i.e. the masonry wall itself), installed on top of the floor, is loaded by the resultant force F_{fill}[kN] which is derived by integrating the horizontal effective stress q_f[kN/m] along a vertical imaginary boundary located at the end of the floor. The lateral force F_{fill} is transferred through the soil and gravity wall to the headstocks, which in turn will transfer the horizontal loads to the piles. Below the floor, the sheet pile is horizontally loaded by a distributed load q_h[kN/m] as a consequence of the horizontal effective soil pressure. The distributed load q_h is transferred to the headstock F_s[kN] and to the pile group q_s[kN/m], with

the pressure of the sheet pile wall on the piles acting over the lower part of the embedded length $L_{s,eff}$[m], which is typically assumed to be 1/3 of the length of the sheet pile L_s[m]. Moment equilibrium at the top of the sheet pile wall (R) is used to calculate the ratio of load transfer towards the headstock and the pile group. The pressure of the sheet pile on the piles is distributed linearly over the pile rows, with a load fraction coefficient β_i per pile. It holds that $\sum_{i=1}^{n} \beta_i = 1$, with n the number of piles. Ultimately, all horizontal loads, whether from the sheet pile onto the headstock or from the sheet pile onto the piles, will act on the entire pile foundation.

In order to describe the effective vertical stresses σ_{zz} in the subsurface behind and above the quay, a soil model has been set up which includes Flamant's theory (Flamant, 1892). The theory of Flamant is the two-dimensional equivalent of the Boussinesq problem and describes the superposition of an infinite amount of point loads uniformly distributed perpendicular to a homogeneous, isotropic, linear-elastic half-space. The theory is used in many studies to describe surface settlements (Zhou et al., 2003), to make predictions of plane-strain/plane-stress (Georgiadis et al., 2008), or to determine static and dynamic pressures caused by waves on breakwaters (Hudson, 1953). Both for a point load and for a distributed line load, the vertical stress σ_{zz} can be determined at any location in the domain, as seen in Figure 5.6 and described by eq. 5.1 and eq. 5.2. In eq. 5.1, F[kN] is the point load and r[m] the distance towards the point of interest with gradient θ[rad]. In eq. 5.2, q[kN/m] is the line load with width $2a$[m] and gradients θ_1[rad] and θ_2[rad] with respect to the point of interest.

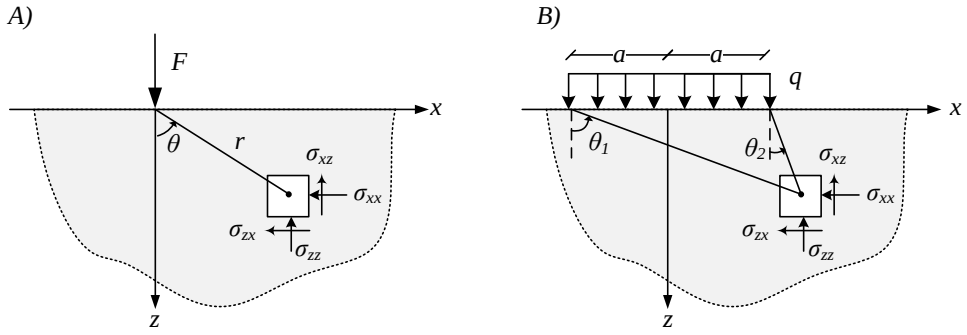

Figure 5.6, Problem of Flamant describing stresses in an homogeneous, isotropic, linear-elastic half-space for A) a point load and B) a distributed load line load.

$$\sigma_{zz} = \frac{2F}{\pi}\frac{z^3}{r^4} = \frac{2F}{\pi r}\cos^3\theta \qquad \textbf{eq. 5.1}$$

$$\sigma_{zz} = \frac{q}{\pi}[(\theta_1 - \theta_2) + \sin\theta_1\cos\theta_1 - + \sin\theta_2\cos\theta_2] \qquad \textbf{eq. 5.2}$$

The vertical stress in the half-space for an arbitrary line load $q(x)$[kN/m], can be obtained by discretizing the line load in point loads. The stress fields associated with each point load can be calculated independently using eq. 5.1, and then combined using the superposition principle. The Flamant theory is a useful tool for analysing the subsurface when no obstacles are present, as it allows for the free bearing of loads. However, when obstacles such as walls exist, caution must be taken in applying the theory. Solutions to include boundaries within a half-space are suggested by a number of researchers (Gorbunov-Posadov, 1972; Zirakashvili, 2020). An interesting application of the theory is the symmetry it offers in the case of two

point loads, as the shear stress σ_{xz}[kN/m] in the symmetry axis of the two point loads is equal to zero (Verruijt et al., 2005). This symmetry can be used to determine the influence of the gravity wall and timber sheet pile on the stress distribution within a soil domain, provided that the boundary conditions stipulate that the shear stress should be zero along the wall. To illustrate the application of Flamant's theory to a quay wall geometry, an example is provided in Figure 5.7. This example involves a 2m high gravity wall on a 3m long floor supported by 3 piles, with a sheet pile wall 1m behind the front of the gravity wall. At the active side of the quay wall the continuum is composed of soil with a unit weight of 1kN/m^2, and is subjected to a unit line load of 1kN/m over a width of 2m. The half-space is divided into two domains, above the floor and below the floor. For each domain, multiple vertical effective stress-fields are calculated and later summed together to obtain the total effective soil stress. The superposed stress-fields are explained and shown in appendix H.2. The total vertical effective soil stress resulting from a superposition of multiple stress-fields is shown in Figure 5.8. In the same figure four boundaries are indicated. Boundary I is used to compute q_G, boundary II to compute q_d, boundary III to compute q_f, and boundary IV to compute q_h. The effective soil stress is based on the assumption that the quay wall does not move and that the gravity wall and the sheet pile wall are both smooth and therefore unable to transmit shear stresses. Furthermore, it is assumed that the piles do not have any effect on the stresses within the half-space.

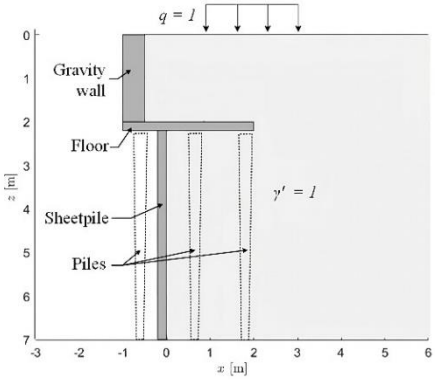

Figure 5.7, Schematic cross-section for illustrating the case of vertical stress distribution by Flamant's theory.

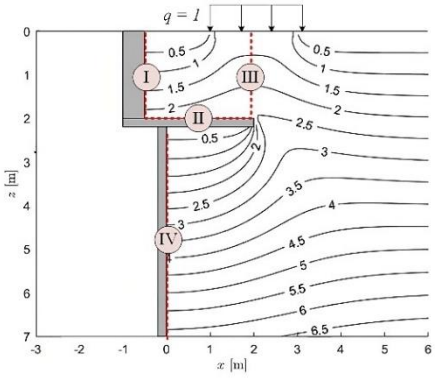

Figure 5.8, A schematic cross-section illustrating the vertical effective stress-field σ_{zz} resulting from superposition of multiple stress-fields.

5.2.3 Pile-headstock interface model

An aspect of modelling inner city quay walls is the interface between the headstock and the piles. The pile-headstock connection has a certain stiffness, which affects the strength of the entire pile foundation. The stiffer the pile-headstock connection, the better the structure can withstand horizontal and vertical loads. The stiffness of the connection also influences the way the pile group deforms, a very stiff connection results in double curvature of the piles and no stiffness in a single curvature. In Figure 5.9, a photograph below a quay wall, showing multiple pile-headstock connections, is shown. The headstocks are mounted directly on top of the pile heads with a pin-hole connection or a steel pin. In addition, it can also be seen that a number of pile heads are rotated underneath the headstocks. In Figure 5.10, a detail of the pin-hole in the headstock of the Grimburgwal is visible. The imprint that the pile head makes in the headstock around the hole can be clearly seen. The tape measure shows that the pin of the pile head must have been 10x10 cm with a head diameter of 20 cm.

Figure 5.9, Photograph of pile-headstock connections below a historic quay wall in Amsterdam (Maarschalkerweerd, 2022).

Figure 5.10, Headstock extracted from collapsed Grimburgwal with pin hole and pile imprint visible (Korff et al., 2021).

In Figure 5.11, a section view of a headstock supported by three piles is shown. Due to the load from the soil behind and on the quay wall, the pile foundation deflects towards the canal. The bending of the pile foundation is accompanied by a rotation φ[rad] in the pile heads. Due to the difference in rotation between pile head and headstock, asymmetrical stresses arise in the timber structural elements, shown in the figure with red. The resultant forces of these stresses form a moment in the head of each pile. Instead of speaking of a pile-headstock stiffness, it is better to speak of the moment that the pile-headstock connection can take. The pile cap moment is indicated by M_{rot}[kNm].

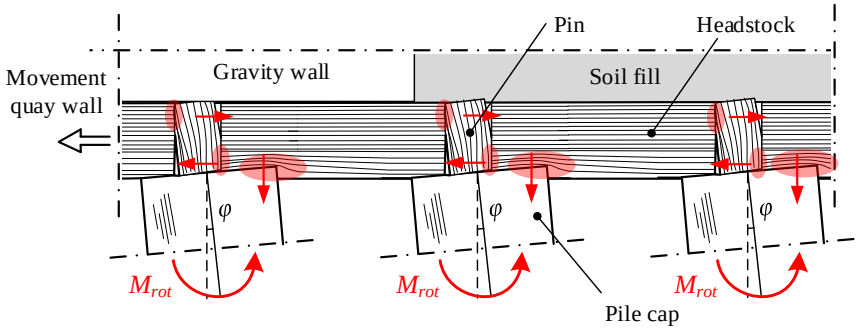

Figure 5.11, A cross-sectional view of a headstock supported by three piles is shown. Stresses and the corresponding resistance forces resulting from pile rotations are highlighted in red.

To determine the magnitude of M_{rot}, a model was set-up. The headstock-pile connection can be seen as a node where three rods come together. The node must be in moment equilibrium, vertical and horizontal force equilibrium. The force equilibrium of the headstock-pile connection is shown in Figure 5.12. In this figure, the pile has a diameter D[m], a headstock height h_d[m], headstock width w_d[m] and rotation difference between headstock and pile described by φ. The width and height of the pin are indicated by w_p[m] and h_p[m]. The bending moment left and right of the headstock connection are described $M_{d,l}$[kNm] and $M_{d,r}$[kNm]. The shear force left of the node is indicated by $V_{d,l}$[kN] and right of the node by $V_{d,r}$[kN]. $N_{d,l}$[kN] and $N_{d,r}$[kN] indicate the normal force in the headstock left and right of the node. In the pile head, the axial force is indicated with N_p[kN], the horizontal component of the shear force by V_p[kN] and the moment in the pile head by M_{rot}.

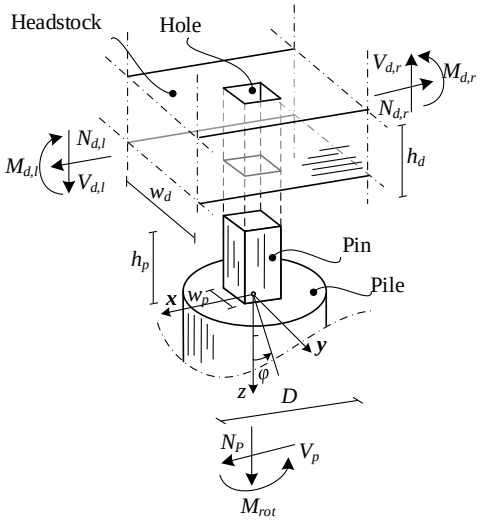

Figure 5.12, Schematic representation of the pile-headstock connection with the internal forces indicated.

The vertical stresses that arise between the headstock and the flat top of the pile must be in balance with the normal force N_p in the pile. The horizontal stresses that arise at the pile pin must balance the transverse force V_p exerted on the pile. Due to the eccentricity of the horizontal stresses in the pin relative to the horizontal axis of the flat top of the pile, a moment M_{pin}[kNm] develops. Due to the eccentricity of the stresses on the flat head of the pile relative to the vertical centre line of the pile, the moment M_e[kNm] arises. When added together, the total pile head moment is delivered, as seen in eq. 5.3. This equation is implicit, the normal force in the pile, the rotation of the pile head, and the transverse force on the pile head are all affected by the magnitude of the pile head moment. An iterative process is required when performing BEF computations.

$$M_{rot} = M_e(\varphi, N_p) + M_{pin}(\varphi, V_p) \qquad \textbf{eq. 5.3}$$

An extensive elaboration of expressions for M_e and M_{pin} can be found in appendix H.3. To demonstrate how the pile cap moment develops for various combinations of the normal force N_p, transverse force V_p and rotation φ, an example computation is carried out. The strength parameters in this case are based on the C20 class described in NEN-EN 338. Structural dimensions are determined based on the dimensions of the Overamstel quay wall and listed (together with the strength parameters) in Table 5.1. For a normal force of 10kN, 20kN, 30kN and 50kN respectively the pile cap moment M_{rot} is plotted as function of the pile cap rotation and the transverse force on the pile cap. The figure with 20kN normal force is discussed briefly. As rotation increases, the cap moment increases linearly with 450kNm/rad. At 0.01rad the cap moment becomes constant and the pile-headstock connection undergoes full plastic deformation. When the transverse force increases, the cap moment reduces roughly linearly. In real cases, the pile cap rotation and the transverse force are interdependent; as lateral forces increase, cap rotations increase as well. To illustrate this relationship, a white line is added that shows a linear dependency between the two parameters and serves as a representation of an arbitrary load trajectory. The load trajectory has a parabolic shape, indicating that an increase in transverse force could, at some point, cause a decrease in the

cap force moment. An increase in axial force results in a corresponding rise in the magnitude of the cap moment; however, the magnitude of this increase becomes smaller with higher axial loads, as there is hardly any distinction between the cap moment readings for the cases with 30 and 50 kN normal force. The gradient of the linear trajectory, which can be seen as a rotational spring stiffness, is slightly influenced by the change in axial force.

Table 5.1, Input parameters for computational example pile cap moment.

Variable	Description	Value	Unit
h_p	Height of the pin	0.20	m
D	Diameter of the pile head	0.26	m
w_p	Width of the pin	0.10	m
$f_{c;90;kesp\perp}$	Compressive strength headstock perpendicular	2.3	N/mm^2
$f_{c;90;pin\perp}$	Compressive strength pin perpendicular	2.3	N/mm^2
$f_{m;0;pin}$	Bending strength of the pin	22	N/mm^2
$E_{90;mean;keps\perp}$	Elastic modulus headstock perpendicular	320	N/mm^2
$E_{90;mean;pin\perp}$	Elastic modulus of the pin perpendicular	320	N/mm^2

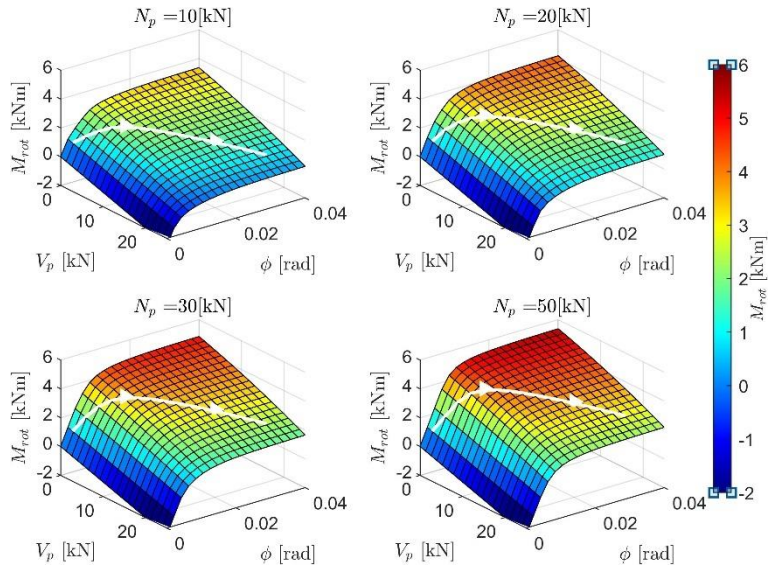

Figure 5.13, The pile cap moment M_{rot} is plotted as a function of pile cap rotation and transverse force on the pile cap in four figures. The axial force on the pile is varied in each figure, ranging from 10kN to 50kN.

Two topics should be emphasized. Firstly, in this model it is assumed that the pin takes all the transverse force of the pile. In reality, some of the transverse force is also taken up by the friction between the pile head and the headstock. An easy way to take this effect into account is to calculate the friction between the headstock and the pile head and subtract it from the transverse force V_p. The resulting horizontal force can then be used in the determination of M_{rot}. The more the pile will press into the headstock, the greater the friction between the pile head and the headstock, enhancing the stiffness of the overall connection. Secondly, as can be seen in Figure 5.9, the headstock and piles are often weathered. This deterioration affects

the headstock-pile connection stiffness. Care should be taken with the model input parameters in order to account for such effects. For example, an effective pile diameter can be applied in case of a significant soft shell. The pile-headstock model is validated with lateral pile group experiment F2 in section 4.7.

5.2.4 Analytical solution elastic beam framework

The timber foundation of the quay is described using a linear elastic framework of beams. The elastic beam framework is schematically represented in Figure 5.14. The headstock is described by elastic beam elements supported by the piles and is presented in eq. 5.4, with $i = 1,2..(m+1)$ where m represents the number of piles. In this equation, the vertical deflection of the headstock is given by w[m], the flexural stiffness of the members is given by EI_d [kNm^2] and the distributed load on the member is given by q_d [kN/m]. The bending of the piles is described by beams on an elastic Winkler foundation of which the general form is presented in eq. 5.5. In this equation, v[m] is the lateral deflection of the piles, EI [kNm^2] the flexural rigidity of the piles, N[kN] the axial load on the piles, z[m] the depth, $k = k_h D$ the stiffness of the elastic foundation, $q(z)$[kN/m] the depth dependent distributed load to describe fully plastified layers and q_s the pressure from the sheet pile on the piles. Furthermore, $j = 1,2..n$ where n is the number of unique soil layers of pile i. For example, if the subsoil around a pile consists of a sand layer and a clay layer that reaches the plastic limit, there are three unique soil layers. Please note that for each pile, the number of unique soil layers n can be different. The headstock is horizontally loaded by an active soil force F_h[kN]which is the sum of F_{fill} and F_s, described in section 5.2.2. The moment in the top of each pile is equal to pile cap moment M_{rot}.

$$EI_d \frac{d^4 w_i(x)}{dx^4} = q_{d,i}(x) \qquad i = 1,2..(m+1) \qquad \textbf{eq. 5.4}$$

$$EI_j \frac{d^4 v_{i,j}(z)}{dz^4} + N_j \frac{d^2 v_{i,j}(z)}{dz^2} + k_{i,j} v_{i,j}(z) = -q_{i,j}(z) + q_{s,j} \qquad \textbf{eq. 5.5}$$
$$i = 1,2..m \qquad j = 1,2..n$$

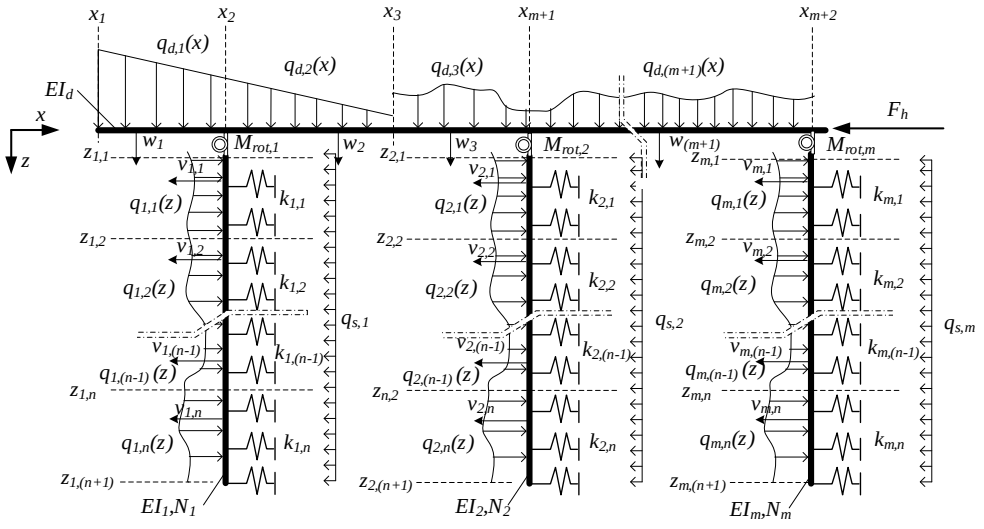

Figure 5.14, Schematic parameter overview elastic beam framework.

The top of the piles is indicated by $z_{m,1}$ and the tip of the piles is indicated by $z_{m,n+1}$. The depth at which interfaces between unique soil layers are present is indicated by $z_{m,2}$, $z_{m,3}$.. $z_{m,n}$. For the depth dependent distributed load *q(z)*, the corrected Brinch Hansen plastic spring limit is used, whose form is a third-order polynomial fit that can be found in eq. 5.6.

$$q_{i,j}(z) = a_{i,j}z^3 + b_{i,j}z^2 + c_{i,j}z + d_{i,j} \qquad i = 1,2..m \quad j = 1,2..n \qquad \textbf{eq. 5.6}$$

The polynomial function is chosen to the third order which makes it possible to find simple particular solutions in the form *q/k* for the general differential equation presented in eq. 5.5. With higher orders, particular solutions become more complex for this problem. The general solution to eq. 5.5, for each pile *j* and each unique soil layer *i*, is formulated in eq. 5.7. It should be noted that for an existent mathematical solution the axial pile force *N* needs to be smaller than $2\sqrt{kEI}$ and thus *k* needs to be given a non-zero value, even for fully plastified soil layers. The solution is written with natural exponential functions which gives computational advantages over trigonometric functions. For the headstock elements, the general solution can be found in eq. 5.8.

$$v_{i,j}(z) = C_{i,(4j-3)}e^{\frac{z\sqrt{\left(-\frac{\sqrt{{N_i}^2 - 4\,EI_i\,k_{i,j}}}{EI_i} - \frac{N_i}{EI_i}\right)}}{\sqrt{2}}} + C_{i,(4j-2)}e^{-\frac{z\sqrt{\left(-\frac{\sqrt{{N_i}^2 - 4\,EI_i\,k_{i,j}}}{EI_i} - \frac{N_i}{EI_i}\right)}}{\sqrt{2}}} + C_{i,(4j-1)}e^{\frac{z\sqrt{\left(\frac{\sqrt{{N_i}^2 - 4\,EI_i\,k_{i,j}}}{EI_i} - \frac{N_i}{EI_i}\right)}}{\sqrt{2}}} + C_{i,4j}e^{-\frac{z\sqrt{\left(\frac{\sqrt{{N_i}^2 - 4\,EI_i\,k_{i,j}}}{EI_i} - \frac{N_i}{EI_i}\right)}}{\sqrt{2}}} + \frac{6\,N_i\,a_{i,j}\,z}{{k_{i,j}}^2} + \frac{2\,N_i\,b_{i,j}}{{k_{i,j}}^2} - \frac{a_{i,j}z^3}{k_{i,j}} - \frac{b_{i,j}z^2}{k_{i,j}} - \frac{c_{i,j}z}{k_{i,j}} - \frac{d_{i,j}}{k_{i,j}} + \frac{q_{s,i}}{k_{i,j}}$$

$$i = 1,2..m\,;\; j = 1,2..n \qquad \textbf{eq. 5.7}$$

$$w_i(x) = C_{d,4i-3} + C_{d,4i-2}\,x + C_{d,4i-1}\,x^2 + C_{d,4i}\,x^3 + \frac{1}{EI_d}\iiint\int q_{d,i}(x)\,dxdxdxdx$$

$$i = 1,2..(m+1) \qquad \textbf{eq. 5.8}$$

In eq. 5.7 and eq. 5.8, *[C]* and *[C_d]* are the integration constants to be determined from the boundary and interface conditions between the various beam elements. A brief elaboration of the interface and boundary conditions can be found in appendix H.5. The general solutions described in eq. 5.4 and eq. 5.5 are substituted into the boundary and interface conditions which gives a linear system of equations. Solving the linear system returns the value of all integration constants [*C*] and [C_d]. Substituting the integration constants back into the general solutions results in the deflection distributions *v(z)* of all laterally loaded piles within the pile group and the deflection of headstock *w(x)* on top of the piles. By using the kinematic and constitutive relations for bending, the rotation φ, moment *M* and shear force *V* distributions can be obtained with eq. 5.9 for the headstock and eq. 5.10 for the piles.

$$\varphi_d = -\frac{dw(x)}{dx}, \quad M_d = -EI_d\frac{d^2w(x)}{dx^2}, V_d = -EI_d\frac{d^3w(x)}{dx^3} \qquad \textbf{eq. 5.9}$$

$$\varphi = -\frac{dv(z)}{dz}, \quad M = -EI\frac{d^2v(z)}{dz^2}, \quad V = -EI\frac{d^3v(z)}{dz^3} \qquad \textbf{eq. 5.10}$$

In practice it is not known in advance which soil layers develop full plasticity because this depends on the deflection of the piles, which is unknown prior to the calculation. Therefore, an iterative process is required in which equilibrium is sought between the lateral load on the headstock and the resistance that elastic and fully plastic soil layers cause. A flow chart of this iterative process is given in Figure 5.15.

First, a fully elastic computation without plastic *p-y* branch is performed which results in the displacement of the pile group. The cap moments are taken zero for the first computation. At each depth, the displacement is multiplied with its elastic spring stiffness to obtain the elastic pressures. For all piles, at each depth, plastic and elastic soil responses are identified. Accordingly, a new 'unique layering' distribution is made with elastic and plastic layers which is used for a new BEF computation. Besides the layering, the pile cap moments are computed based on the outcomes from the previous computation and used in the next computation. This iterative process is repeated until the layering distribution does not change or becomes repetitive. Since the thickness of each unique layer is chosen to be a multiple of the grid height *dz* fewer iteration steps are needed with larger grid size, which is elaborated in section 4.3.1. The downside of this is a decrease in modelling accuracy.

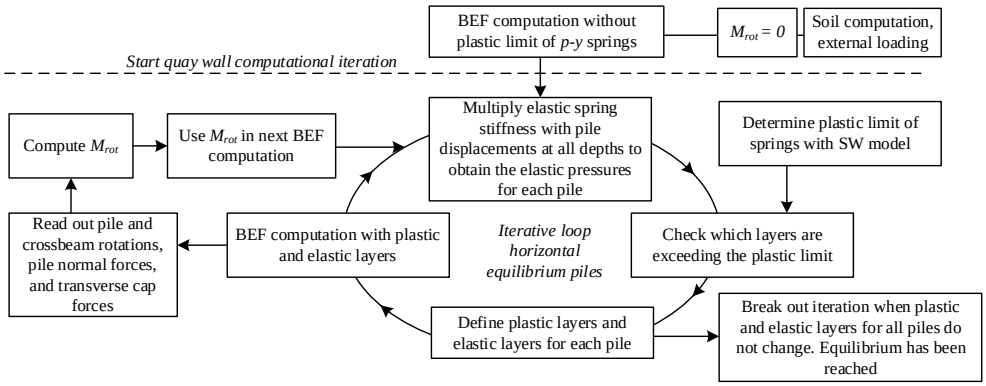

Figure 5.15, Flowchart of iterative solution to solve the non-linear coupled BEF framework problem.

5.2.5 Model limitations

This model has some limitations, the most important ones are shortly explained.

- The model does not take into account the overall stability of the quay but focuses only on the horizontal bending deformation of the timber pile foundation.
- The effective stress field of the soil body around the quay is not affected by displacements of the quay itself.
- The pile-headstock connection is idealized. The pin fits tightly in the hole and the pile head, pin and hole are 'intact'. In reality, these elements might be affected and biologically degraded.
- The piles have a constant diameter over their length, the tapering of the piles is not taken into account. The diameter is taken at the height of the maximum expected moment (+- 2 to 3 meters below the floor). See chapter 4.
- The model does not take into account time-dependent deformation of the timber and of the soil.

- Cyclic loads from past are not taken into account in the calculations. The unloading and reloading stiffness of the subsoil is not considered.
- Negative skin friction on pile foundations and on the sheet pile wall is not taken into account.

5.3 Quay wall experiment Overamstel Amsterdam

To test the lateral response of historic quay walls, a quay wall in Amsterdam Overamstel was proof loaded. Detailed information on the test site, structural and geotechnical information can be found in chapter 2. To accommodate multiple experiments on the 90m long continuous quay wall, a 'segmental approach' is adopted. This approach involves dividing the quay wall into several independent parts, allowing for separate testing and analysis. This segmental approach is chosen for two reasons: first, to simulate a two-dimensional quay wall failure and reduce any potential three-dimensional effects; second, to reduce uncertainty by experiment repetition by performing multiple experiments in which the quay wall geometry, loading, and geotechnical conditions can be varied. In total, five experiments were conducted on four quay wall segments, named A, B, C, and D. On segment A two experiments were carried out, first A.I followed by A.II. A photograph of the site during experiment A.I is presented in Figure 5.16. All segments are visible, progressing from front to back: A, B, C, and D. The segments are 6.5m in width and loaded by a ballast water container with footprint 2.7×6.0m. The loading, applied incrementally in loading steps, results in an increase in soil stress behind the quay wall, initiating lateral movement of the wall towards the water. The quay wall is monitored with an extensive program, detailed in section 5.3.2. The experiments are briefly summarized in Table 5.2. Apart from the modifications to segments C and D, and the deviating loading configuration of segment A.II, the setup of the segments is similar. The experimental setup will first be discussed for segment A.I followed by the other segments.

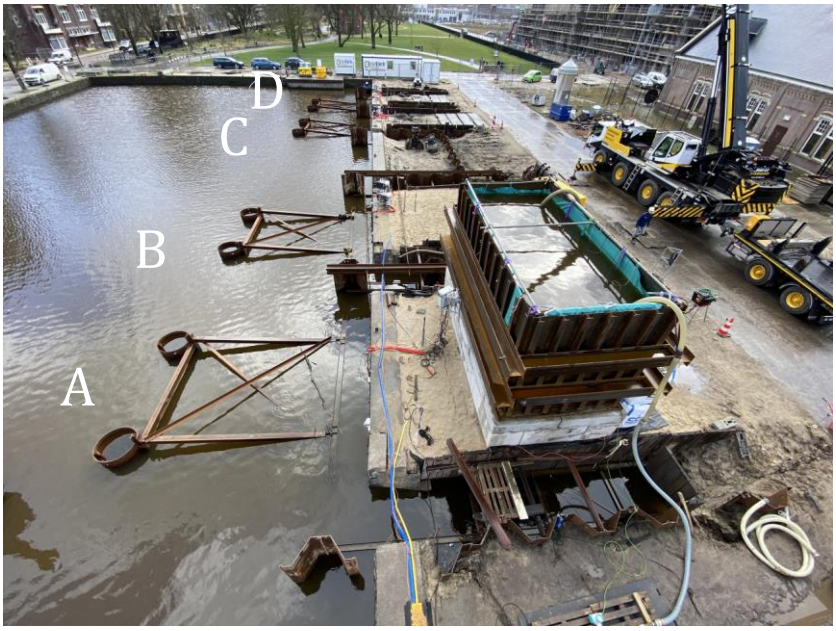

Figure 5.16, Overview photograph on quay wall experiment on segment A.I with maximal load.

Table 5.2, Overview of quay wall experiments.

Segment	Period	Loading steps	Load configuration	Modifications
Segment A.I	22-02-2022 25-02-2022	29	Load 2.7m behind waterfront	-
Segment A.II	24-03-2022 28-03-2022	29	Load 1.0m behind waterfront	Extra ballast added 4.85m behind waterfront at start of the experiment
Segment B	28-02-2022 04-03-2022	30	Load 2.7m behind waterfront	Extra instrumentation array to study three-dimensional effects.
Segment C	09-03-2022 16-03-2022	30	Load 2.7m behind waterfront	Quay wall weakened by removing pile row 2 and lowering canal bed around piles by dredging.
Segment D	17-03-2022 22-03-2022	33	Load 2.7m behind waterfront	Quay wall weakened by removing pile row 2 and lowering canal bed around piles by dredging.

5.3.1 Quay wall experimental set-up

The quay experiment set-up of A.I is presented in Figure 5.17 (a plan view) and Figure 5.18 (a cross-section view). The experiment took place on a 6.5m wide quay wall segment. To isolate it from its neighbouring sides, a bandsaw was used to cut through the gravity wall and timber foundation, as pictured in Figure 5.19A. A 1.8m wide trench was dug at the sides of the segment, ascending towards the back. The quay wall part crossing the trench was removed as pictured in Figure 5.19B. A 'sandwich' type of structure was used to compartmentalise the segment; it was bounded by azobé timber sheet piles (4×0.15×0.08m) and stabilized by struts that transfer their load to steel AZ12-700 sheet piles. Two layers of struts were used, at NAP-0.4m and at NAP-1.6m. The timber sheet piles are short and slender, enabling freedom of motion in the *y-z* plane. The sandwich structure reduced the soil resistance at the sides of the segment and most important, allowed the segment to move towards the water without losing support pressure at the sides. Diagonal extension bars were installed to prevent trench collapse at large displacements, which lock at a 100mm extension. On top of the segment, a compacted sand layer of 20cm was placed.

The quay wall is loaded by a ballast container, the bottom of which is hollow and containing an infill membrane providing uniform pressure on the surface behind the quay. The membrane is able to adopt to the soil surface which deforms during the experiment. The weight can be adjusted by adding or removing water from the water basin. The empty weight of the container is 11.15tonnes and has a height of 3m. The maximal pressure that can be reached with the water basin is 30kN/m^2 with a footprint of 2.7×6.0m. After a load step with a full container, the container is emptied and placed on a gravel fill bounded by concrete LEGIO blocks. The gravel ensures a more or less uniform pressure on the soil surface, while the LEGIO blocks provide stability. The weight of the gravel and LEGIO blocks is almost equal to the weight of a fully filled water basin, and the container now has a footprint of 3.2×6.4m. The full container and the LEGIO blocks, as shown in Figure 5.18, have a combined weight of 115.66 tonnes, which corresponds to a maximum pressure of 56.5kN/m^2. This weight is composed of 11.15 tonnes from the container, 48.6 tonnes from the water basin, and 55.91 tonnes from the LEGIO blocks and gravel.

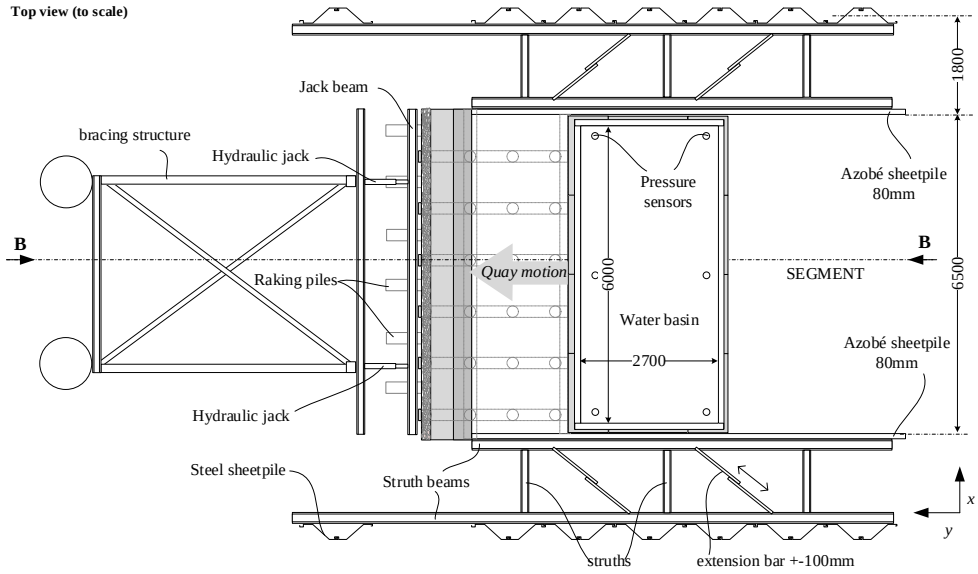

Figure 5.17, Planview of quay wall experiment for segment A.I.

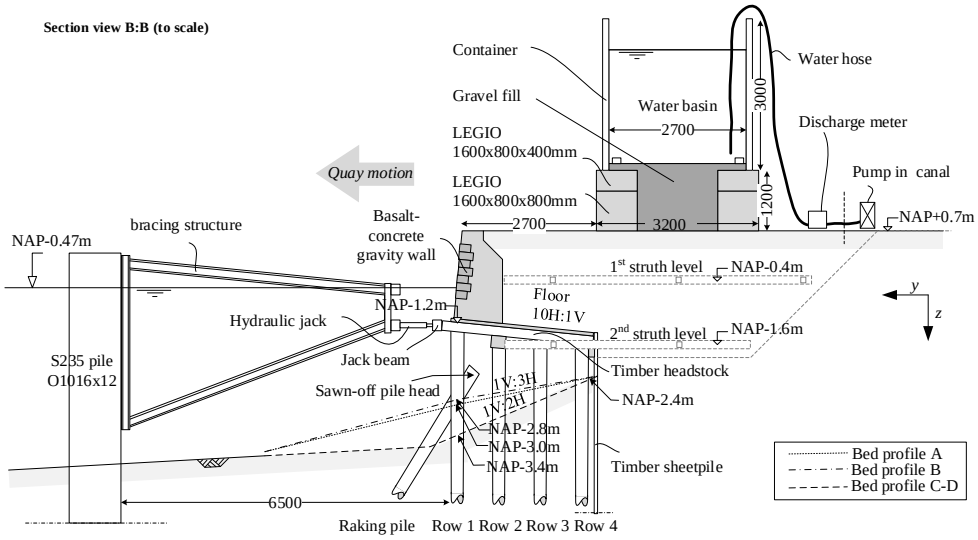

Figure 5.18, Section view B:B of quay wall experiment for segment A.I.

Figure 5.19A, Cutting through the gravity wall and timber foundation with a bandsaw to decouple segment from sides.

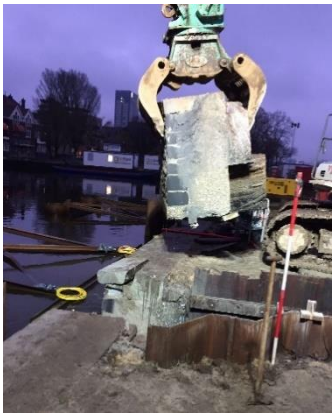

Figure 5.19B, Part of the gravity wall removed after sawing.

Figure 5.19, Isolating the segment from its sides by A) band sawing and B) removal of quay elements.

The amount of water pumped into the container is monitored using a discharge meter. As an extra check on the amount of water and any subsidence in the ground, 6 pressure sensors have been placed in the container. These 6 sensors are ballasted so that they do not move to a different location during the filling of the container. The configuration of the pressure sensors is visualized in the top view. Located 0.7m away from the quay wall segment, a bracing structure is present that provides two key functions. Firstly, it helps protect both people and equipment in the event of a collapse. Secondly, it is used to fixate the quay wall during construction work or installation procedures, such as sawing piles, dredging activities, or installing monitoring equipment. During the experiment preparation, the segment was secured in place using hydraulic jacks and a jack-beam, which is pressed against the headstocks of the quay wall with 30kN/m along the segment. As part of the preparation, the raking piles were intentionally disabled by sawing away 0.5m pile to replicate the historic quay walls found in Amsterdam city centre, where only vertical piles are used. After the quay modifications and installations, the jacks and beam were removed **as part of the experimental start**, creating a 0.7m gap between the quay and the bracing structure, allowing for unhindered quay movement towards the waterfront.

The experiments on segment A.II, B, C and D deviate from experiment A.I in the following way.

- A.II: This experiment, which follows after experiment A.I, aims to study the effect of a load on top of the quay wall that has already experienced considerable out-of-plane deflection. To this end, the ballast container is placed 1.0m from the waterfront, directly behind the gravity wall and loaded similar to experiment A.I. Before the experiment begins, an additional ballast of 58 tons is placed directly behind the container, 4.85m from the waterfront (see Figure 5.20). This extra ballast has a footprint of 2.8x6.4m and creates a load situation similar to the one achieved at the end of experiment A.I.
- B: This experiment is identical to experiment A.I, except for the addition of an extra monitoring array to observe three-dimensional effects. Section 5.3.2 provides a brief explanation of the monitoring instrumentation.

- C: This experiment has two main differences compared to experiment A.I. First: the quay wall is weakened by removing the entire second pile row. Second: the lateral bearing capacity of the piles is reduced by lowering the canal bed in front and between the piles.
- D: This experiment is identical to experiment C. Furthermore, an additional vertical cased inclination sensor was positioned 1m from the side to analyse three-dimensional soil effects.

Another essential difference between the segments A-D is the composition of the subsurface at the back side (behind the quay's sheet pile) of the quay wall. From segment A to D, there is a steadily increasing layer of sand that provides greater stability and support to the ballast container. This thicker layer of sand behind the quay results in a stiffer response, and smaller deflections. Detailed information on the subsurface conditions for the various segments is provided in chapter 2. The canal bed profiles for each segment can be found in Figure 5.18.

Figure 5.20, Extra ballast behind container in experiment A.II.

5.3.2 Instrumentation

The quay wall segment was instrumented to measure the cross-sectional motion of the quay wall, including the surrounding soil body, and water pressures in specified layers. The layout of the instrumentation for a single segment is visualized in Figure 5.21, with figure A representing the top view and figure B showing the cross-section view. For segments A, C, and D, the sensors have been installed in a measuring array at the centre of each segment. An additional array has been placed 1m from the side of segment B in order to study the three-dimensional effects. Ultimately, the outcomes of the individual instruments are combined to contribute to comprehensive understanding of the motion of all structural quay wall elements and the soil surrounding them. The various sensors, along with their distinct functions and interconnections, are explored in detail, starting with the sensors attached to the structure.

To keep track of the top of the gravity wall, each segment is equipped with five equally spaced **Prisms** that measure the *x,y* and *z* coordinate. The prisms are constantly monitored by a RTS (Robotic Total Station) once every 2 minutes.

An aluminium bar is installed on the front of the gravity wall. This bar is then fitted with a **tilt sensor** that measures the rotation in *x,y* and *z* direction. By this solution, we measure not the individual deformation of a part of the quay wall, but the actual rotation over the entire height. By combining the absolute measurement of the RTS with the rotation of the tilt sensors, the bottom of the gravity wall (below water level) can be determined. The tilt

sensors have a accuracy of 0.0001deg. Each segment is equipped with one tilt sensor, while segment B has two.

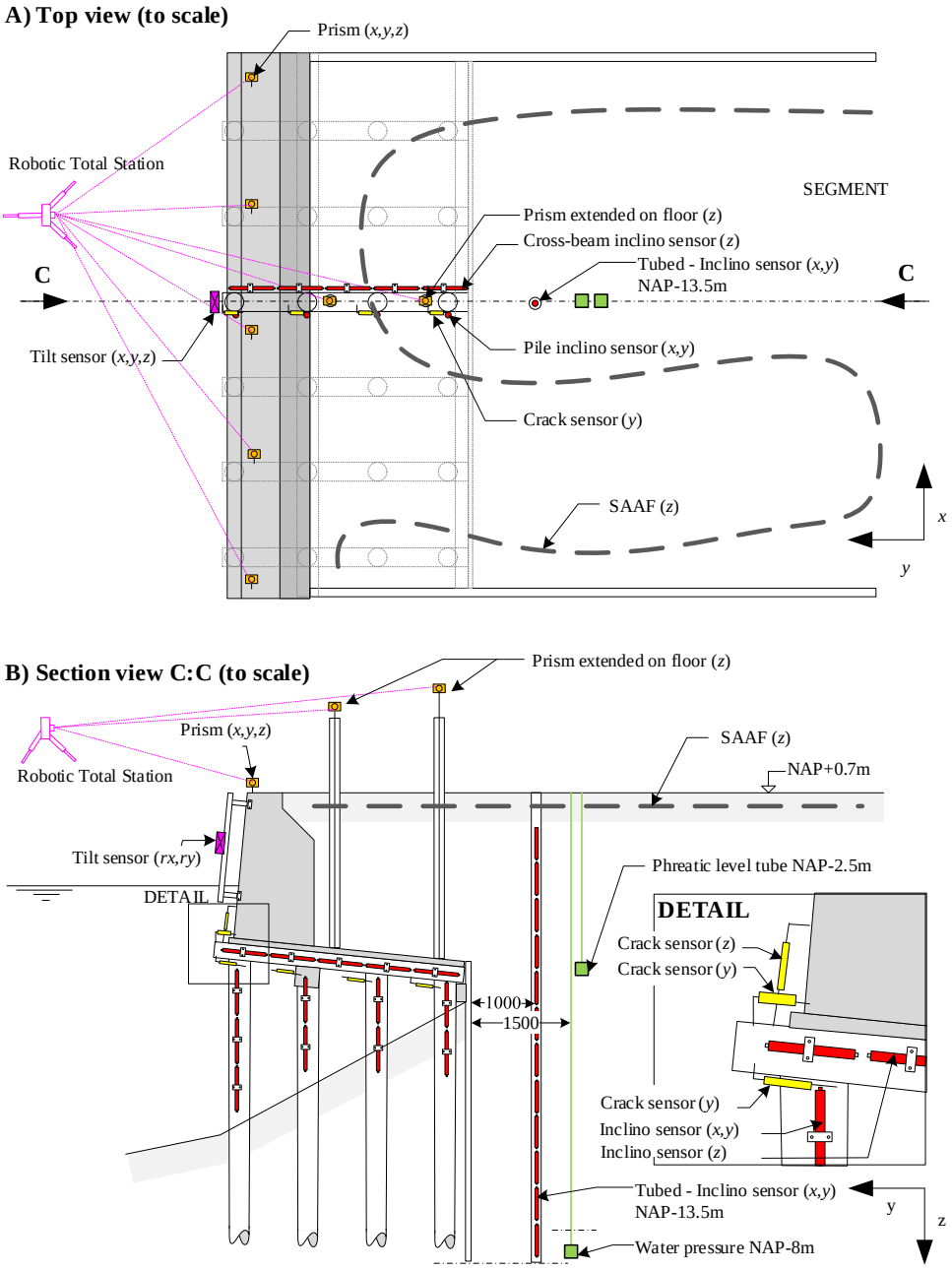

Figure 5.21, Instrumentation quay wall experiment for a single segment. A) Top view on quay wall segmental instrumentation. B) Cross-section view on quay wall segmental instrumentation.

Next, we want to detect if the gravity wall slides over the headstock or that there is space between the gravity wall and the headstock. For this reason, two vibrating wire **crack meter sensors** have been placed in both the *y* and *z* direction. A detailed visualization is present in Figure 5.21B. In addition to the gravity wall-headstock relationship, the pile-headstock link must also be established to evaluate if the piles have detached or shifted in relation to the headstock. Therefore, crack sensors were positioned between each pile and headstock, parallel to the y-axis. This principle was implemented to all piles in the measuring array. The accuracy of the crack sensors is 0.2mm.

Top loading influences the bending of the headstock and thus potentially push the piles further into the ground. The movement and bending of the headstock is measured with IPI (**In-Place-Inclinometers**) that have an accuracy of 0.1deg. By using a sequence of five sensors, the actual displacement of the beam can be determined in the *y*-*z* plane. As a backup, two settlement gauges have been placed on the floor to register the settlement of the headstock. The settlement gauges are connected to prisms that are monitored by the RTS. Depending on the available space, IPI systems have been installed on the positive *x*-side of the piles to measure their deformation. The IPI measuring systems have been attached to the four piles with specially developed brackets and pile clamps. Generally, three IPI sensors are attached to the front pile and two IPI sensors to the rear pile rows as indicated in Figure 5.21B.

Next, monitoring instruments in the soil are discussed. The horizontal soil deformation (in the *x*-*y* plane) 1m behind the quay wall sheet pile is monitored by an array of IPI sensors which is installed in an **inclinometer casing**. The inclinometer casing is vertically installed by pulse drilling of 180mm diameter. The space between the ground and the casing is filled with gravel at the sand layers and with clay at the clay/peat layers. For segment B and D, an additional vertical cased inclination sensor was positioned 1m from the side to analyse three-dimensional soil effects.

During the test, the settlement of the surface level (at NAP+0.6) was continuously monitored using a **SAAF** (Shape Accel Array Field). This consists of a chain of mutually hinged sensors, each containing a multi-axial MEMS accelerometer that measures the slope in the *x* and *y* direction. The accuracy is 1mm. The SAAF was laid out in an S-shape to obtain the vertical deformation of the test field at various locations.

In each segment, one water pressure sensor (WPS) has been installed at NAP-8m and one phreatic level tube sensor (PS) has been installed at NAP-2.5m. Additionally, one WPS at NAP-5.5m was placed in segment C. The water level inside the canal was constantly monitored and stable at NAP-0.47m.

5.3.3 Test procedure

In this section, the test procedure is discussed. For illustrative purpose, the timeline and load procedure of experiment A.I is presented in Figure 5.22. The quay wall experiments are force controlled and their loading steps are listed in Table 5.3. The term LBG stands for LEGIO Blocks with Gravel. Key loading steps in Figure 5.22 are indicated in yellow, corresponding to loading steps indicated in Table 5.3. Before beginning the test, the empty container is placed on a stabilized quay wall section. The experiment starts by systematically decreasing the pressure in the jacks, resulting in the quays fixation to be removed. This force reduction occurs in two sequential steps, with the first step being a decrease of 20 kN/m, followed by an additional decrease of 10 kN/m. Following this, the jacks and the jack-beam are removed and the bracing structure is prepared with a 0.7m gap between bracing structure and quay wall. At this stage, the quay wall is expected to move towards the waterfront, since the

horizontal supporting raking piles have been disabled. From this point onwards, the water basin in the container is filled in increments of 0.3m water column. After taking 10 steps, the container is full. After emptying, the container is removed and a structure of LEGIO blocks and gravel is installed gradually. First, 0.80m high LEGIO blocks are placed in a ring shape, then 0.8m of gravel is placed, followed by 0.40m high LEGIO blocks. Next, the container is put in place and 0.45m of gravel is filled. Finally, the water sack is placed. From this point, the water basin in the container is filled in 0.15m increments. When it reaches step 30, the container is full and has reached its maximum load capacity. The duration of each individual step depends on the time it takes for the quay wall to reach a state of equilibrium with the applied load. The system is considered to be in equilibrium when the lateral deflection of the quay wall remains below 1mm for a period of 15 minutes. For experiment A.I and B, rapid loading was performed on the quay wall after step 30 was completed. The container was emptied and filled at the maximum pumping rate until full. Extra big-backs with gravel (13,5 tons) were placed at the back side of the container. The load procedure timeseries for segment A.II, B, C and D, likewise Figure 5.22, can be found in Appendix D.1.1.

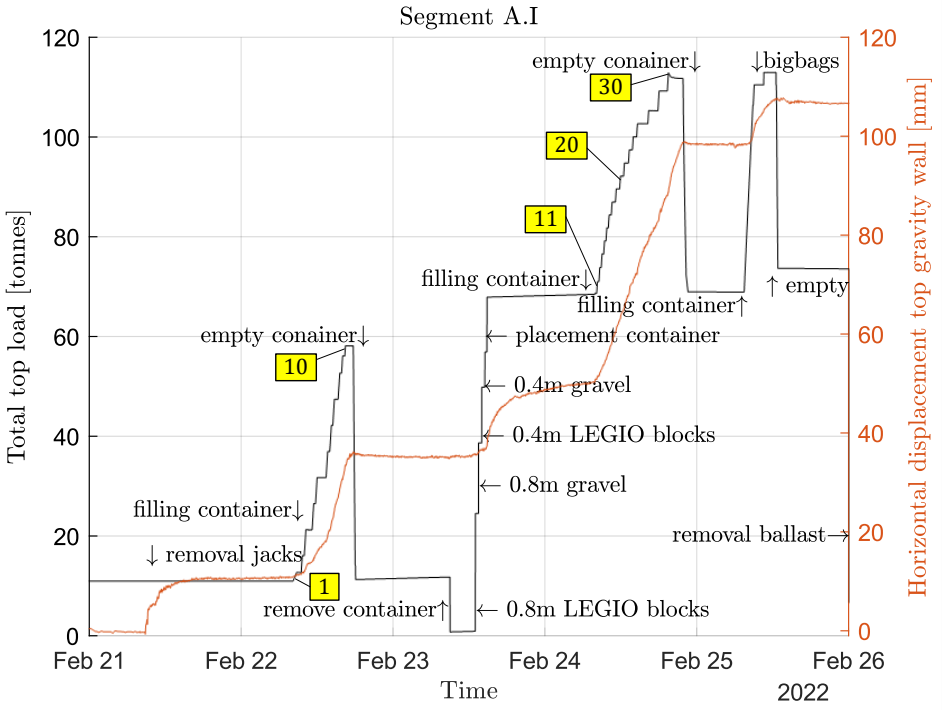

Figure 5.22, Timeseries of quay wall experiment A.I. The left axis presents the load applied on the quay and the right axis presents the corresponding quay displacement (in orange). Descriptions of important handlings are provided in the figure. Key loading steps are indicated in yellow, corresponding to steps in Table 5.3.

Table 5.3, Loading steps for quay wall experiments A.I, A.II, B, C and D. LBG stands for LEGIO Blocks with Gravel.

Step [#]	Water level [m]	Step [#]	Water level [mm]	Step [#]	Water level [mm]
1	0.3	11	0.15 + LBG	21	1.65 + LBG
2	0.6	12	0.30 + LBG	22	1.80 + LBG
3	0.9	13	0.45 + LBG	23	1.95 + LBG
4	1.2	14	0.60 + LBG	24	2.10 + LBG
5	1.5	15	0.75 + LBG	25	2.25 + LBG
6	1.8	16	0.90 + LBG	26	2.40 + LBG
7	2.1	17	1.05 + LBG	27	2.55 + LBG
8	2.4	18	1.20 + LBG	28	2.70 + LBG
9	2.7	19	1.35 + LBG	29	2.85 + LBG
10	3.0	20	1.50 + LBG	30	3.00 + LBG

5.4 Results quay wall experiment Overamstel

5.4.1 Cross-sectional deformation of the quay wall

The cross-sectional deformation of the quay wall segments and their surrounding soil bodies are presented for experiments A.I, B, C and D in Figure 5.23. The deformations, exaggerated by a factor of 8, are plotted for five different load steps, corresponding to a surface pressure of 0kN/m^2, 18.5kN/m^2, 37.0kN/m^2, 46.9kN/m^2 and 53.7kN/m^2. To determine the actual deformations, one square is equal to 0.125m. For segment B, two measuring arrays are displayed. The monitoring array in the middle is plotted with solid lines, while the array located 1m from the segment boundary is plotted with dashed lines. The quay wall segments respond to the imposed load in a similar way as the failure mechanism 'lateral failure of the quay wall foundation', visualized in Figure 5.2. The deflection towards the canal is accompanied by the bending of the timber piles, the settlement of the surface and a horizontal displacement of the soil body. Segment D exhibits the stiffest response, followed by segment C, then segment B, and lastly segment A.I. The pile-headstock connections remained intact throughout the experiments, yet there was a slight lateral flexibility in the connection. The crack sensors between the pile caps and the headstock revealed an average elongation of 5mm, with outliers of up to 15mm throughout loading, indicating that the headstock had experienced minimal sliding over the pile caps.

Furthermore, the headstock exhibited vertical settlements, with larger settlements of 0-5mm observed at the rear of the headstock compared to the front, where settlements ranged from 0-2.5mm. Segment C exhibited a significantly greater settlement of 12.5mm at the rear side compared to segments A.I, B, and D. The monitoring data is inconclusive as to whether this differential settlement is due to pile settlement or the compression of the pile-headstock connection.

No significant change in water pressures was found during all experiments at levels NAP-2.5m, NAP-5.5m and NAP-8m. Figures containing the water pressures during loading can be found in appendix D.1.4.

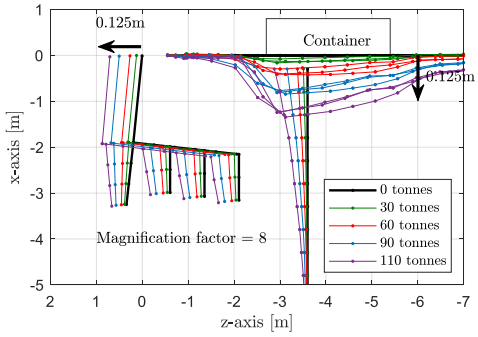

Figure 5.23A, Cross-sectional deformation A.I.

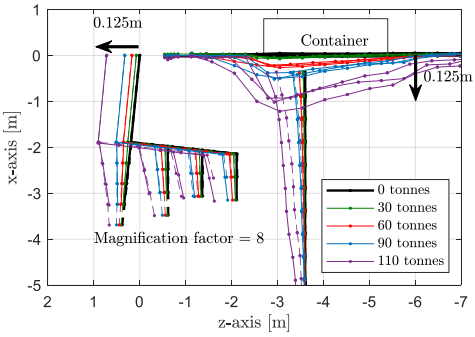

Figure 5.23B, Cross-sectional deformation B.

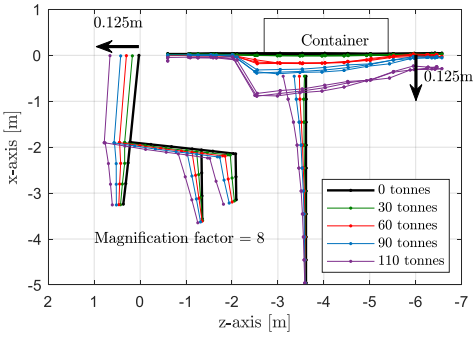

Figure 5.23C, Cross-sectional deformation C.

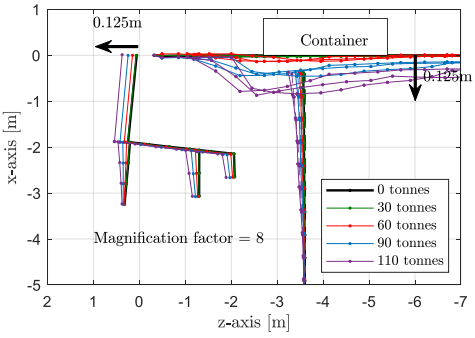

Figure 5.23D, Cross-sectional deformation D.

Figure 5.23, Cross-sectional deformation reconstructed from monitoring for segment A.I,B,C and D. The deformations are exaggerated by a factor of 8.

5.4.2 Rotation and sliding gravity wall

For segment A.I, B and D, the horizontal displacement caused by rotation of the gravity wall was less than 3% of the overall lateral deflection of the gravity wall. For segment C and A.II, this percentage was higher, namely 10%. Rotations as function of the lateral deflection of the pile foundation can be found in Figure 5.24 in which rotations in the clockwise direction are considered to be positive. Segment A.II experienced significant sliding of the gravity wall at the final loading step of 110 tonnes, as evidenced by the cross-sectional deformation presented in Figure 5.25. In this figure, “110 tonnes 1*” indicates the moment when 110 tonnes of load is applied to the quay wall surface, and “110 tonnes 2*” is the same loading step, but three days later. Directly after applying 110 tonnes, the lateral deflection of the pile foundation was 147mm, and over a three-day period, the gravity wall slid more than 40 mm towards the water, accompanied by large surface settlements (up to 375 mm) and headstock settlements (up to 20 mm). During this three-day period, the pile foundation hardly moved. No sliding of the gravity wall was observed in the other segments.

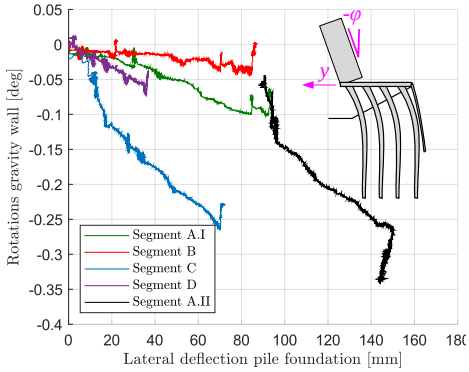

Figure 5.24, Rotation of the gravity wall as function of the lateral deflection of the pile foundation.

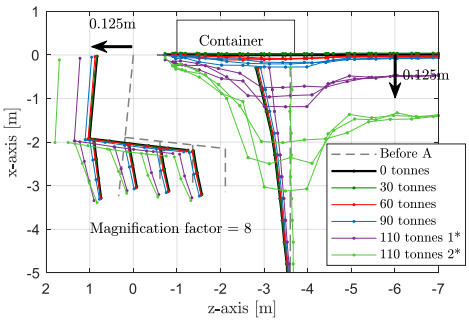

Figure 5.25, Cross-sectional deformation A.II.

5

5.4.3 Lateral movement pile foundation

The surface pressure versus average lateral pile group deflection for all five experiments is presented in Figure 5.26. After the prestressing was removed, the quay wall foundation started to deflect towards the canal, with values of A.I = 9mm, B = 7mm, C = 13mm and D = 3mm. During the experiments, no pile breakage was observed within the monitoring arrays. Experiment A.I had the largest pile deflection of 93mm, and this deflection was increased to 147mm in experiment A.II. Experiment B exhibited a max deflection of 85mm, experiment C a deflection of 70mm, and experiment D a deflection of 37mm. For larger loads, the force displacement curves flattens. For quay wall segment A.I and B a continuous deflection of 20-30mm is observed without the addition of extra load, indicating that the quay wall is near a progressive failure. Segment A.II has a very steep curve up to 40kPa. Approaching a maximum load of 55kPa, the curve flattens rapidly followed by an increase in deflection of 20mm without the addition of extra load, indicating the preliminary stage of failing.

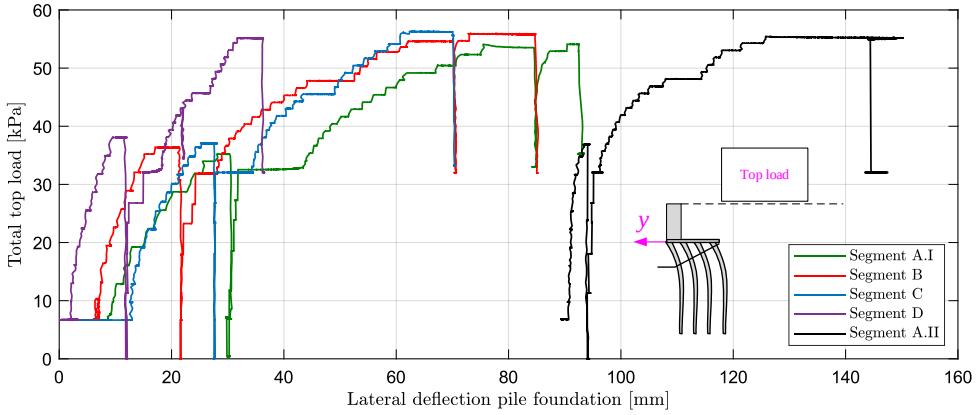

Figure 5.26, Top load versus average group deflection graph for all experiments.

The pile cap rotations, as function of the lateral pile group deflection, are presented in Figure 5.27. The steepest gradients are found for segment segments C and D, followed by segment B and eventually A.I-A.II. The higher the gradient, the larger the rotation of the pile caps for equivalent deflections, indicating a shallow clamping depth of the pile group relative to pile groups with mild gradients. This finding is remarkable since the canal bottom of segment C and D is 0.5-1m deeper than of segment A and B.

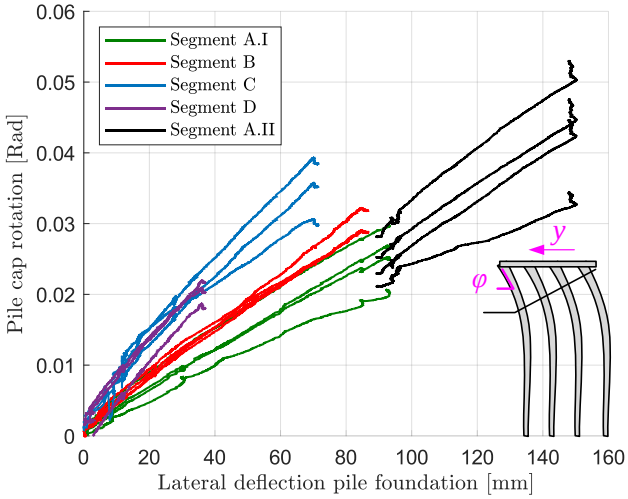

Figure 5.27, Pile cap rotation versus average lateral pile group deflection.

5.4.4 Soil deformations behind the quay wall

A brief analysis of the soil deformation behind the quay wall segments was performed. As seen in Figure 5.28, the soil settlement at the surface level of the quay wall segment A.I increases with increasing surface loading. The settlements are greatest at the front of the container, decreasing towards the hinterland of the quay wall, causing a anti clockwise tilting of the container. Similar effects are observed for the other segments (B, C and D), the settlement plots of which can be found in appendix D.1.2. For segment A.II, a different settlement profile was observed, where the front of the container experienced minimal settlement while the back side of the container had the greatest settlement, causing a clockwise tilting of the container. Minor settlements at the front of the container are likely due to the quay wall floor providing vertical support. Settlement plots of A.II can be found in appendix D.1.2. The settlement behind the quay segments (A.I, B, C and D) is compared to the lateral deflection of the pile group in Figure 5.29, in which the vertical settlement at various locations with respect to the loading container is plotted versus the lateral pile group deflection at pile cap level. A.II is left out due to its alternating loading configuration. A 1:1 ratio line is provided in grey. On average, the vertical settlement at the front of the container is approximately 1.5 times larger than the lateral pile group deflection, while at the back side of the containers, the vertical settlement is approximately equal to the lateral pile group deflection. Settlements are less than half of the lateral pile group deflection at 2m behind the container.

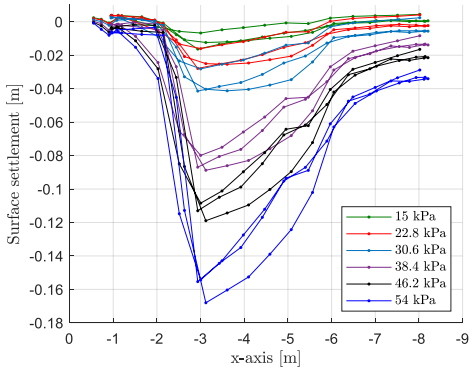

Figure 5.28, Soil surface settlement A.I for multiple surface loads.

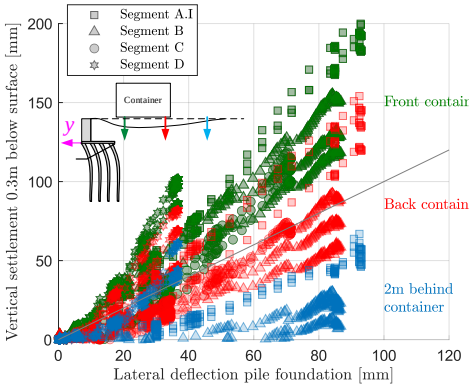

Figure 5.29, Lateral pile group deflection (at cap level) versus vertical settlement at various locations with respect to loading container.

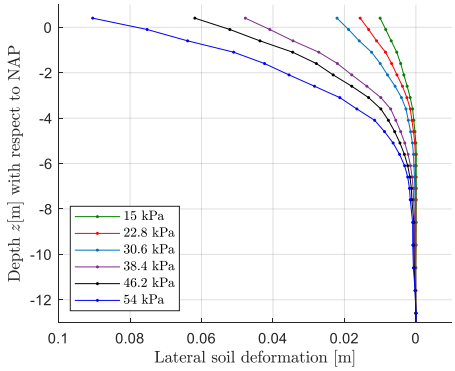

Figure 5.30, Lateral soil deformation 1m behind quay A.I for multiple surface loads.

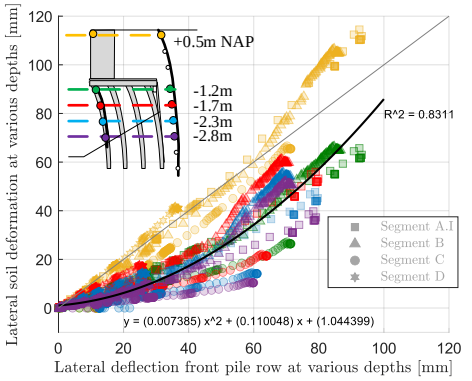

Figure 5.31, Lateral pile group deflection versus lateral soil deformation at various depths. Segments A.I, B,C and D are included. Fit is provided (+0.5m level is not included).

Analysis of lateral soil deformation (obtained with vertical cased inclination sensors 1m behind the quay floor) in response to surface loads was conducted, as seen in Figure 5.30. The lateral soil deformation behind quay wall segment A.I increased progressively, with no soil movement present below NAP-8m. Similar observations were made in the other segments, with no soil movement being detected below NAP-7m (B), NAP-6m (C), and NAP-5m (D). Segment A.II however, exhibited a different behaviour, with the soil being pushed land inward due to the container placed close to the waterfront. No soil movement was observed for this experiment below NAP-5m. Additional figures for the other segments can be found in the appendix D.1.3. The relation between the horizontal soil deformation and the lateral deflection of the first pile row is illustrated in Figure 5.31. The front pile deflection was plotted against the horizontal soil deformation. Four depths (NAP-1.2m, NAP-1.7m, NAP-2.3m and NAP-2.8m) were studied. A squared correlation of 0.83 was found between the two variables. The lateral pile deformations were greater than the horizontal soil deformation behind the quay at similar depths, and the soil deformation increased

exponentially with increasing pile deflections. To demonstrate this, a second order trendline was provided. Furthermore, the soil deformation at NAP+0.5m (close to the surface) was plotted against the deflection of the wall at that same height, and the ratio between wall deformation and the horizontal soil deformation at the surface was almost equal to one.

5.4.5 Three-dimensional effects and segmental friction

In this section, the three-dimensional effects that arose during the experiments are discussed. A horizontal plane evaluation of the orientation of the gravity wall was conducted. It was monitored that neither the neighbouring segments nor the steel sheet piles moved during the executing of the segment. The 6.5m long gravity wall, constructed from reinforced concrete, acted as a rigid and stiff beam and no fractures or cracks were observed. In the *xy*-plane, segment B and D experienced a rotation of less than $5 \cdot 10^{-4}$ rad, resulting in an absolute difference in deflection of 3mm between the left and right sides of the wall. This suggests the wall moved nearly parallel to the waterfront. Segments A.I and D exhibited rotations up to $2.53 \cdot 10^{-3}$rad and $3 \cdot 10^{-3}$rad in the clockwise direction, resulting in an absolute difference between the two sides of 20mm. During experiment A.II, the wall rotation increased to almost $1 \cdot 10^{-2}$rad, causing an absolute difference of 60mm between the two sides; this value was approximately 30% of the wall's total average deflection of 210mm.

For segment B, two measuring arrays were installed to investigate three-dimensional effects within the segment. One array was placed in the centre and the other array was located 1m from the side of the segment. Negligible differences were observed between the two measuring arrays attached to the quay foundation for segment B, demonstrating that this quay segment deflected as one towards the waterfront (see Figure 5.23B). For segment D (likewise segment B), an additional vertical cased inclination sensor was positioned 1m from the side to analyse three-dimensional soil effects. Cased inclination measurements behind the quay for segments B and D revealed that horizontal soil movement behind the quay sheet pile was 10-20% larger in the centre than at the sides. Soil measurements for segment B can be found in Figure D.9 of Appendix D.1.3, while those for segment D can be seen in Figure D.11. Smaller soil deformations at the sides of the segment compared to deformations in the centre of the segment are an indication for friction between the segment and its boundaries.

5.4.6 Recap on results quay wall experiments

The following are the key findings from the Overamstel quay wall experiments:

- Application of a surface load behind the quay wall results in lateral deflection towards the water and bending of the timber pile foundation. This behaviour mirrors the lateral failure mechanism discussed extensively in this thesis.
- Quay wall segments A.I/II, B and C exhibited progressive deflection (up to 93mm) towards the water with surface loads greater than 50 kN/m^2, indicating that these segments are nearing progressive failure.
- Horizontal soil deformations behind the quay showed a strong correlation with the lateral deformation of the pile foundation.
- Cap rotations and lateral pile deformation showed a linear proportional relationship.
- No soil movement was observed below the 'Wadsand' layer.
- With large surface loads behind the quay, settlements were greatest immediately behind the quay and decreased towards the hinterland.
- During the unloading of the quay, it was observed that the quay wall did not revert to its original position but instead remained in its displaced state.
- Although the experiment was designed to be fully two-dimensional, the presence of segmental dividers introduced friction at the sides, leading to corresponding three-dimensional effects, mainly in the soil body behind the quay.
- The quay structure displayed minimal vertical settlements.
- Sliding or tumbling of the gravity wall becomes significant when surface loads are in close proximity to the masonry wall (e.g. <1m).
- The sophisticated monitoring plan was demonstrated to be capable of detecting lateral failure in quays. Elements of this plan can be used within the city centre of Amsterdam. For example one can install inclination sensors on the pile caps or prism measurements combined with tilt sensors on the gravity wall. Other than that, the horizontal deformation of the soil body behind the quay can be monitored with for example vertical arrays of fibre optics.

5.5 Interpretation of the quay wall experiment Overamstel

In this section, the results of the Overamstel quay wall experiments are interpreted. First, the influence of the subsoil conditions on the quay wall response is explored, followed by an examination of the effect of the side friction. Next, the ratio between vertical and horizontal loading is elaborated. Subsequently, the effect of the unloading steps is discussed. Accordingly, the effect of the top load in experiment A.II is explained. Finally a recap is provided.

5.5.1 Influence of subsurface conditions on the quay wall response

A large variation in quay wall deformation response was noticed during the experiments. The difference in the quay wall's stiffness is mainly due to the increasing thickness of the sand layer on the back of the quay wall from segment A to D. Segment A had a sand fill behind the quay of thickness varying from 2.5 to 3.5m. Segment B had a thickness of 3.5m, segment C 5m and for segment D it was between 5 and 5.5m. The sand fill provided support to bear the top load. The deeper the fill layer reaches, the smaller the horizontal load exerted on the pile foundation. Despite reducing the lateral pile group resistance in locations C and D by removing the second pile row and lowering the canal bed, the response was stiffer than A.I and B meaning that the thickness of the sand layer had a dominant influence. It was observed

that the piles at segment C and D had a shallower clamping depth than those at segment A.I and B. This shallower clamping depth was initially expected for A.I and B due to the higher bottom of the harbour, which provides greater lateral support to the pile foundations. However, at local CPT's taken inside the harbour show that the shallow clay and peat layers at segment C and D show higher q_c values compared to A and B, indicating stiffer soil behaviour. The increasing thickness of the sand layer caused soil movement to reduce from NAP-8m (segment A) to NAP-5m (segment D). It is highly likely that the increasing thickness of the sand layer has also caused greater friction with adjacent segments, resulting in a stiffer response. The segmental friction is discussed in the next section.

5.5.2 Effect of segmental friction

A struth structure was employed to reduce segmental friction at the sides and move with the segment itself. In all experiments, the struth structure turned out to be stiffer than designed, most likely due to an installation error in the extension bars which prevented them to elongate. For example, at the end of experiment A.I, the displacement of the struth beam was less than 20mm which is around 20% of total segmental deflection (93mm). The other 80% of the differential movement occurred in between the struth beam and the soil of the segment itself. This is illustrated in Figure 5.32, which shows a top view photo of the segmental struth structure employed to separate the segment from its boundaries, as detailed in section 5.3.1. Four potential friction forces are indicated, 1) Soil-soil friction which is the soil friction within the segment itself, 2) Sheet pile-soil friction, 3) Struth beam-sheet pile friction (it was observed that the Azobé sheet pile wall slid along the steel struth beams) and 4) Strut-structure friction.

For each interface, friction coefficients reported in the literature are discussed. Internal soil friction coefficients, indicated with (1), can be estimated to be tangential to the friction angle φ, resulting in friction coefficients within the segment itself in the range of 0.5 to 0.8. NAVFAC standards state that friction between sheet piles and clean sand, indicated with (2), is usually around $\tan(\delta) = 0.30$, while friction between silty sand mixed with silt or clay is usually around $\tan(\delta) = 0.25$ (Navy, 1986). Interfaces between wet wood and steel, indicated with (3), can vary greatly, depending on factors such as the smoothness of the surface, moisture content, fibre orientation, pressure applied to the interface and the hardness of the wood (Guan et al., 1983; Koubek et al., 2014). For smooth surfaces, the coefficient of friction is typically around 0.15 to 0.3. For interface (4) no reference in literature was found. Since the segmental struth structure is composed of multiple interfaces with each their own friction, it is hard to make an estimate of the overall friction coefficient prior to testing.

It is however essential to include segmental friction in model computations since it contributes significantly to the response of the quay wall. A simplified model is established to analyse the friction experienced by the quay wall segments. The friction force at one of the sides of the segment can be simplified by τ_s[kN] as schematized in Figure 5.33. In this figure, the active wedge is illustrated in grey. For this illustration, the active soil wedge is consisting of two different soil layers with each their own angle of internal friction φ[deg] with corresponding wedge angle β_s[deg]. In eq. 5.11, a formula to compute τ_s is provided. The friction force for one side of the segment can be obtained by integrating the horizontal effective stress ($\sigma_{zz} \cdot K_a$) over the side area of the active wedge and multiplying the outcome by friction coefficient Φ_w[-]. Formulas to evaluate the active soil pressure coefficients are evaluated in appendix H.1 according to (Coulomb, 1776). The total friction per unit meter quay wall F_τ[kN] can be computed with eq. 5.12 in which W_s[m] is the width of the segment.

The friction force can be included in model computations by subtracting the friction force from the total horizontal load on the quay wall F_h as described in section 5.2.4.

$$\tau_s = \iint K_a \Phi_w \sigma_{zz}(y_w, z_w) dy_w dz_w \qquad \textbf{eq. 5.11}$$

$$F_\tau = 2\tau_s / W_s \qquad \textbf{eq. 5.12}$$

In practice it is difficult to estimate Φ_w beforehand since it depends on the stiffness of the strut structure, friction between a variety of interfaces, the loading and the motion of the segment itself. In section 5.6, the value of Φ_w is calibrated for experiment A.I, B, C and D.

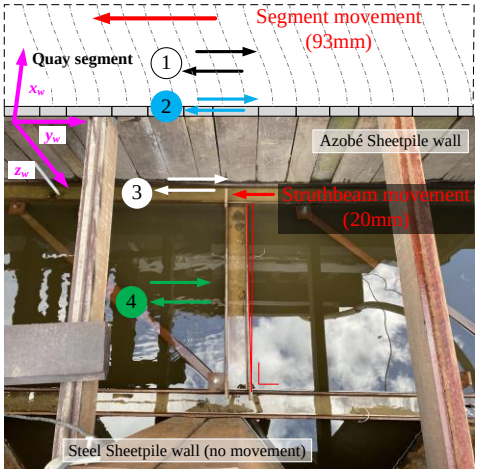

Figure 5.32, Top view edited photograph of segmental divide structure taken at the end of A.I. Local reference system in pink, corresponding to reference system in Figure 5.33.

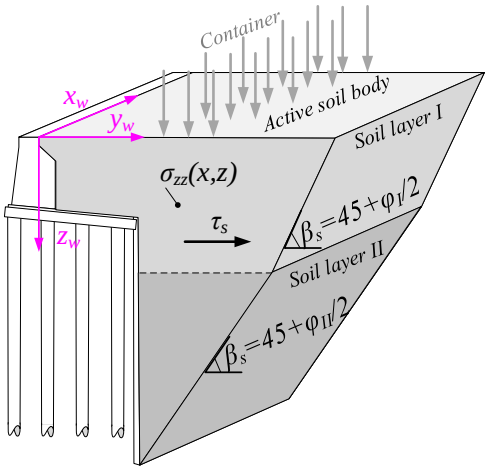

Figure 5.33, Schematization of active soil wedge with width W_s.

5.5.3 Ratio between vertical and horizontal loading

To examine the ratio between the vertical surface load and the actual horizontal loads acting on the pile group, the pile group experiment F2, described in section 4.5, is compared to the quay wall experiments. The $F_{lateral}$-y curve of experiment F2 is divided by the $F_{container}$-y curve of experiment A.I, B, C and D presented in Figure 5.34. Here, $F_{lateral}$ [kN] is the average lateral pile resistance as function of group deflection y and $F_{container}$ [kN] is the pile averaged vertical container load with lateral group deflection y. For small displacements, a peak can be observed because the quay wall segments had already deflected without the application of a vertical load after the reduction of the prestressing force. For larger displacements, it can be seen that the ratios between $F_{lateral}$ and $F_{container}$ become almost constant which implies that increasing the vertical load, linearly increases the lateral load on the pile foundation. Segment A has the highest ratio of 1/3, followed by segment B with a ratio of 0.25, C with a ratio of 0.2, and D with the lowest ratio of 0.15. It can be concluded that linear elastic soil models, such as the Flamant model discussed in section 5.2.2, are suitable for converting vertical surface loads on quay walls into horizontal loads on the pile foundation due to the linear relationships found.

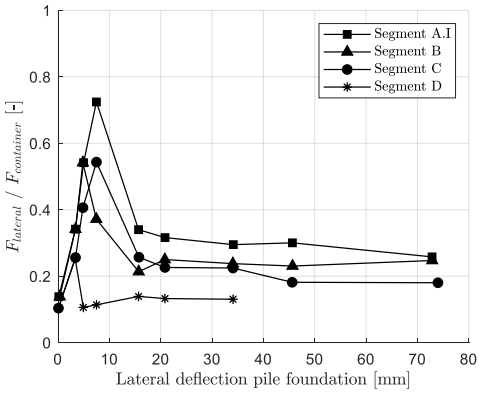

Figure 5.34, Ratio between vertical and horizontal loading for experiments A.I, B, C and D.

5.5.4 Effect of unloading steps

During experiment A.I, B, C, D and A.II, multiple unloading steps took place. It was observed that the quay wall did not return to its original position but remained in place. This differs from the unloading step in experiment F1, outlined in section 4.6.4, wherein the pile group bounced back to half of the applied deflection. The difference between a laterally loaded pile group and the performed quay wall experiments is due to the soil body behind the quay wall that prevents a possible rebound of the pile foundation. When the top load is removed from the active wedge behind the quay wall, the soil wedge appears to have moved down into the gap and becomes passive, which causes the piles to stay in place while experiencing bending stresses. As a new loading cycle continues and the effective soil pressures become greater than before, the quay wall's deflections will increase again.

5.5.5 Effect of top load in experiment A.II on lateral resistance

Experiment A.II took place after A.I, which had a final deflection of 93mm. The loading container was moved 1.7m closer to the water front. The first loading trajectory (up to 37 kN/m^2) produced a 3mm deflection, which was the stiffest response of all segments. This step can be considered a reloading step, as discussed in the previous section. The deflection increased to 54mm with the same ultimate load that was used for segment A.I. The large increase was not only due to reloading effects, but also due to an increase in second order moments in the piles that were not present in experiment A.I. These second-order moments caused higher bending stress in the timber, resulting in greater lateral pile deflections.

5.5.6 Recap on interpretation quay wall experiments

The following are the key findings from the interpretation:

- A thicker layer of sand fill provides greater bearing capacity for the top load, leading to shallow lateral soil deformations, shallow pile clamping depths, and an overall stiffer system with small lateral deflections.
- The presence of segmental dividing structures introduces friction on the sides. This friction can be accurately modelled using equation eq. 5.11, where all the frictional effects are accounted for by a friction coefficient Φ_w.
- 80% of the differential movement occurred in between the struth beam and the soil of the segment itself.

- Linear elastic soil models, such as the Flamant model, are suitable for converting vertical surface loads on quay walls into horizontal loads on the pile foundation due to the linear relationships found.
- The prevention of lateral bounce back of the quay after unloading is due to the active soil wedge transitioning to a passive state, keeping the piles in place and subject to bending stresses.
- Applying a surface load on top of the quay, which is already preloaded and deflected, leads to second-order effects in the pile foundation. These effects result in significant and continuous deformations, which can ultimately lead to failure of the structure.

5.6 Quay wall model validation with Overamstel experiment

In this section, the results of the quay wall experiments conducted at Overamstel are utilized to validate the analytical quay wall model. Initially, a prediction was made prior to the Overamstel experiments and geotechnical site investigation took place. Model input parameters for the prediction are based on studies in literature, expert judgement and one local CPT. The prediction is discussed and compared with the outcomes of the Overamstel experiments. Subsequently, a postdiction is conducted, in which the information from the Overamstel bending tests, lateral pile group experiments, quay wall experiments, and geotechnical site investigation is used to calibrate and validate the analytical quay wall model. Accordingly, the postdiction and the prediction are compared and the differences in the model inputs and outcomes are discussed. Next, the postdiction is compared with FEM computations executed in PLAXIS. Finally, the model validation concludes by evaluating the suitability and predictive value of the model.

5.6.1 Comparison prediction with analytical quay wall model and field measurements

A prediction was made prior to the Overamstel experiments and also prior to geotechnical site investigation using the analytical quay wall model. An extensive analysis of this prediction can be found in the '*Overamstel experiment plan – version 17-02-2022'* (Hemel, Peters, et al., 2022), here a brief summary is provided. To model the quay, a group average pile diameter of 0.24m was applied, for which the moment of inertia I[m^4] was determined with an external diameter. The modulus of elasticity used was 11GPa (C24 timber class) resulting in EI = 1,792kN/m^2. The diameter and flexural rigidity were modelled constant over the pile length (L = 12m), with a centre to centre distance of 0.85m in the direction of loading and 1m side by side. A slope inclination of 1V:3H was used and the level of the canal bed at the front piles was found at NAP-3m. The headstock-pile connection was modelled as described in section 5.2.3 and the modelling parameters are provided in appendix D.2.1. The gravity wall (2.1m heigh and 1m wide) was modelled as a rigid body with dry weight of 22kN/m^3.

The soil parameters used to model the piles and soil body behind the quay were based on a locally-conducted CPT (found in appendix D.2.3), research on the collapsed Grimburgwal in Amsterdam (Korff et al., 2021) and three boreholes that were carried out at the Herengracht in Amsterdam (Dabek et al., 2019; Spannenburg, 2020). The soil layers and their engineering properties to model the piles are summarized in appendix D.2.2. It was assumed that the layers would behave drained due to the long past performance. The fanning angle φ_m was taken to be equal to the angle of internal friction. The soil layering and engineering properties used to model the active soil body are also summarized in D.2.2. The

following friction angles δ[deg] were used in de determination of K_a at interfaces indicated in Figure 5.8; I) $\delta=2/3\varphi$, III) $\delta=\varphi$, IV) $\delta=1/3\varphi$. In the prediction, no segmental friction was included in the model.

First, the load-deflection model prediction is compared with the measurements, displayed in Figure 5.35. The model predicted a quay wall deflection of 50mm after the removal of the raking piles, while it was measured to be only 9mm. With increasing loads, deflections rapidly increase; for a load of 50kN/m^2 the model predicts a deflection of more than 400mm, which is an overestimation of 400% compared to the test. Figure 5.36Figure 5.35 shows the bending moments as function of the top load. The right axis of this figure displays the corresponding bending stresses by dividing the bending moment by the section modulus. On the right side of Figure 5.36 is a histogram, which shows the MOR values from the Overamstel pile bending experiments (described in chapter 3). For consistency with the bending experiments, an effective diameter of 0.20m (20mm soft shell) was used to calculate the bending stresses. The predicted pile moments after raking pile removal were around 12kNm, equivalent to a bending stress of 14N/mm^2, which is just above the 5% lower bound of the MOR values. The estimated point of failure for the first row of piles was determined to be at a surface load of 20kPa, indicating that the quay wall would fail according to the model predictions. Consequently, it was decided to have an excess capacity on the load side, specifically 50kPa. With a surface load of 50kPa, the predicted bending stresses ranged from 45 to 85 N/mm2, which is twice the 95% upper bound of the modulus of rupture (MOR). This provided sufficient ballast to ensure the failure of the quay. It is evident that the quay did not experience complete failure, and it is clear that prior model predictions significantly overestimated both deflections and bending moments. The reasons will be discussed in section 5.6.4.

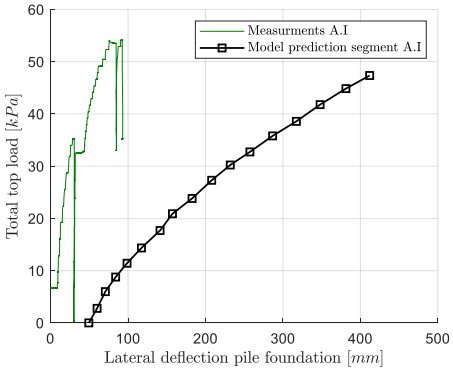

Figure 5.35, Load-displacement curve for model prediction prior to Overamstel quay wall experiment.

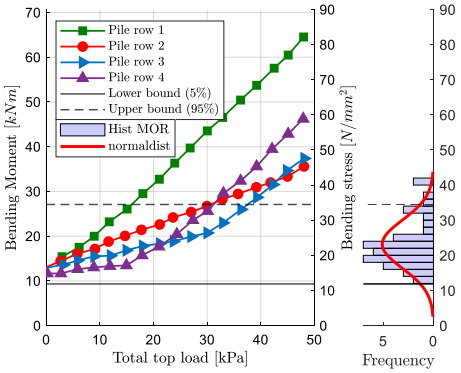

Figure 5.36, Model predictions of bending moments (left axis) and bending stresses (right axis). Right side histogram: *MOR* according to bending tests..

5.6.2 Model input postdiction with analytical quay wall model

Using the data obtained from the Overamstel experiments and the full geotechnical site investigation, a postdiction with the analytical quay wall model was conducted. First, the model input with respect to structural properties of the piles is provided, obtained from the bending experiment described in chapter 3. The flexural rigidity of the piles, obtained directly from the bending experiments, was taken $EI(z=2\text{m}) = 783\text{kNm}^2$. At a depth of 2m, bending moments are maximal. The external diameter of the piles was kept constant at 0.24m and had

a soft shell of 20mm over the entire 12m length of the piles. However, the soft shell does not contribute to the structural strength of the piles.

Second, the model input with respect to the pile group modelling is provided, obtained from the lateral pile group experiments and model validation described in chapter 4. Geotechnical modelling parameters are based on the geotechnical site investigation summarized in chapter 2. It is assumed that the softshell of the pile is able to withstand the lateral earth pressure and thus contributes to the geotechnical resistance of the pile group. As such, the external diameter of 0.24m is used in the formulas of Brinch Hansen and Ménard to determine model spring stiffnesses. The soil layers and their engineering properties to model the piles are summarized in appendix D.3 in sections D.3.2-D.3.5 for segment A.I-D. Cohesive layers are consolidated using undrained shear strength (*su*) and no friction angle ($\varphi = 0$), with a wedge fan angle of $\varphi_m = 15$ degrees as previously validated in section 4.3. The fanning angle for the granular soils is taken equal to the internal friction angle. The canal bed profile for each segment is modelled as depicted in Figure 5.18. The bending moments obtained with the analytical model are corrected according to eq. 4.24. To model the interface between the pile caps and the headstock, the pile-headstock model is used, which is described in section 5.2.3.

Thirdly, the model input with respect to the active soil body is provided, derived from the geotechnical site investigation described in chapter 2. The soil layering and engineering properties used to model the active soil body are summarized in appendix D.3 in sections D.3.2-D.3.5 for segments A.I-D. The following friction angles δ are used in de determination of K_a at interfaces indicated in Figure 5.8; I) $\delta=2/3\varphi$, III) $\delta=\varphi$, IV) $\delta=1/3\varphi$. Equations eq. 5.11 and eq. 5.12 are used to model the segmental friction. The friction coefficient Φ_s is calibrated on the field measurements for each segment separately, and the calibration can be found in appendix D.1.5. Table 5.4 presents the calibrated friction coefficient values, which are discussed briefly.

Table 5.4, Segment friction coefficients calibrated on experimental measurements.

Segment	Φ_w at start	Φ_w at maximum load
A.I	0.32	0.15
B	0.32	0.15
C	0.27	0.19
D	0.31	0.20
A.II	0.15	0.15

The calibration revealed that a constant friction coefficient gave either an excessively stiff or overly flexible system response. The best model fits were obtained for friction coefficients that decreased linearly during the experiment. For all segments, a friction coefficient between 0.27 and 0.32 was calibrated at the start of the quay wall experiments. To achieve a good fit for segments A.I and B, the friction coefficient had to be reduced linearly to 0.15 at maximum load. Similarly, for segments C and D, the friction coefficient at maximum load was calibrated to be 0.19 and 0.2 respectively. Segment A.II is assumed to be 0.15 at the start because the segment was preloaded in experiment A.I. The calibrated friction coefficients are comparable with those reported in the literature (section 5.5.2). In section 5.6.5, the coefficients are compared with values obtained with FEM computations.

A possible explanation for the higher calibrated friction coefficient for C and D compared to A and B is the thicker sand layer at the backside of the quay. As found in literature, interfaces with sandy soils have a higher friction compared to interfaces with

cohesive soils. The likely explanation for the drop in the calibrated friction coefficient is how the friction between the loaded segment and the segmental strut structure builds up. When the segment progresses towards the water, soil-soil friction is first initiated (0.5-0.8), followed by the friction between the soil and the wooden sheet pile wall (0.3-0.25), and then the friction between the wooden sheet pile and the steel strut beam (0.15-0.3). Consequently, the friction develops steadily towards the outer interfaces, which have a lower friction.

Segments A.I, B, C, and D were initially modelled using the basic approach discussed in section 5.2. However, for segment A.II, an incremental approach is utilized, due to its loading history of A.I. In this approach, it is assumed that after the top load is removed, the active wedge behind the quay wall transitions into a passive state. This results in the piles remaining in place while being subjected to bending stresses. Consequently, the soil stresses behind the quay wall are retained within the soil even after the top load is removed.

To implement the incremental approach, the first step involves calculating the effective soil stress behind the quay wall at the last load step of segment A.I. This stress field is then considered as a threshold value for computing the soil stresses in segment A.II. Whenever the soil stresses within the domain of A.II are below the threshold soil stresses obtained from segment A.I, the threshold soil stress is employed for the computation.

5.6.3 Comparison postdiction with analytical quay wall model and field measurements

The results from the postdiction are briefly discussed. First, the load-deflection curves computed with the model are compared with the measurements, displayed in Figure 5.37. In general, the model predictions are in good agreement with the measurements. For segment A.I and B, the model overpredicts the deflection for the first loading cycle (up to 35kPa). Model predictions for C and D display a vertical sawtooth shape for small deflections, which is not observed in the corresponding measurements. This sawtooth shape in the deflection is attributed to the segmental friction that is included as a counteracting force with respect to the quay wall deflection. In cases where the friction force (τ_s) is overestimated, it can lead to a smaller resultant horizontal force (F_h) compared to the previous time step. As a consequence, this smaller force can result in reduced deformation for higher top loads, causing a distinct sawtooth shape to emerge. As the loads increase, this effect becomes less pronounced. Predictions for segment A.II are in very good agreement for the first loading cycle up to 35kPa. The additional displacements obtained are mainly due to an increase in normal forces in the piles. For loads larger than 35kPa, the model predicts a strong increase in deflection, which is a similar trend found in the measurements. For all segments, deformations for larger loads are very accurate. For illustrative purposes, the vertical effective soil stresses for a surface load of 40kPa is provided in Figure 5.38.

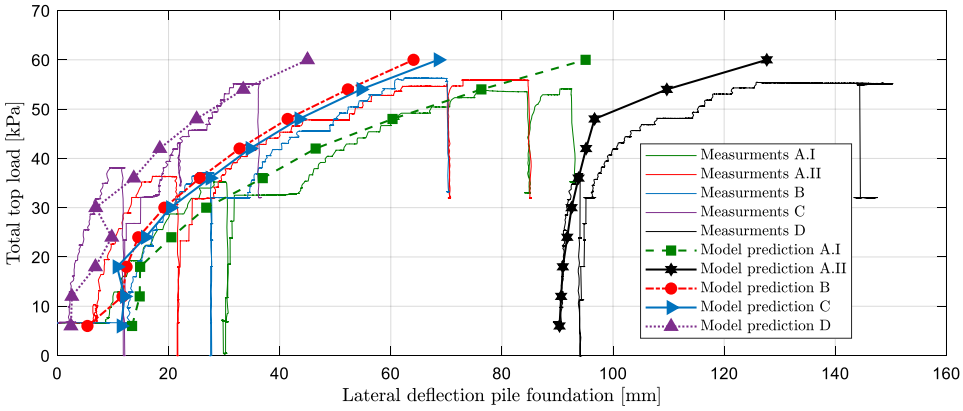

Figure 5.37, Load versus quay deflection. Model postdiction compared with field measurements.

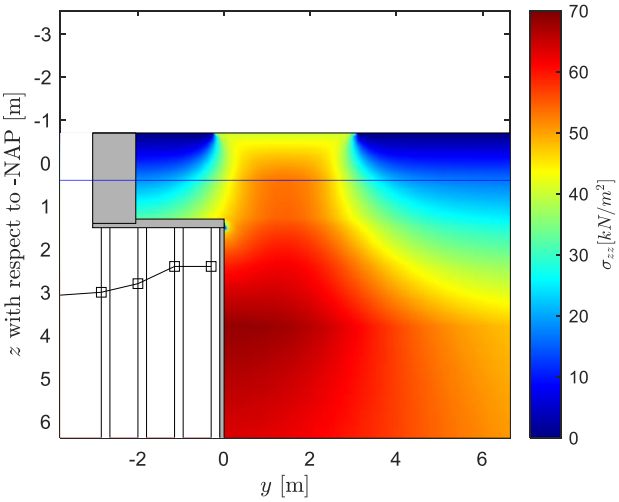

Figure 5.38, Postdiction: Effective vertical soil stresses σ_{zz} at a surface load of 40kN/m^2.

Second, model predictions for the pile cap rotation versus average lateral pile group deflection are compared with the field measurements, depicted in Figure 5.39. The model predicted the steepest gradients for segments C and D, and milder gradients for segments A and B, which is in good agreement with the measurements. The prediction of C and D is accurate, while the gradients for segments A.I-II and B are overpredicted by 30% and 14%, respectively. This indicates that shallow soil layers for A.I-II and B were likely modelled too stiff, resulting in a higher cap rotation per unit deflection.

Thirdly, the predicted bending moments are compared to the MOR values derived from the bending experiments presented in Figure 5.40. It should be noted that the predicted bending moments and stresses could not be validated through direct measurements during the test, as no such measurements were available. The right side of the figure provides a histogram showing the MOR values from the Overamstel bending experiments. Bending stresses are computed with an effective diameter of 0.20m (20mm soft shell). The predicted bending moments at the start of the experiment (excluding A.II) ranged from 1-4kNm, with resulting

stresses below the 5% lower bound of the MOR measurements. Subsequently, the bending moments increased exponentially, ranging from 15-17kNm for segment A.I, 10-14kNm for segment B, 10-16kNm for segment C, and 7-12kNm for segment D. Segment A.II logically had the largest bending moments ranging from 17-23kNm. The corresponding bending stresses, found on the right side of the figure, ranged from 23-28N/mm^2, which falls within the 90% confidence interval of the MOR values. This indicates that it is highly likely that at least part of the piles of segment A.II, A.I, B and C experienced elastic-plastic behaviour. Elastic-plastic behaviour does not mean that piles directly break as was elaborated in chapter 3 and 4. When elastic-plastic pile behaviour takes place, model predictions on deflections are underestimated since the piles in the model are described by linear-elastic members. For large deflections, this phenomenon can be observed in Figure 5.37 where model predicted gradients are steeper than the measurements. Chapter 4 concludes that the analytical pile group model accurately predicted bending moments, aligning well with the Overamstel pile group measurements for various deflections. The close alignment observed in this chapter between measured deflections and pile cap rotations with the post-prediction provides strong evidence to consider the predicted bending moments and corresponding stresses as very reasonable.

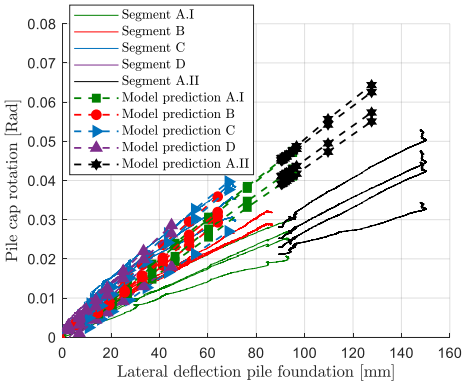

Figure 5.39, Pile cap rotation versus average lateral pile group deflection. Model postdiction compared with field measurements.

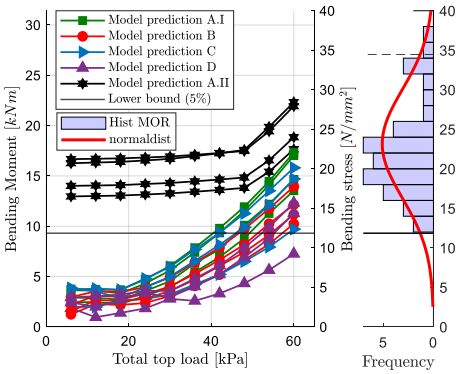

Figure 5.40, Postdiction of bending moments (left axis) and bending stresses (right axis). Right side histogram: MOR according to bending tests.

5.6.4 Comparison between prediction and postdiction

It was predicted that the quay wall would fail with an estimated value of approximately 20 kPa. However, in reality, the quay demonstrated much greater strength, as failure was not even observed for loads as high as 55kPa. This revealed the conservative nature of current models and emphasized the significant potential for improvement. The prediction results showed a significant overprediction of bending moments by 260% and deflections by 400% compared to the post-diction (**note: not with the field measurements)**. Below, the main differences between the prediction and postdiction are listed, along with their respective impacts on the model outcomes. Table 5.6 presents the percentage impact on both bending moment and deflection for each bullet point. Although the sum of individual percentages is lower than the total overprediction due to the independent of effects, summing up specific effects can still provide valuable insights into the overall influence on deflections and moments.

- One of the most fundamental differences between the prediction and the postdiction was the inclusion of the segmental friction. Without segmental friction in the postdiction, lateral quay wall deflections for a 55kPa surface load would have been 200mm, resulting in an overprediction of 131% (see Figure D.14). (overprediction of 131% = factor 2.3). This factor is related to the set-up of the test and does not have an influence on the way quay walls are modelled in general (in 2D).
- The friction angles for the layers at the active body were lower in the prediction than in the postdiction, resulting in higher active soil pressure coefficients and thus a greater horizontal pressure on the pile foundation. Also, the effective weight of these layers is modelled slightly higher in the prediction, giving higher horizontal force on the quay. The low friction angle of the active soil body and higher soil weight caused a deflection overprediction of 112%.
- In the prediction, cohesive layers were incorrectly modelled as drained. In the postdiction, undrained cohesive layers were considered, affecting the plastic limit of the soil springs. For drained layers, the ultimate soil resistance was determined using Brinch Hanssen with parameters c and φ, while for undrained cohesive layers, the parameters were $c = su$ and $\varphi = 0$. A comparison of plastic limits at the centre of each layer for the second pile row is presented in Table 5.5. The comparison is limited to the top four layers as deeper layers do not exhibit plastic behaviour in computations. It is evident that in the postdiction, the first 3m of the pile showed a higher ultimate soil resistance compared to the prediction, resulting in a stiffer response. Modelling drained instead of undrained caused a 95% deflection overprediction. This factor is related to the set-up of the test, which took place within a short period of time. For quays in the city centre, soil layers behave drained due to their long loading time scale.
- The prediction and postdiction had a slightly different soil layering around the piles, which can be observed in Figure 5.41. The most important difference was the absence of the 'geulopvulling' clay layer in the prediction and the shallower 'Wadzand' sand layer in the postdiction. These two differences resulted in a slightly stiffer lateral pile response (3%) in the prediction.
- The results of additional local cone penetration tests conducted in front of the quay revealed that cone resistances were lower than those assumed in the prediction. Consequently, in the postdiction, the Ménard method indicated lower spring stiffnesses (a factor 2), leading to a 9% reduction in deflection. It's important to note that the impact is relatively small for large deflections, as the upper layers exhibit plastic behaviour.
- The flexural stiffness of the piles in the prediction was $EI = 1{,}792\text{kNm}^2$, which was notably higher than the postdiction value of $EI = 783\text{kNm}^2$. This difference in stiffness resulted in an overall stiffer pile behaviour with deflections underpredicted by 41%. The flexural stiffness in the prediction was calculated using an elastic modulus of 11GPa, without accounting for the presence of a soft shell. However, bending tests revealed that the elastic modulus was actually 16.5GPa on average for an effective diameter. Consequently, it is essential to consider the soft shell when determining the flexural stiffness of the piles, or risk overestimating this value.

In conclusion, the overprediction of 106% in bending moments and 226% in deflection can be attributed to the specific test setup, which involved segmental friction and undrained behaviour. These factors were not taken into account during the initial prediction. Excluding these effects, the modelling accuracy, due to the Overamstel experiments, has still

significantly improved. The revised "gain" in modelling accuracy for bending moments and deflection stands at 43% and 37% respectively.[1]

Table 5.5, Plastic limits in the middle of each soil layer for the second pile row.

Layer	$D\sigma_p$ *Prediction [kN/m]*	$D\sigma_p$ *Postdiction [kN/m]*
Geulopvulling	10.3 (modelled as peat)	21.3
Holland veen	10.3	14.8
Oude zeeklei	17.5	14.1
Wad deposit	36.5	17.4

Table 5.6, Influence of differences between prediction on postdiction on bending moment and deflection.

Difference with postdiction	Moment [%]	Deflection [%]
No segmental friction	86.9	131.1
Lower friction angle active soil body	78.9	112.2
Drained vs undrained	19.0	95.0
Different soil layering around piles	-0.1	-3.0
Lower Ménard spring stiffness	-1.5	-9.2
Higher Flexural stiffness *EI*	-1.7	-41.0
Total	181.5	285.0

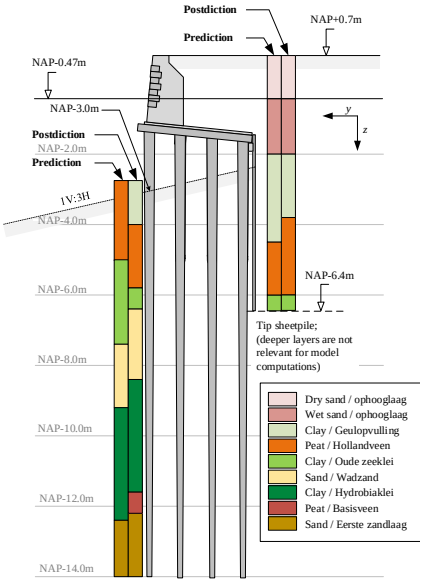

Figure 5.41, Soil layering comparison between prediction and postdiction.

5.6.5 Comparison with finite element computation (Choosrithong, 2023).

As part of the Overamstel project, K. Choosrithong conducted a finite element postdiction analysis using PLAXIS software. The modelling report, titled "*Proefbelasting Overamstel: Geotechnical Aspects, Site Characterization, and Numerical Investigation*", is published at Openresearch.Amsterdam. The results of this analysis are used to validate forces in the foundation as well as the found segmental frictional coefficients in Table 5.4.

Three models were employed, presented in Figure 4.42. They are shortly discussed. The first model is a 2D-plane strain model (fig A). In this model, the soil-pile-soil interaction is incorporated by embedded beam rows. The second model, depicted in (fig B), is a 3D-plane strain model. This model incorporates pile-soil-pile interaction through volume elements and incorporates the three-dimensional spreading of the top load into the soil. The third model is a 3D-plane strain model which includes the segmental trenches and corresponding friction (fig C). The interface friction in this model was incorporated using the equation $\tau[N/mm^2] = R_{int}(\sigma \tan(\varphi)+c)$, where R_{int} represents the interface strength. The interface strength R_{int} is comparable with the segmental friction coefficient Φ_w introduced in the analytical model.

The geotechnical model input is based on the geotechnical site investigation described in chapter 2 and its input can be found in J.1.1. The piles were modelled with an external diameter of 0.24m and flexural stiffness of 1,237MPa. The timber (modelled as class 18) was assigned an elastic-perfect plastic behaviour with plastic moment capacity of 24.4kNm. The pile-headstock connection was modelled hinged. For all models, the

[1] Gain in modeling accuracy = (prediction value – post diction value) / prediction value * 100%.

construction stages from the past were included until the moment of raking pile removal, of which the description can be found in J.1.2.

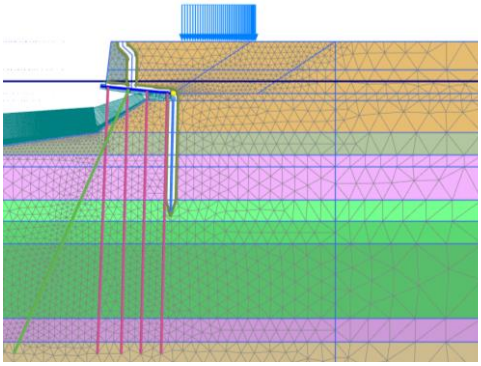

Figure 5.42A, 2D-plae strain

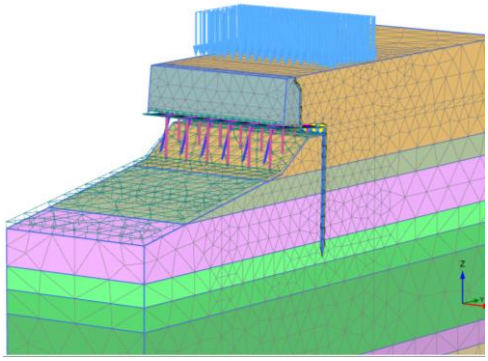

Figure 5.42B, 3D-plane strain

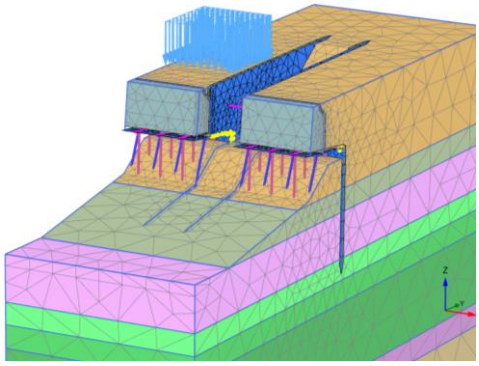

Figure 5.42C, 3D-plane strain with trench model

Figure 5.42, Finite element analysis performed. Three model types are presented in subfigures A, B and C (Choosrithong, 2023).

Firstly, the load versus deflection results for segment A.I are presented in Figure 5.43. The figure includes multiple lines representing the post-diction of the analytical quay wall model, the 2D-FEM model, and the 3D-FEM model with three variations of segmental friction (Rint = 0.15, 0.3, 0.5, and 1.0). Additionally, the measurements are indicated by black round markers. Observing the results, it is apparent that both the 2D-FEM model and the 3D-FEM model tend to overpredict the measurements due to the absence of segmental friction, similar to the analytical model without friction. The 2D-FEM model overpredicts to a larger extent than the 3D-FEM model, which can be attributed to differences in load spread and soil-structure interaction modelling techniques. Moving on to the segment friction FEM model, for small deflections (0-40mm), the best predictions are achieved with R_{int} values of 0.5 and 0.3. Conversely, for larger deflections (100mm), the best prediction corresponds a value of 0.15. This suggests that in the 3D-FEM model, the segmental friction needs to decrease from 0.5-0.3 to 0.15 with increased deflection, in order to achieve a good fit with the measurements. This aligns with the segmental frictional coefficients listed in Table 5.4 which were calibrated to be 0.32 at the start of the experiment and 0.15 at the end.

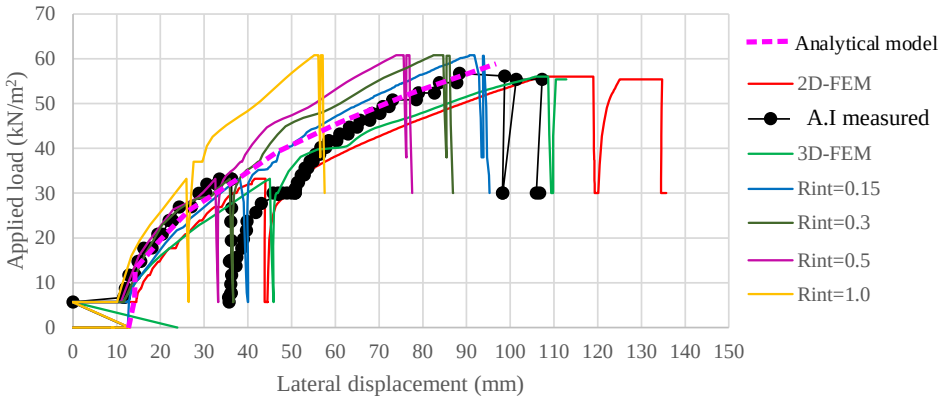

Figure 5.43, Load versus quay deflection for segment A.I. Multiple FEM model post-dictions compared with field measurements.

Finally, the bending moment predictions obtained with FEM are compared to the predictions of the analytical model in Figure 5.44. Unfortunately, bending moment computations were only performed for the 2D-FEM model. It can be observed that the bending moments predicted by the 2D-FEM model are very comparable to those predicted by the (also 2D) analytical quay wall model.

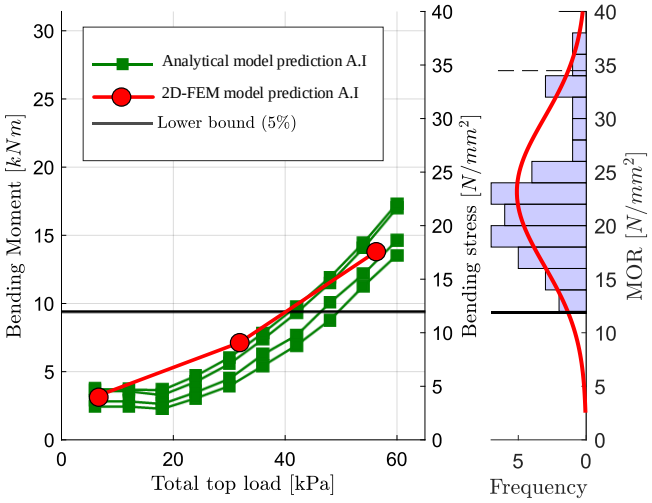

Figure 5.44, Bending moments and stresses for FEM-2D and analytical model vs MOR (segment A.I).

In conclusion, the analytical quay wall model demonstrates good agreement with finite element computations in predicting forces and displacements. Additionally, the calibrated friction coefficients in the analytical model are compared with the friction coefficients used in the 3D-FEM model, and the values of these coefficients are found to be highly comparable.

5.6.6 Conclusion on validation with Overamstel experiment

From the validation with the Overamstel experiments, the following can be concluded. The presented quay wall model is capable of accurately predicting quay wall deflections, pile forces, and pile displacements for historic timber founded quay walls with closely-spaced piles in underwater slopes that are subjected to surface loading. An extensive validation of the pile group, which is integrated into the quay wall model, is provided in chapter 4 and not discussed in this section. An appropriate way to model the active soil body behind the quay wall is with a linear-elastic soil model described by the theory of Flamant. The stiffness of a pile-headstock connection can successfully be described by an elastic-plastic cap moment.

In order to achieve accurate alignment with field measurements, the incorporation of segmental friction is crucial. Without it, quay deformations are greatly overpredicted, reaching up to 2.3 times the actual values. By calibrating the segmental friction based on the measurements, other uncertainties associated with modelling the soil medium are indirectly considered in the fitted segmental friction. Nevertheless, the employed friction coefficients demonstrate a strong correlation with calibrated friction coefficients from 3D FEM software and existing literature studies. This suggests that other uncertainties related to the modelling of the soil medium within the analytical model are of minor significance.

For modelling continues quay walls in Amsterdam's city centre, side friction between neighbouring quay wall sections should only be considered when the loading configuration or configuration of the quay wall in the longitudinal direction varies. This could be due to a local surface load, large variably in subsurface conditions or a locally weakened quay wall. In either of these cases, the adjacent quay wall sections are able to provide stability (and thus friction) to the critical quay wall section. Part of the friction is the redistribution ability of the masonry wall. Conversely, if the loading situation along a non-varying quay does not change, side friction should not be assigned.

It is concluded from the validation with experiment A.II that the analytical quay wall model is capable of taking into account the loading history of a segment using an incremental approach. When considering the loading history, it is important to take into account possible time-dependent effects that have occurred in the past, such as relaxation of wood, creep in soil, relaxation of soil after unloading, or movement of the quay wall. This type of effect did not occur during the Overamstel experiment, given the short timescale.

By comparing prediction and postdiction outcomes, it can be concluded that both structural and geotechnical site investigations play a crucial role in obtaining accurate predictions of quay wall behaviour. The most significant discrepancies between the postdiction and prediction, which heavily influenced the displacements and forces, were identified as follows: the absence of segmental friction inclusion (causing major deflection overpredictions), a smaller friction angle within the active soil body (leading to increased horizontal loads on the quay), the consideration of drained computation (resulting in a less stiff soil response), and an excessively high flexural stiffness (resulting in an underestimation of the deflection). The discrepancies resulted in an overprediction of the bending moment and displacement by 260% and 400% respectively. The modelling accuracy, due to the Overamstel experiments, has significantly improved. The revised "gain" in modelling accuracy for bending moments and deflection stands at 43% and 37% respectively.

5.7 **Conclusion and discussion**

To improve the assessment of historic quay walls, a computationally fast analytical quay wall model is proposed which describes the lateral failure of the pile foundation. The model consists of a framework of elastic beams embedded in an elastic foundation and is externally loaded by a linear elastic soil model based on the theory of Flamant. The beam model is made up of multiple Euler-Bernoulli beams, connected to each other by boundary and interface conditions. To model the lateral bearing pile-soil-pile interactions in layered sloping soil, a validated analytical pile group model is incorporated into the quay wall model. Its key advantages over state-of-the-art finite element modelling software include robustness, computational speed, feedback loops, minimal input requirements, and no numerical stability issues at large deformations.

In order to validate the quay wall model, a series of experiments were conducted in which various quay wall segments were loaded by a ballast container on surface level. The experiments took into account variations in loading location, quay geometry and geotechnical conditions, and the structural and geotechnical response was monitored accordingly. The sophisticated monitoring plan was demonstrated to be capable of detecting lateral failure in quays. Elements of this plan can be used within the city centre of Amsterdam. For example one can install inclination sensors on the pile caps or prism measurements combined with tilt sensors on the gravity wall. Other than that, the horizontal deformation of the soil body behind the quay can be monitored with for example vertical arrays of fibre optics.

The Overamstel tests clearly demonstrate the predicted dominant failure mechanism, known as “lateral failure of the pile foundation”, occurring when a quay wall is loaded from the backside. This failure mechanism causes the quay wall to laterally move towards the waterfront due to increased soil stresses behind the quay. This movement results in bending of the foundation piles, which can ultimately lead to pile breakage. It was predicted that the quay wall would fail with an estimated surface load of approximately 20kN/m^2. However, in reality, the quay demonstrated much greater strength, as failure was not even observed for loads as high as 55kN/m^2. While part of this underprediction can be attributed to experiment-specific effects not considered in the prediction analysis, the substantial underprediction of the failure load still emphasizes the conservatism in current modelling approaches and emphasized the significant potential for improvement.

In the experiment continuous deformations (93mm, 85mm, 70mm) were observed for three segments (A.I, B, C respectively) with surface loads of 55kN/m^2 applied behind the quay. In one preloaded segment (A.II), the 55kN/m^2 load was applied on top of the quay (directly behind the gravity wall), which led to continuous displacements reaching 147mm. For these four segments, computed bending stresses exceeded the modulus of rupture in the timber and indicating timber yielding. The excessive and progressive deformations, coupled with yielding of the timber piles, serve as clear indications of quay walls that are approaching failure or pile breakage.

By comparing the lateral pile group experiments with the quay wall experiments, a linear relation between the top load and lateral pile load was found, providing proof for the utilization of linear elastic soil models such as the proposed Flamant model in this chapter. In this regard, the quay wall test has been successful. However, the selected test approach, involving testing relatively small segments of the quay wall, introduced an additional source of uncertainty. Undesired segmental friction added to the already-accounted-for uncertainty

in the distribution of the top load through the soil medium to the quay foundation. As the model has been calibrated to segmental friction, other potential inaccuracies in the active soil body are factored into the 'friction uncertainty', making it unfeasible to determine the deviation of the soil model. To that extent, the calibrated friction coefficients in the analytical model were compared with the friction coefficients used in a 3D FEM model, and the values of these coefficients are found to be highly comparable, suggesting that the soil model has no major deviations and is thus reliable.

The residual uncertainty in the soil model and segmental friction still considered, the analytical quay wall model is able to accurately forecast the lateral failure mechanism of historic quays. The model is also capable of taking into account the loading history of a segment using an incremental approach. In the postdiction, measured values from the experiment were approximated within a margin of error of 10%. In chapter 4, it was demonstrated that the pile group model accurately predicted bending moments at all depths within the foundation piles when subjected to an imposed deflection. Furthermore, the validity of the predicted bending moments for the quay experiments were successfully confirmed through a comparison with 3D-FEM. This dual confirmation reinforces the reliability and accuracy of the analytical quay model. Due to the model's ability to predict both the lateral displacement of the quay and the magnitude of pile bending moments at various depths, stresses in the timber piles can be accurately determined. This enables the assessment of pile breakage occurring under a specific surface load.

Both structural and geotechnical site investigations are essential for reliable predictions of quay wall performance. Minor changes in soil stratification, quay wall geometry and structural properties can significantly impact the reliability of the model, as evidenced by the comparison between predictions and post-dictions. With most influential parameters, the active load on the structure, stiffness of the soil and the flexural rigidity of the piles. Prioritizing geotechnical site investigation before making predictions or assessments is highly recommended. This helps reduce geotechnical uncertainties and allows a focus on model-related uncertainties.

To conclude, the analytical quay wall model accurately predicts lateral displacement, pile bending moments, and bending stresses at various depths, allowing for the assessment of pile fracture under specific surface loads. Due to its computational speed, robustness and computational stability at large deformations, the model is highly suitable for trend analysis, sensitivity studies, and probabilistic analysis.

6

Collapse of the Grimburgwal

In this chapter, the analytical quay wall model is used to investigate the collapse of the Grimburgwal quay in 2020 using a forensic engineering approach. This chapter can be seen as an extra validation of the quay wall model on a real life failure case.

Photograph by Maarten Brante

6.1 Introduction

On 1 September 2020, a quay wall dating back to around 1870, collapsed along the Grimburgwal (GBW) in Amsterdam, the Netherlands (see Figure 6.1**)**. Within minutes, 25 meters of the quay wall completely disappeared into the canal. During the collapse, video images were taken by a security camera, which show that the quay leans forward during its fall into the canal. The quay wall construction consisted of a masonry cantilever wall on top of a timber floor, which was supported by headstocks situated on multiple timber pile rows, each approximately 12 meters long. Due to the presence of over 200 kilometres of similar quay walls in Amsterdam, and considering the usually busy streets, the collapse raised concerns about the safety of the remaining quay walls in the city. The collapse attracted widespread national and international media attention.

Following the collapse, an extensive rapid assessment was conducted by a large team of researchers using a forensic engineering approach (Korff et al., 2021). This assessment aimed to investigate various failure mechanisms and underlying causes that contributed to the collapse of the GBW, with the goal of preventing any recurrence of such failures in the future. In the assessment it was concluded that the main failure mechanism was the horizontal bending of the piles as a result of a local deepening of the canal followed by breaking of the quay piles (see Figure 6.2). This lateral failure of the pile foundation was studied using the analytical quay wall model developed in this thesis, which is explained in chapter 5. The objective of this chapter is to explain the modelling approach applied in the rapid assessment for the GBW and highlight how it provided valuable insights into the primary collapse mechanisms of the wall. This objective is reflected in the following key research question:

"How can the analytical quay wall model be utilized to understand the collapsed Grimburgwal?"

This chapter exclusively focuses on the analysis of the lateral failure of the pile foundation performed by the author, thereby presenting an incomplete overview of the comprehensive rapid assessment conducted, for which one is referred to the original publications (Korff et al., 2022; Korff et al., 2021). This chapter serves as a demonstration of the potential of the developed analytical quay wall model and can be viewed as an additional validation step, showcasing its effectiveness in assessing a failed inner-city quay wall. The outline of this chapter is as follows. Section 6.2, a summary of (Korff et al., 2022), gives the necessary background information on the GBW prior as well as during and after the failure. Accordingly, the collapse of the GBW is modelled with the analytical quay wall model in section 6.3. Finally, a discussion and conclusion are provided in section 6.4.

Figure 6.1, Grimburgwal directly after failure. Building in the background is the University of Amsterdam (building GB2). Left side of quay is 'East' and right side of quay is 'West'. Photograph: Hugo Logtenberg, 1 September 2020.

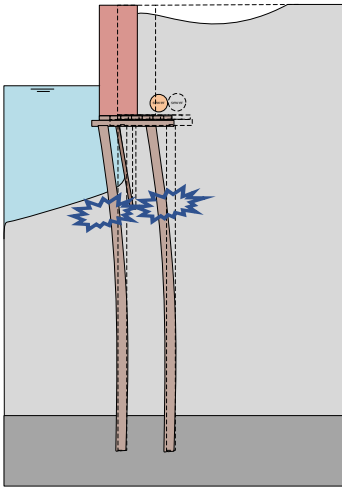

Figure 6.2, Schematization on the lateral failure of the Grimburgwal pile foundation.

6.2 Background information on the Grimburgwal

6.2.1 Grimburgwal geometric layout

The GBW is located in the historic centre of Amsterdam and its location is provided in Figure 6.3. The cross-sectional geometry of the GBW has been determined based on archival drawings from 1875 and a comprehensive dive inspection conducted by *Baars-Cipro*. The findings have been visually presented in Figure 6.5, showcasing the most likely cross-sectional geometry. The quay's top structure consists of a masonry gravity wall with a height of 2.4m and a thickness of 0.8m. The surface of the quay is located at (NAP) +1.44m. The masonry wall is supported by a timber foundation below the waterline, which maintains a height of NAP-0.4m. The foundation consists of two rows of vertical piles of which the pile tip is placed in the first sand layer at approximately NAP -13.0m. The piles are positioned with a longitudinal spacing varying between 1.0m and 1.2m and a perpendicular row spacing of 1.0m. The diameters D[m] of the piles vary slightly between 0.25m and 0.2m of which the majority did visually not show any severe damage or biological decay. Timber headstocks, measuring 1.5m in length, 0.17m-0.18m in height, and 0.25-0.28m in width, are placed on top of the piles. The connection between the headstock and piles is established through a pin-hole connection, as depicted in Figure 6.4. The headstocks serve as support for a longitudinal relief floor constructed using timber planks. The top of the floor is situated at NAP-1.2m and has a thickness of approximately 0.09m. To prevent soil erosion, a timber soil retaining screen (sheet pile) with a length of 3.8m is installed 0.3m behind the front pile row. An underwater survey of the canal along the GBW (after collapse) is provided in Figure 6.6. The depth of the canal in front of the piles varies, with NAP -3.35m on the east side of the quay and NAP -2.8m on the west side. Water depths in the area where the failure occurred could not be measured because of the collapsed material. According to *Waternet*, the water utility company responsible for maintaining the canal depth, the minimal depth in the canals is typically maintained at NAP-2.4m. The slope of the canal in front of the GBW is approximately 1V:3H.

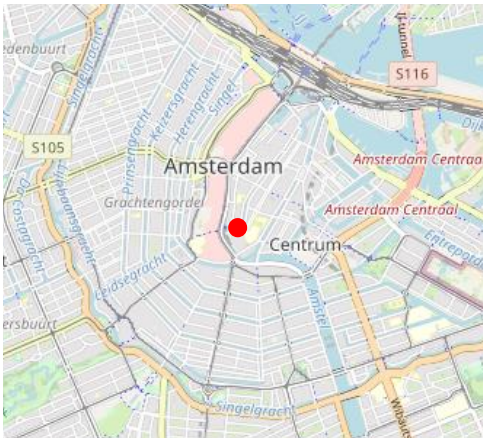

Figure 6.3, Location of the GBW in the historic centre of Amsterdam, indicated with a red dot.

Figure 6.4, Headstock extracted from collapsed Grimburgwal with pin hole and pile imprint visible (Korff et al., 2021).

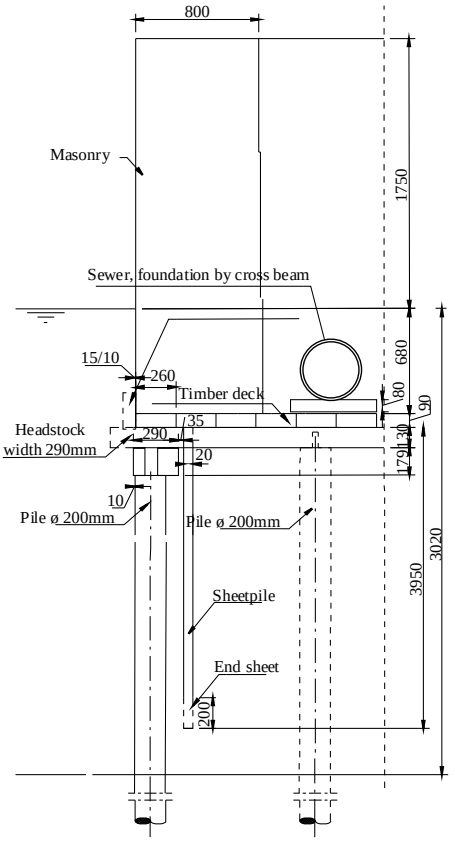

Figure 6.5, Cross-section according to diver's inspection with dimensions are in mm (Baars-Cipro, 2021).

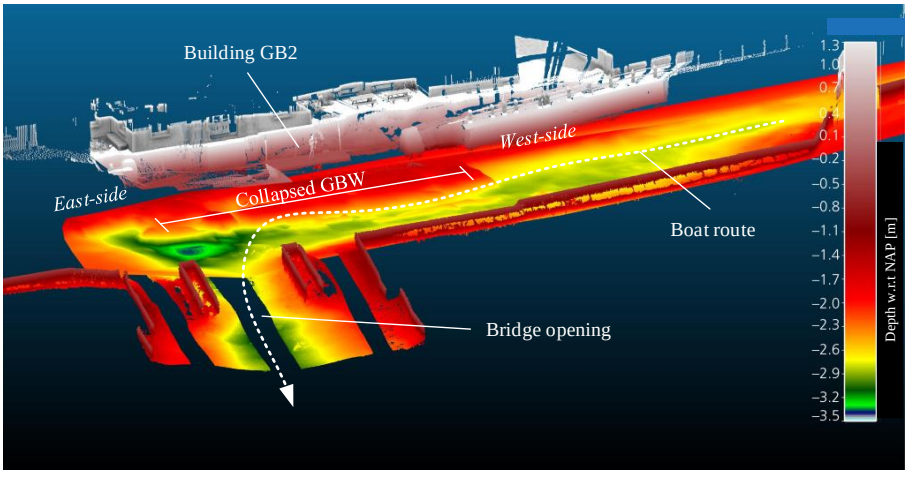

Figure 6.6, Visualization of the multibeam and three-dimensional scan made after collapse of the quay by (Gellecum, 2021). The colour red refers to shallow bed levels, showing debris in canal, and colours green to blue refer to the deepest canal bed level.

Conditions and circumstances of particular interest encompassed the loading conditions and exposure of the structure throughout its service life. The presence of significant traffic loading can be ruled out, as this section of the quay prohibits vehicular access. However, it is worth noting that the collapse occurred precisely at a location where large vessels (e.g. sightseeing boats) are required to turn sharply to navigate through a narrow clearance under an historic bridge facing the failed quay. This route is indicated in Figure 6.6. These manoeuvres have most likely resulted in localized deepening of the canal due to erosion caused by propeller washout as shown in the underwater survey. The occurrence of multiple ship collisions was observed, indicating signs of impact (e.g. cracks) on the masonry and headstocks.

After the collapse of the GBW, an additional inspection of the encountered timber has been carried out by the experts from *Amsterdam Monuments and Archaeology* (Derksen et al., 2021). Their inspection revealed a structure with three piles, which deviates from the diver inspection and archival records but aligns better with what is typically found in the city. The width of the quay was determined to be between 2.5 and 2.9 meters, which does not fit or barely fits on the narrowest part of the quay towards building BG2 (approximately 2.3 meters wide, where it initially collapsed). This leaves open the possibility that there may have been both three and two piles supporting the quay. Therefore, both options (two and three piles) are considered in this study.

6.2.2 Geotechnical site investigation

In total, three CPT's (cone penetration tests) were taken after the collapse, two at the land (CPT-1 and CPT-2), one in the canal (CPT-3). The CPT's can be found in Figure I.1 in Appendix I. Based on the soil investigations along the GBW, the soil composition is as follows. From surface level (NAP +1.44m) up to the top of the floor (NAP -1.2m), the quay fill mainly consists of sand. Behind the quay, starting from NAP +0.5m, the natural soil is encountered, predominantly clay with occasional layers of sand. Additionally, the investigations reveal the presence of sand layers around NAP -2m. Below the floor, clay and peat are found, with peat predominating until NAP -4.5m, and clay prevailing below that until NAP -8.5m. The Wadsand layer is situated between NAP -7.5m and NAP -10m, with the uppermost meter often containing a significant clay content. From NAP -10m to NAP -12.5m, clay is encountered again, and around NAP -12.5m/-13m, there is a 0.5m layer of peat, followed by the first sand layer starting at around NAP -13m. The first sand layer at this location is approximately 2.5 to 3m thick, after which the Allerod layer is encountered, and from NAP -17m, the second sand layer is found, with the upper 2-3 meters potentially still containing clay content.

6.2.3 Failure of the Grimburgwal; signs of the lateral failure mechanism

Photographs capturing the collapse of the GBW are displayed in Figure 6.7. These images illustrate the gradual deformation of the quay wall towards the canal in the moments before the collapse. The collapse initially occurred on the east side of the quay, followed by the subsequent overturning of the western section. As this chapter specifically addresses the lateral failure of the quay, the focus is solely on discussing the signs pertaining to this particular mechanism. Prominent signs of the lateral failure mechanism include settlements and sinkholes observed on the surface both on top and behind the quay wall. These settlements occur as a result of the active soil wedge situated behind the quay sliding into the gap created by the deformation of the quay. After the collapse, diving inspections showed

laterally broken piles (see Figure 6.8). Furthermore, the divers observed that the piles under the non-collapsed section of the GBW were inclined forward at an angle of approximately 20 degrees. This is a clear sign of local geotechnical failure in front of the piles. Unfortunately, there are no photographs or measurements available to document this observation.

Figure 6.7, Photographs taken during the collapse of the Grimburgwal. The quay wall is progressively leaning towards the canal side. Behind and on top of the quay, settlements and sinkholes are present.

Figure 6.8, Diver photo of pile breakage (Baars-Cipro, 2021).

6.3 Modelling the Grimburgwal

This section focuses on modelling and examining the impact of local deepening on the bending stresses σ_b [N/mm^2] in the timber pile foundation using an analytical approach.

6.3.1 Analytical quay wall model

To model the Grimburgwal the analytical quay wall model is used, which is discussed in chapter 5. The model consists of a framework of elastic beams embedded in an elastic foundation and is externally loaded by a soil model based on the theory of Flamant. The beam

model is made up of multiple Euler-Bernoulli beams, connected to each other by boundary and interface conditions. To model the lateral bearing pile-soil-pile interactions in layered sloping soil, the model described in chapter 4 is used. Figure 6.9 offers a model example of the GBW with three piles, providing a visual representation of the interaction between passive pile wedges.

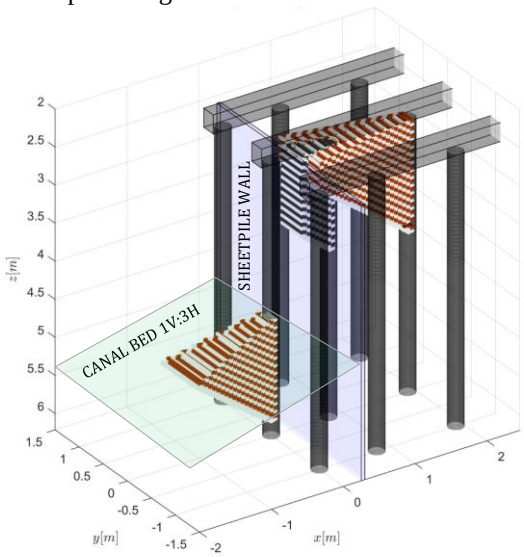

Figure 6.9, Visual representation of pile wedge interaction for the GBW configuration with 3 piles.

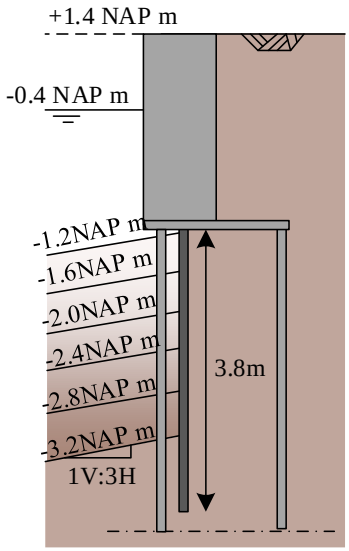

Figure 6.10, Canal deepening levels to be modelled with respect to NAP. GBW configuration with 2 piles.

6.3.2 Variant study

Six alternative model set ups are analysed since a variety of pile diameters was found and there is the possibility that there may have been both three and two pile rows supporting the quay. An overview of the alternative models can be found in Table 6.1. For all models, the effect of canal deepening on the bending stresses in the timber pile foundation is examined by lowering the canal bed in steps of 0.4m from NAP-1.2m to NAP-3.2m as shown in Figure 6.10. During lowering, a 1V:3H slope inclination is maintained.

Table 6.1, Alternative model set ups to be analysed

Model Geometry according to:	Number of piles	Pile diameter *D* [m]	Inclusion axial force *N* [kN]	Longitudinal spacing [m]	Perpendicular spacing [m]
1.Divers inspection + archive study	2	0.2	No	1.0	1.0 row 1-2
2.Divers inspection + archive study	2	0.2	Yes	1.0	1.0 row 1-2
3.Divers inspection + archive study	2	0.25	No	1.0	1.0 row 1-2
4.Divers inspection + archive study	2	0.25	Yes	1.0	1.0 row 1-2
5.Amsterdam Monuments and Archaeology	3	0.2	Yes	1.0	0.8 row 1-2 1.2 row 2-3
6.Reference study Amsterdam area	4	0.2	Yes	1.0	1.0 row 1-2 1.0 row 2-3 1.0 row 3-4

The first four models examine a geometry with two pile rows, based on the diver's inspection and archive study. These models vary the pile diameter and investigate the impact of including axial pile forces. Increasing the pile's free height amplifies the bending moments resulting from the second-order effects caused by axial loads from the weight of the wall and overlying soil. Additionally, a fifth model study is performed based on the geometry identified in the Amsterdam Monuments Archeology investigation, which involves three piles. Finally, a reference model 6 with four piles is analysed for comparison with the Amsterdam areal, as pile configurations with three or fewer piles are uncommon in the Amsterdam quay wall area. Model 5 and 6 involve a pile diameter of 0.2m with the inclusion of the axial load, which are considered governing compared to larger pile diameters without the influence of the axial force. In all models, a constant diameter is assumed along the length of the piles. The pile diameters (0.2m and 0.25m) are not directly measured at the cap but are estimated at the depth where the highest bending moments occur.

6.3.3 Model input

First, the model input with respect to structural properties of the quay are provided. The modulus of elasticity of the piles was set at 7,000 kN/m^2. The flexural rigidity of the piles, represented by the product of the moment of inertia I[m^4] and the modulus of elasticity E[kN/m^2], was calculated for different outer diameters. For D = 0.2m, the flexural rigidity was determined to be EI = 549.5kNm^2, while for D = 0.25m, the value was EI = 1341kNm^2. The headstocks were modelled with a flexural rigidity of EI = 987 kNm^2. The interface between the pile caps and the headstock was simplified as hinged. The flexural stiffness and external diameter of the piles remained constant along the pile length of 12m. Bacterial decay was not considered in the assessment of the structural strength of the piles. Additionally, the dry weight of the masonry was assumed to be 25 kN/m^3.

Table 6.2 presents the geotechnical modelling parameters, including the effective weight γ[kN/m^3], cone resistance q_c[kPa], cohesion c[kN/m^2], and friction angle φ[deg]. These parameters are based on three locally conducted CPTs as described in section 6.2.2, along with three boreholes carried out at the Herengracht in Amsterdam (Dabek et al., 2019; Spannenburg, 2020). The formulas of Brinch Hansen and Ménard utilize the external diameter of 0.20m and 0.25m to calculate the elastic-perfect-plastic spring stiffnesses. It is assumed that the soil layers behave drained due to their long-term performance. The pile wedges are assigned a fanning angle φ_m[deg] equal to the angle of internal friction. To calculate the external horizontal loading on the quay, the vertical effective soil stresses derived from the Flamant soil model are integrated along the height of the wall and sheet pile. These integrated values are then multiplied by the corresponding depth averaged active soil pressure coefficient K_a, assuming the entire soil body behind the quay acts active. The masonry wall is assigned an K_a value of 0.25, while the sheet pile has a K_a value of 0.59. K_a is determined according to Coulomb's theory. Note that no surface load is included in the computations.

Table 6.2, Geotechnical engineering properties Grimburgwal

Depth [m]	Sort [-]	γ' [kN/m^3]	q_c [kPa]	c [kN/m^2]	φ [deg]
0 – 1.8	Sand dry	18.0	-	0.0	32.5
1.8 – 2.4	Sand wet	9.0	-	0.0	32.5
2.4 – 6.0	Peat	1.0	200	6.2	14.9
6.0 – 8.0	Sea clay	7.2	200	3.7	28.8
8.0 – 10.0	Wadsand	7.9	5,000	2.2	25.0
10.0 - 12.0	Clay	7.2	1,000	3.7	23.6
12.0 – 20.0	Sand	10.0	10,000	0.1	35

6.3.4 Results of model studies

First, the models with two piles are discussed (model 1 - 4). Figure 6.11 illustrates the bending stresses in both the front and rear piles plotted against the canal bed level. Each plot includes four lines representing the models 1-4. On the right side of the front pile figure, a histogram of the 'best estimate' *MOR*[N/mm^2] values is presented, which were obtained from the bending experiments conducted in chapter 3. Given that the structural properties of the piles were determined based on an external pile diameter, the corresponding *MOR* values obtained using the external diameter (represented by red dots in Figure 3.29) are employed. This ensures consistency in evaluating the bending behaviour of the piles. The 90% confidence interval of the *MOR* is represented by the green shading in Figure 6.11. When bending stresses exceed the modulus of rupture ($\sigma_b > MOR$), the timber fibres in the pile cross-section begin to exhibit plastic behaviour (yielding), resulting in permanent damage to the fibres. Pile breakage is likely to occur when the timber cross-section reaches full plasticity. From the bending experiments a ratio of 1.7 was found between first yield moment and plastic moment. As a rule of thumb, full yielding and thus pile breakage is expected at 1.7·*MOR*, which is on average at 10.6·1.7 = 18.2 N/mm^2

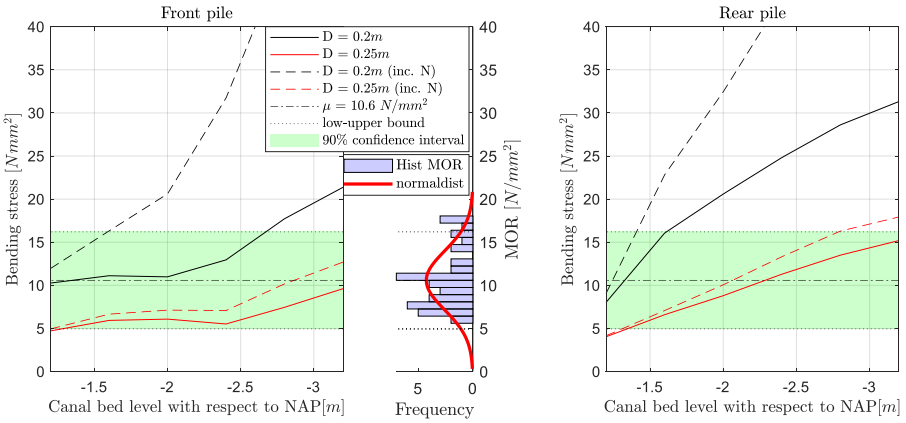

Figure 6.11, Maximum bending stresses in the timber pile group for models 1-4. Left figure shows the front pile and right figure the rear pile. On the right side the front pile figure, the MOR (based on external diameter) is plotted, obtained during the bending experiments in chapter 3.

As the canal deepens, bending stresses increase, attributed to a decrease in passive soil resistance acting against the piles. With smaller diameters (0.2m), the bending stresses surpass the 90% confidence interval for both piles as the canal depth exceeds NAP-2.6m. For larger diameters (0.25m), the rise in bending stresses is less pronounced; however, for the rear pile, the 90% confidence interval is exceeded when the canal bed depths exceed NAP-3m. The impact of the axial load on the bending stress within the piles is large, especially for smaller diameters. Notably, the impact of the axial load on the bending stresses in the timber diminishes with increasing pile diameter.

Similar computations were conducted for the model 5 and 6, involving 3 and 4 piles. Table 6.3 presents a comprehensive overview of the maximum bending stresses observed in the pile foundation concerning the deepening of the canal for all models. Numbers in red indicate pile breakage (σ_b [N/mm^2] > 18.2), in orange timber yielding (18.2 > σ_b [N/mm^2] > 5.0) and blue no yielding (σ_b [N/mm^2] < 5). It is observed that with an increased number of piles, the bending stresses are significantly lower and less influenced by the deepening of the

canal. With 3 piles (model 5), the bending stresses fall within the 90% confidence interval of the MOR values, although still below the average *MOR*, indicating a likelihood of plastic timber behaviour. On the other hand, for the scenario with 4 piles (model 6), the bending stresses do not exceed the 5% lower bound of the *MOR* values, suggesting the absence of plastic timber behaviour.

The model studies indicate the following conclusions: Two-pile configurations are prone to pile breakage (for 0.2m diameter) within the depth range of NAP-2.0 to NAP-3.2m, while three-pile configurations are expected to experience pile yielding (but not breakage) for all depths. Four-pile configurations are unlikely to encounter pile yielding at any of the simulated depths. Considering that depths up to NAP-3.35 are measured in front of the GBW (see Figure 6.6), computational evidence supports the likelihood of the GBW section with two piles experiencing pile breakage as a result of canal bed lowering.

Table 6.3, Maximum bending stresses in the pile group as function of the canal deepening for all models. Numbers in red indicates pile breakage (σ_b [N/mm^2] > 18.2), in orange timber yielding (18.2 > σ_b [N/mm^2] > 5.0) and blue no yielding (σ_b [N/mm^2] < 5).

Canal bed level with respect to NAP->		-1.2m	-1.6m	-2.0m	-2.4m	-2.8m	-3.2m
Model /	Bending stress ->	[N/mm^2]	[N/mm^2]	[N/mm^2]	[N/mm^2]	[N/mm^2]	[N/mm^2]
1. D = 0.2m	2 piles	10.3	16.1	20.6	24.8	28.6	31.3
2. D = 0.2m with N	2 piles	12.0	22.8	32.4	43.3	55.9	68.5
3. D = 0.25m	2 piles	4.7	6.6	8.8	11.3	13.5	15.2
4. D = 0.25m with N	2 piles	4.9	7.1	10.1	13.3	16.3	17.9
5. D = 0.2m with N	3 piles	5.1	5.2	5.1	6.5	7.0	8.0
6. D = 0.2m with N	4 piles	3.0	3.2	3.0	2.8	3.0	3.3

6.3.5 Sensitivity study

A sensitivity study was conducted for model 5, which included three piles with a canal depth of NAP-3.2m. This model was chosen for the sensitivity study because pile breakage is not expected for this configuration, but it could still occur if parameters turn out to be unfavourable. The study aimed to assess the influence of three parameters, namely the K_a of the wall, parallel pile spacing, and the pile-headstock connection, on the bending stresses experienced by the piles. This analysis aims to demonstrate the possibility of exceeding the 90% confidence interval when influential parameters enforce each other negatively in terms of bending stresses. The influence of external loading was examined by increasing the active soil coefficient K_a of the masonry wall from 0.25 to 0.3 and 0.35. Additionally, the effect of parallel pile spacing was investigated by varying it from 1.0 to 1.25 and 1.5m. The influence of a pile cap moment instead of a hinged pile-headstock connection was examined by exerting a cap moment of 1.9kNm of each pile. The estimated maximum moment in the connection is approximately $N \times e$, where N[kN] represents the axial force in the pile and e[m] is the eccentricity relative to the pile's centre. The eccentricity is estimated as $D/4$.

Table 6.4 presents the results of the sensitivity study. The increase in bending stresses is shown as a percentage compared to the three-pile base model (found in the bottom of the table). Higher external loads can lead to a significant increase in bending stresses, up to 133% in some cases. Similarly, an increase in pile spacing, particularly at 1.5m, can result in a substantial 233% increase in bending stresses for the front pile row. Incorporating cap moments to simulate the pile-headstock connection reduces bending stresses in the middle

and rear pile rows with approximately 30%. As stated, parameters can negatively enforce each other when added. For example, with K_a = 0.35 and pile spacing of 1.25, bending stresses can increase by 200%, 71%, and 131% for the front, middle, and rear piles, respectively. This would result in bending stresses of 9N/mm^2, 12N/mm^2, and 18.5N/mm^2 in the three piles. For the rear pile, this results in an exceedance of the 90% confidence interval, indicating a significant degree of yielding in the timber, potentially leading to pile breakage.

Table 6.4, Sensitivity study for model 5 with canal depth NAP-3.2m.

	Bending stress increase/decrease		
Difference with 3 pile case	Front pile [%]	Middle pile [%]	Rear pile [%]
Increase Ka to 0.30	66.7	8.6	37.5
Increase Ka to 0.35	133.3	64.3	106.3
Parallel pile spacing 1.25m	66.7	7.1	25.0
Parallel pile spacing 1.5m	233.3	78.6	112.5
Pile-headstock Mcap = 1.9kNm	6.7	-28.6	-35.0
Bending stress 3 pile case	3.0 [N/mm2]	7.0 [N/mm2]	8.0 [N/mm2]

6.3.6 Conclusion on results

It has been demonstrated that the deepening of the canal bed in front of the GBW has a significant impact on the forces within the timber pile foundation. Bending stresses can increase rapidly as the canal bed deepens. The extent of the increase in bending stresses varies depending on the pile configuration.

In the models with a two-pile configuration, it is highly likely that pile breakage occurs at canal bed depths of NAP-3.2m (greater depths of NAP-3.35m were found on the east side of the collapsed GBW). The two-pile configuration is supported by the archive and dive inspection, and it is also plausible considering the very short distance between the quay and the building BG2. However, it is expected that on both sides of the two-pile configuration, the quay was supported by three piles.

With three piles, the likelihood of plastic deformations in the piles is certainly present, although it does not necessarily lead to pile breakage. Only in the case of a local increase in pile spacing combined with slightly higher horizontal forces on the quay, this can ultimately result in the failure of a three-pile configuration due to pile breakage. It is unlikely that a configuration with four piles would fail.

6.4 Discussion and conclusion

6.4.1 Discussion on modelling; Grimburgwal compared to Overamstel.

The rapid assessment of the GBW was conducted prior to the Overamstel test program. The modelling parameters and approach used in the GBW assessment are compared to the structural and geotechnical properties identified in the Overamstel experiments.

The elastic modulus used in the modelling (E = 7,000MPa) is comparable to the modulus of elasticity obtained in the bending experiment (E = 6,000MPa) with the external diameter considered. Based on the Overamstel experiments, a flexural stiffness of 16,590MPa is recommended when using an effective diameter in which the soft shell is excluded. Applying this approach for the GBW with a soft shell of 20mm (see chapter 3), results in flexural stiffnesses of 1,583kNm^2 and 533kNm^2 for D = 0.25 and 0.2m respectively. These values align well with the flexural stiffness values (1341kNm^2 and 549.5kNm^2) used

in the modelling. Hence, it can be concluded that the flexural stiffnesses of the piles were accurately modelled, noting that possible bacterial deterioration was not accounted for. The pile-headstock connection was modelled with a cap moment of 1.9kNm, similar to the magnitudes obtained in chapter 5 analysis (0-6kNm).

The geotechnical engineering properties used in the GBW case are compared to the site investigation at Overamstel (chapter 2). The comparison results are presented in Table 6.5. The differences and their impact are discussed below. The sandfill in the GBW case has a lower friction angle, resulting in higher external forcing (proportional to K_a), and a slightly higher soil unit weight, leading to increased second order forces. The peat layer is modelled similarly, except for the friction angle, which is twice as large in Overamstel, as that value in Overamstel was based on laboratory testing. This has two major effects, the loading on the sheet pile is lower (proportional to K_a) and the lateral soil resistance against the piles is greater. The clay layer is nearly identical, with a small difference in cohesion. The Wadsand layer is comparable in thickness, cohesion and effective weight but modelled stiffer in Overamstel due to the higher friction angle. The clay and sand layer below the Wadsand layer have minimal influence on the lateral pile group modelling since the piles behave more or less clamped in the Wadsand layer. The foundation of the GBW is modelled with lower soil resistance and higher external loading compared to Overamstel. When the foundation was modelled with Overamstel parameters, it would have resulted in lower bending stresses in the GBW piles. However, it is expected that the differences are not significant enough to invalidate the calculations supporting the lateral failure due to pile breakage.

Finally, the approach is discussed, focusing primarily on the limitations of the model. These limitations include the absence of loading history, time effects such as soil and timber creep, and biological degradation over time. The analytical quay wall model was successfully validated using the Overamstel experiments, which exhibited less pronounced effects of these factors due to the presence of a raking pile that carried the lateral loads. Another effect that is not included in the model (nor in the Overamstel Experiments) is the redistribution effect facilitated by the masonry wall. Weaker sections of the quay wall can stabilize themselves by transferring their load to adjacent stable sections. The other way around, weaker sections can destabilize stable sections. The assessment of the Grimburgwal could be further enhanced by incorporating the aforementioned effects into the modelling process.

Table 6.5, Geotechnical engineering properties, a comparison between GBW and Overamstel.

	Grimburgwal			Overamstel		
Sort [-]	γ' [kN/m^3]	c [kN/m^2]	φ [deg]	γ' [kN/m^3]	c [kN/m^2]	φ [deg]
Sand dry	18.0	0.0	32.5	15.0	0.0	38
Sand wet	9.0	0.0	32.5	9.0	0.0	38
Peat	1.0	6.2	14.9	0.1	3.0	30
Sea clay	7.2	3.7	28.8	6.5	3.0	28
Wadsand	7.9	2.2	25.0	8.5	3.0	30
Clay	7.2	3.7	23.6	4.5	4.0	27
Sand	10.0	0.1	35	9.0	3.0	33

6.4.2 Conclusion

The lateral failure of the Grimburgwal was studied using an analytical quay wall model. With the model, it was demonstrated that bending stresses in the timber piles rapidly increase when the canal bed deepens in front of the quay. These bending stresses can reach critical levels, leading to pile yielding or pile breakage. The deepening in front of the GBW was most likely caused by propellor washout of boats that make sharp turns in front of the quay.

Both the two-pile and three-pile configurations of the quay were considered in the modelling process, as it was uncertain which configuration was present. The bending stresses for each configuration were then compared to the modulus of rupture obtained from the bending experiments conducted in chapter 3. Depth measurements in front of the quay revealed depths exceeding NAP-3m. At these greater depths, the two-pile configuration exhibited a high probability of pile yielding or even breakage. The three-pile configuration, on the other hand, is also expected to experience yielding, but to a lesser degree, and is unlikely to result in pile breakage. Cracks in the masonry prevented redistribution along the longitudinal direction of the quay, causing configurations with two piles to collapse.

The structural and geotechnical parameters used to model the GBW align with those employed in modelling the Overamstel quays, but with a slightly lower soil resistance and higher external loading. This similarity lends credibility to the assessment of the GBW, even with lower soil resistance the outcomes would be only slightly different. To enhance the accuracy of the assessment, several considerations can be taken into account, such as incorporating the load history, accounting for soil and timber creep, addressing timber degradation over time, and including the redistribution effects of the masonry.

To conclude, this study demonstrates the feasibility of employing analytical models to comprehend the failure mechanisms of historic structures like quay walls, offering valuable insights into their behaviour. The conducted analyses serve as an additional validation step for the developed quay wall model, specifically for applications to the quay walls of Amsterdam’s historical centre.

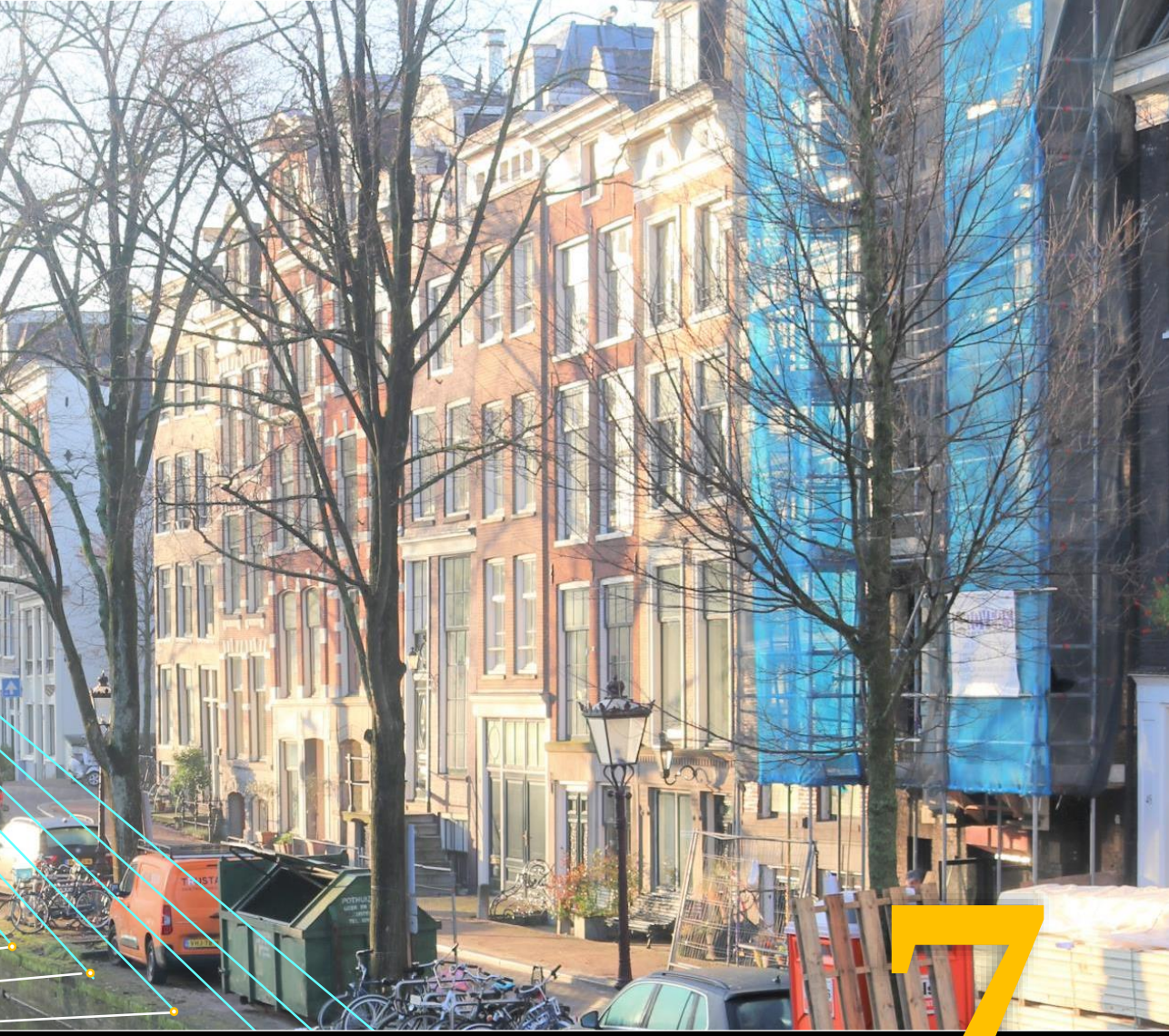

7

Reliability updating for lateral failure of quay walls[1]

In this chapter the analytical quay wall model is used to demonstrate the potential of Bayesian updating for historical inner city quay walls. The work in this chapter has been reviewed and advised by dr.ir. Timo Schweckendiek, a specialist in Bayesian updating and an expert in reliability and risk analysis for civil engineering applications.

[1] This chapter is part of the publication "Reliablity updating for lateral failure of historic quay walls", which is currently under review by Georisk (Hemel et al., 2023)

Photograph by the author

7.1 Introduction

Amsterdam faces the challenge of maintaining a 200km historic quay wall area, which is a vital part of the city's historical landscape. The quay wall construction consists of a masonry cantilever wall on top of a timber floor, which is supported by headstocks situated on three to six timber pile rows. These piles are often founded on sloping canal beds. A historic technical drawing, containing the terminology of quay wall components, is presented in Figure 1.5. The quays are over a century old, have various configurations, and are heavily used by road traffic, including heavy vehicles. However, signs of damage, partial collapse, and warnings of future failures have been observed (Korff et al., 2021). Calculating the stability and resistance of historic quay walls has shown that it is difficult to demonstrate sufficient safety. It seems that these models are too conservative, because in reality, the majority of the existing structures that proof unsafe on paper is performing quite well, referring to them as "metastable". Historical quay walls may be subject to a variety of identified failure mechanisms (see chapter 1 for details). This research focuses on the lateral failure of timber pile foundations, which is the most critical failure mechanism observed in Amsterdam's city centre. The mechanism involves soil pressure pushing the quay wall towards the canal side, countered by the lateral resistance of the pile foundation. If the active horizontal force exceeds the resistance of the pile group, lateral failure of the pile foundation can occur due to geotechnical or bending capacity failures, or a combination of them. This type of failure can result in the entire quay and its foundation collapsing into the canal, having significant consequences. Limited understanding of the lateral behaviour of historic quay walls is attributed to factors such as poor documentation of their geometry, bacterial deterioration of the timber piles, and the complex interaction between closely-spaced timber piles and cohesive soils. Additionally, there are uncertainties regarding the geotechnical input data and how the soil transfers its weight, the depth of the canals and the occurrence of surface loads.

This chapter aims to implement Bayesian updating to reduce uncertainties in geotechnical and structural parameter distributions associated with the lateral failure mechanism of historic quay walls. Bayesian updating is a powerful method that effectively can reduce uncertainties in structural and geotechnical model input parameters, leading to a more precise understanding of the structural safety (Beck et al., 2002; Straub et al., 2015). Information on engineering systems through monitoring, direct observations or measurements of system performances can be used to update the system reliability estimate (Straub, 2011). This principle is also referred to as proven strength or reliability updating and is a well-known technique within the geotechnical and civil engineering sector (Yuen, 2010).

Examples in literature are found in a variety of fields within the engineering sector. Enright et al. conducted a study focused on enhancing the prediction of future bridge conditions (Enright et al., 1999). The study incorporated inspection information and engineering judgment into a quantitative assessment through the application of Bayesian updating. This was achieved using adaptive importance sampling and numerical integration methods. In the same field, Bayesian updating was used to include laboratory test data, field observations and engineering judgement into the assessment of reinforced concrete bridge columns under seismic excitation (Choe et al., 2007). Chung et al. applied Bayesian techniques to a simulation model of the North Edmonton Sanitary Trunk tunnel project, demonstrating significant improvement in projection accuracy (Chung et al., 2006). Past performance, such as the survival of a loading condition, is an example of valuable information that can be utilized to enhance reliability estimates. Examples of such studies are

survival of a phreatic level when analysing slope stability (Li et al., 2015; Zhang et al., 2011) or an extreme observed water level into the assessment of the piping mechanism of dikes (Schweckendiek, 2010; Schweckendiek et al., 2014). Following that same analogy, pile proof load tests are used to reduce uncertainties in the design and construction of pile foundations (Ching et al., 2011; Zhang, 2004). Other forms of survived loading conditions during the lifetime of the structure can be traffic loads (Gao et al., 2021; Yu et al., 2019) or other service loads (such as soil retaining function or own weight).

The utilization of Bayesian Updating in the context of quay walls is not a fully novel concept. A study conducted by (Den Adel et al., 2019) explored the feasibility of incorporating performance information in the assessment of quay walls. The researchers conducted a case study involving an existing combi-wall quay structure and employed fictitious measurement data to showcase the potential impact of test loading on the reliability of the structure. To model the combi-wall quay a Blum model, which was verified using Finite Element Method (FEM), was employed. The effect of corrosion-induced degradation on the reliability of service-proven quay combi-walls was studied by (Roubos et al., 2020). Including successful service conditions helped to reduce time-independent uncertainties such as the uncertainty in soil strength, leading to an increase in reliability.

The studies mentioned demonstrate that incorporating the past performance of structures or observations into the reliability assessment can enhance the accuracy of reliability estimates and reduce uncertainties associated with individual parameters. Up to now, the application of Bayesian updating has not been explored in relation to (the lateral failure of) historic inner-city quay walls. These quays face specific challenges such as unknowns in geometric layout, complex pile-soil-pile interaction and timber degradation for which Bayesian updating can improve the assessment, thereby preventing the need for large-scale and time-sensitive replacements.

Thereto this chapter presents a methodology for incorporating survival and observational information, such as the survival of extreme surface loads and observed deformations, into the reliability analysis of lateral failing historic inner-city quay walls. By integrating this information, not only does it result in a more precise and realistic estimation of failure probability, but it also allows for the reduction of uncertainties associated with individual parameters. Thus, this chapter provides an answer to the key research question formulated below.

"How can Bayesian updating be applied to reduce uncertainties in failure probabilities and refine geotechnical and structural parameter distributions associated with the lateral failure mechanism of historic quay walls?"

The lateral pile-soil-pile interaction is an essential component to include when modelling the lateral failure of quays. Soil-structure interaction is a complex and nonlinear process involving the influence of piles on the soil and vice versa, impacting neighbouring piles. Key factors influencing this pile-soil-pile interaction include pile spacing, diameter, material, soil properties, loading type, and bed slope (Kavitha et al., 2016). Currently, computational Finite Element Method (FEM) software, such as ANSYS, ABAQUS, or PLAXIS, is commonly used to solve soil-structure interaction problems accurately. However, these software models involve a significant number of mesh nodes, leading to increased computational effort (Farmaga et al., 2011; Lou et al., 2011). Bayesian updating, which requires many simulations, poses a challenge due to the demand for fast computational time (Ehre et al., 2018). To

overcome this challenge, this chapter employs the analytical quay wall model presented in chapter 5 to simulate the lateral failure of a fictious quay wall. This model (briefly explained in 7.3.1) is computationally fast, enabling many realizations in a short period of time. With this model, forces in the pile foundation and corresponding displacements can be obtained. The model has later been calibrated and proven adequate and sufficiently accurate for calculation of limit states.

The structure and approach of this chapter is as follows. First the theory of Bayesian updating and its application for inner-city quay walls is discussed in section 7.2. Two methods are discussed, Monte Carlo and Fragility curves. In section 7.3, a case study on a fictive quay wall is performed, demonstrating the potential of Bayesian updating. In this case study, an a-priori probability of failure is predicted for a reference period of 15 years. The probability of failure is then updated based on two types of observational evidence. The first type is evidence from an extreme survived load, while the second type involves incorporating deformation measurements taken during the extreme load event. The results of the case study are compared with NEN8700, which represents safety standards for existing buildings. Section 7.4 discusses the approach and obtained results. Finally, conclusions are provided in section 7.5.

7.2 Bayesian updating for lateral failing historic quay walls

This section provides the theory of Bayesian updating and its application on the lateral failure of historic inner-city quay walls.

7.2.1 A-priori reliability analysis of lateral quay wall failure

The safety of a structure can be expressed through the resistance R of the structure, which ideally must be greater than the load S throughout its lifetime. The resistance and load of a structure are typically considered as random variables, and the probability of failure P_f is the probability that the load S is greater than the strength R, as expressed in eq. 7.1.

$$P_f = P[R < S] \qquad \textbf{eq. 7.1}$$

The probability of failure can be expressed using a limit state function formulated as $Z = R - S$ (Roubos et al., 2020) in which failure of the system occurs when Z reaches a negative value. The associated failure probability is then $P_f = P[Z<0]$ and its probability of survival or reliability is defined as $P_s = 1- P_f$. The degree of safety is often expressed by the reliability index β, which is directly related to the failure probability as per $P_f = \Phi(-\beta)$. Here, Φ is the cumulative normal distribution. For cases where the resistance and load follow simple distributions, the failure probability can be easily solved analytically. However, in the case that the system consists of various (non-linear) components, each with its own distributions, the solution of the failure probability becomes complex. A general approach of such a complex system can be described using a continuous performance function $g(\underline{X})$ (Deng, 2006). The vector $\underline{X}$ consists of a collection of random variables such as material properties, geometric properties, loads and model uncertainties. For each of these variables, an appropriate stochastic distribution must be chosen. Parameters that do not have uncertainties can be distributed deterministically. The probability of failure (or an undesired event) is given in eq. 7.2 (Jonkman et al., 2015). In this equation, $f_{\underline{X}}(\underline{X})$ is the common probability density function (PDF) of $\underline{X}$.

$$P_f = P\left(g\left(\underline{X}\right) < 0\right) = \int_{g(\underline{X})<0} f_{\underline{X}}\left(\underline{X}\right) d\underline{X} \qquad \textbf{eq. 7.2}$$

The system failure considered in this study is the lateral failure of the historic quay wall pile foundation, depicted in Figure 7.1. In this mechanism, the soil pressure at the backside of the quay wall is increased by a surface load q[kN/m^2], causing a quay deflection w[m] towards the canal side accompanied by the bending of the timber piles. As such, quay wall foundation piles are not only loaded axially N[kN], but also laterally, introducing significant bending moments M[kNm] in the piles, which in their turn cause bending stresses σ_b [N/mm^2]. Pile breakage is expected to occur when the bending stresses in the timber pile exceed the modulus of rupture MOR [N/mm^2] of the timber. The quay wall system as a whole is considered 'failed' when one or more piles break, and subsequent progressive collapse is expected. Possible redistribution between piles after pile breakage is not considered here. The performance function $g(\underline{X},q)$ of this system is provided in eq. 7.3. In here, the external diameter of the piles is indicated with D[m]. No model uncertainty for σ_b is included. The corresponding a-priori probability of failure is given by eq. 7.4.

$$g\left(\underline{X}, q\right) = MOR - \sigma_b = MOR - \left(\frac{M}{\frac{\pi}{32}D^3} + \frac{N}{\frac{\pi}{4}D^2}\right) \qquad \textbf{eq. 7.3}$$

$$P_f = P\left(g\left(\underline{X}, q\right) < 0\right) \qquad \textbf{eq. 7.4}$$

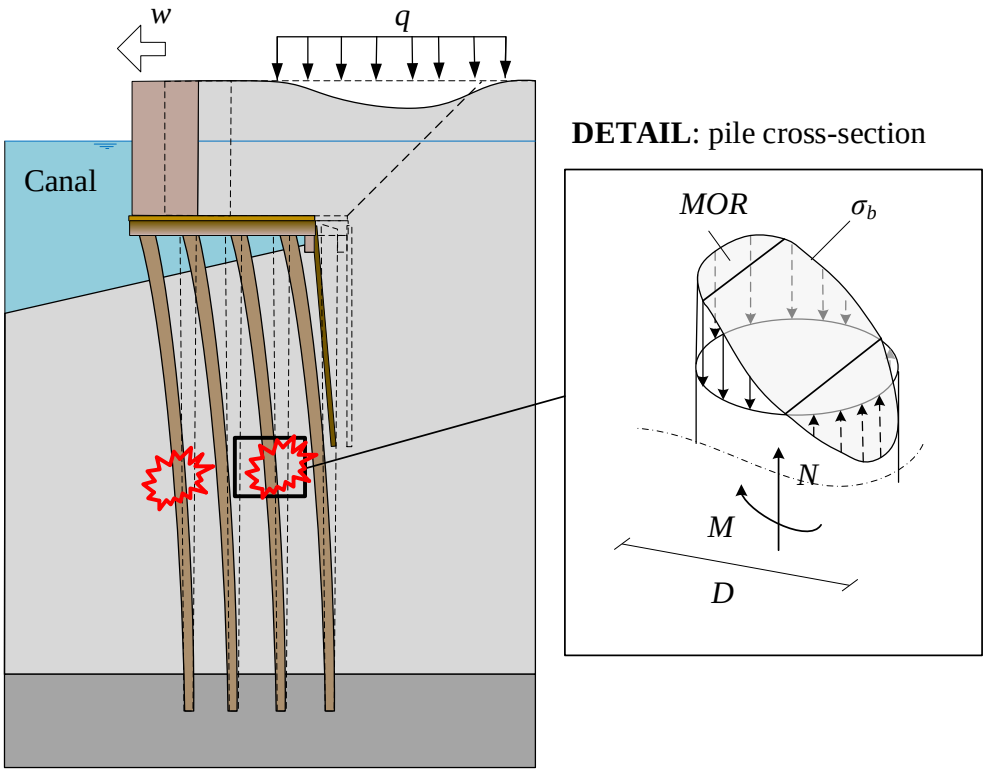

Figure 7.1, Failure mechanism 'Lateral failure of the quay wall foundation'. Detail of pile cross-section is provided in which bending stresses are indicated.

To describe the performance function $g(\underline{X},q)$, the analytical quay wall model is used, described in in 7.3.1. To determine the failure probability for this particular system, several probabilistic methods are available. In this study, two methods are considered for determining the probability of failure and updating it through Bayesian techniques. These methods are Crude Monte Carlo (MC) and fragility curves (FC). The theory for estimating the a-priori probability of failure using both methods is briefly outlined.

The Monte Carlo technique is a commonly used method for determining failure probabilities in complex systems with many stochastically distributed variables (Beck et al., 2002; Jiang et al., 2015; WANG, 2011). This methodology involves the use of random sampling, whereby thousands or more of calculations are performed. For each calculation, a random value is generated for each model input variable according to the corresponding chosen probability distribution. The failure probability can be determined by dividing the number of failed simulations $n_f = 1[g(X)<0)]$ by the total number of simulations n ($P_{f;MC} = n_f /n$). If the sample size goes to infinity, the exact failure probability is determined. With complex computations, a Monte Carlo calculation can take a considerable amount of time or even become unfeasible.

The second method applied in this study is the use of fragility curves (Kim et al., 2004; Schweckendiek et al., 2017). A FC represents the conditional probability of failure P_f as function of a (dominant) loading variable s, formulated in eq. 7.5. Here f represents 'failure' and $\underline{X}$ all random variables except for s. Fragility curves can be constructed by calculating the failure probability, in this study with FORM[1], for a number of deterministic loads s. Between the 'fragility points' linear interpolation can be used. Outside the fragility points, extrapolation can be used as long as the extrapolation takes place outside the boundaries of the area of interest. An example of a fragility curve for dominant load s is provided in Figure 7.2 and indicated in black. The observation fragility curve (in red) is discussed in section 7.2.2 and will be used in the posterior analysis.

$$P_{f;FC} = P(f|s) = P\left(g\left(\underline{X},s\right) < 0\right) \qquad \textbf{eq. 7.5}$$

Once a fragility curve has been constructed, it is possible to determine failure probabilities for any stochastic distributed load s without requiring additional computationally expensive model simulations. To do so, a limit state function is used in the form $Z = s_c - s$, in which s_c is the critical load. The critical load can be determined according to eq. 7.6 (Schweckendiek et al., 2016).

$$s_c = G^{-1}(u) \qquad \textbf{eq. 7.6}$$

where u is the realization of a standard normal random variable and G^{-1} is the inverse of the interpolated β-s curve $G(s)=\beta$. The problem $P_{f;FC} = P[Z<0]$ can be solved using Monte Carlo sampling.

[1] FORM (First Order Reliability Method) is seen as a good alternative to the 'brute force' Monte Carlo method (Bai, 2003). The method is an accurate approximation that requires significantly fewer calculations to determine the failure probability. FORM approximates the failure probability by linearizing the performance function g($\underline{X}$) with the help of Taylor series at the design point. With the FORM method, the sensitivity factor a_i can be determined for each variable.

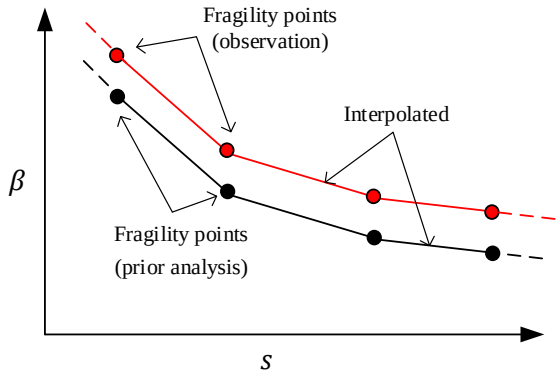

Figure 7.2, Example of fragility curves of dominant load *s*. In black, the FC for the reliability analysis. In red, FC including observational information of past performance.

7.2.2 Posterior analysis including evidence

Past performance of an existing structure is evidence η of its reliability and safety (Hall, 1988). The simplest example is that of a proof load. A structure survives a certain load, thus demonstrating that the resistance is at least equal to or greater than the load at the time of the proof load. This reduces the level of uncertainty associated with the resistance prior to the proof load. By taking the proof of the successful test load as evidence, the likelihood of failure will decrease and thus the reliability of the construction will increase. In addition to conducting proof load tests, there are alternative approaches to incorporate observational information into the posterior reliability analysis. For instance, one can examine successful loading conditions that the structure has endured throughout its lifespan, and integrate information derived from test data, measurements, monitoring, and direct observations (Papaioannou et al., 2012; Straub, 2011). The posterior probability of failure $P_{f,p}$, given evidence η, is determined according to Bayes' rule (Bayes, 1763) and presented in eq. 7.7. In here, the evidence η is described in terms of an arbitrary observational exceedance limit state function *O*, described by eq. 7.8.

$$P_{f,p} = P(f|\eta) = \frac{P(f \cap \eta)}{P(\eta)} = \frac{P\left(\left[g(\underline{X}) < 0\right] \cap \left[O(\underline{X}) < 0\right]\right)}{P([O(\underline{X}) < 0])} \quad \textbf{eq. 7.7}$$

$$\eta \equiv O(\underline{X}) < 0 \quad \textbf{eq. 7.8}$$

In the situation of multiple (*k)* simultaneous observations, the evidence is given by their intersection: $\eta \equiv \cap_k \{O_k(\underline{X}) < 0\}$ (Schweckendiek et al., 2014).

7.2.3 Evidence for historic quay walls

The posterior probability of failure for the historic quay wall system (described in section 7.2.1), given evidence η, is presented in eq. 7.9. In here, $g(\underline{X},q)$ is the performance function of the quay system. To conduct a posterior failure probability assessment, two types of evidence are considered in this study.

$$P_{f,p} = P(f|\eta) = \frac{P\left(\left[g(\underline{X},q) < 0\right] \cap \eta\right)}{P(\eta)} \quad \textbf{eq. 7.9}$$

The first evidence η_1 is the survival of the quay wall over its lifetime given an extreme surface load q_η [kN/m^2]. This evidence is formulated in eq. 7.10. Here, $\underline{X}_\eta$ is a vector of all random variables (except surface load q_η) at the time of observed survival of the quay wall. At the time of the observed extreme load, there is a positive performance function. Practical examples of extreme surface loads can be temporary storage of cargo or heavy vehicles such as fire trucks, garbage trucks or construction equipment.

$$\eta_1 \equiv g\left(\underline{X_\eta}, q_\eta\right) > 0 \qquad \textbf{eq. 7.10}$$

The second type of evidence η_2 involves expanding on the evidence presented in eq. 7.10 by incorporating deformation measurements. These measurements are specifically obtained at the same time as the extreme surface load was observed. Pile foundation deformations are physical coupled to timber bending stresses, which directly impact the limit state function. When large deformations occur, bending stresses are likely to be higher compared to situations with smaller deformations. If the model predictions on deformation do not align with the actual deformation measurements (i.e., if they are either too stiff or too flexible), it is a clear indication that the model input for simulating soil-structure interaction is incorrect. Given the variation in deformation measurements along quay walls, the deformation evidence is presented as a range, including both an upper and a lower boundary. The evidence of a range of deformation measurements at the time of an extreme surface load is provided in eq. 7.11. Here, $W(\underline{X}_\eta, q_\eta)$ is the model predicted quay wall displacement during the observation. Furthermore, $w_{\eta,min}$[m] and $w_{\eta,max}$[m] are the lower and upper bound of the deformation measurements.

$$\eta_2 \equiv \left[g(\underline{X}_\eta, q_\eta) > 0\right] \cap \left[w_{\eta,min} < W(\underline{X}_\eta, q_\eta) < w_{\eta,max}\right] \qquad \textbf{eq. 7.11}$$

7.2.4 Uncertainties in random variables

To calculate the posterior probability of failure of the quay system, two moments in time are considered. These are the end of the reference period for which the reliability prediction is made, and second, the moment in time when the evidence was gathered (e.g. observation of an extreme load and corresponding deformations). As stated before, a random vector $\underline{X}$ is used in the reliability prediction, while vector X_η is used at the time of evidence. Often, in the uncertainty of these vectors, a distinction can be made between epistemic uncertainty and aleatory uncertainty (Der Kiureghian et al., 2009). Epistemic means that the modeller may have possibilities to reduce the uncertainty of the variable by collecting more information or refining the model. Aleatory uncertainties are uncertainties that cannot be reduced by collection of information. Parameters such as an annual traffic load (other than an extreme traffic or test load) or phreatic water levels influenced by rainfall, describe a purely random process over time, and therefore are an aleatory uncertainty.

The "learning effect" in updating epistemic uncertainties is most pronounced when perfect auto-correlation in time exists. This means that parameters at the time of observation are perfectly correlated with the parameters used for the reliability prediction. Conversely, there is little to no learning effect for aleatory uncertainties. Consequently, treating an aleatory uncertainty as an epistemic uncertainty (assuming auto-correlation when there is none) may result in an underestimation of the posterior failure probability. When determining the probability of failure without utilizing historical evidence data (referred to as the "prior probability of failure"), the distinction between epistemic uncertainties and aleatory uncertainties is irrelevant.

7.2.5 Time dependent variables

In this study, a reliability prediction for a reference period of 15 years is made, as specified by NEN8700 "Veiligheidsfilosofie bestaande bouw" (Steenbergen et al., 2012). Because the observations are being made presently, there is a 15-year gap between the time of observation and the projected end-of-life for the quay wall. Hence, it is crucial to consider the (time-dependent) variations that may occur during this period when evaluating the reliability. Differences can be included in the random vector $\boldsymbol{X}$ at the end-of-life and random vector $\boldsymbol{X}_{\eta}$ at the time of the observation, allowing for a relative "best-estimate" difference (Schweckendiek et al., 2017).

Three differences between the observation and the projected end-of-life are considered in this study:

- **Pile degradation:** Timber piles are subjected to bacterial deterioration (Harmsen et al., 1965; Varossieau, 1949) influencing the strength and stiffness properties of the timber over time. The outer layers of the piles are mostly effected, creating a soft shell (without neglectable structural strength) around the core-wood (Pagella et al., 2021; van de Kuilen et al., 2021). In chapter 3, micro drillings were conducted on foundation piles of a quay wall that were 115 years old. The purpose of these drillings was to determine the thickness of the soft shell, which is illustrated in Figure 7.3. Based on the findings, the average thickness of the soft shell in the quay wall was determined to be 20mm. Assuming a linear degradation of the piles over time, an effective diameter reduction of 0.34mm/year is found. This implies that at the time of the observation, the piles are 5mm thicker compared to their expected thickness at the end of the 15-year reference period.
- **Canal bed deepening:** Deepening by bow thrusters of ships or dredging activities takes place in the canals of Amsterdam and was one of the main causes of the collapse of an Amsterdam quay wall named the 'Grimburgwal' (Korff et al., 2022). Lowering of the canal bed causes a reduction in lateral pile resistance and thus an increase in bending moments and bending stresses. A deepening of 0.2m is assumed over a 15 year reference period.
- **Surface load restrictions:** In the observation, 40-ton vehicles with a surface load of 10 kN/m^2 drove through the city centre. However, due to stricter traffic regulations, only lighter vehicles with a maximum surface load of 7 kN/m^2 are allowed during the remaining service life. As a result, the maximal surface load for the reliability prediction over a 15-year period is 3kN/m^2 lower than in the observation.

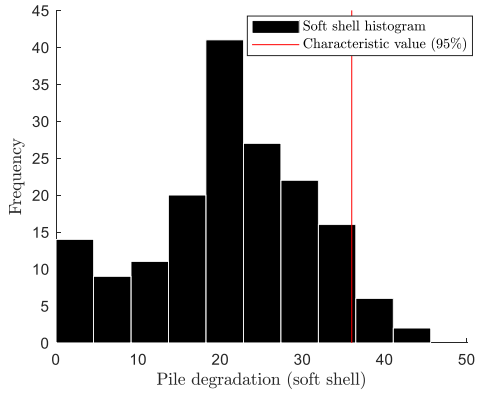

Figure 7.3, Pile degradation obtained with micro drilling (discussed in chapter 3).

Assuming a greater strength in observation does not lead to an underestimation of the posterior failure probability, but is rather a conservative assumption. The greater the difference between observation and the projected end-of-life, the more the posterior failure probability $P_{f,p}$ will approach the a-priori probability of failure P_f. It is important that the epistemic uncertainty in the structural and geotechnical modelling must be small (the computational model should not diverge much from reality). Otherwise, the effect of reliability updating is small and possibly unreliable.

7.2.6 Implementation for Bayesian updating

The posterior failure probabilities described in eq. 7.9 with evidence η_1 (in eq. 7.10) and η_2 (in eq. 7.11) is solved with Monte Carlo simulations and fragility curves. First, the sampling method Monte Carlo is evaluated. To this end, four steps are followed according to (Schweckendiek et al., 2014).

1. **Simulation of the event to be predicted:** n realizations of each parameter from vector $\underline{X}$ are generated according to the respective probability distributions. The j^{th} realization of the random variable i is denoted by $\underline{X}_{ij}$. The j^{th} realization of the random vector is denoted by $\underline{X}_j$.
2. **Prior probability of failure:** The prior probability of failure is determined by dividing the number of negative realizations of the performance function by n; $P_{f;MC} = \sum_j 1\left[g\left(\underline{X}_j, q\right) < 0\right]/n$, using the indicator function[1].
3. **Simulation of the event observed:** All epistemic variables maintain the same value as in simulation step 1: $\underline{X}_{\eta,ij} = \underline{X}_{ij}$ for all i where the uncertainty is to be reduced. For aleatoric variables, new realizations must be made according to their chosen distribution. For epistemic variables for which an average relative difference between observation and assessment is expected (but there is still autocorrelation in time) $\underline{X}_{\eta,ij} = \Delta + \underline{X}_{ij}$ applies, where Δ is the estimated difference between observation and assessment.
4. **Posterior probability of failure:** The posterior probability of failure can be calculated using eq. 7.12, given the evidence η_1. This formula is obtained by substituting eq. 7.10

[1] The indicator function is represented by 1[]. This means that if the criterion inside the brackets is met, the output of 1[] is equal to 1; if not, it is equal to 0.

into eq. 7.9. The posterior probability of failure for the evidence η_2 is expressed in eq. 7.13. This formula is obtained by substituting eq. 7.11 into eq. 7.9. The evidence η_2 is incorporated in the posterior analysis by inequality updating instead of equality updating, having the advantage of postprocessing $W(\underline{X}_\eta, q_\eta)$ without performing additional computations.

$$P_{f,p;MC,\eta 1} = \frac{\sum_j \left(\mathbf{1}\left[g\left(\underline{X_j}, q_j\right) < 0 \right] \cdot \mathbf{1}\left[g\left(\underline{X_{\eta,j}}, q_{\eta,j}\right) > 0 \right] \right)}{\sum_j \left(\mathbf{1}\left[g\left(\underline{X_{\eta,j}}, q_{\eta,j}\right) > 0 \right] \right)} \qquad \textbf{eq. 7.12}$$

$$P_{f,p;MC,\eta 2} = \frac{\sum_j \left(\mathbf{1}\left[g\left(\underline{X_j}, q_j\right) < 0 \right] \cdot \mathbf{1}\left[g\left(\underline{X_{\eta,j}}, q_{\eta,j}\right) > 0 \right] \cdot \mathbf{1}\left[w_{\eta,min} < W\left(\underline{X_{\eta,j}}, q_{\eta,j}\right) < w_{\eta,max} \right] \right)}{\sum_j \mathbf{1}\left[g\left(\underline{X_{\eta,j}}, q_{\eta,j}\right) > 0 \right] \cdot \mathbf{1}\left[w_{\eta,min} < W\left(\underline{X_{\eta,j}}, q_{\eta,j}\right) < w_{\eta,max} \right]} \qquad \textbf{eq. 7.13}$$

Next, the fragility curve method is evaluated. The use of fragility curves has two major drawbacks; the first one is that deformation evidence cannot be taken into account in the assessment because the deformation is an output value that is not fully correlated with the limit state function. Second, distributions of individual random parameters cannot be refined/updated. Consequently, with the FC method, only evidence η_1 is considered. Four steps are followed according to (Kanning et al., 2017; Schweckendiek et al., 2016).

1. **Fragility curve of the prediction:** Using the FORM method, the fragility curve is constructed with variable distributions from vector $\underline{X}$. For different deterministic values of q, the a-priori reliability index β is determined. Depending on the non-linearity of the β-q curve, the number of fragility points is determined.
2. **Fragility curve of the observation:** Using the FORM method, the observation fragility curve is constructed with variable distributions from vector $\underline{X}_\eta$. For different deterministic values of q, the observation reliability index β is determined. The fragility curves for the a-priori prediction and observation are presented in Figure 7.10.
3. **Critical surface load q_c:** The critical surface load is determined for the reliability prediction by $q_c = G^{-1}(u)$ and for the observation by $q_{c,\eta 1} = G_\eta^{-1}(u)$. Here, G_η^{-1} is the inverse of the interpolated β-q observation curve $G_\eta(q)=\beta$ and u is the realization of a standard normal random variable
4. **Posterior probability of failure:** System failure due to an excessive surface load is caused by a surface load q that is greater than the critical surface load; $f = [q_c<q]$. With n realizations, the prior probability of failure can be determined using $P_{f;FC} = \sum_j 1\left[G^{-1}(u_j) < q_j\right]/n$. The posterior probability of failure can be calculated using eq. 7.14, given the evidence η_1.

$$P_{f,p;FC,\eta 1} = \frac{\sum_j \left(\mathbf{1}\left[G^{-1}(u_j) < q_j\right] \cdot \mathbf{1}\left[G_{\eta,j}^{-1}(u_j) > q_{\eta 1,j} \right] \right)}{\sum_j \left(\mathbf{1}\left[G_{\eta,j}^{-1}(u_j) > q_{\eta 1,j} \right] \right)} \qquad \textbf{eq. 7.14}$$

7.3 Bayesian updating for historic quay walls: a case study

In this section, a case study is performed in which the reliability of a fictive historic quay wall is predicted for a reference period of 15 years and compared with reliability standards according to NEN8700. The prior probability of failure for the fictive historic quay wall is determined using Monte Carlo and fragility curves. The prior probability of failure is then updated to a posterior probability using the Bayesian approach as discussed in 7.2.6. In this approach, two types of evidence are considered. The first evidence η_1 is the survival of the quay wall over its lifetime given an extreme surface load. The second type of evidence η_2 involves expanding on evidence η_1 by incorporating deformation measurements. These measurements are specifically obtained at the same time as the extreme surface load was observed. First, the quay wall model and its inputs is discussed.

7.3.1 Quay wall model

To describe the performance function $g(\underline{X},q)$ and displacement $W(\underline{X},q)$, an analytical quay wall model is used, depicted in Figure 7.4. The quay wall model is extensively discussed in chapter 5. The model consists of a framework of elastic beams embedded in an elastic foundation and is externally loaded by a soil model based on the theory of Flamant. The beam model is made up of multiple Euler-Bernoulli beams, connected to each other by boundary and interface conditions. To model the lateral bearing pile-soil-pile interactions in layered sloping soil, a method developed by (Hemel, Korff, et al., 2022) is used, which is described in chapter 4. The analytical quay wall model has been successfully validated through experiments found in literature (Hemel, Korff, et al., 2022), as well as experiments conducted on historical timber quay walls in Amsterdam (chapter 4 and 5), which makes it an accurate tool for describing failure mechanisms of quay walls with regards to lateral pile behaviour, considering both structural and geotechnical aspects.

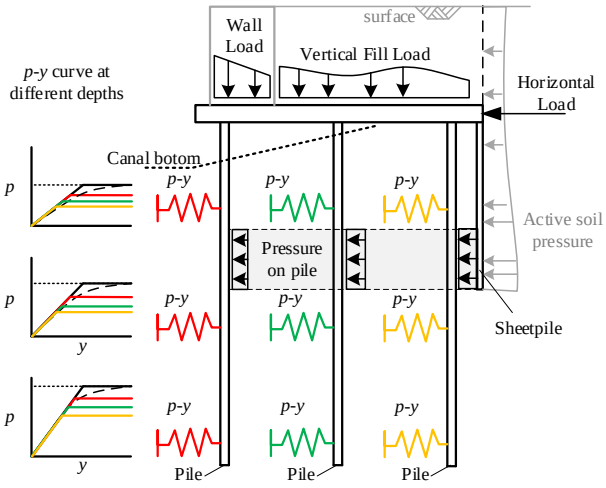

Figure 7.4, Schematic of analytical quay wall model in which structural members are described by beams on elastic foundations, externally loaded by an elastic soil model.

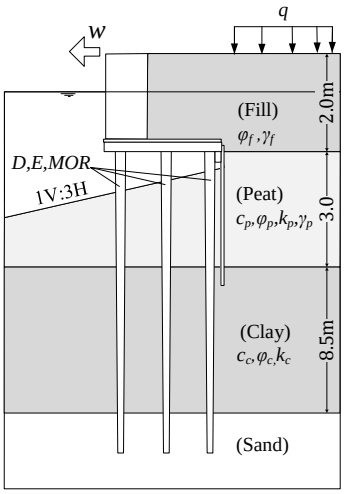

Figure 7.5, Schematic cross section of quay wall layout. Stochastic variables are indicated. Lateral deflection of the quay is described by *w*.

7.3.2 Quay wall layout and model input

The quay wall layout used in this case study is shown in Figure 7.5. Within this case study, it is assumed that the quay wall has a successful past performance during its lifetime. The layout is based on common quay wall geometries in the city centre of Amsterdam, literature, and previous research (Korff et al., 2021; Kuiper et al., 2020; Spannenburg, 2020). The quay is comparable to the 3 pile model of the Grimburgwal (see chapter 6). The quay wall consists of a gravity wall 0.8m wide and 2.0m high located on a floor with length 2.5m. The floor is supported by 3 piles with diameter *D*, modulus of elasticity *E*[MPa] and modulus of rupture *MOR*. The piles have their toe into the first sand layer, 13.5m below surface level. The piles have a spacing of 1m both parallel and perpendicular to the canal. At 0.3m behind the 3rd pile row a soil-retaining screen with a length of 4m is present. The water level is 0.7m below surface level, similar to the groundwater level. The fill of the quay consists of a 2m thick sand layer, ending at floor level. Below the floor lies a peat layer with a thickness of 3m. Below that a thick clay layer is present that goes up to the sand layer. The quay wall is loaded at a distance 2.5m from the canal by surface load *q* which has a width of 2m.

For the reliability analysis, stochastic distributions are assigned to the most dominant parameters. For the timber structure, these are the diameter, elastic modulus, and *MOR* of the piles. For the geotechnical parameters of pile embedded layers, the most dominant ones are the cohesion c, friction angle φ, effective weight γ, and stiffness k. Additionally, the friction angle and effective weight of the active soil volume behind the quay are considered dominant due to their effect on the load distribution. Table 7.1 shows the prior expected stochastically distributed parameters with their associated probabilities of occurrence during the remaining life. The parameters are assumed to be uncorrelated and epistemic, which is a simplification of the problem. The choice of dominant parameters is not fixed and is a choice of the designer. It must be ensured that parameters do not assume unrealistic parameters according to their distribution, e.g. negative values.

The reliability prediction is performed for a surface load of q = 7kN/m^2. This is the maximal allowed traffic load that is permitted in the remaining service life of the quay, based on a 15ton truck. This case study thus assumes that over the next 15 years, there will be a regular occurrence of critical loads of 7kN/m^2 with certainty. The surface load q is stochastically distributed with a coefficient of variation (CV) of 0.2 since there is an uncertainty in the force distribution from the truck wheels towards the soil. This distribution uncertainty is autocorrelated in time. For instance, if the surface load at the observation is 10% larger than the mean, it can be expected that the surface load will also be 10% larger than the mean at the end-of-life period. At the observation (now), the diameter is measured 0.245m on average and expected to degrade to 0.24m at the end of the 15-year reference period. The diameter has a CV=0.1 based on field experiments described in chapter 3, dive reports and data studies. The *MOR* is taken 22N/mm^2 with CV= 0.1 and the modulus of elasticity is taken 9,000MPa with CV=0.2. The (NEN-EN9997-1, 2012) is used to estimate the variation coefficients of the geotechnical parameters. Cohesive soil layers are modelled as drained due to the long time scale.

Table 7.1, Stochastic distributed input parameters and their distributions.

Variable	Unit	Type	Mean	CV
q	kN/m^2	Normal	7	0.2
D	Mm	Normal	240	0.1
MOR	N/mm^2	Normal	22	0.1
E	MPa	Normal	9,000	0.2
φ_p	deg.	Normal	15	0.1
c_p	kN/m^2	Normal	6	0.2
φ_f	deg.	Normal	30	0.1
φ_c	deg.	Normal	28	0.1
c_c	kN/m^2	Normal	4	0.2
k_p	kN/m^3	Normal	10,000	0.2
k_c	kN/m^3	Normal	4,300	0.2
γ_v	kN/m^3	Normal	2	0.05
γ_z	kN/m^3	Normal	8-18	0.05

7.3.3 Prior probability of failure

The prior probability of failure is made for a 15 year service life time. As such, a degraded pile diameter of 0.24m, a canal bed deepening of 0.2m and a 7kN/m^2 surface load are used in the prediction. A summary of the prior probability of failure analysis for the Monte Carlo and Fragility curves methods is given in Table 7.2. The probability of failure after 15 years service life, obtained with MC is $P_{f;MC}$ = 0.0651 and with FC is $P_{f,;FC}$ = 0.0603. For MC, 10,000 realizations were performed. For the FC approach, 6 fragility points are computed with the FORM method, requiring only 5% of the number of MC simulations. Another advantage of FC compared to MC simulations is the ability to calculate the prior probability of failure for any stochastic distribution of the surface load q after constructing the fragility curve, without requiring additional computationally expensive model simulations. The fragility curve is provided in Figure 7.10 (in black). The critical surface load q_c[kN/m^2] (without evidence) can be determined according to eq. 7.6 and is presented in Figure 7.11. The joint probability density function of the quay wall system is presented in Figure 7.6, which includes both failing and surviving samples from the Monte Carlo simulations. The sensitivity factors, obtained with FORM are presented in Figure 7.7. It can be seen that the uncertainty in the pile diameter has the biggest impact on the system reliability with a sensitivity factor of α^2= 0.668. Other dominant parameters (α^2> 0.04), are the cohesion of the peat c_p (α^2= 0.125), the surface load q (α^2= 0.067), effective weight of the fill γ (α^2= 0.048) and the friction angle of the peat φ_p (α^2= 0.041).

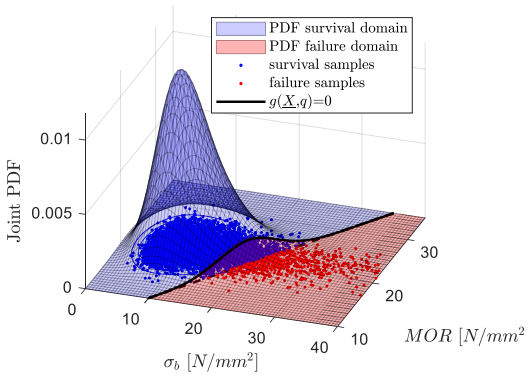

Figure 7.6, Joint PDF of quay wall system indicating the failure and survival domain.

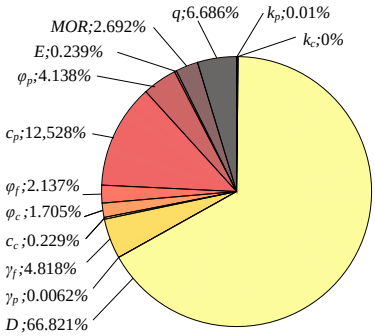

Figure 7.7, Sensitivity factors α^2 obtained with FORM computation.

Table 7.2, Prior probability of failures for historic quay wall example.

Method	P_f	β	Realisations	Simulation time (single pc)
MC	$6.51 \cdot 10^{-2}$	1.51	10,000	~ 3.5 day
FC	$6.03 \cdot 10^{-2}$	1.55	318	~ 4.8 hour

7

Based on NEN8700, the Dutch regulations for existing structures, three consequence classes are applicable to structures with a reference period of 15 years: CC3, CC2, and CC1b. These consequence classes correspond to reliability indexes of 3.3, 2.5, and 1.8 respectively. However, with a predicted reliability of approximately 1.5, the quay wall in this case study does not meet any of the requirements for the three consequence classes. Consequently, this quay wall fails to meet the necessary safety requirements.

7.3.4 Posterior probability of failure – Extreme load survival

In this section, the prior probability of failure is updated with evidence η_1, which is the survival of the quay wall over its lifetime given an extreme surface load q_η. Between the moment of observation and the time for which the reliability prediction is made, changes to the quay wall have taken place. As discussed in section 7.2.5, three time effects are taken into account. Firstly, the pile diameter at the observation is 0.245m, which degrades to 0.24m at the end-of-life period. Secondly, the canal bed is 0.2m higher at the observation than at the end of the 15 year reference period as a consequence of bow thrusters and dredging maintenance. Lastly, for the reliability prediction, the surface load is taken as q = 7kN/m^2, while during the observation, the surface load is q_η = 10kN/m^2. A summary of the posterior probabilities of failure analysis for the Monte Carlo and Fragility curves methods is given in Table 7.3. For reference, the prior probabilities of failure are also provided. The probability of failure is reduced by a factor 3.

Table 7.3, Prior and posterior probabilities of failure; given evidence η_1.

	Prior		**Posterior**	
Method	P_f	β	$P_{f,p;\eta 1}$	$\beta_{p;\eta 1}$
MC	$6.51 \cdot 10^{-2}$	1.51	$2.15 \cdot 10^{-2}$	2.02
FC	$6.03 \cdot 10^{-2}$	1.55	$1.94 \cdot 10^{-2}$	2.07

First, the effect of Bayesian updating is demonstrated by the Monte Carlo sampling method. In Figure 7.8, sampling calculations have been made using random vector $\underline{X}_\eta$ and q_η as model inputs. It is not possible to have the realizations (in grey) where the performance function $g(\underline{X}_\eta, q_\eta)$ is negative, as there is evidence that the quay wall has not failed in the observation. The dark blue and light blue dots are the remaining realizations where the quay wall does not fail. The remaining realizations $g(\underline{X}_\eta, q_\eta) > 0$ are used in the reliability prediction (with eq. 7.12) which is shown in Figure 7.9. In this figure, the blue dots are the survival realizations while the red dots are the failing realizations. The light blue points in Figure 7.8 indicate realizations that survive in the observation but fail in the reliability prediction. Light blue realizations in the observation fail in the prediction due to time-related effects considered, which weaken the quay wall over time. The decrease in pile diameter increases bending moments and reduces the moment of inertia, leading to higher bending stresses in the timber piles. Additionally, the canal bed deepening reduces lateral support, further increasing bending moments and stresses in the timber.

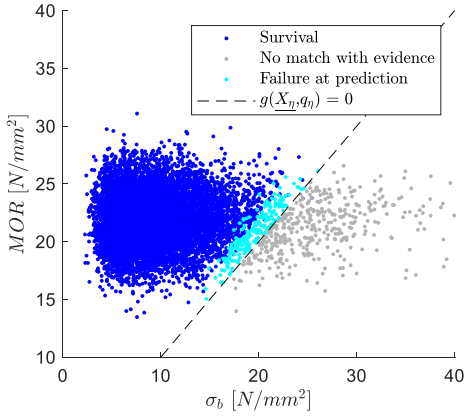

Figure 7.8, Posterior Monte Carlo sampling of observation with extreme surface load evidence.

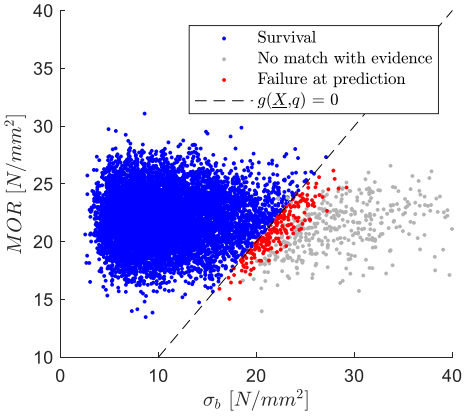

Figure 7.9, Posterior Monte Carlo sampling of reliability prediction.

Second, the effect of Bayesian updating is demonstrated using the fragility curve method. The fragility curves for the prediction and observation are presented in Figure 7.10. The fragility curve for the observation has on average a higher reliability which is due to the elevated canal bed and a larger pile diameter. Figure 7.11 displays multiple critical surface loads. The critical surface load for the a-priori prediction, denoted as q_c, represents the scenario without any evidence at the end of the service life time. On the other hand, the critical surface loads at the moment of an observed extreme surface load, q_η, is denoted as $q_{c,\eta 1}$. Both q_c and $q_{c,\eta 1}$ are utilized in eq. 7.14 to calculate the posterior probability of failure, $P_{f,p;FC,\eta 1}$. The resulting posterior probabilities of failure are presented in Table 7.4. It is observed that with larger extreme loads observed in the past, the left tail of the critical surface load $q_{c,\eta 1}$ at the time of observation shifts to the right, ultimately increasing the reliability of the structure in the prediction for a reference period of 15 years. Even without an observed surface load (q_η = 0 kN/m²), the reliability of the structure increases. This is because the pile foundation of the quay is laterally loaded by the active soil volume behind the quay, even in the absence of any surface load. Quay walls can fail without the presence of top loads, as

observed in the case of Grimburgwal (see chapter 6). Therefore, evidence of "survival" without any observed top load is already valuable.

Table 7.4, Posterior probability of failures for multiple observed extreme load survivals obtained with fragility curve method.

q_η [kN/m^2]	0	5	7	10	15	Prediction (no evidence $\eta 1$)
$P_{f;p;FC,\eta 1}$ [-]	5.58E-2	4.45E-2	3.36E-2	1.94E-2	0	$P_{f;FC}$ = 6.03E-2
$\beta_{p;FC,\eta 1}$ [-]	1.59	1.70	1.79	2.06	∞	β_{FC} = 1.55

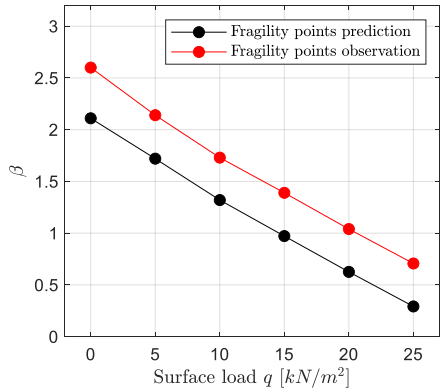

Figure 7.10, Fragility curves obtained with FORM. Fragility curve at observation in black and at prediction in red.

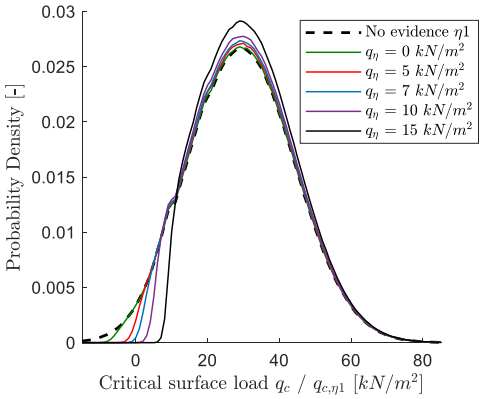

Figure 7.11, Critical surface load PDF. Dashed line represents prior analysis without evidence. Coloured lines represent observed surface loads.

7.3.5 Posterior probability of failure – Extreme load survival with deformation measurements

In this section, the prior probability of failure is updated using evidence η_2. This evidence pertains to the quay's successful past performance given an extreme observed surface load of 10 kN/m^2, while simultaneously considering the availability of quay wall deformation measurements taken at the same time of the observation. The deformation measurements, which capture a range of displacements along the quay wall and span the interval [$w_{\eta,min}$, $w_{\eta,max}$]. In this case study, it is assumed that all displacements of the quay wall are caused solely by the deflection of the pile foundation below the quay. Deformations resulting from, for instance, the sliding of the gravity wall or the tilting of the gravity wall are not considered. Time effects between observation and prediction are included as discussed in section 7.2.5.

The interval [$w_{\eta,min}$ = 0.02m, $w_{\eta,max}$ = 0.08m] is considered at the time of the observation. The Monte Carlo sampling at observation is presented in Figure 7.12. The horizontal axis contains the performance function $g(\underline{X}_\eta, q_\eta)$ (see eq. 7.3) and the vertical axis the displacement $W(\underline{X}_\eta, q_\eta)$. The relationship between displacement and the performance function shows a negative correlation, as larger deflections are associated with higher bending stresses. Consequently, quay walls with greater deflections are considered weaker. However, it's important to note that displacements and deflections are not fully correlated to the bending stresses. This lack of full correlation is the reason why the FC method cannot incorporate deformation evidence. The grey realizations in Figure 7.12 represent realizations where the performance function is negative (indicating failure) and the displacement

observation function is not fulfilled. The dark blue and light blue dots are the remaining realizations where the quay wall does not fail and deflects within the range of measured deflections. The remaining realizations are used in the prediction which is shown in Figure 7.13. In this figure, the blue dots are the survival realizations while the red dots are the failing realizations. Observing the "survived realizations" (in Figure 7.12) represented by the light blue and blue dots, it becomes apparent that the deflection and bending stress values increase when utilized in the prediction (in Figure 7.13). This increase is a result of the time effects that take place over the remaining lifespan of the quay wall, ultimately leading to failure for certain realizations. The posterior probability is updated according to eq. 7.14 from $P_{f;MC}$ = 6.51*E*-2 to $P_{f,p;MC,\eta 2}$ = 2.90*E*-3 which is an increase in reliability from β_{MC} = 1.51 to $\beta_{p;MC,\eta 2}$ = 2.75.

Observations do not necessarily lead to a reduction of the a-priori probability of failure. To demonstrate the effect of observed deformations on the posterior failure probability, the reliability index was set against the observed mean deformation w_η[m], depicted in Figure 7.14. The mean deformation is defined by $w_\eta = (w_{\eta,min}+w_{\eta,max})/2$. The difference between $w_{\eta,min}$ and $w_{\eta,max}$ is kept constant with 0.06m. For comparison, the a-priori reliability index is plotted. It can be seen that an increase in observed deformations results in a decrease of the reliability of the quay wall. With 0.1m of displacement, the posterior reliability becomes smaller than the prior reliability. The maximal reliability which can be obtained with 10^4 samples is $\Phi^{-1}(10^{-4})$ = 3.72, resulting in no reliability estimate for deflections smaller than 0.03m. Note the β-w plot in Figure 7.14 is influenced by surface load q and also by the observed surface load q_η.

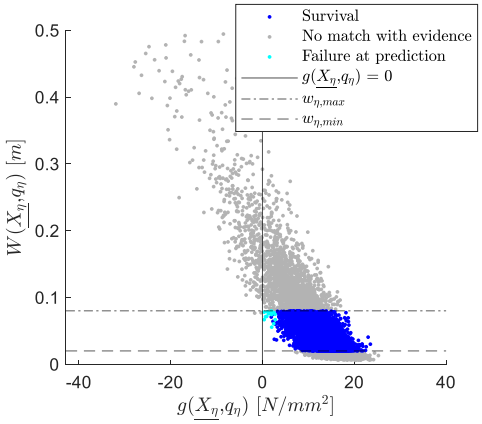

Figure 7.12, Posterior Monte Carlo sampling of observation with extreme surface load evidence in combination with deformation measurements.

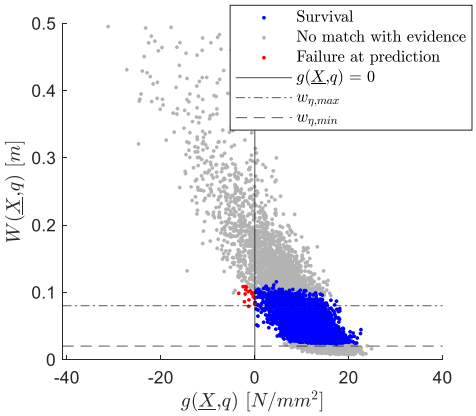

Figure 7.13, Posterior Monte Carlo sampling of reliability prediction.

A more general way to present the updated system is in terms of modulus of rupture (*MOR*) and model computed bending stresses (σ_b) which are the two main parameters in the performance function. For displacement range [$w_{\eta,min}$ = 0.00m, $w_{\eta,max}$ = 0.06m], the prior *MOR* and σ_b are visualized in Figure 7.15. It can be seen that Bayesian updating for quay walls primarily updates the model computed bending stress of the system, as 97% of the influence factors affect this parameter. The modulus of rupture of piles is hardly updated, as its influence factor is less than 3%. The posterior estimation shows a considerable reduction in the right tail of the bending stress compared to the prior estimation. This reduction leads

to higher posterior system reliability. Figure 7.16 shows the impact of Bayesian updating for the most dominant parameters, namely the pile diameter D, cohesion of the peat c_p, the surface load q as well as the effective weight of the fill γ for displacement range [$w_{\eta,min}$ = 0.00m, $w_{\eta,max}$ = 0.06m]. Parameter updating has the most significant impact the diameter and cohesion of the peat layer (together 80% of the influence factors). When evidenced deformations are small, the pile diameter tends to shift towards larger values, and the cohesion, which provides support pressure to the piles, shifts towards higher values during the postdiction. The reduction of the right tail in the a-priori computed bending stress shown in Figure 7.15 is primarily attributable to the updating of the pile diameter and the cohesion of the peat layer.

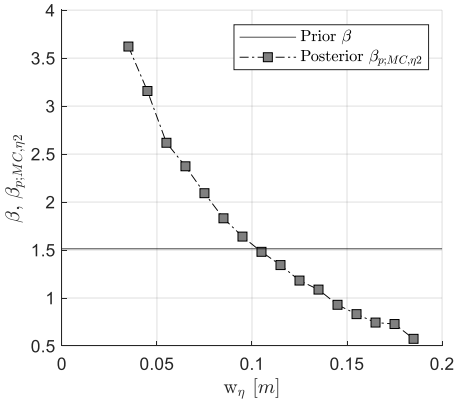

Figure 7.14, Posterior reliability index as function of displacement evidence for q = 7kN/m² and q_η = 10kN/m².

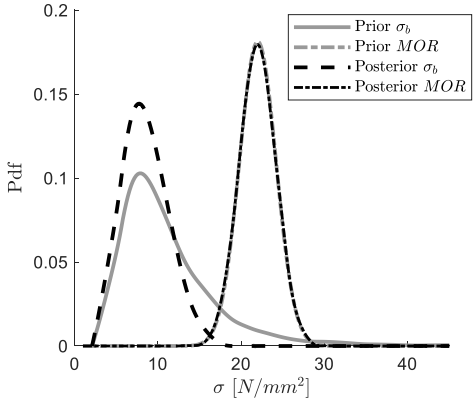

Figure 7.15, Prior and posterior *MOR* and σ_b. For $w_{\eta,min}$ = 0.00m and $w_{\eta,max}$ = 0.06m. Surface loads are q = 7kN/m² and q_η = 10kN/m².

7.3.6 Interpretation of case studies

Observations from the past can have a significant impact on the posterior reliability of historic quay walls. A summary of the various simulations and methods can be found in Table 7.5. Evidence of extreme observed surface loads during a test load (e.g. $q << q_\eta$) without failing, can increase the reliability of quay walls by multiple orders of magnitude. The same is true for deformation evidence, in which the reliability index can increase to over 3.7 in case of small deflections observed in the past (e.g.<0.04m). However, evidence of large deformations (e.g. >0.1m) can be proof that a quay wall has a high risk to fail. The case study presented in this chapter were conducted for a reference period of 15 years. To interpret the values listed in Table 7.5, the guidelines specified in NEN8700, known as "Veiligheidsfilosofie bestaande bouw" in Dutch, are employed. For structures with a reference period of 15 years, three consequence classes are defined: CC3, CC2, and CC1b, each corresponding to specific reliability indexes of 3.3, 2.5, and 1.8, respectively. The case studies indicate that, depending on the evidence, the posterior reliability can fall within any of the 3 consequence classes, if the a-priori prediction suggests insufficient safety.

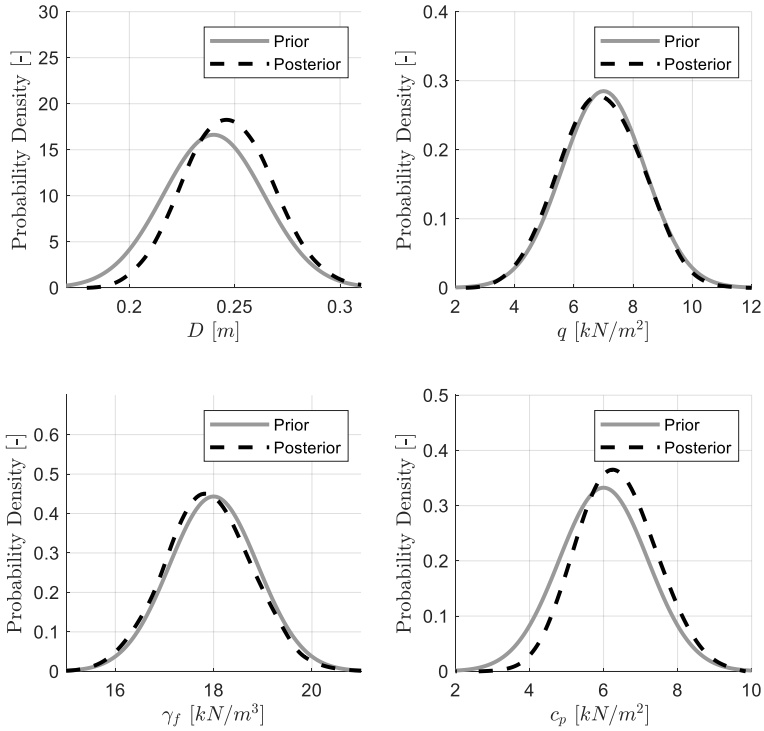

Figure 7.16, Prior and posterior stochastic distributions of individual parameters - evidence $w_{\eta,min}$ = 0.00m and $w_{\eta,max}$ = 0.06m. Surface loads are q = 7kN/m² and q_η = 10kN/m². Top left is the diameter D, top right is the surface load q, bottom left is soil weight of the sand fill and bottom right is the cohesion of the peat layer c_p .

Table 7.5, Summary on prior and posterior reliability index for various observations.

Method	Observation evidence	Prior β	Posterior β_p
MC	q_η = 10kN/m²	1.51	2.15
	q_η = 10kN/m² & 0m <w_η< 0.04m	1.51	>3.72 – 3.2
	q_η = 10kN/m² & 0.04m <w_η< 0.10m	1.51	3.2 – 1.5
	q_η = 10kN/m² & 0.10m <w_η< 0.20m	1.51	1.5 – 0.5
FC	q_η = 0kN/m²	1.55	1.59
	q_η = 5kN/m²	1.55	1.70
	q_η = 7kN/m²	1.55	1.79
	q_η = 10kN/m²	1.55	2.06
	q_η = 15kN/m²	1.55	∞

7.4 Discussion

First, the limitations of the used quay wall model, and its effect on the results are discussed. The applied analytical quay wall model does not take into account loading history. Repetitive loadings from the past causes (plastic) deformations in the long term. Combined with time effects such as soil creep and timber relaxation, model deformations but also bending stresses may be inaccurate, but are believed to be conservative. Furthermore, the modulus of rupture and the modules of elasticity of the timber are time- and load dependent (van de Kuilen et al., 2021). This effect is not included, possibly overestimating the posterior reliability. The dependence of timber strength on its loading history is one of the greatest challenges for the intended application. This aspect should be further considered by timber experts. To take into account these kinds of effects, more complex software is needed. However, increasing the complexity of models results in greater computational times, making sampling methods less attractive. It is necessary to find a balance between the computational complexity and the computational speed. To overcome this challenge, it is advised to perform deterministic time-dependent computations using FEM software. These computations should include the effects mentioned earlier and assess their impact on the overall force distribution within the foundation. By calibrating the analytical model based on these computations, it can still be used in the probabilistic Bayesian analysis conducted in this chapter. If the use of FEM models is still desired, it is advised to employ the fragility curve approach as it significantly reduces computational effort (more than 18 times in this study) compared to Monte Carlo simulations.

Second, a discussion on Bayesian updating on lateral failing quay walls is provided. In this analysis a simplification has been made; the maximum deformation of the quay wall is only due to the greatest load the quay has experienced during its lifetime. Furthermore, extreme events from the past may have weakened the quay wall structure. As a result, there will no longer be a perfect correlation between the moment of observation and the prediction. Moreover, assuming stochastic parameters to be uncorrelated may lead to an overestimation of the system's reliability. For instance, it is observed that the modulus of rupture and modulus of elasticity are strongly correlated (see chapter 3). Other examples of correlations between stochastically distributed parameters include the densities of soils and friction angles, as well as the stiffness of the soil and cohesion and friction angle.

Third, a discussion on the applied probabilistic methods is given. In the Monte Carlo analysis, 10,000 samples were used to demonstrate the potential of reliability updating, which is a bit low. For further analysis, it is advised to perform more computations in order to get a higher accuracy. Promising methods to drastically reduce computational time are importance sampling or surrogate modelling which is roughly similar to the computational time needed for FORM.

Lastly, the practical implementation and applicability of Bayesian updating for quay walls in the city centre of Amsterdam are discussed. The quay configuration, as well as the soil and structural parameters used in this study, are highly representative of the quay walls found in the city centre of Amsterdam. Notably, examples such as Grimburgwal and Herengracht (Spannenburg, 2020) feature quay walls with three piles, although the exact length in meters this type of quay is not known. However, Amsterdam has many quay walls which all have a unique configuration. Variation in the number of piles, the retaining height, the location of the soil retaining screen, the presence of trees, and the traffic intensity may be present. Therefore, it cannot be said in advance whether the impact of proven strength will be similar to other quay wall configurations. Further exploratory studies should be undertaken to demonstrate the impact of Bayesian updating on different configurations of

quay walls, utilizing similar observations. Furthermore, only two types of evidence are included in the posterior assessment of lateral failing quays. However, evidence can be collected through various monitoring methods, such as measuring pile rotations, surface settlements, or lateral soil deflections behind the quay.

A more general aspect to consider is that the method in this chapter includes only one failure mechanism. The failure of a quay wall is usually a combination of different failure mechanisms, as the study of the collapsed Grimburgwal (Korff et al., 2021) showed. By taking into account multiple failure mechanisms in the analysis, it can be better clarified what the impact of proven strength is on the posterior reliability. It is important to note that different failure mechanisms may require different types of evidence. For instance, to assess the overturning of the masonry wall, deflection and rotation measurements can be utilized. Similarly, settlement data from the masonry wall or the piles themselves can be used to evaluate the vertical settlement of the entire pile foundation.

7.5 Conclusion

This chapter describes how evidence of survived loading situations and related deformations that occurred in the past can be quantitatively taken into account in the reliability assessment of historical quay walls. The application of the available theory to a quay wall on laterally loaded piles is, as far as is known, done for the first time and the results show that this is feasible and has a lot of potential. Two methods, Monte Carlo sampling and fragility curves, were used to implement the theory of proven strength. With MC individual parameters , individual parameters such as pile diameter and cohesion of soils can be updated, which is not possible with fragility curves. However, the MC method is computationally expensive compared to the fragility curve method. Once a fragility curve has been constructed, it is possible to determine failure probabilities for any stochastic distributed load without requiring additional computationally expensive model simulations.

A case study on a fictitious quay wall was performed, demonstrating the potential of Bayesian updating. In this case study, an a-priori probability of failure was predicted for a reference period of 15 years. Subsequently, the probability of failure was updated by considering two types of observational evidence. The first type involved evidence derived from an extreme survived load, while the second type incorporated deformation measurements obtained during the extreme load event. Based on the findings, the following conclusions can be drawn:

- Depending on the evidence, the posterior reliability can fall within any of the 3 consequence classes (CC3, CC2, and CC1b outlined in NEN8700), if the a-priori prediction suggests insufficient safety and strength. Updating can thus have a significant effect on the reliability estimate.
- The greater the observed extreme surface load compared to the surface load used in the prediction, the greater the difference between prior and posterior reliability of the quay wall.
- If there is a large difference between the condition of the quay wall at the time of observation and the time of the reliability prediction, the effect of the observations on the posterior reliability decreases. Large differences between observation and prediction can be caused by, for example, pile degradation, deepening of the canal or a reduction of the timber strength due to time effects.

- Deformation measurements at the time of observation have a strong influence on the updating of a prior determined failure probability. Small deformations lead to a small failure probability while large deformations lead to a large failure probability. The deformation of the pile foundation is strongly correlated with the bending stresses within the foundation itself. It is anticipated that larger deformations correspond to higher bending stresses, and vice versa.
- Bayesian updating has the greatest impact on parameters with high influence factors. In the case study, the pile diameter and the cohesion of the shallow peat layer showed the largest differences between prior and posterior parameter uncertainties.

The following recommendations are given:

- In order to test the applicability and robustness of Bayesian updating on quay walls, it is important to consider different case studies. Variations can be made in the main characteristics of the quay wall for each case.
- Further research is needed in methods to include the load history of quay walls. Repetitive loading, soil- and timber creep, and strength reduction over time are effects that are of paramount importance to be included in the reliability prediction of historical quay walls.
- By performing non-destructive tests in the city centre (operational load testing), additional evidence can be obtained about quay walls. For example, a truck can be parked as a static load for a certain period of time on a quay wall while the deformations are measured at the same time. This methodology must be carefully studied to determine the extent to which the load test has caused permanent damage to the quay wall. In the case of a load test, it is necessary to make an estimation in advance of the probability of damage/failure and corresponding deformations, both of which should be sufficiently low.
- To make more reliable failure probability analyses, it is important to conduct further research into the correlation between randomly distributed parameters.
- Uncertainties concerning parameters can be reduced by conducting on-site inspections and investigations. It has been revealed that pile diameter is the most dominant parameter. By conducting further research into the pile diameter at the location to be assess, a large part of the uncertainty can be eliminated.
- It is recommended to systematically apply the method to any structures whose exact geometry and loading history are known. Ideally, a simple model similar to the one used in this study should be used, but calibrated with finite element models and/or with a loading test.
- The principle of Bayesian updating can significantly influence the failure probability related to various failure mechanisms in quay walls. It is recommended to explore the potential of Bayesian updating for assessing other failure mechanisms as well.

8

Conclusions and recommendations

Photograph source: AMS institute

8.1 Conclusions of this study

The primary objective of this study has been to gain a comprehensive understanding of the quay wall failure mechanism known as "lateral failure of the pile foundation" through full-scale experiments conducted on historic quays. In parallel, a second and equally important objective in this thesis has been the development of a reliable computational quay wall model that accurately predicts the resistance against lateral failure, excluding excessive conservatism. Based on the defined objectives, a main research question along with its corresponding key research questions were formulated. These questions will be addressed below, starting with the main research question and followed by the key questions. A concise discussion is provided for each key question. A general discussion and reflection are provided in section 8.2.

8.1.1 Answering the main research question

How can the lateral failure of the pile foundation of historic inner-city quay walls be understood and predicted with computational models?

The lateral failure of the pile foundation of historic quays is a serious issue that can lead to the complete collapse of the quay and its foundation into the canal. A unique extensive full-scale experimental program was conducted on a quay wall in Amsterdam Overamstel to understand this failure mechanism, revealing that it is most likely to occur when a quay wall experiences large surface loading at its backside. This load causes an increase in soil stresses, pushing the foundation towards the canal and resulting in bending of the timber piles, which can ultimately lead to pile fractures. The failure load was found to be at least 2.6 times higher than predicted by state-of-the-art models. While part of this underprediction can be attributed to experiment-specific effects not considered in the prediction analysis, the substantial underprediction of the failure load emphasizes the conservatism in current modelling approaches. Indicators of lateral failure include inclined piles, settlements at the backside, and lateral deflection of the foundation with masonry wall. This study proved the effectiveness of a sophisticated monitoring plan for detecting lateral failure in quays. Elements of this plan can be implemented in Amsterdam's city centre. For instance, inclination sensors on the pile caps, monitoring soil motions behind the quay, or tracking the deflection of the masonry wall combined with a tilt sensor.

Fracture of foundation piles happens when piles reach full yielding, meaning that over the entire pile cross-section, bending stresses exceed the modulus of rupture. Lateral load carrying capacities vary greatly in pile groups, primarily attributed to the natural variation and biological degradation that affect pile stiffness and bending capacity. For the subsoil at the Overamstel site, elastic-plastic behaviour (partly yielding) starts at approximately 100mm of group deflection, with the first pile fracture occurring at 140mm and group failure at 200mm. It is important to note that the transition from elastic-plastic (partly yielding) to group failure requires only a slight additional lateral load (15%), emphasizing that the onset of pile yielding should not be perceived as a safe condition.

The resistance against the lateral failure of historic quays can be predicted with a newly developed analytical quay wall model. The model consists of a framework of elastic beams embedded in an elastic foundation and is externally loaded by a linear elastic soil model

based on the theory of Flamant. Pile-soil-pile interactions and sloping surfaces are included. It accurately predicts lateral displacement, pile bending moments, and bending stresses, enabling the assessment of pile fracture under specific loads. It has advantages over FEM software in terms of robustness, computational speed, feedback loops, minimal input requirements, and suitability for trend analysis, probabilistic analysis and sensitivity studies. The model is successfully validated with field experiments from literature, from experiments on the Overamstel quay in Amsterdam and FEM computations. It was applied in two studies, one investigating the failure of the Grimburgwal quay in 2021, providing insights for Amsterdam's historical centre, and the other showcasing the potential of Bayesian updating to refine reliability predictions and estimates of parameter distributions.

To conclude, the modelling accuracy, as a result of the Overamstel experiments, significantly improved. The revised "gain" in modelling accuracy for bending moments and deflection was 43% and 37% respectively (excluding experiment specific effects such as segmental friction, which increased the strength of the quay wall). This improvement can be attributed to advancements in modelling techniques, such as accurately simulating pile-soil-pile interaction and modelling the pile-headstock connection, as well as utilizing precise location-specific geotechnical and structural material properties as model input. The improved modelling accuracy results in a less conservative evaluation of the quay walls, leading to a reduction in the number of unnecessarily rejected quay walls for the Amsterdam quay wall domain.

8.1.2 Answers to the key research questions

I. How can an experimental program be designed to enhance our understanding of the lateral failure of historic quay walls, and to validate and calibrate computational quay wall models?

Answer: Other than for many – more predictable – systems is was expected that a proof load on a historic quay wall would greatly increase the insight in the real behaviour and capacity under overload and/or a critical deformed state. Since every quay wall structure interacts with the local subsoil in various ways, a clever experiment design was needed. Thereto, a comprehensive unique full-scale proof load testing program was conducted on a historic quay wall (dating back to 1905) in Overamstel, Amsterdam, to enhance our understanding of its lateral failure. The program involved three levels of experiments, targeting different aspects of the quay wall system. Level 1 focused on timber pile bending, level 2 on lateral pile groups (3x4), and level 3 on isolated 6.5m wide quay wall segments overloaded by a ballast container. This stepwise approach allowed for validation and calibration of computational models, reducing accumulation of uncertainties and providing a comprehensive understanding of the lateral failure mechanisms in quay wall systems. The experiments were conducted multiple times, incorporating slight variations in the set-up, in order to ensure consistency in the results and investigate specific effects. For instance, in the case of the pile group experiments, variations were introduced by testing with and without top load, enabling validation of the pile-headstock model. Similarly, in the quay wall experiments, different scenarios were explored by varying the location of the surface load or adjusting the number of pile rows. For each experiment an sophisticated monitoring plan was designed to closely measure forces and motions of both structural elements and subsoils.

Discussion: The pile foundation of the Overamstel quay wall is constructed using diagonal raking piles that provide horizontal stability to the quay, effectively preventing bending of the timber piles and subsequent lateral failure over its lifetime. As a result, it is not possible to ascertain time-dependent effects from the past with respect to the lateral failure mechanism. Note that in order to enable the lateral failure of the quay wall foundation, the raking piles were intentionally disabled. Also during the execution of the experiments it was not possible to study time-dependent effects due to the short time scale (less than a week).

II. What are the bending properties of centuries old timber quay wall foundation piles?

Answer: In bending experiments conducted on spruce foundation piles (level 1), notable variations were observed in both modulus of elasticity (variation coefficient = 0.26) and modulus of rupture (variation coefficient = 0.30) among individual piles. These coefficients of variation are larger than values found in literature for 'new' spruce piles. Based on effective pile diameter measurements, the mean values were determined to be 16.5GPa for the modulus of elasticity and 23.2N/mm^2 for the modulus of rupture. Despite these variations, a strong correlation was found between the two bending properties. The average flexural stiffness (in terms of a Young's modulus) at the critical location, situated 2m from the cap, was determined to be 783kN/m^2. The variations in mechanical properties are attributed to natural variability and bacterial deterioration, predominantly affecting the outer layers of the piles. This deterioration results in a soft shell with an average thickness of 21mm. The soft shell represents approximately 10% of the external pile diameter which is on average 0.24m at 2m below the cap. The observed soft shell contributes minimally to the overall strength, advising to perform bending capacity checks with effective diameters. Interestingly, bacterial deterioration appears to be independent of pile diameter and longitudinal pile location. Micro-drilling proves effective in identifying the soft shell, and correlations have been established between drill resistance and the modulus of elasticity/modulus of rupture. This enables the estimation of location-specific mechanical bending properties for individual piles through in-situ micro-drillings.

Discussion: Only a small population of six piles was subjected to bending tests. It is important to acknowledge that the results obtained from this limited sample may not fully capture the variability and characteristics present in a larger population of piles. Furthermore, pile foundations of quay walls are challenging to access using micro-drillings as they are embedded in soil. In practical terms, the first meter of the front pile row can be easily reached, but accessing the rear piles is more difficult due to soil retaining screens, inclined bed slopes, and the presence of the front pile row. As a result, in practice, drillings can only be conducted, if feasible, at the pile caps rather than at various depths along the piles. Bacterial deterioration in piles can occur randomly along their length, making it risky to rely solely on micro-drillings at the uppermost part for estimating timber strength properties.

III. How can the lateral pile group interaction of historic foundation piles be modelled and validated through testing?

Answer: The lateral pile group interaction of historic foundation piles can be described and modelled well by an analytical pile group model proposed in this thesis. It is decided to use

an analytical model instead of a finite element model (such as PLAXIS) because analytical methods offer several advantages in terms of robustness, computational speed, feedback loops, and minimal input requirements. In contrast, finite element software often requires significant computation time to model complex soil-pile-soil interactions and often has numerical stability issues with large deformations. The faster computation times and robustness associated with analytical models allows for trend analysis, probabilistic analysis, and sensitivity studies, which are of interest in this thesis.

In the proposed modelling method, the bending of a pile, which is subjected to a lateral load and axial load, is described by a beam on a Winkler elastic foundation in which the soil behaviour is represented by a series of independent p-y springs, idealized with a bilinear elastic-perfect-plastic approximation. The plastic limit is computed with Brinch Hansen ultimate soil resistance and the elastic soil response by the Ménard stiffness. The plastic limit is corrected for each depth, based on the reduction of the passive soil wedge due to pile group effects and the presence of a sloping surface. From validations with three field experiments from literature it is concluded that the model can accurately describe pile-soil-pile interactions of laterally loaded pile groups. The use of precisely installed steel piles in all three experiments eliminated uncertainties related to pile diameter variation, pile degradation, material properties, and spatial variation within the pile group.

To validate the applicability of this analytical pile group model to historic quay walls in Amsterdam, lateral pile group experiments were conducted (level 2). These experiments involved one group with a top load and another group without a top load. The cap loads, pile cap deformations and cap inclinations were monitored. For a selection of piles, strain measurements were successfully obtained along the piles by installing fibre optic wires. As of now, there have been no previous instances of applying this particular technique to measure lateral in-ground deformations in century-old degraded timber piles. From the experiments, it was found that piles within a row exhibited large variations in lateral resistance, with force ratios of up to 5 between the maximum and minimum load-carrying piles. The largest contributing factors to the variance (87%) are natural variability in piles and soils, as well as pile degradation. These factors lead to significant variations in flexural pile stiffness, bending strength, and geotechnical strength. Only a small part (13%) of the variance can be attributed to typical pile group effects (pile free height, in-line, side-by-side and diameter). The inclusion of a top load resulted in a stiffer lateral response and a more brittle failure, while the average pile group failure load remained unchanged at 16.4kN/pile. Elastic-plastic behaviour occurs at approximately 100mm of group deflection, and pile breakage is likely at full plasticity of the timber cross-section. Piles are clamped in the Wad deposit, with maximum moments observed at NAP-3m to NAP-4.5m. The experiment without top loading led to deeper pile fractures, primarily occurring in the middle of the pile field. Cyclic loading significantly reduces lateral resistance and increases bending moments, resulting in earlier pile fractures.

Based on the validation conducted with the Overamstel tests, the analytical model has proven its capability in accurately predicting bending moment distributions and pile deflections for piles within a pile group. However, it is crucial to have detailed information on individual piles and subsoils for precise computations. In cases where such information is unavailable, group-averaged computations can still be performed.

Discussion: With large deflections (>100mm), the model starts to overpredict the cap force and underpredicts the bending moment. This is due to the fact that pile elements are modelled as linearly elastic, while they actually tend to deform plasticly. Furthermore, the analytical model fails to consider the increase in radial stress caused by axial loading, resulting in a

possible underestimation of the lateral resistance of vertical loaded pile groups. Lastly, the model is not capable of including cyclic loading effects, overestimating the resistance of the pile group after unloading steps. Consequently, the model's accuracy could be improved if it were to take these factors into account.

A more general discussion point is the time-scale of the tests used for the validation of the analytical model. All experiments (both from literature as from the Overamstel site) had a short time-scale, causing the cohesive layers to respond undrained. As pile-soil-pile interaction for quay walls in the city centre have a long time-scale of years to decades, these cohesive layers respond drained. As a consequence, the ability to conduct drained computations with the analytical model, utilized in modelling the Grimburgwal (chapter 6) and in Bayesian updating studies (chapter 7), remains unvalidated.

IV. How can the lateral failure of the pile foundation of historic quay walls be modelled and validated through testing?

Answer: The lateral failure of the pile foundation of historic quay walls can be described using an analytical quay wall model. The model consists of a framework of elastic beams embedded in an elastic foundation and is externally loaded by a linear elastic soil model based on the theory of Flamant. The beam model is made up of multiple Euler-Bernoulli beams, connected to each other by boundary and interface conditions. The connections between piles and headstocks are considered by means of a pile-headstock interface model. To model the lateral pile-soil-pile interactions in layered sloping soil, the analytical pile group model is incorporated in the analytical quay wall model. This pile group model is described and validated in key question III.

In order to validate the quay wall model, a series of experiments (level 3) were conducted in which various quay wall segments (5 in total), with a width of 6.5m, were overloaded by a ballast container on surface level. An extensive and innovative monitoring plan was used to track the position of the entire quay wall structure as well as the deformation of the soil volume behind the quay. Elements of this monitoring plan can be used within the city centre to detect signs of lateral failure (see section 8.4.2).

The Overamstel tests clearly demonstrate the predicted dominant failure mechanism, known as "lateral failure of the pile foundation", occurring when a quay wall is loaded from the backside. This failure mechanism causes the quay wall to laterally move towards the waterfront due to increased soil stresses behind the quay. This movement results in bending of the foundation piles, which can ultimately lead to pile breakage. While the failure load of the quay was predicted to be around 20kN/m^2, it did not fail when subjected to loads as high as 55kN/m^2 (in total 120 tonnes), demonstrating that the quay is significantly stronger than initially thought. Continuous deformations up to 93mm were observed for three segments with surface loads of 55kN/m^2 applied behind the quay. In one preloaded segment, the load was applied on top of the quay, which led to continuous displacements reaching 147mm. For four segments, it was observed that the calculated bending stresses exceeded the modulus of rupture in the timber, indicating that the timber had reached its yielding point. The excessive and progressive deformations, coupled with yielding of the timber piles, serve as clear indications of quay walls that are approaching pile breakage and thus lateral failure.

The most important findings are discussed. During loading, the quay foundation displayed minimal vertical settlements. The lateral deflection resulted in soil settlements behind the quay which were highest near the quay and decreased towards the hinterland. Horizontal soil deformations behind the quay were strongly correlated with lateral pile

deformation. No soil movement was observed below the 'Wadsand' layer, likewise in the lateral pile group experiments. The unloading of the quay revealed an interesting behaviour: the quay wall did not return to its initial position but remained displaced. This phenomenon is attributed to the transition of the active soil wedge to a passive state, which effectively keeps the piles in place and exposes them to bending stresses. By comparing the lateral pile group experiments with the quay wall experiments, a linear relation between the top load and the lateral pile load was found, providing proof for the utilization of linear elastic soil models such as proposed in the quay wall model.

The analytical quay wall model was successfully validated with the experiments. Furthermore, the validity of segmental friction and predicted bending moments were confirmed through a validation using 2D and 3D-FEM. It was proven that the quay model is capable of taking into account the loading history of a segment using an incremental approach. Due to the model's ability to predict both the lateral displacement of the quay and the magnitude of pile bending moments at various depths, stresses in the timber piles can be accurately determined. This enables the assessment of pile breakage occurring under a specific surface load. The most influential factors of the model are the active load on the structure, stiffness of the soil, number of piles and the flexural rigidity of the piles. As such, both structural and geotechnical site investigations are essential for reliable predictions of quay wall performance. Prioritizing a geotechnical site investigation is highly recommended before making predictions. The investigation should include obtaining soil layering and classification for both the soil volume behind the quay and the soil around/in front of the piles, as they may differ at shallow depths. Essential parameters like the effective soil weight, friction angle, cohesion (or undrained shear strength for undrained cohesive layers), and the CPT tip resistance are necessary to determine the soil stiffness (p-y springs) of the piles within the analytical model. Furthermore, the friction angle and effective weight of the soil volume behind the quay are important in calculating the active load on the quay foundation.

To conclude, the analytical model is highly suitable for trend analysis, sensitivity studies, and probabilistic analysis due to its short computational time in seconds, compared to complex three-dimensional FEM software that takes minutes to hours. With minimal input, a proper estimate of the quay wall and its pile group behaviour can be obtained.

Discussion: The model limitations are discussed. Firstly, it focuses solely on the horizontal bending deformation of the timber pile foundation, without considering the overall stability of the quay. The elastic soil model can only be used for external forcing and not for settlement predictions. The idealized pile-headstock connection assumes a tight fit and intact elements, not including biological degradation, possibly overestimating the stiffness of the connection. Additionally, the analytical model assumes constant diameter piles and does not account for tapering. Although bending moments are corrected for the tapering, small deviations might be present. Time-dependent deformation of both the timber and soil is not considered, and cyclic loads and the unloading/reloading stiffness of the subsoil are not taken into account. Lastly, negative skin friction on pile foundations and the sheet pile wall is not incorporated in the calculations.

The selected test approach, involving testing of relatively small segments of the quay wall, introduced an additional source of uncertainty. Undesired segmental friction added to the already-accounted-for uncertainty in the distribution of the top load through the soil medium to the quay foundation. As the segmental friction was calibrated on the experiment measurements, other potential inaccuracies in the active soil body were factored into the 'friction uncertainty', making it unfeasible to determine the deviation of the soil

model. Another crucial aspect for discussion is the representativeness of this quay wall experiment in relation to the inner city quay walls of Amsterdam. Due to the deviation of the quay layout and subsurface conditions in relation to inner-city quays, the findings of this experiment do not directly apply to the typical Amsterdam's inner-city quays. The experiments solely serve as a verification of the lateral failure mechanism of historic quays and the validation of the modelling approach.

V. How can the analytical quay wall model be utilized to understand the collapsed Grimburgwal?

Answer: On September 1, 2020, the Grimbrugwal collapsed. After the collapse, it was hypothesized that the cause of failure was the local deepening of the canal due to propeller washout from boats making sharp turns. The collapse was triggered by the renewal of the street, which increased the soil stress behind the quay. To investigate this hypothesis, the analytical quay wall model was utilized. Through this analytical model, it was demonstrated that the bending stresses in timber piles increase when the canal bed deepens in front of the quay. Deepening causes the piles to have less passive resistance against lateral loads. In the modelling process, various pile configurations were evaluated, and computed bending stresses were compared to the modulus of rupture values obtained from bending tests. The analysis revealed that the two-pile configuration had a high probability of yielding or breakage given the measured depths from post-failure multi-beam surveys, while the three-pile configuration showed comparatively less significant yielding. Overall, this research demonstrates the effectiveness of analytical models in understanding the failure mechanisms of historic structures like quay walls, providing valuable insights for Amsterdam's historical centre.

Discussion: Three significant discussion points limit the study's conclusiveness. Firstly, the exact geometry of the Grimburgwal remains uncertain, with multiple configurations proposed by different inspection teams. Second, the strength properties of the timber and soil have not been thoroughly examined. Third, the model lacks consideration for important factors such as loading history, time effects including soil and timber creep, and biological degradation over time. Moreover, the redistribution effect of the masonry was excluded. To improve the accuracy of the assessment, these discussion points need to be addressed and enhanced.

VI. How can Bayesian updating be applied to reduce uncertainties in failure probabilities and refine geotechnical and structural parameter distributions associated with the lateral failure mechanism of historic quay walls?

Answer: Bayesian updating can refine geotechnical and structural parameters and reduce uncertainties and conservatism in failure probability estimates for historic quay walls. By considering evidence of survived loading situations and deformations (as a consequence of the survived load), a case study demonstrated the potential of Bayesian updating for a hypothetical but realistic quay wall. The findings showed that depending on the evidence, the posterior reliability can fall within any of the 3 consequence classes (CC3, CC2, and CC1b outlined in NEN8700), if the a-priori prediction suggests insufficient safety and strength. In one case study, a quay wall with an a-priori reliability of $\beta = 1.5$ has been increased to $\beta = 3.2$ by including evidence of an extreme survived load of 10 kN/m^2 that resulted in

displacements of less than 4mm. The greater the observed extreme surface load compared to the surface load used in the reliability prediction, the greater the difference between prior and posterior reliability of the quay wall. Next to extreme loads, deformation measurements strongly influence the updating of the a-priori probability of failure, with small deformations leading to a decrease in failure probability and large deformations leading to an increase. Bayesian updating has the greatest impact on parameters with high influence factors, such as pile diameter and cohesion of the shallow peat layer, resulting in significant differences between prior and posterior parameter uncertainties. Overall, Bayesian updating provides a valuable approach to reduce uncertainties and refine geotechnical and structural parameters in the assessment of the lateral failure mechanism of historic quays.

Discussion: The applied analytical quay wall model in the study overlooks loading history, and time effects like soil creep and timber relaxation/degradation, leading to potential inaccuracies in long-term deformations and bending stresses. Addressing these challenges requires the involvement of wood experts and the use of more complex software, although this may increase computational times. A balance must be struck between complexity and computational speed. To overcome this challenge, a limited number of deterministic time-dependent computations using FEM software could be performed. Faster analytical models can be calibrated on those more complex FEM models, and can then be used in the probabilistic Bayesian analysis conducted in this study.

Two additional discussion points are addressed, which were not included in the applied methodology. Firstly, it is crucial to consider the impact of extreme events from the past, which might have weakened the quay wall structure and disrupted the correlation between observations and predictions. Second, in reality, maximum quay deformations are the result of multiple loading situations and time effects as discussed earlier. However, this analysis simplifies the maximum deformation of the quay wall by attributing it solely to the greatest load experienced throughout its lifetime.

8.2 General discussion and reflection

The findings of this research, both in terms of experimental and modelling aspects increase our understanding with respect to the lateral failure mechanism of historic quay walls. However, it is important to acknowledge the limitations and shortcomings of this study, which will be addressed in this section. Furthermore, a reflection on the research is provided in the context of the overall quay wall issues in Amsterdam.

In general, this study could have been further enhanced by considering two important aspects that were not taken into account. The first aspect is the influence of time-dependent effects, which encompass a range of factors including soil layer consolidation and creep, changes in undrained and drained conditions, reductions in lateral loads on quays as deformations increase, strength reduction, compaction of soil layers due to repeated loading or vibrations, as well as the shortening and settlement of timber piles under high axial loads and the creep in timber piles, leading to the dissipation of bending stresses through relaxation. The second aspect to consider is the redistribution capacity of the masonry wall and the pile foundation in the longitudinal direction. Although both time-dependent effects and redistribution effects were effectively eliminated in both the experiment and the modelling approach, they would improve the modelling accuracy of the quay wall assessment in the inner-city centre of Amsterdam.

The previous section concluded that the thesis findings improve modelling accuracy, leading to a less conservative evaluation of quay walls and reducing unnecessary rejections within the Amsterdam quay wall domain.

However, determining the amount of kilometres of quay wall saved from replacement is challenging due to the large variations within Amsterdam. The quays span over 200km in total, divided into approximately 50m sections, resulting in theoretically 4000 potentially unique configurations. The lack of archival drawings and the unknown geometry of many quay walls present significant challenges. Even with access to archive drawings and multiple inspections, conclusive geometry determination remains elusive, as demonstrated in the Grimburgwal study. Moreover, the difficulty in acquiring accurate location-specific structural and geotechnical strength properties adds to the complexity. As the author of this study, I find it necessary to temper the expectations surrounding the computational assessment with models of the entire quay wall domain. Analysing a quay wall in a highly detailed manner, while uncertainties exist regarding its geometry, essentially results in reliable fiction. For an accurate assessment of a quay, crucial information includes the number of pile rows, average diameter, stiffness and bending strength of the piles, as well as the stiffness of the soil around the piles and the composition of the active soil volume behind the quay.

Given that the uncertainties in these model inputs outweigh the potential improvement in modelling accuracy expected from future studies, it is very likely that the level of complexity in analytical modelling developed within this thesis is already more than adequate for its implementation in the quay wall assessment. This is particularly true when observations of the past performance of quay walls are included in the analytical modelling approach.

8.3 Implications for practice

This section explores the most important implications of the study findings on the broader field of research and practise.

- In the field of lateral pile modelling, a new method has been developed in this thesis that incorporates pile-soil-pile interactions and considers the presence of downward sloping soil. This method can be practically applied to design lateral loaded pile foundations or piles on (underwater) slopes. Examples are jetty/pier type of structures, offshore platforms or turbines founded on pile groups. To fully leverage the strength of the model, it is particularly advantageous to utilize it during the early stages of design. By utilizing parametric design and conducting multiple simulations, an optimal and sustainable design can be achieved. Advanced software can then be employed to further refine the design.
- A foundation has been laid for the applicability of Bayesian updating to historical quay walls, specifically laterally failing quay walls. Although the methodology has not been fully developed yet, it has the potential to significantly influence the way we currently assess quay walls and potentially extend their remaining service life, thereby saving money but most of all contributing to a more sustainable world.
- The developed quay wall model is a valuable tool for students and researchers that study the lateral failure of quays. Additionally, they can improve the model further by incorporating time effects and longitudinal redistribution effects. Beyond academia, this model holds practical value in the assessment of quay walls by the

Municipality of Amsterdam. Moreover, it has the potential to benefit other cities with historical quay walls constructed in a similar manner. The full MATLAB computer program is open source and available for download at: https://doi.org/10.4121/4fd90d71-ffd9-4db2-a358-8576f5b19a32 . A user manual is included.

- Several key elements from this study, including the pile-headstock interface model, bending properties of timber piles, and outcomes from field experiments, can be effectively incorporated into the ongoing assessment protocol being developed by Amsterdam (known as the TAK-protocol). The stiffness of the pile-headstock connection has already been embraced by engineers and is being utilized in the practical assessment of quay walls.
- Multiple datasets were collected from the Overamstel experiment, encompassing experimental results from bending experiments, lateral pile group experiments, and quay wall experiments. These data have been compiled and are accessible through the following link: https://doi.org/10.4121/d2d001b5-ec3f-4518-a90c-8461c1ff9ff3. Researchers and practitioners can utilize this data to validate their computational models or to conduct future studies.
- The extensive geotechnical site investigation conducted, provide valuable insights into the strength and stiffness properties of the subsoil at the Overamstel site. Given that the subsurface conditions in the city centre of Amsterdam are very similar to those at the Overamstel site, the strength and stiffness properties derived from the site investigation can be utilized for modelling quay walls in the inner city, provided that proper layering and classification have been carried out on-site.
- The full-scale Overamstel experimental program serves as a fundamental validation and calibration benchmark for researchers and engineers engaged in modelling historic quay walls. This step-wise validation protocol provides a base case for validating and ensuring the proper functionality of all components within the model.
- This study demonstrated the effectiveness of a sophisticated monitoring plan capable of detecting lateral failure in quays. Elements of this plan can be used within the city centre of Amsterdam. For example one can install inclination sensors on the pile caps or prism measurements combined with tilt sensors on the gravity wall. Other than that, the horizontal deformation of the soil body behind the quay can be monitored with for example vertical arrays of fibre optics.
- One practical implication that has already been implemented is the monitoring of water depths at specific locations along the quay wall area of Amsterdam, particularly where large vessels make sharp turns. This practice was introduced as a result of the Grimburgwal study.
- The interdependence of failure mechanisms allows insights gained from one mechanism (in this study, lateral failure) to enhance the understanding and improvement of others. For instance, a better understanding of the degradation and strength/stiffness properties of piles can contribute to an improved understanding of the overall stability of the quay (sliding plane) or the axial failure of foundation piles.

8.4 Recommendations

8.4.1 Theoretical recommendations

- To obtain more reliable predictions for quay deflections and bending stresses in historic quays located in Amsterdam's city centre, it is advisable to incorporate **time-dependent effects** and **three-dimensional redistribution** effects, as discussed in the general discussion section, into the analytical quay wall model. A simplified approach is preferred to maintain the computational speed advantages.
- It is recommended to compare complex finite element models, which incorporate time-dependent effects, with the analytical model that includes a simplified time-dependent approach. This comparison will provide insights into the differences and the actual impact of time-dependent effects on bending stresses and displacements. This would enable engineers to continue using the simplified models.
- In order to test the applicability and **robustness of Bayesian updating** on quay walls, it is important to consider different case studies within Amsterdam. Variations can be introduced in the main characteristics of the quay wall for each case, including the number of piles, retaining height, or soil composition.
- To make more reliable failure probability analyses, it is important to conduct further research into the **correlation between** randomly distributed **parameters**.
- The principle of **Bayesian updating** can significantly influence the failure probability related **to various failure mechanisms** in quay walls. It is recommended to explore the potential of Bayesian updating for assessing other failure mechanisms as well.
- It is recommended to explore promising methods such as importance sampling or surrogate modelling in Bayesian updating research to achieve a significant **reduction in computational time**.
- It would be both interesting and recommended to perform a **Bayesian analysis on the Overamstel quay wall experiment**. Given that the deformations and loads are precisely known, this analysis can help determine whether the reduction of parameter uncertainty aligns with the strength values obtained from geotechnical or bending experiments for soils and structural elements. If there are discrepancies between the outcomes of the Bayesian analysis and the measurements, a model uncertainty can be included, thereby improving the accuracy of Bayesian predictions for other quay configurations.
- It is recommended to **explore timber construction for quay walls** as a superior alternative to concrete and steel. The historic quay at Overamstel has proven its durability, withstanding heavy loads (>120 ton) without even applying raking piles. Timber-founded quay walls can easily last for a century. By using timber, we can possibly achieve advantages in terms of durability (material renewal), emissions (NO_x, CO_2), cost (<100 euro per new timber pile in 2022), and installation noise. It also preserves the historical significance and building techniques of our quays, rather than relying on generic concrete prefab walls.
- It is highly recommended to conduct a thorough investigation into **the potential impact of future droughts on inner city quay walls** and their timber foundations. Given the anticipated effects of climate change, droughts are expected to intensify, leading to a decline in the groundwater table and an accelerated biological degradation of timber piles. Other factors that may affect the flow and thus the

structural integrity of timber foundations include; the construction of new quays with impermeable foundations, soil improvement methods, underground spaces, or steel sheet pile structures designed to stabilize quays (which can remain in place for extended periods, sometimes up to 10 years).

- It is recommended to develop a safety philosophy for historic quay walls to determine acceptable levels of reliability (β).

8.4.2 Practical recommendations

- It is advised to **implement the analytical model** in future quay wall studies and in the assessment of Amsterdam quay walls. To that extent, it is recommended to convert the model to C++ instead of MATLAB (C++ is much more efficient with its memory) and build an interface around it. This will further reduce the computation time and make it more easy to use.
- **Avoid conducting calculations for individual piles**. To achieve a more representative analysis, it is advisable to investigate the resistance of groups considering the significant variations observed in experiments. One approach is to obtain multiple in-situ drilling samples within a group and determine the average diameter, as well as the soft shell modulus of rupture and modulus of elasticity. Subsequently, the group resistance can be calculated using these averaged values.
- **Prioritizing geotechnical site investigation before making predictions** is highly recommended. This helps reduce geotechnical uncertainties and allows a focus on model-related uncertainties.
- **It is highly recommended to implement a comprehensive monitoring system for quay walls** to effectively detect lateral failure mechanisms. Relying solely on façade (masonry wall) measurements is insufficient, as they can indicate various failure modes. Several monitoring ideas are proposed for consideration. First, it is advised to measure pile inclinations at the pile caps. Pile cap rotations can be correlated with lateral deformations of the piles, utilizing the linear relations found in this thesis. Another approach involves installing vertical fibres behind the quays to measure soil deformations in close proximity to the quay. This technique is already available and cost-effective. These deformations exhibit a strong correlation with pile deformations, providing valuable insights. Monitoring settlements behind quays can be achieved using satellite imagery. An increase in local settlements can potentially indicate progressive lateral deformations and even the possibility of sudden failure. Recognizing such patterns using AI systems can aid in the automated detection of hazardous locations. By implementing a combination of these monitoring techniques, a comprehensive understanding of quay wall behaviour can be achieved. This will enable proactive measures to mitigate potential failures and enhance overall safety.
- It is highly recommended to undertake the development or market inventory of **techniques for accurately mapping out quay wall configurations**. Key parameters such as the number of piles, spacing, pile diameter, and wall height are of utmost importance. Without precise knowledge of the pile geometry, it is not meaningful to strive for perfection in improving quay wall models capable of computing an unknown geometry. Several methods have already been studied or are currently being studied, including geophysical methods, hydro physical methods, divers inspections, digging a trench sections in the wall, and dynamic response methods.

- It is strongly advised to **avoid** subjecting the quay to **excessive dynamic frequencies**. Examples are the pavements of new roads, vibrating piles or sheet piles, or excessive dynamic response experiments. The reason for this recommendation is that during the installation of steel sheet piles (by vibrating) to create the segmental divides, unintended liquefaction occurred in one segment. This resulted in the formation of large sinkholes behind the gravity wall due to small openings in the timber floor. Vibrations can easily liquefy the soil around the foundation piles and reduce the lateral support pressures, thereby increasing the risk of lateral failure of the pile foundation. Furthermore significant vibrations behind the quay, can also lead to increased soil stresses and higher lateral loads on the quays. In cases where the streets exhibit excessive settlements, it is advisable to conduct a thorough investigation into the underlying cause before constructing new roads (which involves vibrations), as this could further amplify the load on the quay.
- By performing **non-destructive tests** in the city centre, additional evidence can be obtained about quay walls. For example, a truck can be parked as a static load for a certain period of time on a quay wall while the deformations are measured at the same time. This methodology must be carefully studied to determine the extent to which the load test has caused permanent damage to the quay wall. In the case of a load test, it is necessary to make an estimation in advance of the probability of damage/failure and corresponding deformations, both of which should be sufficiently low.
- Uncertainties concerning parameters can be reduced by conducting **on-site inspections and investigations**. It has been revealed that pile diameter is the most dominant parameter. By conducting further research into the pile diameter at the location to be assess, a large part of the uncertainty can be eliminated.
- In-situ **micro drillings** need to be employed to estimate the soft shell, the modulus of rupture and the modulus of elasticity of the timber. The relationships found in this thesis between drill resistance and MOR/modulus of elasticity can be utilized.
- Apply **soil stabilizing methods** behind the quay (or weight reducing methods), lowering loads on quays. Think of light weight foam blocks or gravel columns.
- When undertaking the demolition of historic quays, it is recommended to **conduct bending tests on the piles** using the methodology described in chapter 3 of this thesis. By examining the bending properties of piles in inner-city quays, valuable insights can be gained and applied to further enhance the understanding of quays in the historic centre.
- **Timber creep/relaxation experiments** can be performed on timber piles to gain insights into their long-term behaviour. E.g. by subjecting the piles to a bending force (similar to tensioning a bow) and immersing them underwater for an extended period, such as one year, we can study how the internal forces within the pile diminish over time while maintaining the same deformed shape.
- Risk assessments can be made based on damages, deformations, or other observations. For this type of assessments, “signal values” are required. The magnitude of these signal values can be obtained from studies with computational models.

REFERENCES

Abdelhalim, R. A., El Sawwaf, M., Nasr, A. M., & Farouk, A. (2020). Experimental and numerical studies of laterally loaded piles located near oil-contaminated sand slope. *Engineering Science and Technology, an International Journal, 23*(4), 744-757.

Al-Baghdadi, T. A., Brown, M. J., Knappett, J. A., & Al-Defae, A. H. (2017). Effects of vertical loading on lateral screw pile performance. *Proceedings of the Institution of Civil Engineers-Geotechnical Engineering, 170*(3), 259-272.

Alyami, M., Rouainia, M., & Wilkinson, S. (2009). Numerical analysis of deformation behaviour of quay walls under earthquake loading. *Soil Dynamics and Earthquake Engineering, 29*(3), 525-536.

American Petroleum, I. (1989). *Recommended practice for planning, designing, and constructing fixed offshore platforms* (Vol. 2): American Petroleum Institute.

Amsterdam, G. (1975). Amsterdam op palen - de geschiedenis van het funderen *Maandblad van de Dienst der publieke werken van Amsterdam, jaargang 25*.

Amsterdam, G. (2020a). *Handboek voor (tijdelijke) natuur bij veiligheidsmaatregelen voor kademuren* Retrieved from Openresearch Amsterdam:

Amsterdam, G. (2020b). *Herstellen en verbinden, Bouwen aan het fundament van de stad*. Retrieved from Openresearch Amsterdam:

Amsterdam, I. G. (2019). Innovatiepartnerschap Kademuren (IPK). Retrieved from https://www.amsterdam.nl/ingenieursbureau/tegels-homepage/innoveren-bruggen-kademuren/innovatiepartnerschap-kademuren-(ipk)-2/#hb4cf0da9-3e66-4819-9864-c43498e95c6e

Anagnostopoulos, C., & Georgiadis, M. (1993). Interaction of axial and lateral pile responses. *Journal of Geotechnical Engineering, 119*(4), 793-798.

Ashour, M., Norris, G., & Pilling, P. (1998). Lateral loading of a pile in layered soil using the strain wedge model. *Journal of geotechnical and geoenvironmental engineering, 124*(4), 303-315.

Ashour, M., Pilling, P., & Norris, G. (2004). Lateral behavior of pile groups in layered soils. *Journal of Geotechnical and Geoenvironmental Engineering, 130*(6), 580-592.

Baars-Cipro. (2021). *Onderzoek instorting kade Grimburgwal; Concept rapportage met bevindingen duikonderzoek inclusief 3D scan en Multibeam data; project 20p102*. Retrieved from

Baguelin, F. (1982). *Rules for the structural design of foundations based on the selfboring pressuremeter test.* Paper presented at the Symp. on the Pressuremeter and Its Marine Application, IFP, Paris.

Baguelin, F., & Jézéquel, J. (1972). Etude experimentale du comportement de pieux sollicites horizontalement. *ANN. ITBTP-SERIE SOLS ET FONDATIONS-91*(297).

Bai, Y. (2003). *Marine structural design*: Elsevier.

Balestrini, F., Draganov, D., Staring, M., Singer, J., Heijmans, J., & Karamitopoulos, P. (2021). *Seismic Modelling for Monitoring of Historical Quay Walls and Detection of Failure Mechanisms.* Paper presented at the NSG2021 2nd Conference on Geophysics for Infrastructure Planning, Monitoring and BIM.

Banerjee, P. K., & Davies, T. G. (1978). The behaviour of axially and laterally loaded single piles embedded in nonhomogeneous soils. *Geotechnique, 28*(3), 309-326.

Bayes, T. (1763). LII. An essay towards solving a problem in the doctrine of chances. By the late Rev. Mr. Bayes, FRS communicated by Mr. Price, in a letter to John Canton, AMFR S. *Philosophical transactions of the Royal Society of London*(53), 370-418.

Beck, J. L., & Au, S.-K. (2002). Bayesian updating of structural models and reliability using Markov chain Monte Carlo simulation. *Journal of engineering mechanics, 128*(4), 380-391.

Björdal, C. G., & Elam, J. (2021). Bacterial degradation of nine wooden foundation piles from Gothenburg historic city center and correlation to wood quality, environment, and time in service. *International biodeterioration & biodegradation, 164*, 105288.

Blum, H. (1932). *Wirtschaftliche dalbenformen und deren berechnung*: Verlag nicht ermittelbar.

Bonte, S. (2020). Belastingsproef op historische kaaimuren antwerpen *Geotechniek 24*(3), 26-29. Retrieved from https://issuu.com/uitgeverijeducom/docs/geotechniek.aug2020_web

Bowman, E. R. (1958). *Investigation of the lateral resistance to movement of a plate in cohesionless soil*. University of Texas at Austin,

Bransby, M. F. (1999). Selection of p–y curves for the design of single laterally loaded piles. *International Journal for numerical and analytical methods in geomechanics, 23*(15), 1909-1926.

Briançon, L., & Simon, B. (2012). Performance of pile-supported embankment over soft soil: full-scale experiment. *Journal of geotechnical and geoenvironmental engineering, 138*(4), 551-561.

Briaud, J.-L. (2013). *Geotechnical engineering: unsaturated and saturated soils*: John Wiley & Sons.

Briaud, J. L., Smith, T., & Meyer, B. (1983). *Using the pressuremeter curve to design laterally loaded piles.* Paper presented at the Offshore Technology Conference.

Broms, B. B. (1964). Lateral resistance of piles in cohesionless soils. *Journal of the Soil Mechanics and Foundations Division, 90*(3), 123-156.

Brown, D. A., Morrison, C., & Reese, L. C. (1988). Lateral load behavior of pile group in sand. *Journal of Geotechnical Engineering, 114*(11), 1261-1276.

Brown, D. A., & Shie, C.-F. (1990a). Numerical experiments into group effects on the response of piles to lateral loading. *Computers and Geotechnics, 10*(3), 211-230.

Brown, D. A., & Shie, C.-F. (1990b). Three dimensional finite element model of laterally loaded piles. *Computers and Geotechnics, 10*(1), 59-79.

Ceccato, F. (2013). *Effect of Wood Degradation and Soil Creep on the Behavior of Wooden Pile Foundation in Venice*. Paper presented at the Proceedings of the 5th International Young Geotechnical Engineers' Conference.

Cerda, G., & Wolfe, R. W. (2003). Bending strength of Chilean radiata pine poles. *Forest products journal. Vol. 53, no. 4 (2003): Pages 61-65*.

Chae, K. S., Ugai, K., & Wakai, A. (2004). Lateral resistance of short single piles and pile groups located near slopes. *International Journal of Geomechanics, 4*(2), 93-103.

Chandrasekaran, S., Boominathan, A., & Dodagoudar, G. (2010). Experimental investigations on the behaviour of pile groups in clay under lateral cyclic loading. *Geotechnical and Geological Engineering, 28*(5), 603-617.

Ching, J., Lin, H.-D., & Yen, M.-T. (2011). Calibrating resistance factors of single bored piles based on incomplete load test results. *Journal of engineering mechanics, 137*(5), 309-323.

Chitchumnong, P., Brooks, S., & Stafford, G. (1989). Comparison of three-and four-point flexural strength testing of denture-base polymers. *Dental Materials, 5*(1), 2-5.

Choe, D.-E., Gardoni, P., & Rosowsky, D. (2007). Closed-form fragility estimates, parameter sensitivity, and Bayesian updating for RC columns. *Journal of engineering mechanics, 133*(7), 833-843.

Choosrithong, K. (2023). *Proefbelasting Overamstel - Geotechnical aspects, Site characterisation and Numerical investigation*. Retrieved from Openresearch.amsterdam: https://openresearch.amsterdam/nl/page/101492/overamstel-geotech

Choosrithong, K., & Korff, M. (2023). *Overamstel Project - Geotechnical Base report of Overamstel Project*. Retrieved from Openresearch.amsterdam: https://openresearch.amsterdam/en/page/101481/geotechnical-base-report-of-overamstel-project

Christensen, N. H. (1961). Model tests with transversally loaded rigid piles in sand. *Danish Geotech. Ins., Bull. Copenhagen*(12), 10-16.

Christoforo, A. L., Lahr, F. A. R., Morales, E. A. M., Zangiácomo, A. L., & Panzera, T. H. (2012). Influence of displacements on calculus of the longitudinal modulus of elasticity of Pinus caribaea structural round timber beams. *International Journal of Agriculture and Forestry, 2*(4), 157-160.

Chung, T. H., Mohamed, Y., & AbouRizk, S. (2006). Bayesian updating application into simulation in the North Edmonton Sanitary Trunk tunnel project. *Journal of Construction Engineering and Management, 132*(8), 882-894.

Cline, M., & Heim, A. L. (1912). *Tests of structural timbers* (Vol. 108): US Department of Agriculture, Forest Service.

Cloo, P. (2019). *Factor 20*. Retrieved from https://wob.amsterdam.nl/2020/december/wob-besluit-onderzoeksrapportage-pieter/

Coulomb, C. (1776). Essai sur une application des rèles des maximis et minimis a quelques problems de statique. *Memoires Acad. Royale des Sciences, 7*.

COWN, D., & Hutchison, J. (1983). Wood density as an indicator of the bending properties of Pinus radiata poles. *New Zealand Journal of Forestry Science [en línea], 13*(1), 87.

Dabek, A., & van Geloven, I. W. (2019). *1900913-XL. Technical Report 1820215, Lankelma Geotechniek Zuid*

B.V. Retrieved from

Das, B. M. (2010). *Geotechnical engineering handbook*: J. Ross publishing.

De Gijt, J. G. (2010). A History of Quay Walls: Techniques, types, costs and future.

Den Adel, N., De Gijt, J., Wolters, H., & Schweckendiek, T. (2019). *The potential of using performance information in the assessment of existing quay walls.* Paper presented at the IOP Conference Series: Materials Science and Engineering.

Deng, J. (2006). Structural reliability analysis for implicit performance function using radial basis function network. *International journal of solids and structures, 43*(11-12), 3255-3291.

Der Kiureghian, A., & Ditlevsen, O. (2009). Aleatory or epistemic? Does it matter? *Structural Safety, 31*(2), 105-112.

Derksen, D., & Veerkamp, J. (2021). *Reconstructie kademuur Grimburgwal, Archeologische Begeleiding Grimburgwal, Amsterdam (2020)*. Retrieved from Openresearch Amsterdam:

Ding, X., Luan, L., Zheng, C., & Zhou, W. (2017). Influence of the second-order effect of axial load on lateral dynamic response of a pipe pile in saturated soil layer. *Soil Dynamics and Earthquake Engineering, 103*, 86-94.

Dong, J., Li, Z., Lu, P., Jia, Q., Wang, G., & Li, G. (2012). Design ice load for piles subjected to ice impact. *Cold regions science and technology, 71*, 34-43.

Duffy, K., Gavin, K., Askarinejad, A., Korff, M., de Lange, D., & Roubos, A. (2022). *Field testing of axially loaded piles in dense sand for the.* Paper presented at the

Proceedings of the 20th International Conference on Soil Mechanics and Geotechnical Engineering.

Duncan, J. M., Robinette, M. D., & Mokwa, R. L. (2005). Analysis of laterally loaded pile groups with partial pile head fixity. In *Advances in Designing and Testing Deep Foundations: In Memory of Michael W. O'Neill* (pp. 235-250).

Ehre, M., Papaioannou, I., & Straub, D. (2018). Efficient Conditional Reliability Updating with Sequential Importance Sampling. *Proceedings in Applied Mathematics and Mechanics*.

Enkele kademuren in Centrum dreigen te bezwijken. (2018). *het Parool*. Retrieved from https://www.parool.nl/nieuws/enkele-kademuren-in-centrum-dreigen-te-bezwijken~b31cdb6d/

Enright, M. P., & Frangopol, D. M. (1999). Condition prediction of deteriorating concrete bridges using Bayesian updating. *Journal of Structural Engineering*, *125*(10), 1118-1125.

Fan, C.-C., & Long, J. H. (2005). Assessment of existing methods for predicting soil response of laterally loaded piles in sand. *Computers and Geotechnics*, *32*(4), 274-289.

Farmaga, I., Shmigelskyi, P., Spiewak, P., & Ciupinski, L. (2011). *Evaluation of computational complexity of finite element analysis.* Paper presented at the 2011 11th International Conference The Experience of Designing and Application of CAD Systems in Microelectronics (CADSM).

Flamant, A. (1892). Sur la répartition des pressions dans un solide rectangulaire chargé transversalement. *CR Acad. Sci. Paris*, *114*(1892), 1465-1468.

Gabr, M. A., & Borden, R. H. (1990). Lateral analysis of piers constructed on slopes. *Journal of Geotechnical Engineering*, *116*(12), 1831-1850.

Gao, X., Duan, G., & Lan, C. (2021). Bayesian Updates for an Extreme Value Distribution Model of Bridge Traffic Load Effect Based on SHM Data. *Sustainability*, *13*(15), 8631.

Gard, W., & Van de Kuilen, J. (2018). *Micro-drilling resistance measurements of dense hardwoods for hydraulic structures.* Paper presented at the WCTE-World Conference on Timber Engineering, Seoul, South-Korea.

Gellecum, A. v. (2021). *Onderzoek Instorting Kade Grimburgwal; Concept Rapportage met Bevindingen Duikonderzoek Inclusief 3D Scan en Multibeam Data Baars-Cipro Lijnden, the Netherlands (in Dutch)*. Retrieved from

Georgiadis, H., & Anagnostou, D. (2008). Problems of the Flamant–Boussinesq and Kelvin type in dipolar gradient elasticity. *Journal of Elasticity*, *90*, 71-98.

Gleser, S. M. (1953, 1953). *Lateral load tests on vertical fixed-head and free-head piles*.

Goodwin, J., Woods, J. E., & Hoult, N. A. (2022). Assessing the structural behaviour of glued-laminated timber beams using distributed strain sensing. *Construction and Building Materials*, *325*, 126844.

Gorbunov-Posadov, M. I. (1972). Solution of the problem of a concentrated force applied at the boundary of a half plane, with displacements vanishing at infinity. *Soil Mechanics and Foundation Engineering*, *9*(2), 74-80.

Green, D. W., Gorman, T. M., Evans, J. W., & Murphy, J. F. (2006). Mechanical grading of round timber beams. *Journal of materials in civil engineering.(Jan./Feb. 2006): Pages 1-10*.

Guan, N., Thunell, B., & Lyth, K. (1983). friction between steel and some common Swedish wood species. *Holz als Roh-und Werkstoff*.

Hall, W. B. (1988). Reliability of service-proven structures. *Journal of Structural Engineering*, *114*(3), 608-624.

Han, Y., & Vaziri, H. (1992). Dynamic response of pile groups under lateral loading. *Soil Dynamics and Earthquake Engineering, 11*(2), 87-99.

Hansen, J. B. (1961). The ultimate resistance of rigid piles against transversal forces. *Bulletin 12, Danish Geotech. Institute*, 1-9.

Hansen, J. B., & Lundgren, H. (1960). *Hauptprobleme der Bodenmechanik*: Springer-Verlag.

Harmsen, L., & Nissen, T. V. (1965). Timber decay caused by bacteria. *Nature, 206*(4981), 319-319.

Hartsuijker, C. (2001). *Spanningen, vervormingen en verplaatsingen*: Academic Service.

Heidari, M., El Naggar, H., Jahanandish, M., & Ghahramani, A. (2014). Generalized cyclic p–y curve modeling for analysis of laterally loaded piles. *Soil Dynamics and Earthquake Engineering, 63*, 138-149.

Hein, P. R. G., & Brancheriau, L. (2018). Comparison between three-point and four-point flexural tests to determine wood strength of Eucalyptus specimens. *Maderas. Ciencia y tecnología, 20*(3), 333-342.

Hemel, M.-J., Korff, M., & Peters, D. J. (2022). Analytical model for laterally loaded pile groups in layered sloping soil. *Marine Structures, 84*, 103229.

Hemel, M.-J., Peters, D. J., Korff, M., Choosrithong, K., & Hutcheson, E. (2022). *Draaiboek Proefbelasting Overamstel*. Retrieved from

Hemel, M.-J., Peters, D. J., Schweckendiek, T., & Jonkman, S. N. (2023). Reliability updating for lateral failure of historic quay walls (under review). *Georisk*.

Heming, S. (2019). *De Amsterdamse kademuren op de schop*. Van Hall Larenstein,

Honardar, S. (2020). Geotechnical Bearing Capacity of Timber Piles in the City of Amsterdam: Derivation of bearing capacity prediction factors based on static load tests conducted on instrumented timber piles.

Hudson, R. Y. (1953). Wave forces on breakwaters. *Transactions of the American Society of Civil Engineers, 118*(1), 653-674.

Huisman, D., Kretschmar, E., & Lamersdorf, N. (2008). Characterising physicochemical sediment conditions at selected bacterial decayed wooden pile foundation sites in the Netherlands, Germany, and Italy. *International biodeterioration & biodegradation, 61*(1), 117-125.

Humar, M., Balzano, A., Kržišnik, D., & Lesar, B. (2021). Assessment of Wooden Foundation Piles after 125 Years of Service. *Forests, 12*(2), 143.

Iai, S., & Kameoka, T. (1993). Finite element analysis of earthquake induced damage to anchored sheet pile quay walls. *Soils and foundations, 33*(1), 71-91.

Ichii, K. (2004). Fragility curves for gravity-type quay walls based on effective stress analyses. *13th WCEE, Vancouver, BC*.

Ido, H., Nagao, H., Kato, H., & Miura, S. (2013). Strength properties and effect of moisture content on the bending and compressive strength parallel to the grain of sugi (Cryptomeria japonica) round timber. *Journal of wood science, 59*(1), 67-72.

Inagaki, H., Iai, S., Sugano, T., Yamazaki, H., & Inatomi, T. (1996). Performance of caisson type quay walls at Kobe port. *Soils and foundations, 36*, 119-136.

Instorten Amsterdamse kademuur deels veroorzaakt door boten. (2020). *NOS*. Retrieved from https://nos.nl/artikel/2376021-instorten-amsterdamse-kademuur-deels-veroorzaakt-door-boten

Jeanjean, P. (2009, 2009). *Re-assessment of py curves for soft clays from centrifuge testing and finite element modeling*.

Jiang, S.-H., Li, D.-Q., Cao, Z.-J., Zhou, C.-B., & Phoon, K.-K. (2015). Efficient system reliability analysis of slope stability in spatially variable soils using Monte Carlo

simulation. *Journal of geotechnical and geoenvironmental engineering, 141*(2), 04014096.

Jonkman, S., Steenbergen, R., Morales-Nápoles, O., Vrouwenvelder, A., & Vrijling, J. (2015). Probabilistic design: risk and reliability analysis in civil engineering. *Collegedictaat CIE4130*.

Kademuur bij Nassaukade ingestort; lek waterleiding weer gedicht (2018). *Echt Amsterdams Nieuws*. Retrieved from https://www.at5.nl/artikelen/179152/kademuur-bij-nassaukade-ingestort

Kanning, W., & Schweckendiek, T. (2017). *Handreiking Faalkansanalyse en Faalkans Updating- Groene Versie - Macrostabiliteit Binnenwaarts*. Retrieved from helpdeskwater https://www.helpdeskwater.nl/onderwerpen/waterveiligheid/primaire/nieuwe-methoden-technieken/bewezen-sterkte/

Karamitopoulos, P. (2022). *Hydrographic inspection of historic quay walls in Amsterdam using multibeam echosounder and acoustic camera*. Retrieved from Open Research Amsterdam

Kavitha, P., Beena, K., & Narayanan, K. (2016). A review on soil–structure interaction analysis of laterally loaded piles. *Innovative Infrastructure Solutions, 1*, 1-15.

Kemper, A. R., McNally, C., Pullins, C. A., Freeman, L. J., Duma, S. M., & Rouhana, S. W. (2007). The biomechanics of human ribs: material and structural properties from dynamic tension and bending tests. *Stapp car crash journal, 51*, 235.

Kim, S.-H., & Shinozuka, M. (2004). Development of fragility curves of bridges retrofitted by column jacketing. *Probabilistic Engineering Mechanics, 19*(1-2), 105-112.

Kim, Y., Jeong, S., & Lee, S. (2011). Wedge failure analysis of soil resistance on laterally loaded piles in clay. *Journal of geotechnical and geoenvironmental engineering, 137*(7), 678-694.

Klaassen, R. K. W. M. (2008). Bacterial decay in wooden foundation piles—Patterns and causes: A study of historical pile foundations in the Netherlands. *International biodeterioration & biodegradation, 61*(1), 45-60.

Klaassen, R. K. W. M., & Creemers, J. G. M. (2012). Wooden foundation piles and its underestimated relevance for cultural heritage. *Journal of cultural heritage, 13*(3), S123-S128.

Korff, M., Hemel, M.-J., & Peters, D. J. (2022). Collapse of the Grimburgwal, a historic quay in Amsterdam, the Netherlands. *Proceedings of the Institution of Civil Engineers-Forensic Engineering, 175*(4), 96-105.

Korff, M., Hemel, M., & Esposito, R. (2021). Bezwijken Grimburgwal: Leerpunten voor het Amsterdamse Areaal.

Koubek, R., & Dedicova, K. (2014). Friction of wood on steel. In.

Kruyswijk, M. (2021). Gemeente komt bijna half miljard tekort voor aanpak bruggen en kades. *Het Parool*.

Küçükarslan, S., & Banerjee, P. (2003). Behavior of axially loaded pile group under lateral cyclic loading. *Engineering structures, 25*(3), 303-311.

Kuiper, M., Peters, D.-J., Hemel, M.-J., & Karamitopoulos, P. (2020). *Proef kade Overamstel*. Retrieved from

Larson, D., Mirth, R., & Wolfe, R. (2004). Evaluation of small-diameter ponderosa pine logs in bending. *Forest products journal. Vol. 54, no. 12 (Dec. 2004): Pages 52-58*.

Leung, C., & Chow, Y. (1987). Response of pile groups subjected to lateral loads. *International journal for numerical and analytical methods in geomechanics, 11*(3), 307-314.

Li, D.-Q., Zhang, F.-P., Cao, Z.-J., Zhou, W., Phoon, K.-K., & Zhou, C.-B. (2015). Efficient reliability updating of slope stability by reweighting failure samples generated by Monte Carlo simulation. *Computers and Geotechnics, 69*, 588-600.

Lim, J., Oh, J.-K., Yeo, H., & Lee, J.-J. (2013). Behavior of center-bored round timber beams in center-point bending test. *Journal of wood science, 59*(5), 389-395.

Lin, C., Han, J., Bennett, C., & Parsons, R. L. (2016). Analysis of laterally loaded piles in soft clay considering scour-hole dimensions. *Ocean Engineering, 111*, 461-470.

Lopez-Anido, R., Michael, A. P., & Sandford, T. C. (2003). Experimental characterization of FRP composite-wood pile structural response by bending tests. *Marine Structures, 16*(4), 257-274.

Lou, M., Wang, H., Chen, X., & Zhai, Y. (2011). Structure–soil–structure interaction: Literature review. *Soil Dynamics and Earthquake Engineering, 31*(12), 1724-1731.

Maarschalkerweerd, J. v. (2022). Scherpe keuzes in achterstallig onderhoud bruggen en kademuren Amsterdam. *OTAR*. Retrieved from https://www.otar.nl/scherpe-keuzes-in-achterstallig-onderhoud-bruggen-en-kademuren-amsterdam/

Manna, B., & Baidya, D. (2009). Vertical vibration of full-scale pile—analytical and experimental study. *Journal of geotechnical and geoenvironmental engineering, 135*(10), 1452-1461.

Maouche, H. Analyse numerique de la reponse non lineaire d'un pieu sous sollicitations laterales.

Matlock, H. (1970). Correlations for design of laterally loaded piles in soft clay. *Offshore technology in civil engineering's hall of fame papers from the early years*, 77-94.

McVay, M., Casper, R., & Shang, T.-I. (1995). Lateral response of three-row groups in loose to dense sands at 3D and 5D pile spacing. *Journal of Geotechnical Engineering, 121*(5), 436-441.

McVay, M., Zhang, L., Molnit, T., & Lai, P. (1998). Centrifuge testing of large laterally loaded pile groups in sands. *Journal of Geotechnical and Geoenvironmental Engineering, 124*(10), 1016-1026.

Ménard, L., Bourdon, G., & Gambin, M. (1971). Methode generale de calcul d'un rideau ou d'un pieu sollicite horizontalement en fonction des resultats pressiometriques. *Sols Soils, 6*(22/23).

Mezazigh, S., & Levacher, D. (1998). Laterally loaded piles in sand: slope effect on py reaction curves. *Canadian Geotechnical Journal, 35*(3), 433-441.

Mirzoyan, A. D. (2007). *Lateral resistance of piles at the crest of slopes in sand*: Brigham Young University.

Morales-Conde, M. J., & Machado, J. S. (2017). Evaluation of cross-sectional variation of timber bending modulus of elasticity by stress waves. *Construction and Building Materials, 134*, 617-625.

Mu, L., Huang, M., Zhang, J., & Feng, C. (2015). *Influence of vertical loads on behaviour of laterally loaded large diameter pile in sand.* Paper presented at the Proceedings of 3rd International Symposium on Frontiers in Offshore Geotechnics, Oslo, Norway.

Mujika, F. (2006). On the difference between flexural moduli obtained by three-point and four-point bending tests. *Polymer testing, 25*(2), 214-220.

Navy, U. D. o. (1986). *NAVFAC Engineering Manual EM7.02*. Retrieved from

Neijzing, L., Cherkaoui, A., Pijpers, R., & Wesstein, R. (2023). *Toetskader Amsterdamse Kademuren (TAK) van toepassing op kademuren op houten palen in beheer bij gemeente Amsterdam*. Retrieved from Amsterdam:

NEN-EN9997-1. (2012). *Eurocode 7 - Geotechnical design of structures - Part 1: General rules*. Retrieved from

Neukirchner, R. (1987). Analysis of laterally loaded piles in permafrost. *Journal of Geotechnical Engineering, 113*(1), 15-29.

Ng, C. W. W., & Zhang, L. M. (2001). Three-dimensional analysis of performance of laterally loaded sleeved piles in sloping ground. *Journal of Geotechnical and Geoenvironmental Engineering, 127*(6), 499-509.

Nimbalkar, S., & Basack, S. (2022). Pile group in clay subjected to cyclic lateral load: Numerical modelling and design recommendation. *Marine Georesources & Geotechnology*, 1-21.

Nimityongskul, N., Kawamata, Y., Rayamajhi, D., & Ashford, S. A. (2018). Full-scale tests on effects of slope on lateral capacity of piles installed in cohesive soils. *Journal of geotechnical and geoenvironmental engineering, 144*(1), 04017103.

Norris, G. M. (1986, 1986). *Theoretically based BEF laterally loaded pile analysis*.

NWO. (2022). Urban Bridge and Quay Wall Innovations. Retrieved from https://www.nwo.nl/en/researchprogrammes/dutch-research-agenda-nwa/thematic-programming/urbiquay

Ophof, O. (2021). Modelling interactions between quay walls and utility lines: In the inner-city of Amsterdam.

Pagella, G., Mirra, M., Ravenshorst, G., & Van De Kuilen, J. (2022). Influence of knots and density distribution on compressive strength of wooden foundation piles. In *Current Perspectives and New Directions in Mechanics, Modelling and Design of Structural Systems* (pp. 1689-1695): CRC Press.

Pagella, G., Ravenshorst, G., Gard, W., & van de Kuilen, J. W. Characterization and assessment of the mechanical properties of spruce foundation piles retrieved from bridges in Amsterdam.

Pagella, G., Ravenshorst, G., Gard, W., & van de Kuilen, J. W. (2021). Characterization and assessment of the mechanical properties of spruce foundation piles retrieved from bridges in Amsterdam.

Pagella, G., Ravenshorst, G., Gard, W., & van de Kuilen, J. W. (2022). *Characterization and assessment of the mechanical properties of spruce foundation piles retrieved from bridges in Amsterdam*. Paper presented at the 4th International Conference on Timber Bridges Switserland

Pais, J. C., & Harvey, J. (2012). *Four point bending*: CRC Press.

Pandit, D., & Patel, B. N. (2022). On numerical moment-curvature relationship of a beam. *Sādhanā, 47*(1), 1-9.

Papaioannou, I., & Straub, D. (2012). Reliability updating in geotechnical engineering including spatial variability of soil. *Computers and Geotechnics, 42*, 44-51.

Peng, W., Zhao, M., Xiao, Y., Yang, C., & Zhao, H. (2019). Analysis of laterally loaded piles in sloping ground using a modified strain wedge model. *Computers and Geotechnics, 107*, 163-175.

Peters, D. J., Broos, E., Gresnigt, A., & Van Es, S. (2015). *Local buckling resistance of sand-filled spirally welded tubes.* Paper presented at the The Twenty-fifth International Ocean and Polar Engineering Conference.

Poulos, H. G. (1971). Behavior of laterally loaded piles I. Single Piles. *Journal of Soil Mechanics & Foundations Div*.

Poulos, H. G. (1976). Behaviour of laterally loaded piles near a cut or slope. *Australian Geomechanics Journal, 6*(1).

Poulos, H. G., & Davis, E. H. (1980). *Pile foundation analysis and design*.

Rankine, W. J. M. (1857). II. On the stability of loose earth. *Philosophical transactions of the Royal Society of London*(147), 9-27.

Ranta-Maunus, A., Denzler, J. K., & Stapel, P. (2011). Strength of European Timber: Part 2. Properties of spruce and pine tested in Gradewood project.

Ravage door sinkhole in Amsterdam. (2017). *Telegraaf*. Retrieved from https://www.telegraaf.nl/nieuws/1417613/ravage-door-sinkhole-in-amsterdam

Reese, L. C. (1956, 1956). *Non-dimensional solutions for laterally loaded piles with soil modulus assumed proportional to depth*.

Reese, L. C. (1986). Behavior of piles and pile groups under lateral load. *Report No. FHWA/RD-85/106, 276*.

Reese, L. C., Cox, W. R., & Koop, F. D. (1975, 1975). *Field testing and analysis of laterally loaded piles om stiff clay*.

Reese, L. C., & Van Impe, W. F. (2010). *Single piles and pile groups under lateral loading*: CRC press.

Robertson, P. K., Hughes, J. M., Campanella, R. G., Brown, P., & McKeown, S. (1985). *Design of laterally loaded piles using the pressuremeter.* Paper presented at the The pressuremeter and its marine applications: Second International Symposium.

Rollins, K. M., Lane, J. D., & Gerber, T. M. (2005). Measured and computed lateral response of a pile group in sand. *Journal of geotechnical and geoenvironmental engineering, 131*(1), 103-114.

Rollins, K. M., Olsen, K. G., Jensen, D. H., Garrett, B. H., Olsen, R. J., & Egbert, J. J. (2006). Pile spacing effects on lateral pile group behavior: Analysis. *Journal of geotechnical and geoenvironmental engineering, 132*(10), 1272-1283.

Rollins, K. M., Olsen, R. J., Egbert, J. J., Jensen, D. H., Olsen, K. G., & Garrett, B. H. (2006). Pile spacing effects on lateral pile group behavior: load tests. *Journal of geotechnical and geoenvironmental engineering, 132*(10), 1262-1271.

Rollins, K. M., Peterson, K. T., & Weaver, T. J. (1998). Lateral load behavior of full-scale pile group in clay. *Journal of geotechnical and geoenvironmental engineering, 124*(6), 468-478.

Roubos, A., Blokland, T., & Van Der Plas, T. (2014). *Field tests propeller scour along quay wall.* Paper presented at the PIANC World Congress, San Francisco-USA.

Roubos, A. A., Allaix, D. L., Schweckendiek, T., Steenbergen, R. D., & Jonkman, S. N. (2020). Time-dependent reliability analysis of service-proven quay walls subject to corrosion-induced degradation. *Reliability Engineering & System Safety, 203*, 107085.

Ruesta, P. F., & Townsend, F. C. (1997). Evaluation of laterally loaded pile group at Roosevelt Bridge. *Journal of Geotechnical and Geoenvironmental Engineering, 123*(12), 1153-1161.

Salgado, R., Tehrani, F. S., & Prezzi, M. (2014). Analysis of laterally loaded pile groups in multilayered elastic soil. *Computers and Geotechnics, 62*, 136-153.

Schweckendiek, T. (2010). Reassessing reliability based on survived loads. *COASTAL ENGINEERING*, 2. Retrieved from https://repository.tudelft.nl/islandora/object/uuid:2569afed-b3f4-4427-85cd-d8cb0c49dbe5?collection=research

Schweckendiek, T., & Kanning, W. (2016). *Reliability updating for slope stability of dikes: Approach with fragility curves (background report)*: Deltares.

Schweckendiek, T., Van Der Krogt, M. G., Teixeira, A., Kanning, W., Brinkman, R., & Rippi, K. (2017). Reliability updating with survival information for dike slope stability using fragility curves. *Geo-Risk 2017*, 494-503.

Schweckendiek, T., Vrouwenvelder, A., & Calle, E. (2014). Updating piping reliability with field performance observations. *Structural Safety, 47*, 13-23.

Selby, A. R., & Arta, M. R. (1991). Three-dimensional finite element analysis of pile groups under lateral loading. *Computers & Structures, 40*(5), 1329-1336.

Sharma, S., Longo, M., & Messali, F. (2023). A novel tier-based numerical analysis procedure for the structural assessment of masonry quay walls under traffic loads. *Frontiers in Built Environment, 9*.

Simone, A. (2007). An Introduction to the Analysis of Slender Structures. In: TU Delft.

Sinkhole Marnixstraat zorgt nog langer voor hinder. (2017). *Parool*. Retrieved from https://www.parool.nl/nieuws/sinkhole-marnixstraat-zorgt-nog-langer-voor-hinder~bd66652c/

Snyder, J. L. (2004). *Full-scale lateral-load tests of a 3x5 pile group in soft clays and silts*: Brigham Young University.

Spannenburg, T. (2020). Timber Creep of Historic Urban Quay Walls: The influence of timber creep on the assessment of inner-city quay walls.

Stacul, S., & Squeglia, N. (2018). Analysis method for laterally loaded pile groups using an advanced modeling of reinforced concrete sections. *Materials, 11*(2), 300.

Steenbergen, R., Vrouwenvelder, A., & Scholten, N. (2012). Veiligheidsfilosofie bestaande bouw. toepassing en interpretatie NEN 8700.

Straub, D. (2011). Reliability updating with equality information. *Probabilistic Engineering Mechanics, 26*(2), 254-258.

Straub, D., & Papaioannou, I. (2015). Bayesian updating with structural reliability methods. *Journal of engineering mechanics, 141*(3), 04014134.

Sun, K. (1994). Laterally loaded piles in elastic media. *Journal of Geotechnical Engineering, 120*(8), 1324-1344.

Tan, H., Jiao, Z., & Chen, J. (2018). Field testing and numerical analysis on performance of anchored sheet pile quay wall with separate pile-supported platform. *Marine Structures, 58*, 382-398.

Thurston, R. H. (1879). On the strength of American timber. *Journal of the Franklin Institute, 108*(4), 217-235.

Tussenbroek, G. (2012). *Historisch hout in Amsterdamse monumenten: dendrochronologie, houthandel, toepassing*: Gemeente Amsterdam, Bureau Monumenten & Archeologie.

Van Alboom, G., & Baertsoen, A. (2005). *Geotechnical characterisation and monitoring versus FEM calculation results for a massive quay wall in the harbour of Antwerp, Belgium.* Paper presented at the Proceedings of the 16th International Conference on Soil Mechanics and Geotechnical Engineering.

Van Casteren, A., Sellers, W., Thorpe, S., Coward, S., Crompton, R., & Ennos, A. (2012). Why don't branches snap? The mechanics of bending failure in three temperate angiosperm trees. *Trees, 26*(3), 789-797.

van de Kuilen, J. W., Beketova-Hummel, O., Pagella, G., Ravenshorst, G., Gard, W., van de Kuilen, J., . . . Gard, W. (2021). *An integral approach for the assessment of timber pile foundations.* Paper presented at the World Conference on Timber Engineering 2021, WCTE 2021.

Van de Kuilen, J. W. G., & Dias, A. M. (2011). Long-term load–deformation behaviour of timber–concrete joints. *Proceedings of the Institution of Civil Engineers-Structures and Buildings, 164*(2), 143-154.

van Hulten, C. (2021). Recognizing critically damaged quay wall structures using a three-dimensional numerical model.

van Tussenbroek, G. (2012). Historisch hout in Amsterdamse monumenten. Dendrochronologie–houthandel–toepassing.

Varossieau, W. (1949). Opgegraven en aangetast hout uit biologisch oogpunt bezien.

Venmans, A. A., Op De Kelder, M., De Jong, J., Korff, M., & Houtepen, M. (2020). Reliability of InSAR satellite monitoring of buildings near inner city quay walls. *Proceedings of the International Association of Hydrological Sciences, 382*, 195-199.

Verruijt, A., & van Baars, S. (2005). *Grondmechanica*: VSSD.

WANG, Y. (2011). Reliability-based design of spread foundations by Monte Carlo simulations. *Geotechnique, 61*(8), 677-685.

Wennekes, E., & Grijp, L. P. (2002). *De hele dag maar op en neer. Over heien, heiliedjes en hoofdstedelijke muziekgebouwen*: Het Muziekgebouw ism Meertens Instituut.

Wilkinson, T. L. (1968). *Strength evaluation of round timber piles* (Vol. 101): Forest Products Laboratory.

Winkler, E. (1867). *Die Lehre von der Elasticitaet und Festigkeit: mit besonderer Rücksicht auf ihre Anwendung in der Technik für polytechnische Schulen, Bauakademien, Ingenieue, Maschinenbauer, Architecten, etc* (Vol. 1): Dominicus.

Winsen, M. v., Velzen, H., Dasselaar, M., & van der Mark, A. (2015). Archeologisch en bouwhistorisch bureauonderzoek van de historische binnenstad van Gouda–In het kader van het projectplan "stevige stad op slappe bodem". *FlexusAWC/ArcheoMedia Bv. Archeologisch en cultuurhistorisch bureauonderzoek, 50*.

Wolfe, R., & Murphy, J. (2005a). Strength of small-diameter round and tapered bending members. *Forest Products Journal, 55*(3), 50-55.

Wolfe, R., & Murphy, J. (2005b). *Strength of small-diameter round and tapered bending members*. Retrieved from

Wolters, H., Bakker, K., & de Gijt, J. (2014). Reliability of quay walls using finite element analysis. *Plaxis Bulletin, Spring issue*, 12-15.

Wright, S. G. (1982). Laterally loaded pile groups. *Preprints for Short Course on Deep Foundations*, 1-20.

Xu, L.-Y., Cai, F., Wang, G.-X., & Ugai, K. (2013). Nonlinear analysis of laterally loaded single piles in sand using modified strain wedge model. *Computers and Geotechnics, 51*, 60-71.

Yang, M., Deng, B., & Wang, Y. (2019). A Simplified Calculation Method for the Near-Slope Laterally Loaded Pile Based on a Passive Wedge Model. *Advances in Civil Engineering, 2019*.

Yin, Y., Qiao, Y., & Hu, S. (2019). Four-point bending tests for the fracture properties of concrete. *Engineering Fracture Mechanics, 211*, 371-381.

Yu, Y., & Cai, C. (2019). Prediction of extreme traffic load effects of bridges using Bayesian method and application to bridge condition assessment. *Journal of Bridge Engineering, 24*(3), 04019003.

Yuen, K.-V. (2010). *Bayesian methods for structural dynamics and civil engineering*: John Wiley & Sons.

Zeng, X., & Steedman, R. (1993). On the behaviour of quay walls in earthquakes. *Geotechnique, 43*(3), 417-431.

Zhang, J., Zhang, L., & Tang, W. H. (2011). Slope reliability analysis considering site-specific performance information. *Journal of geotechnical and geoenvironmental engineering, 137*(3), 227-238.

Zhang, L. (2004). Reliability verification using proof pile load tests. *Journal of geotechnical and geoenvironmental engineering, 130*(11), 1203-1213.

Zhou, D., & Jin, B. (2003). Boussinesq–Flamant problem in gradient elasticity with surface energy. *Mechanics Research Communications*, *30*(5), 463-468.

Zirakashvili, N. (2020). Solution of contact problems for half-space by boundary element methods based on singular solutions of flamant and boussinesq's problems. *International Journal of Applied Mechanics*, *12*(02), 2050015.

Acknowledgements

At the beginning of a career, there are numerous possibilities to shape one's professional life. As a newly graduated civil engineer, I also faced this decision in 2019, and honestly, I wasn't entirely sure of the answer. One of my Master thesis supervisors, Dirk Jan Peters, approached me with a one-year position as a research fellow at the Amsterdam Institute for Advanced Metropolitan Solutions (AMS) to study the strength of historic inner-city quay walls. It didn't take long before I became captivated by the quay walls, and this journey eventually led to a unique PhD trajectory. During this trajectory, I had the privilege of collaborating with multiple knowledge institutions and universities, establishing close partnerships with the Municipality of Amsterdam, work together with engineering companies and be out in the field on the construction site. Now that this journey has come to an end, I would like to express my appreciation to the many people who have played significant roles in various ways.

First, I would like to express my gratitude to my co-promoters Dirk Jan Peters and Mandy Korff for their support and guidance throughout the project. From the very beginning, we formed a cohesive quay wall team, collaborating seamlessly. Dirk Jan Peters' ability to interweave theory and practice in a creative manner is remarkable. Our discussions and brainstorms, combined with his approach, have shaped the unique way in which we tested and modelled quay walls. Mandy Korff's precise and consistently positive approach, along with her accessibility for discussions and reflections on the current work, ensured stability and quality throughout the research. I am truly grateful to have benefited from the collaboration with both of them.

Furthermore, I would like to thank my supervisor Bas Jonkman for his clear and comprehensive vision on the research. His ability to illuminate the overarching theme of the entire study and corresponding targeted advice has resulted in a cohesive and integral doctoral thesis. Together with Roelof Moll, you ensured that I could pursue my doctoral research at the Section of Hydraulic Structures and Flood Risk within the department of Hydraulic Engineering at Delft University of Technology.

Many thanks go out to the AMS Institute and all my colleagues and fellow researchers who have provided me with support and advice throughout this journey. I would especially like to express my gratitude to Kenneth Heijns for the past four years at the institute. The opportunities you provided me with have greatly benefited my growth and development. I would also like to extend my gratitude to Henk Wolfert for providing guidance within AMS.

I would like to acknowledge the Municipality of Amsterdam for placing their trust in us and providing the financial resources to conduct a full-scale experimental program in the city. Their confidence in our research has been immensely valuable, and I would like to thank Annemarij Kooistra, Sarah Bork, Jan Dijstelbloem, Rik Hoogeveen, Erik Hutcheson, Geeralt van der Ham, Remco Kleinlugtenbelt, and other colleagues from the Municipality of Amsterdam.

When it comes to the experimental program, there are numerous individuals I would like to extend my gratitude to. Firstly, I want to thank Erik Hutcheson. You were not only my closest colleague but also my nearest helpline on the construction site. Your experience and

accessibility contributed significantly to my steep learning curve. Additionally, I would like to thank IV-Infra for providing high-quality monitoring services. Special thanks go to Jelle van Ophuizen, Eric Valckenier and Roland Ras; your dedication played a vital role in our success. The time we spent in the construction trailer was very enjoyable. I would also like to acknowledge and thank De Klerk, Werkendam for their engineering and construction efforts in the testing program. My gratitude goes to Jan-Willem Oome, Peter van Santen, and Lucas Kamphuis for their valuable contributions. Furthermore, I extend my thanks to the divers of Maksor Diving B.V., particularly Michael Pellicaan, for their exceptional work under challenging conditions. Lastly, I want to express my appreciation to Willem van Bommel from Gemeente Rotterdam for the installation of fiber optics.

Last and most importantly, I would like to say a big thankyou to my friends and family. In particular, I am thankful to my parents, brother, sister-in-law, and my girlfriend Silke for their unconditional support, love, and help throughout the completion of this thesis. Their presence and encouragement have been invaluable to me.

As my grandpa used to say, “Keep learning until your fingers have the same length”.
I presume that I have a long way to go...

Curriculum vitae

Mart-Jan Hemel was born on July 20th, 1995 in Utrecht. He grew up in Zeist and in 2013 he received his secondary school diploma (Atheneum NT) from Katholieke Scholengemeenschap de Breul. In that same year, he started his study in civil engineering at Delft University of Technology. During his studies, he actively contributed as a student assistant in a technical drawing and graphical modelling course, where he delivered lectures to a class of students on a weekly basis for over two years. In the final stages of his studies, he conducted an international multidisciplinary port development project in Chile, collaborating closely with the UCSC University of Concepción and the San Vicente Port. In October 2019, he graduated in the field of hydraulic engineering on a Master thesis that studied the dynamic response of a submerged floating tunnel in a wave current environment. The study was awarded the Schreudersstudy-audience-price.

After graduating, Mart-Jan Hemel joined the Amsterdam Institute for Advanced Metropolitan Solutions (AMS) as a research fellow in 2019, focusing on the strength of historic quay walls in Amsterdam's city centre. In 2021, he continued his work as a PhD candidate while maintaining his role as a research fellow at AMS. Over a period of four years, his research encompassed the development of a computational quay wall model, the design and execution of a full-scale quay wall testing program, and the exploration of Bayesian updating for historic inner-city quay walls. His research on historic quay walls contributed to the development of the assessment protocol known as TAK (Toetskader Amsterdamse Kademuren). Additionally, Hemel has presented at various events. He gave the Leeuwenhoek Lecture for the residents of Delft, presented his research to Mayor Halsema of Amsterdam but also to the boards of Delft University and Wageningen University, presented his findings at a KIVI Engineering Society quay symposium and organized a symposium on historic quay walls at AMS. In collaboration with a select team of researchers, he took part in a study on the collapse of the Grimburgwal, which received national media attention. The findings were published and the paper was awarded the Telford Premium Prize.

Hemel has published technical reports and journal papers on topics on the above topics. An overview can be found on google scholar:
https://scholar.google.com/citations?user=gEZ1ywEAAAAJ&hl=nl

Linkedin: https://nl.linkedin.com/in/mart-jan-hemel

APPENDIX

Appendix A Overamstel experimental site

A.1 Overamstel quay wall site

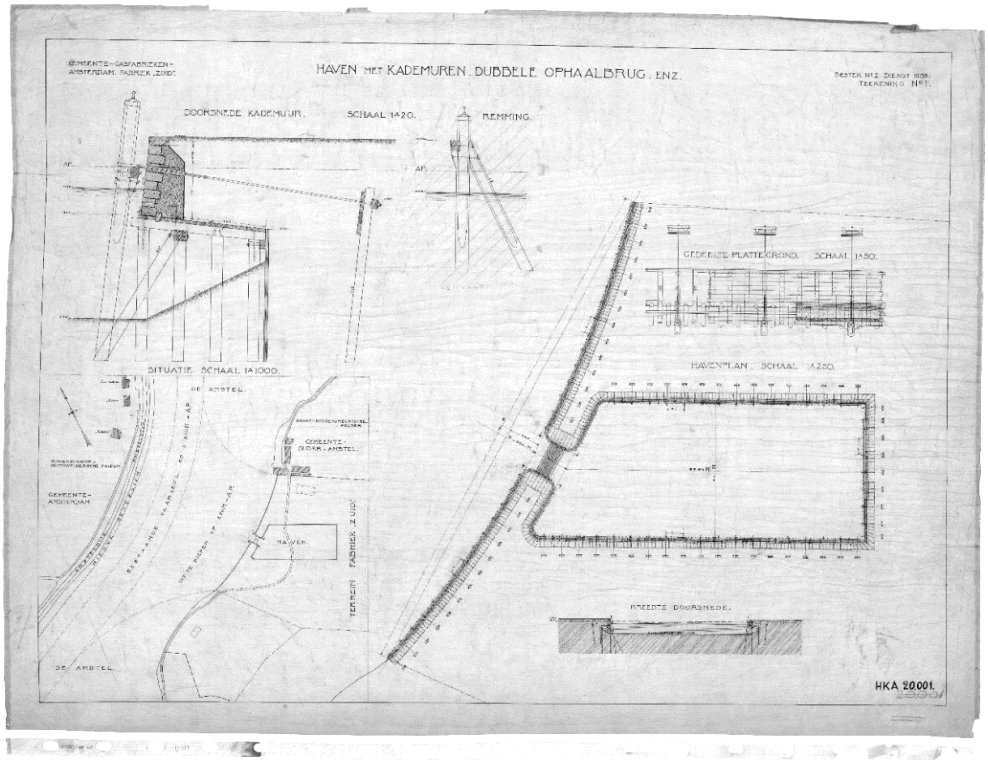

Figure A.1, Archive drawing on Overamstel quay wall including: Top left quay wall cross-section. Bottom left Top view on Amstel river and location of the Overamstel port. Right Detailed top view on port layout and its pile plan. Date 1908.

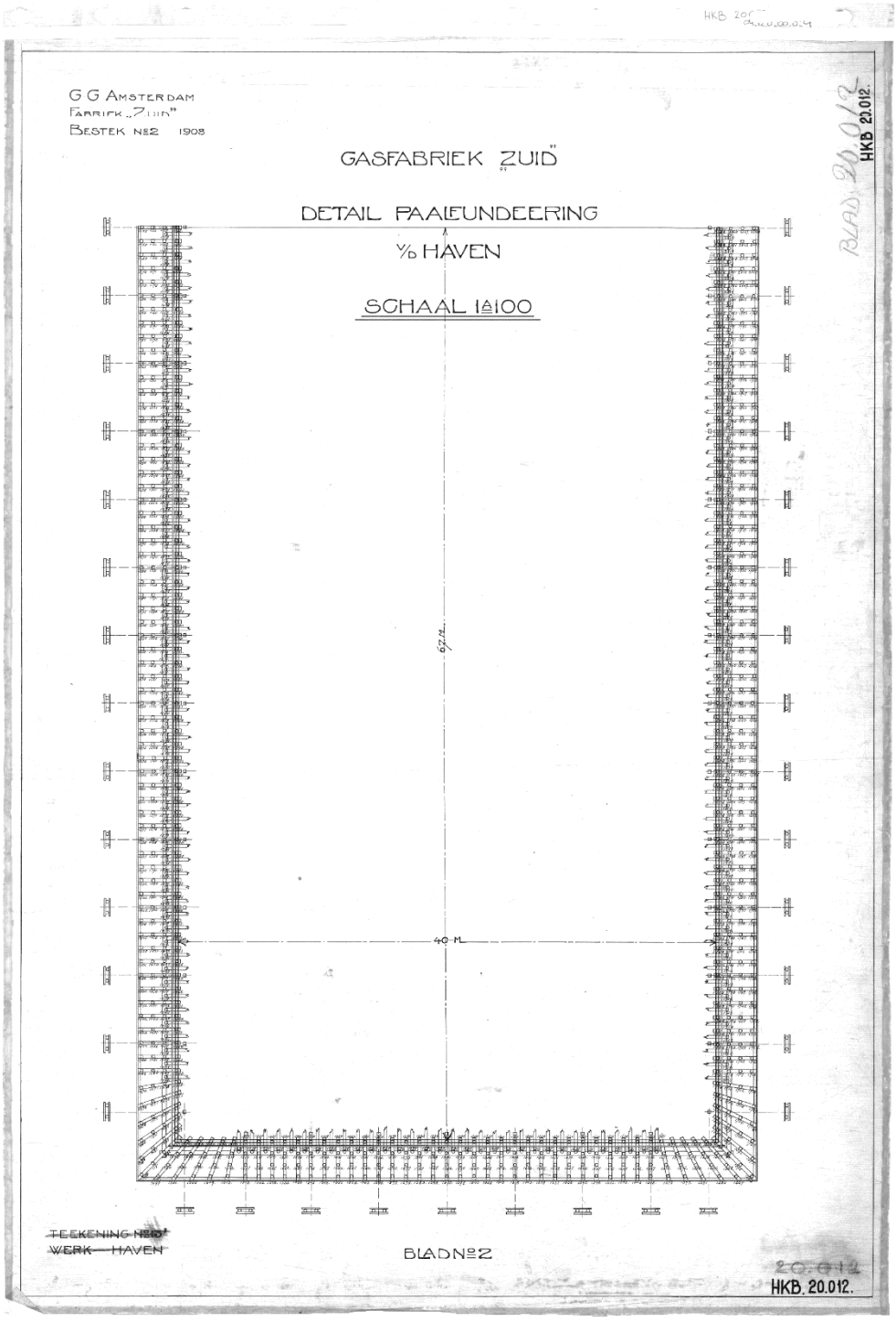

Figure A.2, Archive drawing on Overamstel quay wall with a detailed top view on the most land-inward port side and its pile plan. Date 1908.

A

A.2 Geotechnical site investigation Overamstel

A.2.1 Geotechnical conditions segments

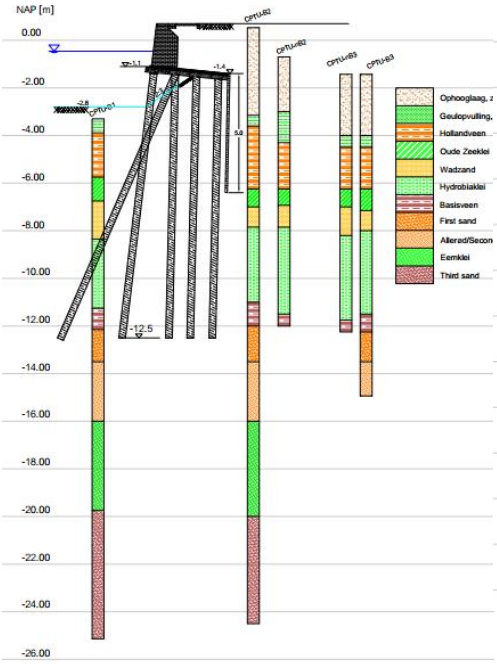

Figure A.3, Cross-sectional geotechnical conditions for segment B (Choosrithong et al., 2023).

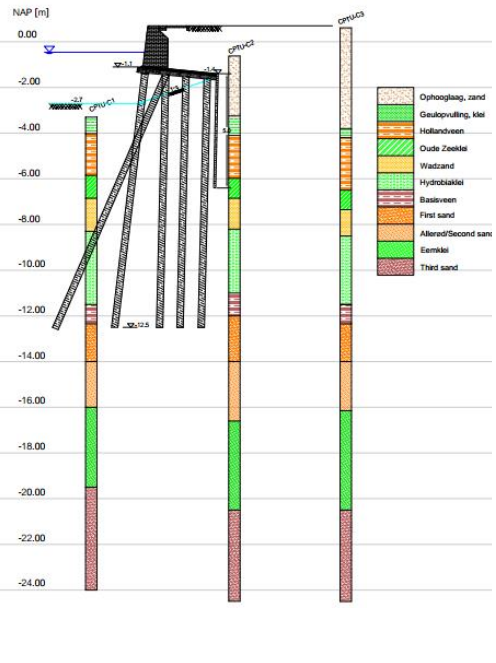

Figure A.4, Cross-sectional geotechnical conditions for segment F (Choosrithong et al., 2023).

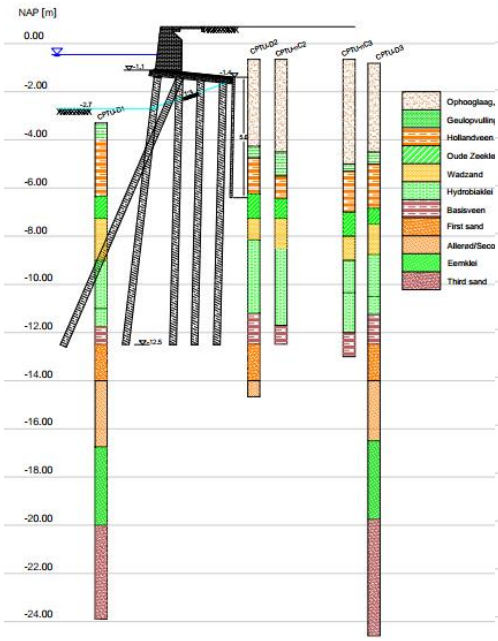

Figure A.5, Cross-sectional geotechnical conditions for segment C1 (Choosrithong et al., 2023).

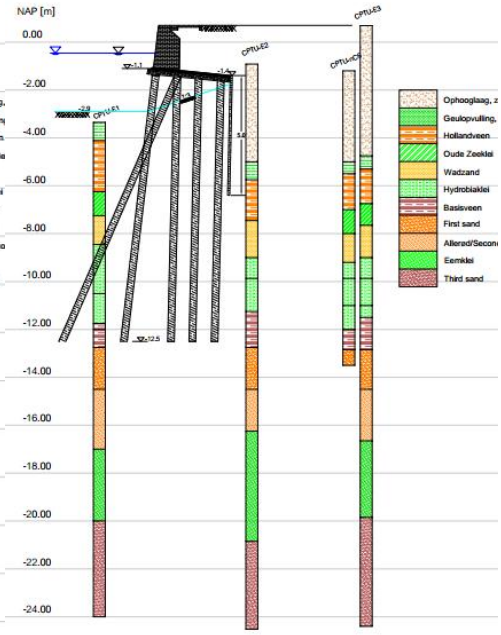

Figure A.6, Cross-sectional geotechnical conditions for segment C2 (Choosrithong et al., 2023).

A

Appendix B Four-Point bending experiments – Overamstel

B.1 Bending moments and force ratio

The pile deflection y[m] is described by an Euler Bernoulli beam of which the bending equation is provided in eq. B.1. In here, ρ_t[kg/m^3] is the density of the timber, a[mm/mm] the tapering of the pile per meter and D_l [m] the diameter at the location of the local reference system.

$$\frac{d^2}{dx^2}\left(E_b \frac{\pi(D_l - \mathrm{a}x)^4}{64}\frac{d^2y}{dx^2}\right) = \rho_t \frac{1}{4}\pi(D_l - ax)^2 \qquad \textbf{eq. B.1}$$

The pile is divided into three fields A, B and C for which the general solution of each field can be found in eq. B.2. In here, A_i, B_i and C_i are the integration constants.

$$y_A(x) = \frac{\left(\frac{A_1}{D_l - \alpha x} + \frac{A_2}{(D_l - \alpha x)^2} + \frac{4\rho_t x^2}{E_b}\right)}{6\alpha^2} + A_4 x + A_3$$
$$y_B(x) = \frac{\left(\frac{B_1}{D_l - \alpha x} + \frac{B_2}{(D_l - \alpha x)^2} + \frac{4\rho_t x^2}{E_b}\right)}{6\alpha^2} + B_4 x + B_3 \qquad \textbf{eq. B.2}$$
$$y_C(x) = \frac{\left(\frac{C_1}{D_l - \alpha x} + \frac{C_2}{(D_l - \alpha x)^2} + \frac{4\rho_t x^2}{E_b}\right)}{6\alpha^2} + C_4 x + C_3$$

To solve the system of equations, the following boundary and interface conditions are used in which the rotation φ[rad], bending moment M[kNm] and shear force V[kN] are described by the kinematic and constitutive relations in eq. B.3.

$x = 0$	$y_A = 0$	$M_A = 0$		
$x = L_1$	$y_A = y_B$	$M_A = M_B$	$V_A = V_B + F_1$	$\varphi_A = \varphi_B$
$x = L_2$	$y_B = y_C$	$M_B = M_C$	$V_B = V_C + F_2$	$\varphi_B = \varphi_C$
$x = L$	$y_C = 0$	$M_C = 0$		

$$\varphi(x) = -\frac{dy}{dx};\ M(x) = -E_b \frac{\pi(D_l - \alpha x)^4}{64}\frac{d^2y}{dx^2};\ V(x) = -E_b \frac{\pi(D_l - \alpha x)^4}{64}\frac{d^3y}{dx^3} \qquad \textbf{eq. B.3}$$

Substituting the general solutions of eq. B.2 into the boundary conditions results in a system of equations. Solving this set of equations results in the following bending moment equations for field A,B and C presented in eq. B.4.

$$M_A(x) = \frac{(L^4\pi\alpha^2\rho_t - 4D_l L^3\pi\alpha\rho_t + 6D_l^2L^2\pi\rho_t + (-x\pi(\alpha^2x^2 - 4D_l\alpha x + 6D_l^2)\rho_t - 48F_1 - 48F_2)L + 48L_1F_1 + 48F_2L_2)x}{48L}$$
$$M_B(x) = \frac{L^4\pi\alpha^2\rho_t x - 4D_l L^3\pi\alpha\rho_t x + 6D_l^2L^2\pi\rho_t x + (-\pi\alpha^2\rho_t x^4 + 4\pi D_l\alpha\rho_t x^3 - 6D_l^2\pi\rho_t x^2 - 48L_1F_1 - 48F_2 x)L + 48x(L_1F_1 + F_2L_2)}{48L}$$
$$M_C(x) = \frac{(L - x)(L^3\pi\alpha^2\rho_t x + \rho_t\alpha x\pi(\alpha x - 4D_l)L^2 + x\pi(\alpha^2x^2 - 4D_l\alpha x + 6D_l)\rho_t L - 48L_1F_1 - 48F_2L_2)}{48L} \qquad \textbf{eq. B.4}$$

From the bending moment, the bending stresses in the outer-fibre can be determined by dividing the bending moment by the section modulus, expressed in eq. B.5.

$$\sigma_{outer,i}(x) = \frac{32M_i(x)}{(D_l - \alpha x)^3\pi} \qquad i = A, B, C \qquad \textbf{eq. B.5}$$

The ratio $a_F = F_1/F_2$ for which σ_{outer} are the same at L_1 and L_2 can be found by solving $\sigma_{outer,A}(L_1) = \sigma_{outer,B}(L_2)$ for a_F. The enclosed expression for this ratio is load dependent and therefore an implicit function. The force ratio as function of F_1, for each individual pile, is visualized in Figure B.1. It can be seen that with larger loads, the force ratio approaches an asymptotic value. For practical reasons, the choice is made to keep the force ratio constant

during the test. Since the piles are expected to fail around a load of 10kN, the force ratios are based on this value. The force ratios used can be found in Table 3.2.

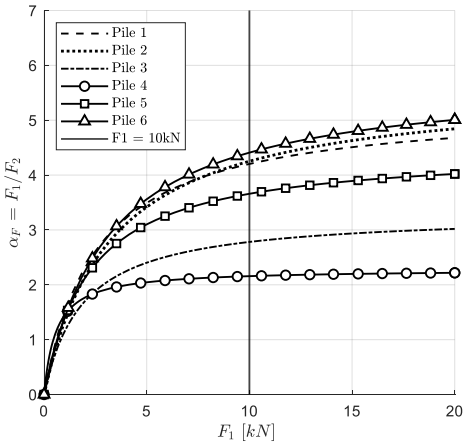

Figure B.1, Force ratio a_F as function of F_1 for all six piles.

B.2 Displacement, curvature and bending moments of piles

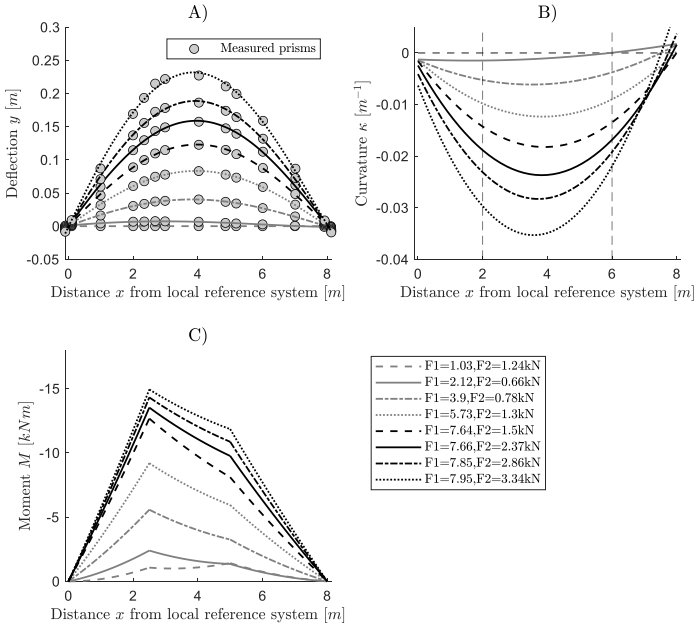

Figure B.2, Bending test results PILE 1, A) Displacement obtained by measuring prisms, B) Curvature obtained from deflection polynomial fit, C) Bending moment obtained by load cells and eq. B.4.

B

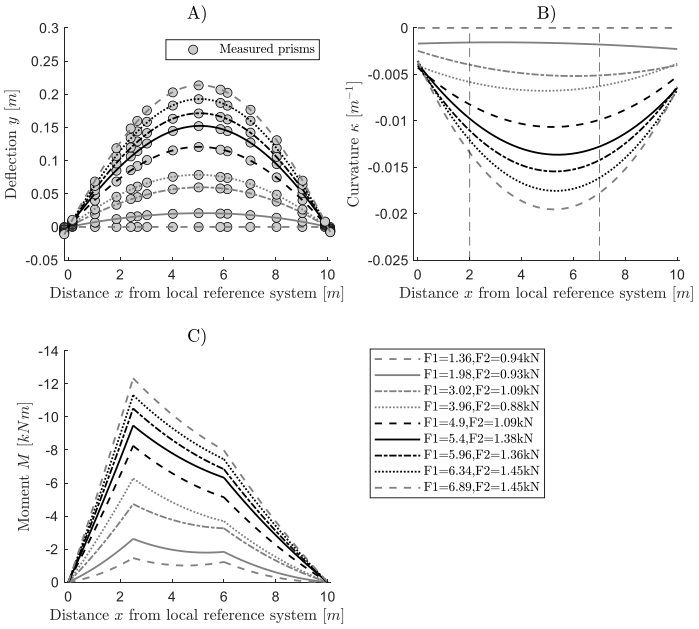

Figure B.3, Bending test results PILE 2, A) Displacement obtained by measuring prisms, B) Curvature obtained from deflection polynomial fit, C) Bending moment obtained by load cells and eq. B.4.

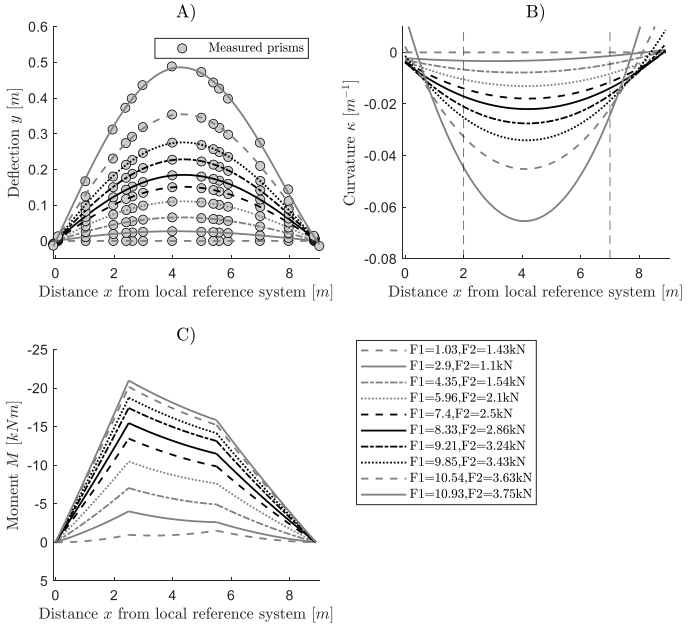

Figure B.4, Bending test results PILE 3, A) Displacement obtained by measuring prisms, B) Curvature obtained from deflection polynomial fit, C) Bending moment obtained by load cells and eq. B.4.

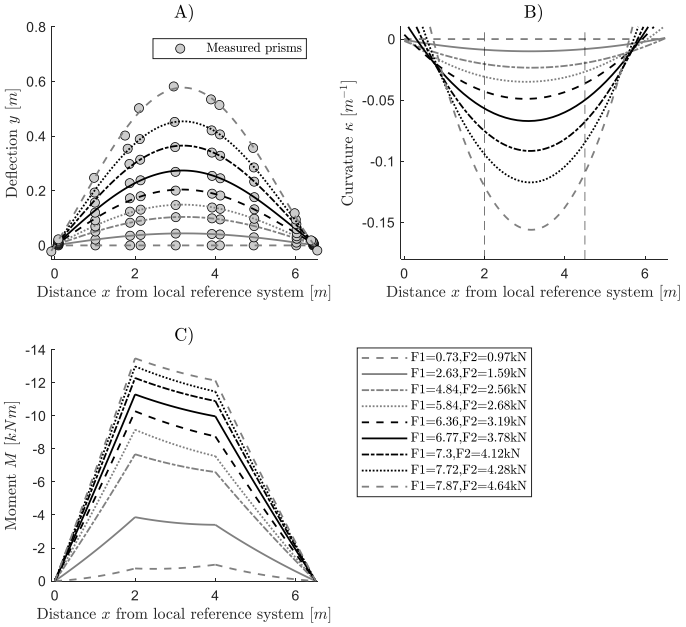

Figure B.5, Bending test results PILE 4, A) Displacement obtained by measuring prisms, B) Curvature obtained from deflection polynomial fit, C) Bending moment obtained by load cells and eq. B.4.

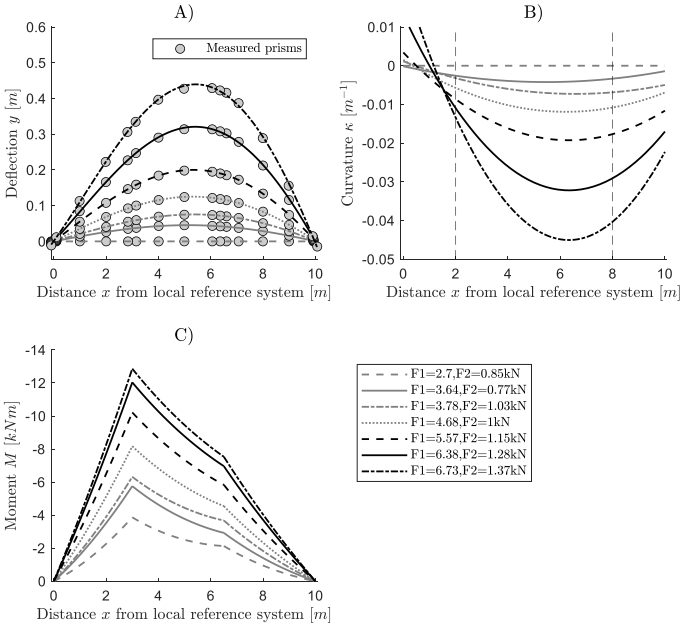

Figure B.6, Bending test results PILE 6, A) Displacement obtained by measuring prisms, B) Curvature obtained from deflection polynomial fit, C) Bending moment obtained by load cells and eq. B.4.

B.3 Curvature-moment diagrams

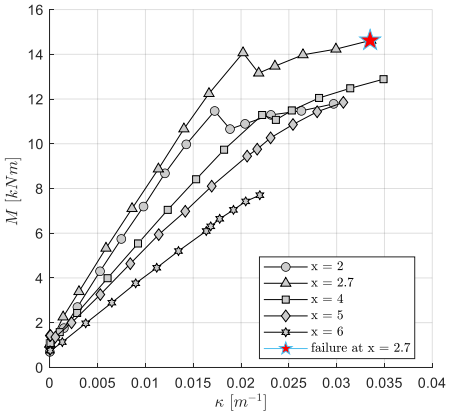

Figure B.7, Curve-Moment diagram pile 1.

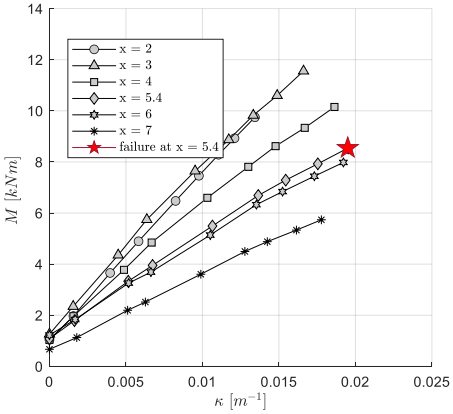

Figure B.8, Curve-Moment diagram pile 2.

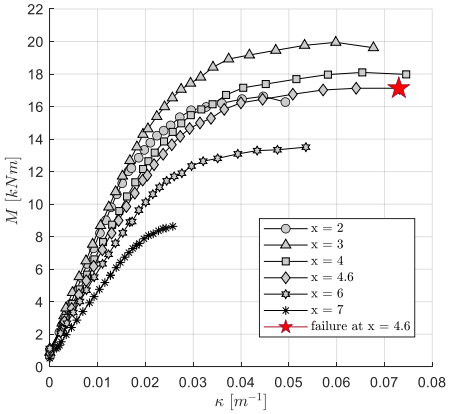

Figure B.9, Curve-Moment diagram pile 3.

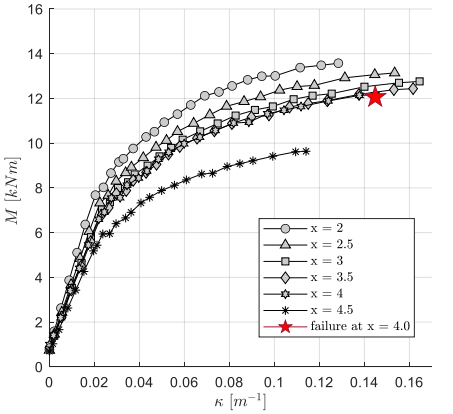

Figure B.10, Curve-Moment diagram pile 4.

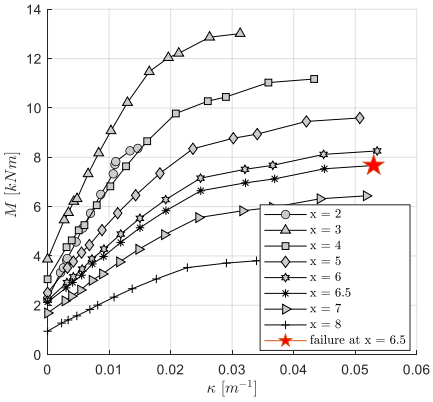

Figure B.11, Curve-Moment diagram pile 6.

B.4 Derivations

B.4.1 Derivation of deflection from curvature

To derive the deflection from the curvature profile $\kappa_t(x)$, a simply supported beam is considered (see Figure B.12) (Hartsuijker, 2001). The deflection y on location x can described by eq. B.6.

$$y(x) = \varphi_a x - (x - x_1)\theta \qquad \textbf{eq. B.6}$$

In eq. B.6, the rotation φ_a[rad] at support A is described by eq. B.7 and θ[rad] the area of the integrated area between $x = 0$ and $x =$ *'x'* (see Figure B.12 in red) given by eq. B.8. The distance from A to the metric centre of the integrated area between $x = 0$ and $x = x$ is indicated by x_1 [m] and can be determined according to eq. B.9.

$$\varphi_a = \int_0^L \left(1 - \frac{x}{L}\right) \kappa_t(x)\mathrm{d}x \qquad \textbf{eq. B.7}$$

$$\theta = \int_0^x \kappa_t(x)\,\mathrm{d}x \qquad \textbf{eq. B.8}$$

$$x_1 = \frac{\int_0^x x\,\kappa_t(x)\,\mathrm{d}x}{\int_0^x \kappa_t(x)\,\mathrm{d}x} \qquad \textbf{eq. B.9}$$

Substituting eq. B.7, eq. B.8 and eq. B.9 into eq. B.6 results an expression for $y(x)$ which is dependent on $\kappa_t(x)$ and L. After simplifying, $y(x)$ can be described by eq. B.10.

$$y(x) = -\frac{\left(\int_0^L (1-x)\kappa_t(x)dx\right)x - L\left(x\left(\int_0^x \kappa_t(x)dx\right) - \left(\int_0^x x\kappa_t(x)dx\right)\right)}{L} \qquad \textbf{eq. B.10}$$

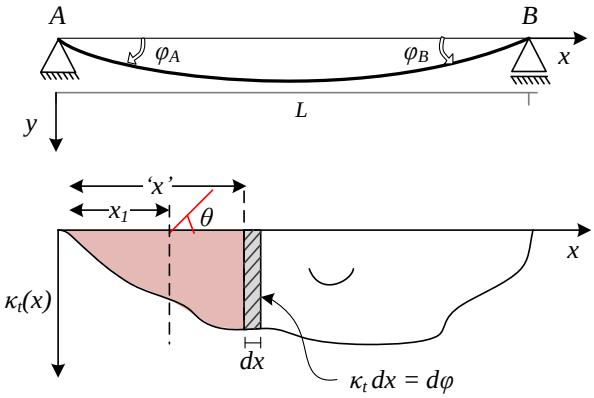

Figure B.12, Illustrative figure of simply supported beam in bending with corresponding curvature diagram.

B.4.2 Derivation of stress-strain relation

Mathematical expressions for the theoretical normalized moment-curvature of a circular cross-section can be found in eq. B.11, where $\sin(a^*)=1/\kappa^*$ (Pandit et al., 2022).

$$M^* = \frac{16}{3\pi}\left(1 - \frac{1}{\kappa^{*2}}\right)^{3/2} + \frac{2\kappa^*}{\pi}\left(\alpha^* - \frac{\sin(4\alpha^*)}{2}\right) \qquad \textbf{eq. B.11}$$

B

in which:

$$\alpha^* = \arcsin\left(\frac{1}{\kappa^*}\right) \qquad \textbf{eq. B.12}$$

$$\kappa^* = \frac{\kappa E_b h}{2\sigma} \qquad \textbf{eq. B.13}$$

Substituting eq. B.12 and eq. B.13 into eq. B.11 and multiplying this with the first yield moment M_0 (given in eq. B.14), results in an expression for the bending moment presented in eq. B.15.

$$M_0 = \frac{\pi h^3 \sigma}{32} \qquad \textbf{eq. B.14}$$

$$M = \frac{\left(\frac{16\left(1-\frac{4\sigma^2}{\kappa^2 E_b^2 h^2}\right)^{\frac{3}{2}}}{3\pi} + \frac{\kappa E_b h\left(\arcsin\left(\frac{2\sigma}{\kappa E_b h}\right) - \frac{\sin\left(4\arcsin\left(\frac{2\sigma}{\kappa E_b h}\right)\right)}{4}\right)}{\sigma\pi}\right)\pi h^3\sigma}{32} \qquad \textbf{eq. B.15}$$

Substitution of the curvature κ with $2\varepsilon/h$ and after simplification of eq. B.15 results in an expression for the bending moment as function of E_b, h, ε and σ, presented in eq. B.16.

$$M = \frac{h^3\left(\left(\frac{8}{3}E_b^2\varepsilon^2\sigma - \frac{8}{3}\sigma^3\right)\sqrt{\frac{E_b^2\varepsilon^2-\sigma^2}{E_b^2\varepsilon^2}} + E_b^3\varepsilon^3\left(\arcsin\left(\frac{\sigma}{E_b\varepsilon}\right) - \frac{\sin\left(4\arcsin\left(\frac{\sigma}{E_b\varepsilon}\right)\right)}{4}\right)\right)}{16E_b^2\varepsilon^2} \qquad \textbf{eq. B.16}$$

Appendix C Lateral pile group experiments – Overamstel

C.1.1 Technical drawings lateral pile group experiment

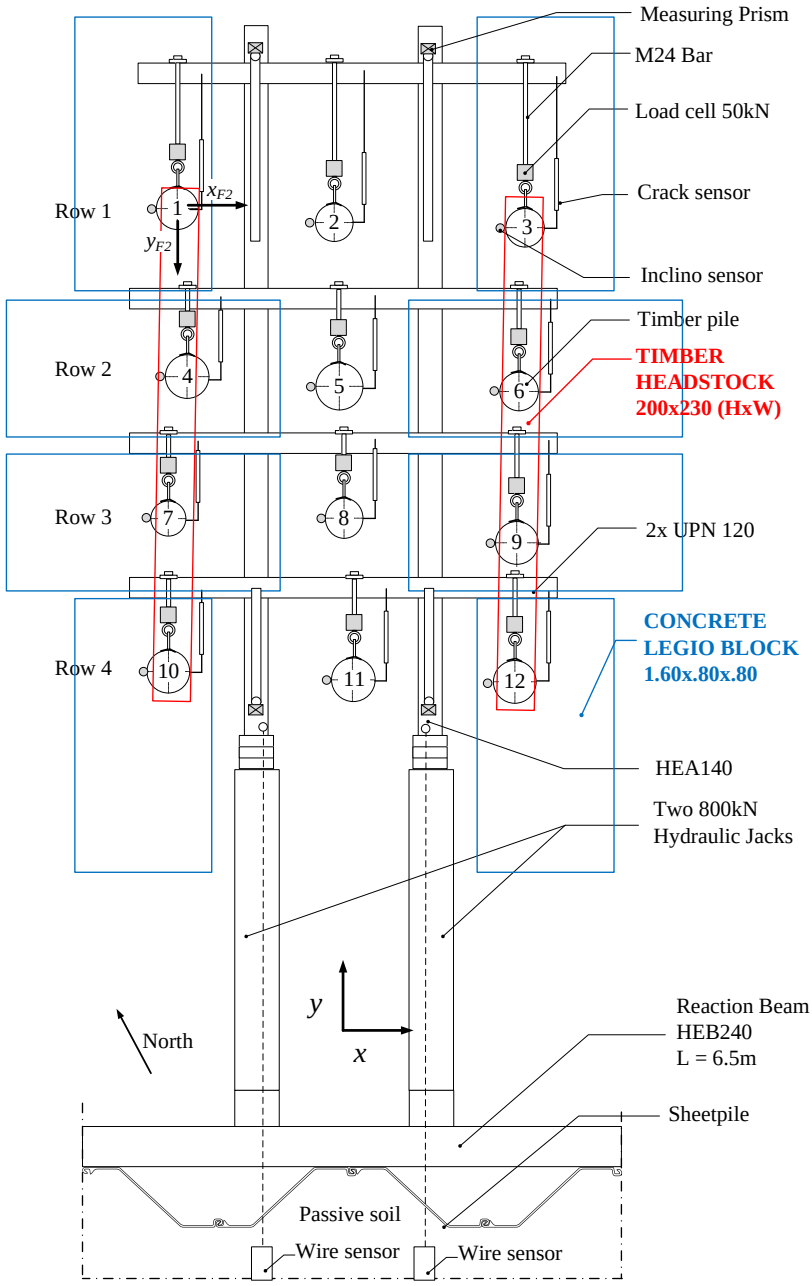

Figure C.1, Planview of lateral pile group experiment without top load.

C

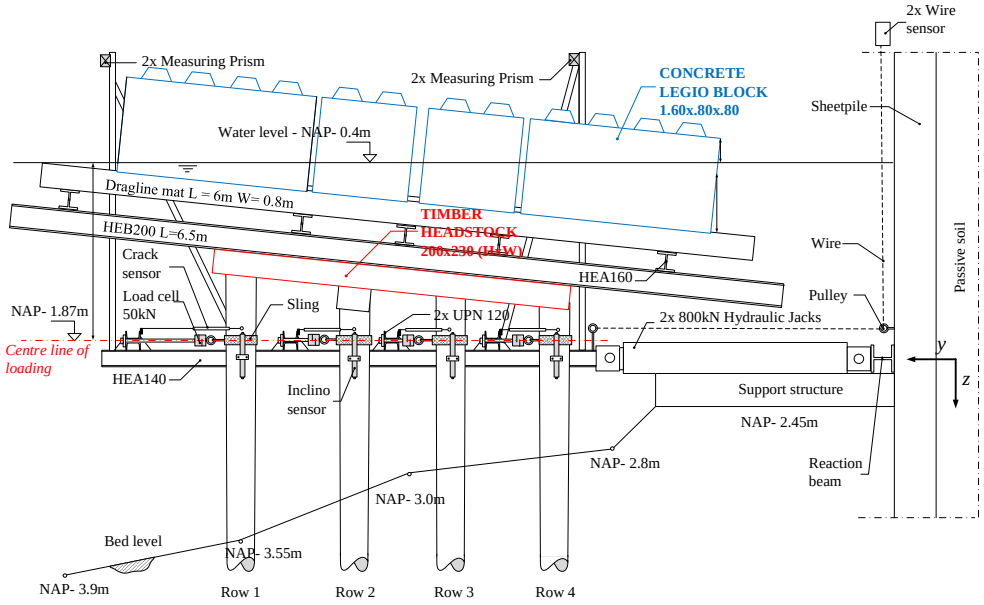

Figure C.2, Sideview of lateral pile group experiment without top load (F2).

Figure C.3, Photograph of lateral pile group experiment with top load. LEGIO-blocks are visible above the water level.

C.1.2 Sling extensions during lateral pile group experiments

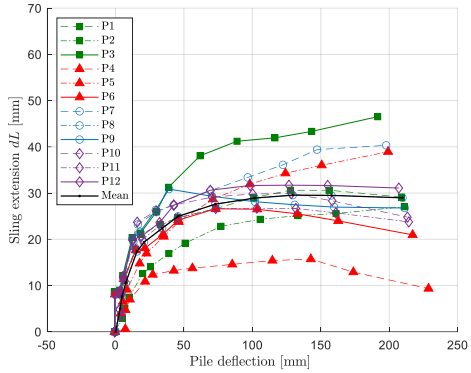

Figure C.4, Sling extensions per pile for test F2.

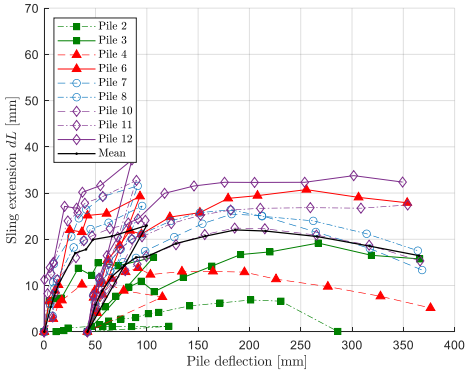

Figure C.5, Sling extensions per pile for test F1. Crack sensors for pile 1,5 and 9 are broken. For further computations, these piles are assigned the mean sling extension.

C.1.3 Calibration of the flexural stiffness for fibre optic instrumented piles

In Figure C.6, the measured cap force and calibrated shear force for piles P8F2, P2F2, P2F1 and P8F1 are presented. The shear force at the flee length of the timber pile fits the measured cap load well for scalar parameters Φ_{EI} = 1.7, 1.1, 1.2 and 1.5.

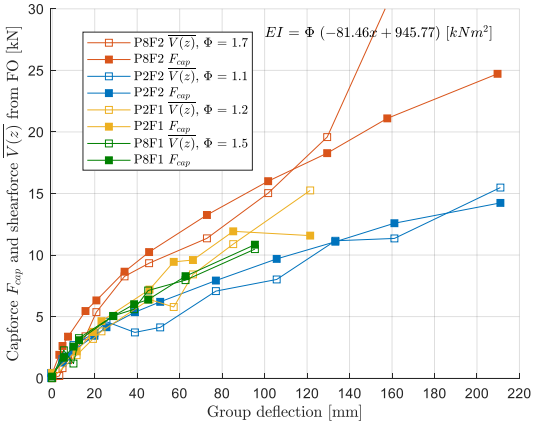

Figure C.6, Lateral load and calibrated shear force versus pile deflection plotted for piles P2F2, P8F2, P2F1 and P8F1. Values for the calibrated scalar parameters Φ_{EI} are provided.

C.1.4 Multi-regression analysis lateral resistance

This section analyses four effects: pile free height, side-by-side effects, in-line effects and pile diameter, to study their influence on the lateral capacity within the pile group. Figure C.7 plots the four effects separately, with linear trendlines and individual correlations provided. Applying a multi-variable linear regression model in the form $y = \beta_0 + \beta_1 x_1 + \beta_2 x_2 + \beta_3 x_3 + \beta_4 x_4$ on the four effects, results in an overall R^2 = 0.133 (ρ = 0.36) which states that side by side, free height, in-line and pile diameter together take account for 13% of the variance in lateral pile group resistance. The regression model was significant with a *p*-value

C

of 1.64e-12 smaller than the 5% significance level. The individual *p*-values and coefficient estimates are listed in Table C.1. It can be seen that the free height, side-by-side effect and in-line effects all are significant parameters (*p*-value <0.05) with respect to the lateral pile resistance. However the diameter is no significant parameter (*p*-value >0.05). Each parameter is discussed briefly.

The measurements show a negative correlation of -0.31 between free height and lateral resistance, indicating that higher pile free heights lead to lower pile resistance, consistent with literature. The side-by-side effect has a low but positive correlation meaning that side piles carry more lateral load than middle piles. This is corresponding to the theory that edging piles have higher lateral resistance than middle piles (Reese et al., 2010). The in-line effect, which typically causes front piles to carry more load than trailing piles, is observed to have the opposite trend in the measurements, with trailing piles carrying more load than leading piles. The free height of piles has a greater influence on lateral load than the in-line effect. Despite the expectation that larger pile diameters would result in greater lateral resistance, the multi-variable regression reveals that the diameter is insignificant. This is consistent with the bending experiments in chapter 3, which showed a wide range of flexural stiffness, bending strength, and shell thickness with no significant correlation to pile diameter.

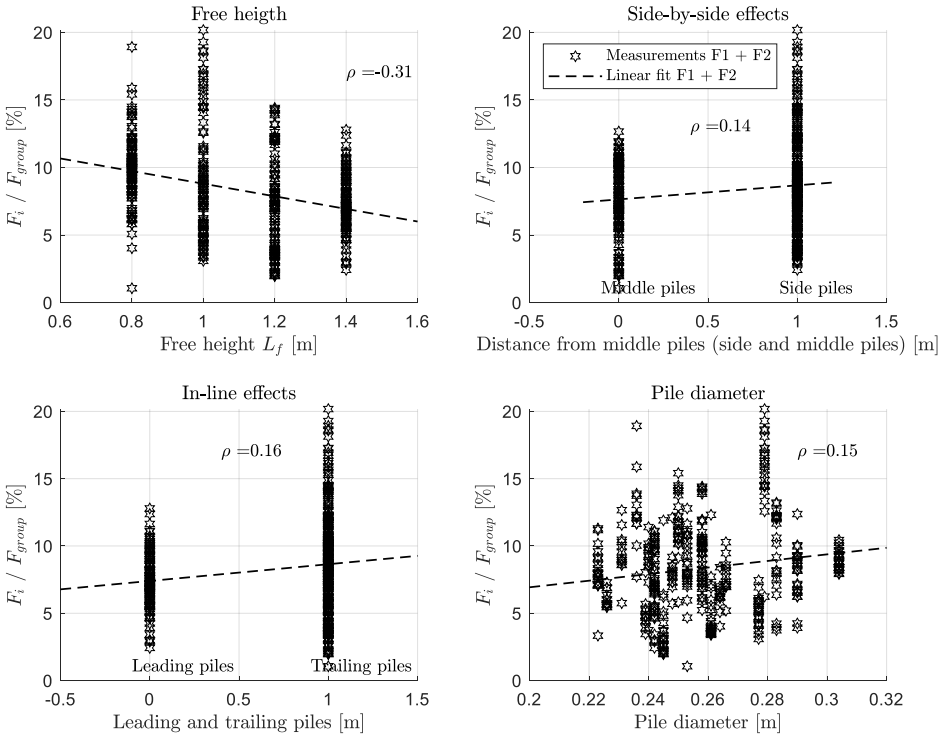

Figure C.7, Loads taken by individual piles F_i [kN] as percentage of the group average pile load F_{group} [kN] plotted for *top left*: pile free height, *top right*: side and middle piles, *bottom left*: leading and trailing piles, *bottom right*: pile diameter.

Table C.1, Multi-variable linear regression output.

	Estimate [%]	*p*-value
Intersection	13.75 (β_0)	2.3997e-07
Free height (x_1)	-6.92 (β_1)	5.1984e-10
Side-by-side (x_2)	0.79 (β_2)	0.034147
Diameter (x_3)	11.10 (β_3)	0.1898
In-line (x_4)	-1.58 (β_4)	0.0051265

Appendix D Quay wall experiments – Overamstel

D.1 Experimental results

D.1.1 Time series quay wall experiments

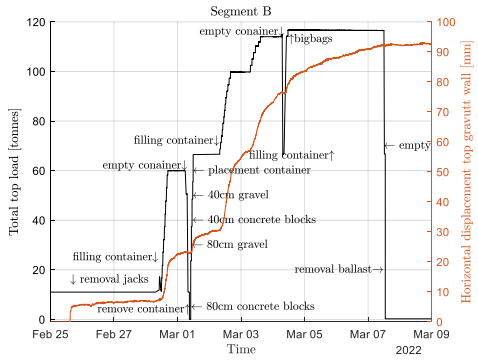

Figure D.1, Time series test-procedure B.

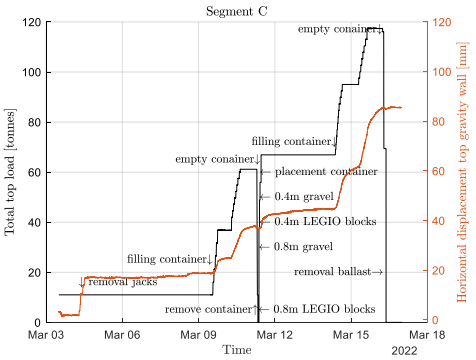

Figure D.2, Time series test-procedure C.

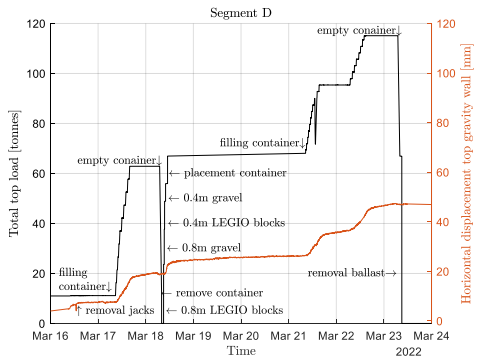

Figure D.3, Time series test-procedure D.

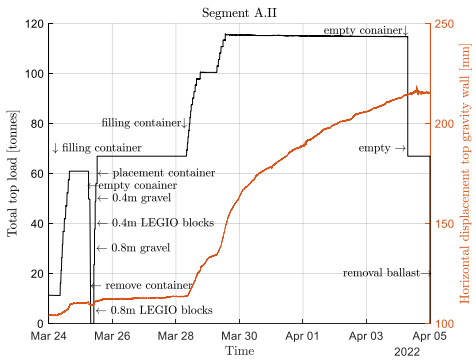

Figure D.4, Time series test-procedure A.II.

C

D.1.2 Soil settlements

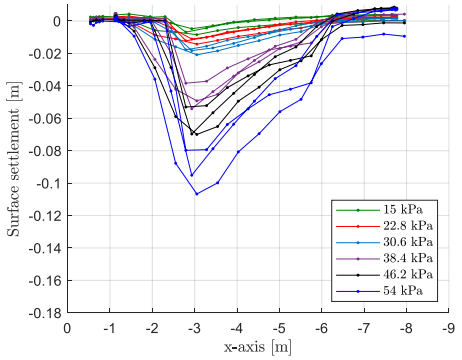

Figure D.5, Soil surface settlement B for multiple surface loads.

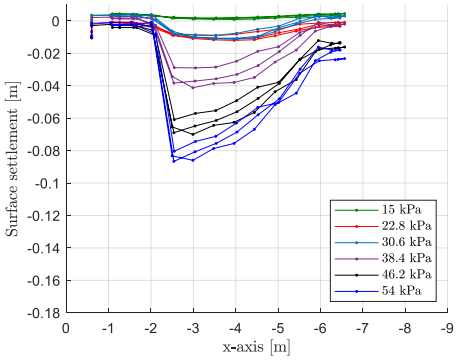

Figure D.6, Soil surface settlement C for multiple surface loads.

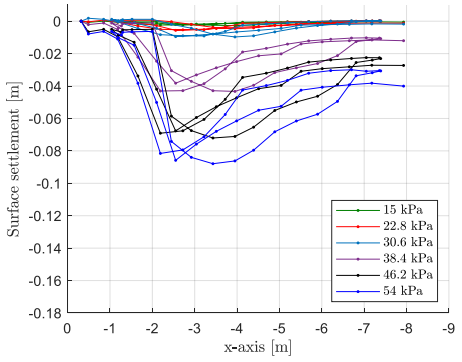

Figure D.7, Soil surface settlement D for multiple surface loads.

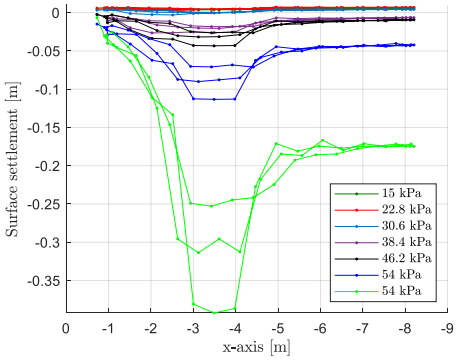

Figure D.8, Soil surface settlement A.II for multiple surface loads.

D.1.3 Horizontal soil deformation behind quay wall

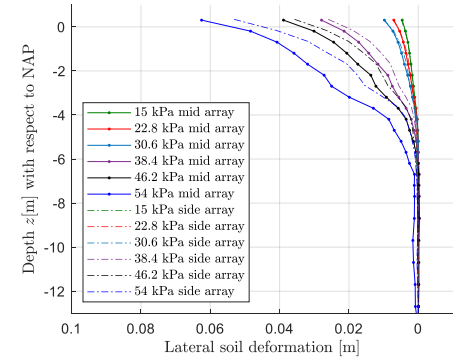

Figure D.9, Lateral soil deformation 1m behind quay B for multiple surface loads.

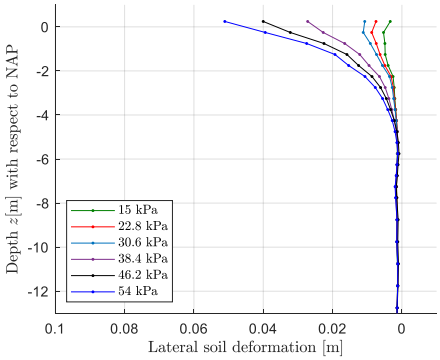

Figure D.10, Lateral soil deformation 1m behind quay C for multiple surface loads.

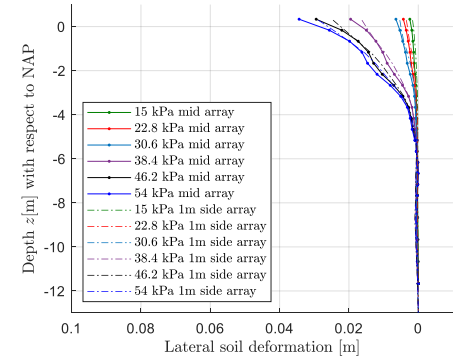

Figure D.11, Lateral soil deformation 1m behind quay D for multiple surface loads.

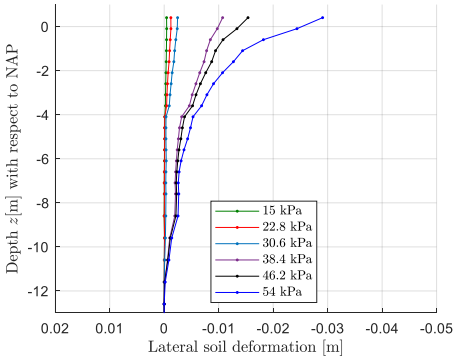

Figure D.12, Lateral soil deformation 1m behind quay A.II for multiple surface loads.

D.1.4 Water pressures

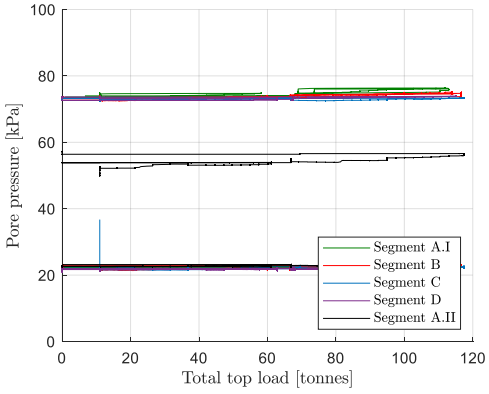

Figure D.13, Water pressures as function of applied container load for segment A.I, A.II, B, C and D.

D.1.5 Segmental friction calibration

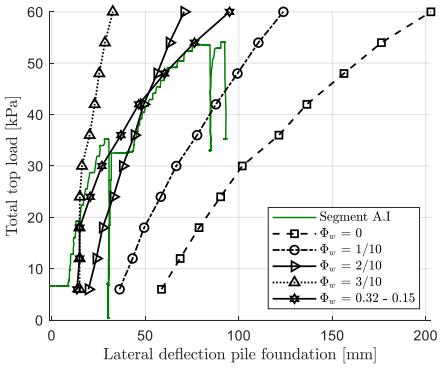

Figure D.14, Calibration of segmental friction factor Φ_w on measurements for segment A.I.

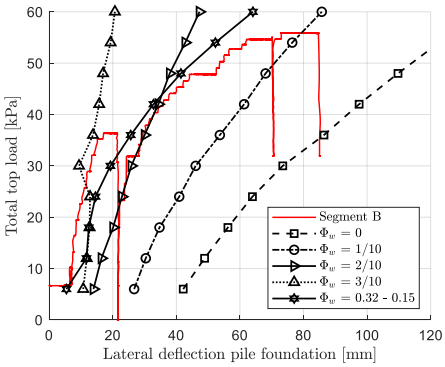

Figure D.15, Calibration of segmental friction factor Φ_w on measurements for segment B.

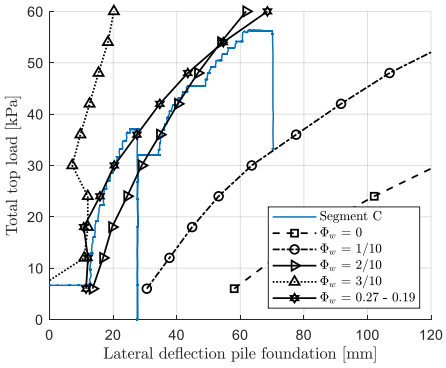

Figure D.16, Calibration of segmental friction factor Φ_w on measurements for segment C.

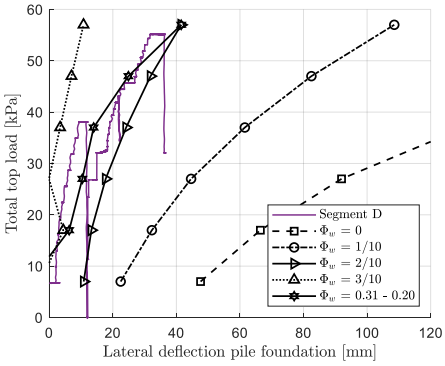

Figure D.17, Calibration of segmental friction factor Φ_w on measurements for segment D.

D.2 Prediction analytical model input

D.2.1 Structural model input quay wall

Table D.1, Input parameters for pile-headstock interface model in quay wall prediction.

Variable	Description	Value	Unit
h_p	Height of the pin	0.20	m
D	Diameter of the pile head	0.30	m
w_p	Width of the pin	0.10	m
$f_{c;90;kesp}\perp$	Compressive strength headstock perpendicular	2.2	N/mm^2
$f_{c;90;pin}\perp$	Compressive strength pin perpendicular	2.2	N/mm^2
$f_{m;0;pin}$	Bending strength of the pin	18	N/mm^2
$E_{90;mean;keps}\perp$	Elastic modulus headstock perpendicular	300	N/mm^2
$E_{90;mean;pin}\perp$	Elastic modulus of the pin perpendicular	300	N/mm^2

D.2.2 Geotechnical model input

Appendix Table D.2, Geotechnical model input for pile group model prediction.

Depth -NAP [m]	γ_{sat} [kN/m^3]	γ' [kN/m^3]	Sort [-]	Dutch name [-]	q_c [kPa]	c' [kN/m^2]	Φ [deg]
start soil – 5.0	12.0	2.0	peat	Holland veen	200	6.2	14.9
5.0 – 7.4	17.2	7.2	clay	Oude zeeklei	400	3.65	28.8
7.4 – 9.2	18.1	8.1	sand	Wad deposit	1800	2.17	25.0
9.2 – 12.4	15.5	5.5	clay	Hydrobiaklei	1000	10.9	23.6
12.4 – 14.0	18.9	8.9	sand	Eerste zandlaag	10000	0.0	35.0

Table D.3, Geotechnical model input for active soil body in quay wall prediction.

Depth -NAP [m]	γ_{sat} [kN/m^3]	γ' [kN/m^3]	Sort [-]	Dutch name [-]	φ [deg]
-0.7 – 0.4	18.0	18.0	fill	Ophooglaag, dry	32.5
0.4 – 2.0	19.0	9.0	fill	Ophooglaag, wet	32.5
2.0 – 4.5	18.0	8.0	silt	Geulopvulling slappeklei	30.0
4.5 – 6.0	12.0	2.0	peat	Holland veen	14.9
7.4 – 9.2	18.1	8.1	sand	Wad deposit	25.0
9.2 – 12.4	15.5	5.5	clay	Hydrobiaklei	23.6
12.4 – 12.4	18.9	8.9	sand	Eerste zandlaag	35.0

D.2.3 CPT – Overamstel

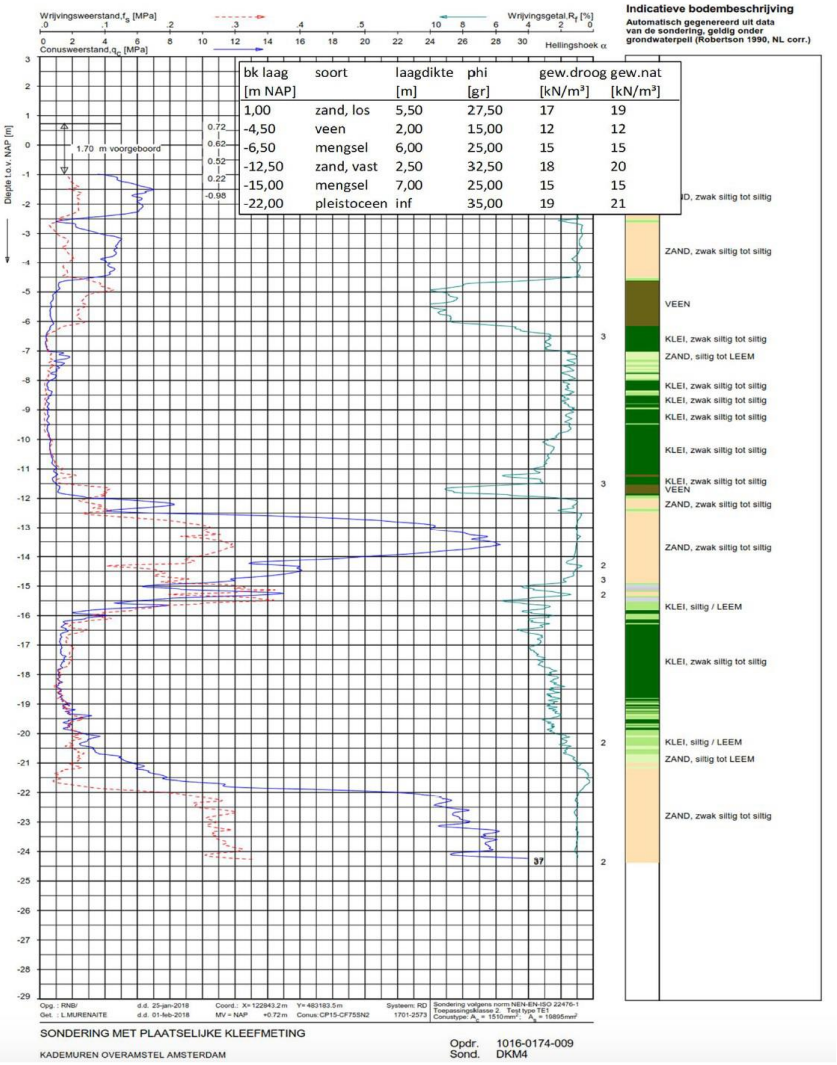

Figure D.18, Locally conducted CPT- prior to Overamstel experiments and geotechnical site investigation.

D.3 Postdiction analytical model input

D.3.1 Structural model input quay wall

Table D.4, Input parameters for pile-headstock interface model in quay wall postdiction.

Variable	Description	Value	Unit
h_p	Height of the pin	0.20	m
D	Diameter of the pile head	0.26	m
w_p	Width of the pin	0.10	m
$f_{c;90;kesp\perp}$	Compressive strength headstock perpendicular	2.3	N/mm^2
$f_{c;90;pin\perp}$	Compressive strength pin perpendicular	2.3	N/mm^2
$f_{m;0;pin}$	Bending strength of the pin	22	N/mm^2
$E_{90;mean;keps\perp}$	Elastic modulus headstock perpendicular	320	N/mm^2
$E_{90;mean;pin\perp}$	Elastic modulus of the pin perpendicular	320	N/mm^2

D.3.2 Geotechnical model input for segment A.I and segment A.II

Table D.5, Geotechnical model input for pile group model postdiction, segment A.I and A.II.

Depth -NAP [m]	γ_{sat} [kN/m^3]	γ' [kN/m^3]	Sort [-]	Dutch name [-]	q_c [kPa]	s_u [kN/m^2]	φ [deg]
Start soil – 4.0	16.9	6.9	clay	Geulopvulling	150	30	0
4.0 – 5.8	10.1	0.1	peat	Holland veen	150	30	0
5.8 – 6.4	19.1	9.1	clay	Oude zeeklei	200	45	0
6.4 – 8.4	18.0	8.0	sand	Wad deposit	1000	0	34
8.4 – 11.6	17.0	7.0	clay	Hydrobiaklei	400	50	0
11.6 – 12.2	11.7	1.7	peat	Basisveen	1000	0	0
12.2 – 14.0	19.0	9.0	sand	Eerste zandlaag	10000	0	33

Table D.6, Geotechnical model input for active soil body in quay wall postdiction, segment A.I-II.

Depth -NAP [m]	γ_{sat} [kN/m^3]	γ' [kN/m^3]	Sort [-]	Dutch name [-]	φ [deg]
-0.7 – 0.4	15.0	15.0	fill	Ophooglaag, dry	38
0.4 – 2.0	19.0	9.0	fill	Ophooglaag, wet	38
2.0 – 3.8	16.9	6.9	clay	Geulopvulling slappeklei	30
3.8 – 6.0	10.1	0.1	peat	Holland veen	30
6.0 – 7.0	19.1	9.1	clay	Oude zeeklei	28.4
7.0 –	10.1	8.0	sand	Wad deposit	34

D.3.3 Geotechnical model input for segment B

Table D.7, Geotechnical model input for pile group model postdiction, segment B.

Depth -NAP [m]	γ_{sat} [kN/m^3]	γ' [kN/m^3]	Sort [-]	Dutch name [-]	q_c [kPa]	s_u [kN/m^2]	φ [deg]
Start soil – 4.0	16.9	6.9	clay	Geulopvulling	150	30	0
4.0 – 5.8	10.1	0.1	peat	Holland veen	150	30	0
5.8 – 6.6	19.1	9.1	clay	Oude zeeklei	200	45	0
6.6 – 8.2	18.0	8.0	sand	Wad deposit	1000	0	34
8.2 – 11.6	17.0	7.0	clay	Hydrobiaklei	500	50	0
11.6 – 12.2	11.7	1.7	peat	Basisveen	1000	0	0
12.2 – 14.0	19.0	9.0	sand	Eerste zandlaag	10000	0	33

Table D.8, Geotechnical model input for active soil body in quay wall postdiction, segment B.

Depth -NAP [m]	γ_{sat} [kN/m^3]	γ' [kN/m^3]	Sort [-]	Dutch name [-]	φ [deg]
-0.7 – 0.4	15.0	15.0	fill	Ophooglaag, dry	38
0.4 – 3.0	19.0	9.0	fill	Ophooglaag, wet	38
3.0 – 3.4	16.9	6.9	clay	Geulopvulling slappeklei	30
3.4 – 6.2	10.1	0.1	peat	Holland veen	30
6.2 – 7.0	19.1	9.1	clay	Oude zeeklei	28.4
7.0 –	10.1	8.0	sand	Wad deposit	34

D.3.4 Geotechnical model input for segment C

Table D.9, Geotechnical model input for pile group model postdiction, segment C.

Depth -NAP [m]	γ_{sat} [kN/m^3]	γ' [kN/m^3]	Sort [-]	Dutch name [-]	q_c [kPa]	s_u [kN/m^2]	φ [deg]
Start soil – 4.0	16.9	6.9	clay	Geulopvulling	200	30	0
4.0 – 6.2	10.1	0.1	peat	Holland veen	300	30	0
6.2 – 7.2	19.1	9.1	clay	Oude zeeklei	400	45	0
7.2 – 8.4	18.0	8.0	sand	Wad deposit	1500	0	34
8.4 – 11.6	17.0	7.0	clay	Hydrobiaklei	500	50	0
11.6 – 12.6	11.7	1.7	peat	Basisveen	1000	0	0
12.6 – 14.0	19.0	9.0	sand	Eerste zandlaag	10000	0	33

Table D.10, Geotechnical model input for active soil body in quay wall postdiction, segment C.

Depth -NAP [m]	γ_{sat} [kN/m^3]	γ' [kN/m^3]	Sort [-]	Dutch name [-]	φ [deg]
-0.7 – 0.4	15.0	15.0	fill	Ophooglaag, dry	38
0.4 – 4.0	19.0	9.0	fill	Ophooglaag, wet	38
4.0 – 4.4	16.9	6.9	clay	Geulopvulling slappeklei	30
4.4 – 6.2	10.1	0.1	peat	Holland veen	30
6.2 – 7.0	19.1	9.1	clay	Oude zeeklei	28.4
7.0 –	10.1	8.0	sand	Wad deposit	34

D.3.5 Geotechnical model input for segment D

Table D.11, Geotechnical model input for pile group model postdiction, segment D.

Depth -NAP [m]	γ_{sat} [kN/m^3]	γ' [kN/m^3]	Sort [-]	Dutch name [-]	q_c [kPa]	s_u [kN/m^2]	φ [deg]
Start soil – 4.0	16.9	6.9	clay	Geulopvulling	300	30	0
4.0 – 5.8	10.1	0.1	peat	Holland veen	400	30	0
5.8 – 6.4	19.1	9.1	clay	Oude zeeklei	400	45	0
6.4 – 8.4	18.0	8.0	sand	Wad deposit	1500	0	34
8.4 – 11.6	17.0	7.0	clay	Hydrobiaklei	500	50	0
11.6 – 12.6	11.7	1.7	peat	Basisveen	1000	0	0
12.6 – 14.0	19.0	9.0	sand	Eerste zandlaag	10000	0	33

Table D.12, Geotechnical model input for pile group model postdiction, segment D.

Depth -NAP [m]	γ_{sat} [kN/m^3]	γ' [kN/m^3]	Sort [-]	Dutch name [-]	φ [deg]
-0.7 – 0.4	15.0	15.0	fill	Ophooglaag, dry	38
0.4 – 5.0	19.0	9.0	fill	Ophooglaag, wet	38
5.0 – 5.8	16.9	6.9	clay	Geulopvulling slappeklei	30
5.8 – 7.6	10.1	0.1	peat	Holland veen	30
7.6 –	10.1	8.0	sand	Wad deposit	34

Appendix E IML measurements and soft shell

E.1 IML measurements

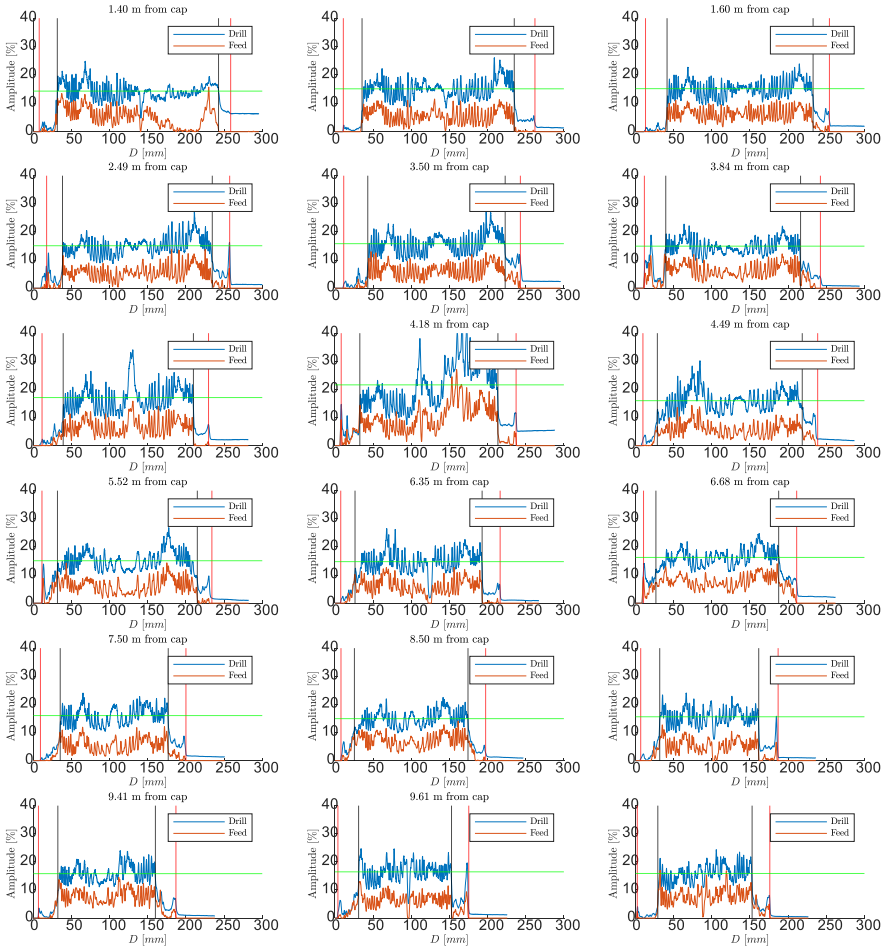

Figure E.1, IML drillings for pile 1 in the *y*-direction. This is the directing of bending.

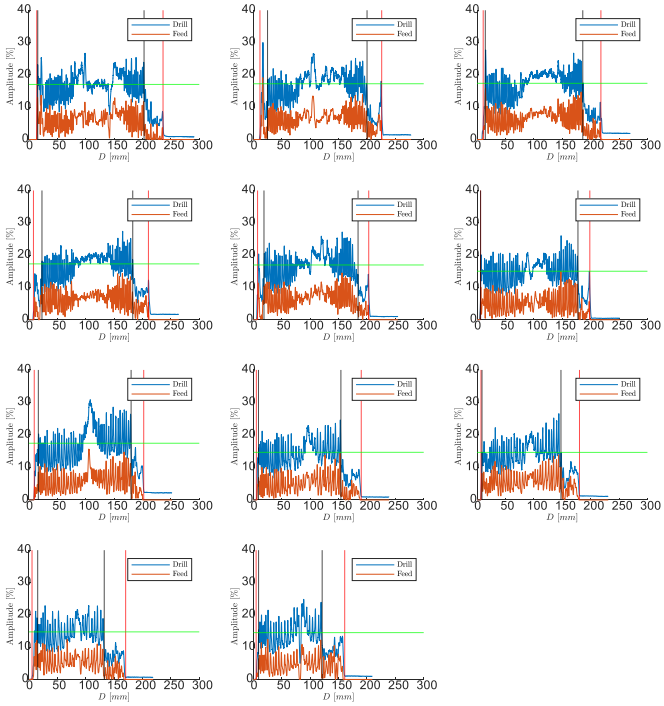

Figure E.2, IML drillings for pile 2 in the *y*-direction. This is the directing of bending.

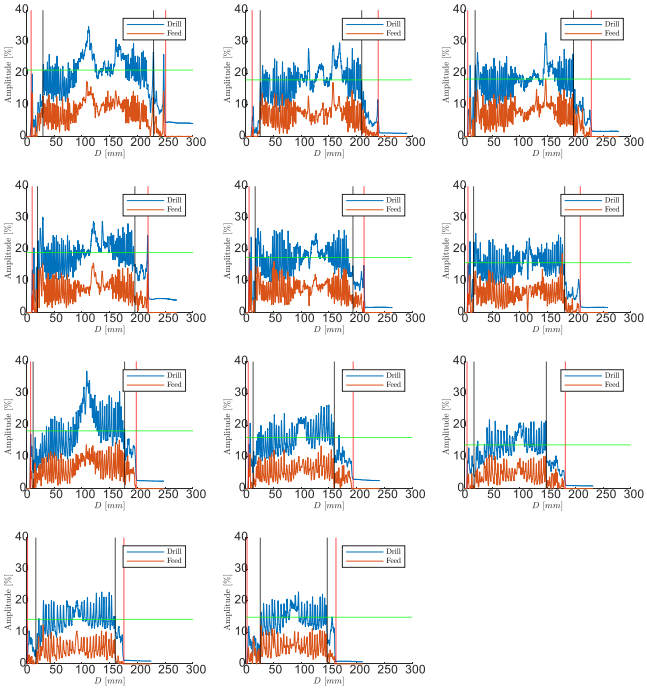

Figure E.3, IML drillings for pile 2 in the *p*-direction. This is perpendicular to bending.

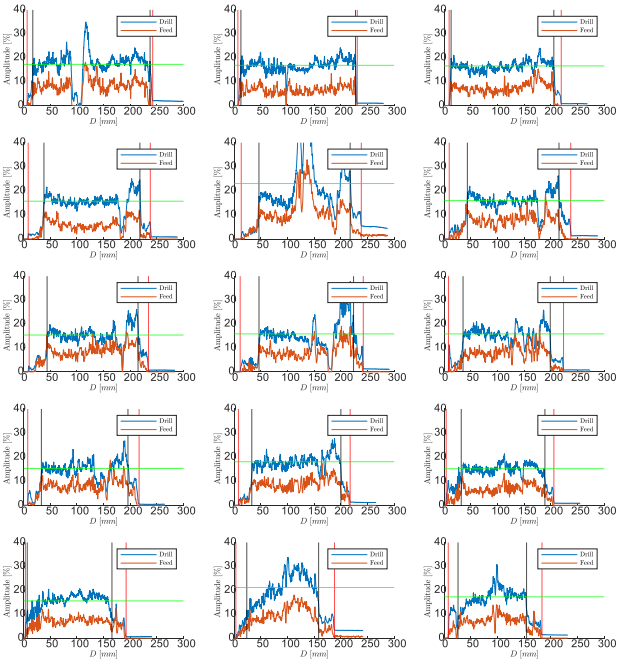

Figure E.4, IML drillings for pile 3 in the *y*-direction. This is the directing of bending.

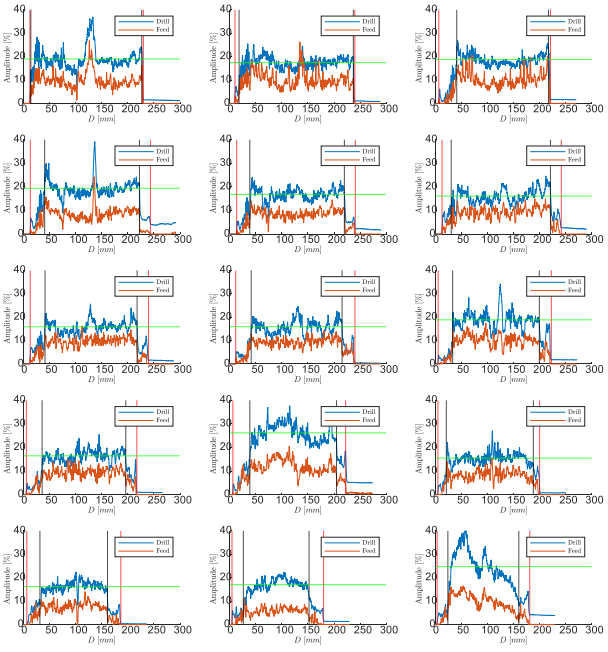

Figure E.5, IML drillings for pile 3 in the *p*-direction. This is perpendicular to bending.

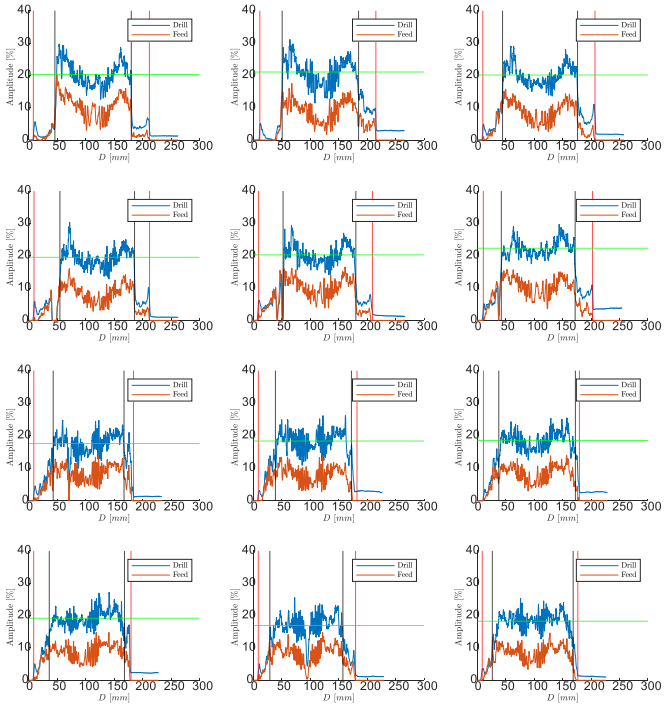

Figure E.6, IML drillings for pile 4 in the *y*-direction. This is the directing of bending.

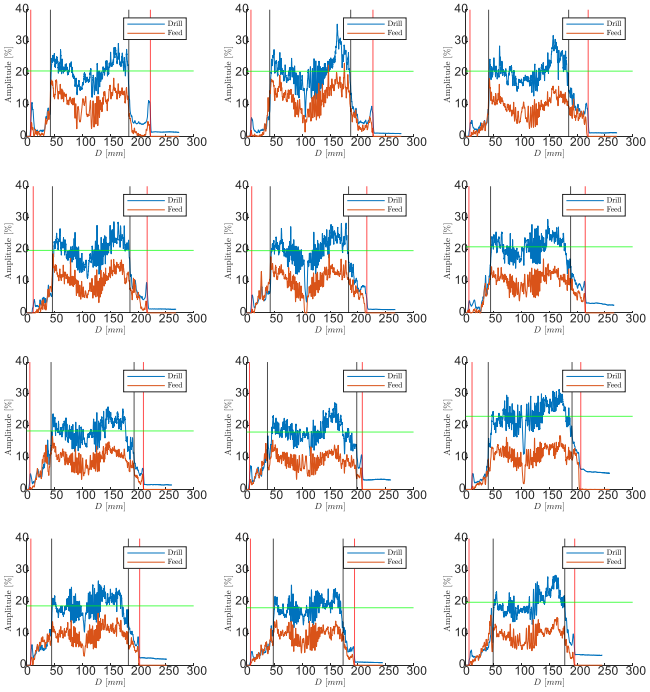

Figure E.7, IML drillings for pile 4 in the *p*-direction. This is perpendicular to bending.

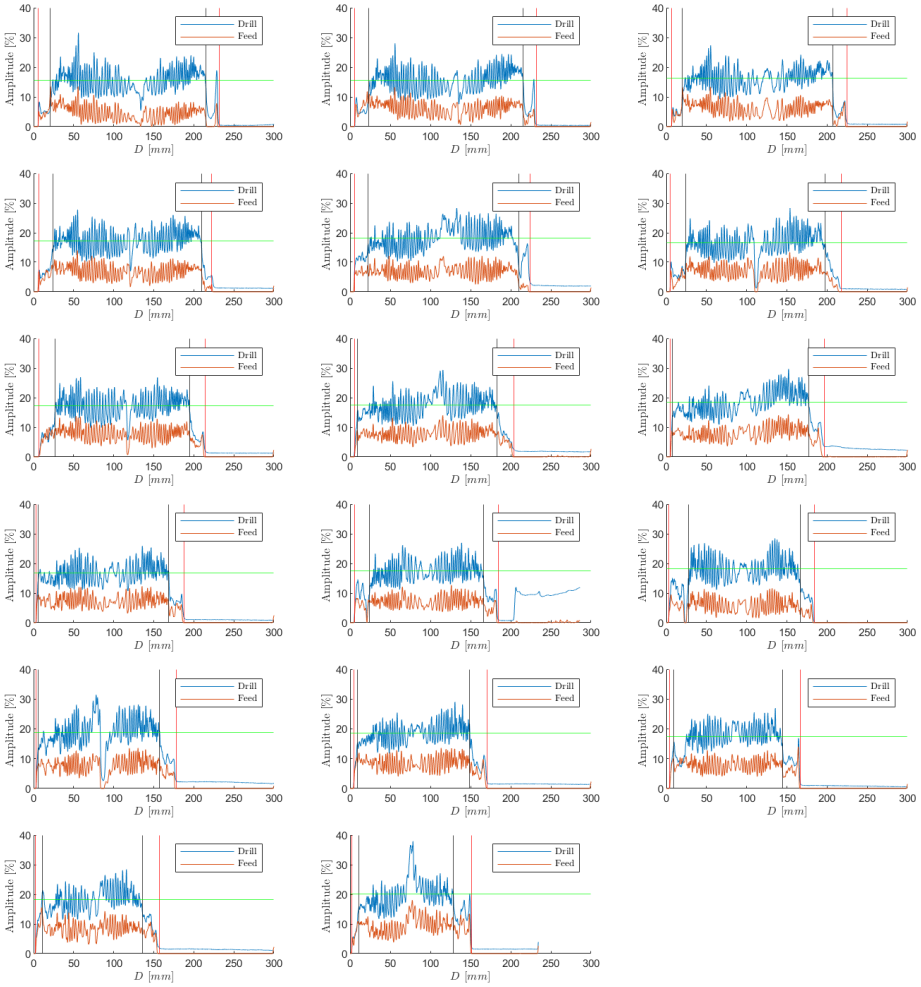

Figure E.8, IML drillings for pile 5 in the *y*-direction. This is the directing of bending.

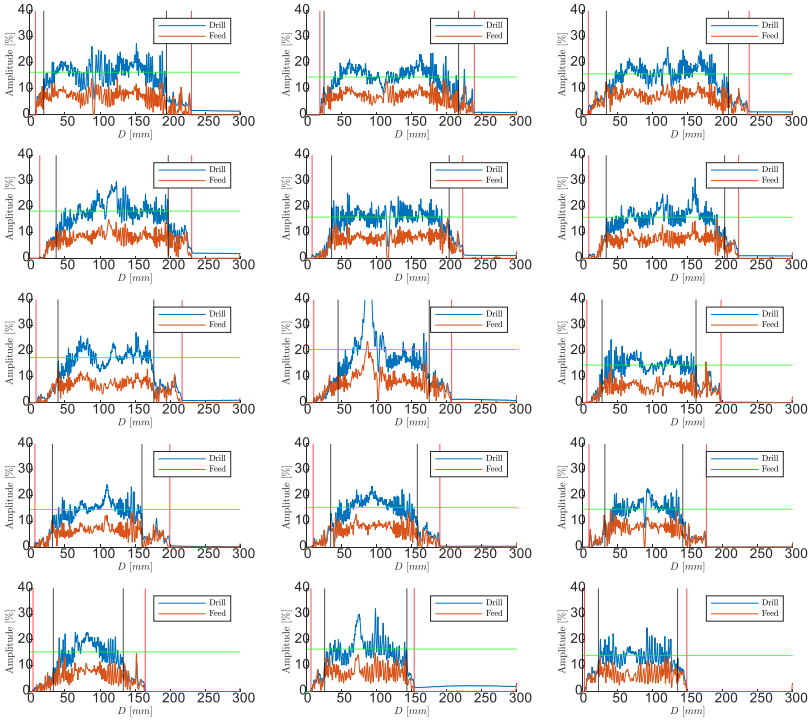

Figure E.9, IML drillings for pile 6 in the *y*-direction. This is the directing of bending.

E.2 Soft shell estimation

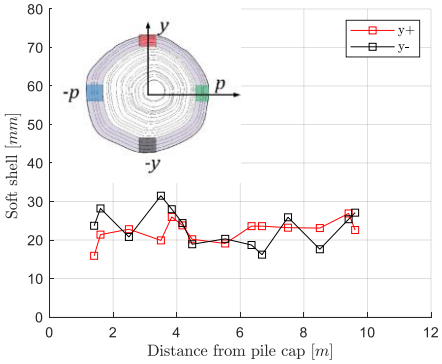

Figure E.10, Soft shell estimation for pile 1.

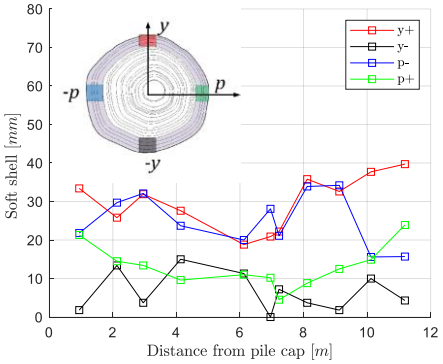

Figure E.11, Soft shell estimation for pile 2.

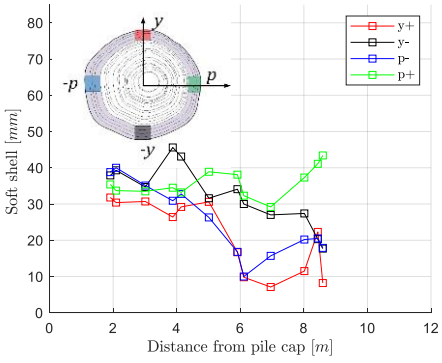

Figure E.12, Soft shell estimation for pile 4.

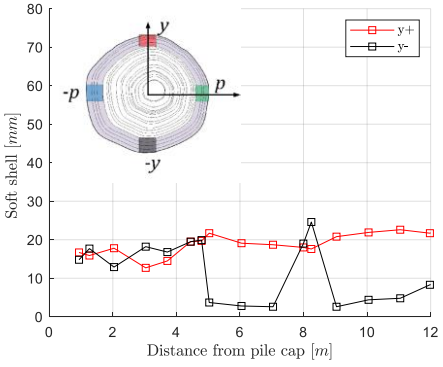

Figure E.13, Soft shell estimation for pile 5.

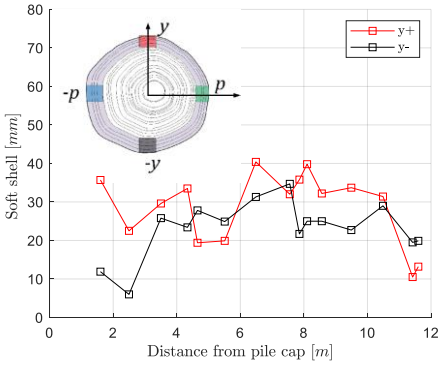

Figure E.14, Soft shell estimation for pile 6.

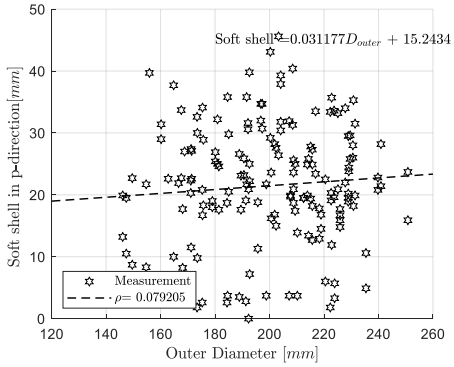

Figure E.15, Soft shell vs outer pile diameter for pile 1-6.

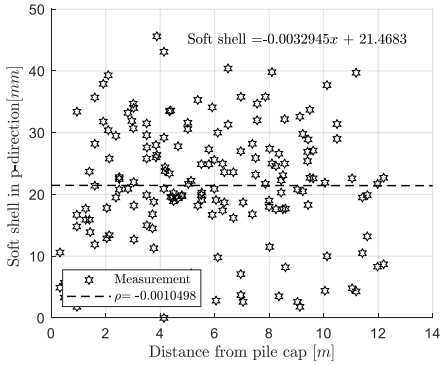

Figure E.16, Soft shell vs distance from pile cap for pile 1-6.

Appendix F Fibre optic installation details and measurements

F.1 Fibre optic installation details

Table F.1, Fibre optical installation details of pile 5 and pile 6 used in four-point bending tests and pile P2F1 in lateral pile group experiment F1.

	Pile PILE 5 **Pile code** R9 P6 N-S		**Pile** PILE 5 **Pile code** R9 P3 E-W		**Pile** PILE 6 **Pile code** R1P1 N-S		**Pile** PILE 6 **Pile code** R1P1 E-W		**Pile** PILE F1P2 **Pile code** R3P1 N-S		**Pile** PILE F1P2 **Pile code** R3P1 E-W	
Distance from toe [cm]	h_{NS} [cm]	D_{NS} [cm]	h_{EW} [cm]	D_{EW} [cm]	h_{NS} [cm]	D_{NS} [cm]	h_{EW} [cm]	D_{EW} [cm]	h_{NS} [cm]	D_{NS} [cm]	h_{EW} [cm]	D_{EW} [cm]
0	11.5	13.1	12.0	13.2	11.5	13.2	12.0	13.6	11.9	13.7	11.3	13.2
50	12.6	14.0	12.7	14.4	12.1	13.7	12.5	14.3	13.2	14.6	12.5	14.2
100	13.2	14.7	12.4	14.8	12.8	14.5	12.8	14.7	13.8	15.0	13.1	14.5
150	13.3	15.0	12.7	15.0	13.8	15.0	13.5	15.4	14.5	15.8	13.6	15.9
200	13.6	15.7	13.3	15.8	14.4	15.3	13.9	15.4	14.9	16.5	14.3	15.8
250	14.2	15.9	13.9	16.2	15.8	16.7	14.3	16.1	15.3	16.6	14.4	16.5
300	14.4	16.4	14.4	16.3	15.8	16.9	14.6	16.5	16.1	17.3	15.3	17.0
350	15.2	17.3	15.1	17.1	15.9	17.4	15.0	17.0	16.8	17.7	15.5	17.4
400	15.3	17.3	15.3	17.3	16.7	17.1	16.3	18.2	17.0	18.2	16.2	17.8
450	15.5	17.6	15.8	17.7	16.9	18.3	16.9	18.5	17.1	18.6	16.2	17.8
500	16.3	18.0	16.0	17.9	17.3	18.8	17.1	18.7	17.8	19.1	16.8	18.5
550	16.6	18.3	16.4	18.2	17.8	19.3	17.6	19.3	18.3	19.3	17.3	19.3
600	16.7	18.6	16.7	18.5	18.3	19.8	18.1	19.6	19.3	20.5	17.5	19.3
650	16.9	18.9	16.9	18.9	18.3	20.1	19.0	20.1	19.5	20.8	7.9	20.2
700	17.3	19.3	17.3	19.3	18.8	20.2	18.8	20.8	19.3	20.9	17.4	20.2
750	17.8	19.8	17.8	19.8	19.4	21.0	19.2	20.9	20.7	21.3	18.7	20.4
800	18.6	20.4	18.0	19.9	19.8	21.3	19.6	21.3	20.0	21.4	19.0	21.1
850	19.1	20.8	18.2	19.3	20.2	21.5	19.2	21.3	20.2	21.8	19.8	21.4
900	19.1	20.8	18.9	20.6	20.3	22.0	19.2	22.0	20.3	21.8	19.8	21.1
950	20.2	21.2	19.2	21.2	20.9	22.3	19.4	22.1	20.6	22.5	20.1	22.1
1000	19.7	21.5	19.8	21.7	20.9	22.5	19.9	22.4	21.5	22.6	20.3	22.3
1050	19.2	21.3	19.2	21.3	21.0	22.9	20.1	22.6	21.3	22.8	20.4	22.3
1100	19.2	21.2	19.5	21.7	22.3	23.6	20.8	23.8	22.2	23.2	20.9	23.0

1150	19.1	21.3	20.0	21.9	20.3	22.1	20.4	22.0	22.7	23.4	21.4	23.3
1200	20.0	21.4	20.9	22.6	21.0	23.1	20.0	23.8	22.9	23.9	21.3	23.3
1250	20.4	22.3	21.2	23.2	22.3	24.1	20.0	22.1	22.2	22.8	20.8	23.0
1300	19.9	22.0	20.6	23.1	20.5	21.4	17.8	20.3	22.2	23.1	20.9	21.5
1340	-	-	-	-	18.8	20.0	18.8	21.8	20.1	21.2	19.4	21.3

Table F.2, Fibre optical installation details pile F1P2, pile F2P2 and pile F2P8 used in lateral pile group experiment F1 and F2.

	Pile PILE F1P8 **Pile code** R1 P6 N-S		**Pile** PILE F1P8 **Pile code** R1 P6 E-W		**Pile** PILE F2P2 **Pile code** R3P10 N-S		**Pile** PILE F2P2 **Pile code** R3P10 E-W		**Pile** PILE F2P8 **Pile code** R1P5 N-S		**Pile** PILE F2P8 **Pile code** R1P5 E-W	
Distance from toe [cm]	h_{NS} [cm]	D_{NS} [cm]	h_{EW} [cm]	D_{EW} [cm]	h_{NS} [cm]	d_{OW} [cm]	h_{EW} [cm]	D_{EW} [cm]	h_{NS} [cm]	d_{OW} [cm]	h_{EW} [cm]	D_{EW} [cm]
0	9.9	13.3	12.0	13.0	10.8	12.8	11.2	13.7	8.8	11.0	9.8	11.7
50	11.2	13.8	12.2	13.2	12.5	14.9	12.9	15.2	10.6	12.4	10.8	12.3
100	13.3	15.0	13.1	14.9	12.8	14.8	13.1	15.2	11.5	13.3	11.5	12.9
150	14.3	15.2	13.5	15.2	13.5	15.3	13.8	15.8	11.8	13.7	12.4	14.8
200	13.9	16.0	14.0	15.5	13.9	16.2	13.9	16.3	12.8	14.7	13.4	15.1
250	14.3	16.3	15.0	16.2	14.2	16.4	14.3	16.6	13.3	15.3	13.8	15.8
300	15.0	16.5	15.4	16.5	14.8	16.8	14.8	16.9	14.1	15.9	15.0	16.3
350	14.6	16.9	15.0	16.4	15.7	17.4	15.4	17.3	15.1	16.8	15.7	17.1
400	15.1	17.3	15.3	17.2	16.1	18.2	15.7	17.8	15.2	17.0	15.4	17.4
450	16.3	17.9	15.9	17.7	16.4	18.3	16.2	18.3	16.0	17.9	16.0	17.9
500	16.8	18.2	15.9	17.9	17.9	19.3	16.9	18.9	16.3	18.2	16.6	18.4
550	17.4	19.1	16.5	18.4	18.4	20.3	16.4	19.3	17.2	18.9	17.2	19.0
600	17.3	19.2	16.8	18.7	17.5	19.9	17.4	19.6	17.3	19.2	18.0	19.8
650	17.9	19.5	17.8	19.3	17.9	19.9	18.1	19.9	18.2	19.8	18.4	20.2
700	17.8	20.0	18.0	19.9	18.0	20.0	18.1	19.5	18.3	19.9	18.8	20.4
750	18.9	20.4	18.5	19.9	18.5	20.3	18.3	20.2	18.8	20.2	19.3	20.5
800	19.6	21.0	18.5	20.3	18.3	20.4	18.2	20.2	18.4	20.2	19.4	21.0
850	19.9	21.2	18.9	20.5	18.8	20.8	18.7	20.3	19.1	20.4	20.2	21.2
900	20.0	21.8	19.3	20.9	19.4	21.4	18.7	20.6	18.9	20.8	20.4	21.5
950	20.0	22.1	19.6	21.5	19.8	21.6	19.2	21.1	19.9	21.1	20.6	22.2
1000	20.7	22.3	19.4	21.8	20.0	22.2	19.3	21.6	19.1	21.1	20.3	22.2
1050	20.6	22.5	20.4	22.0	20.0	22.1	20.4	21.9	20.5	21.3	21.7	23.4
1100	19.8	21.1	18.4	20.2	20.5	22.5	20.3	22.3	20.0	22.0	20.8	22.9
1150	20.8	23.2	18.5	20.4	20.1	22.1	21.2	23.2	20.2	22.1	21.1	22.7
1200	20.8	23.2	18.9	20.9	20.4	22.4	21.0	22.8	20.2	22.3	20.9	23.2
1250	-	23.8	18.9	21.0	20.3	22.2	22.9	25.0	20.8	22.6	21.6	23.1
1300	-	20.5	16.9	18.9	20.7	22.7	21.7	24.1	20.3	21.8	21.5	23.2
1340	-	-	-	-	18.9	21.9	21.7	23.9	20.5	21.5	22.9	25.0

F.2 Strain measurements

F.2.1 Four-point bending experiment strain measurements

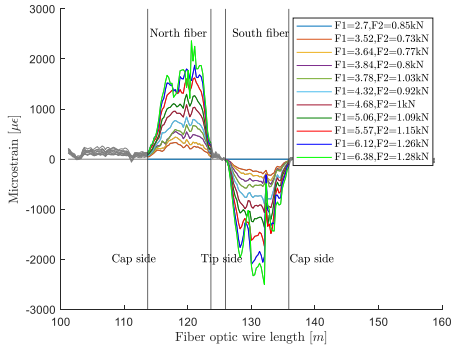

Figure F.1, Measured strain in pile 6. North-South direction.

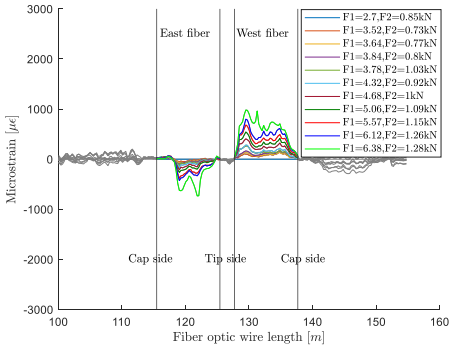

Figure F.2, Measured strain in pile 6. East-West direction.

F.2.2 Four-point bending test validation of fibre optics

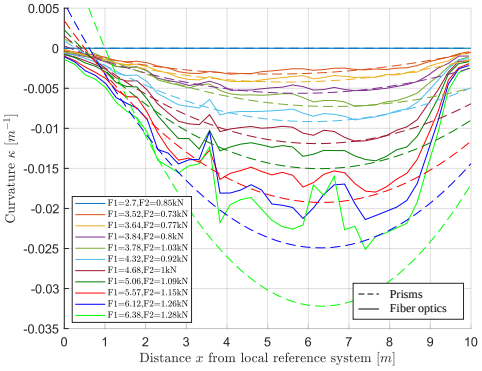

Figure F.3, Curvature of pile 6 obtained from fibre strains.

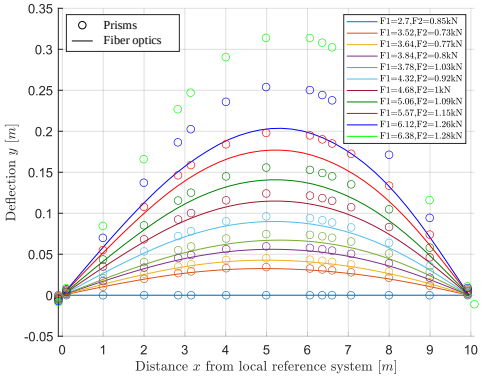

Figure F.4, Deflection of pile 6 obtained from curvature profile.

F.2.3 Lateral pile group experiment strain measurements

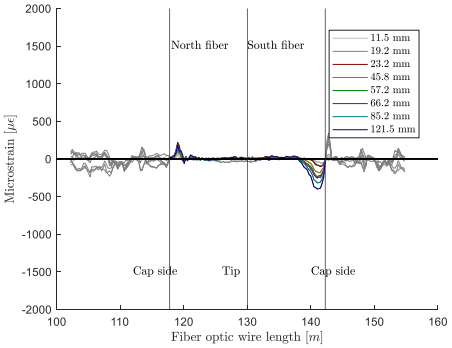

Figure F.5, Measured strain in pile P2F1. North-South direction.

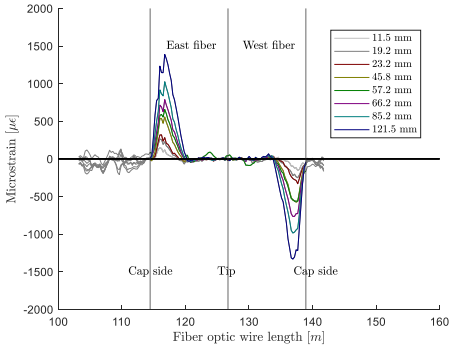

Figure F.6, Measured strain in pile P2F1. East-West direction.

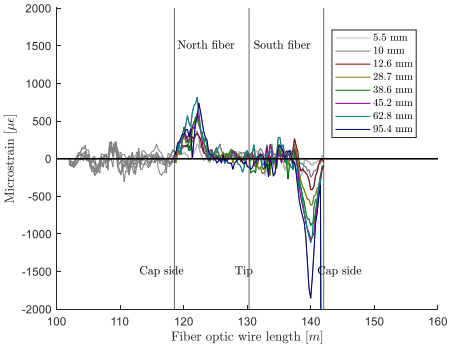

Figure F.7, Measured strain in pile P8F1. North-South direction.

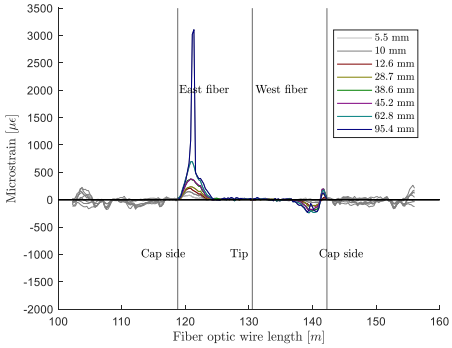

Figure F.8, Measured strain in pile P8F1. East-West direction.

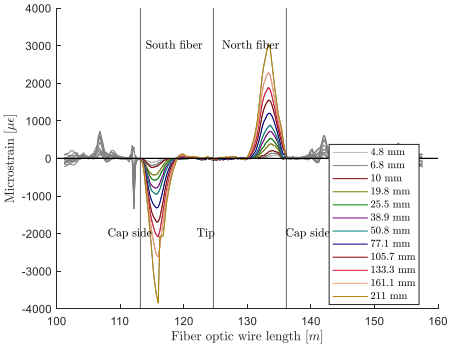

Figure F.9, Measured strain in pile P2F2. North-South direction.

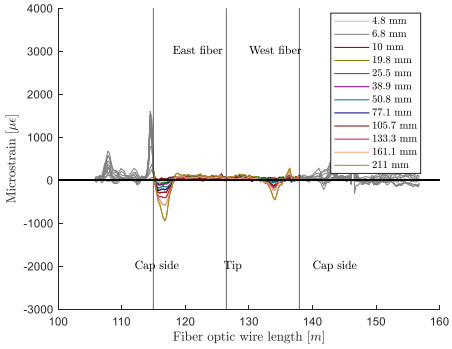

Figure F.10, Measured strain in pile P2F2. East-West direction.

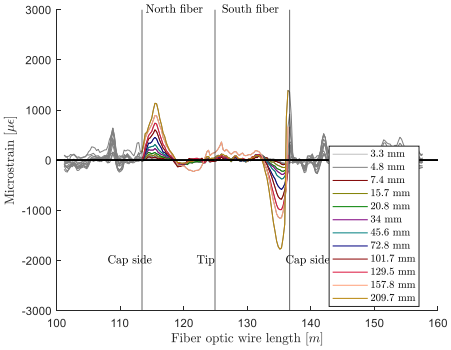

Figure F.11, Measured strain in pile P8F2. North-South direction.

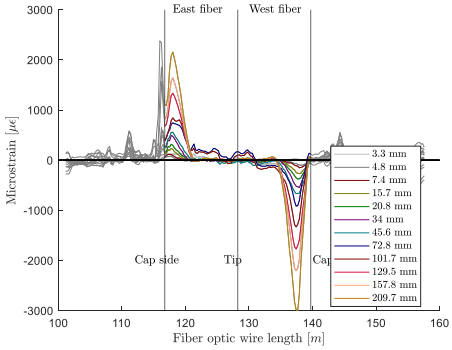

Figure F.12, Measured strain in pile P8F2. East-West direction.

Appendix G Brinch Hansen and Ménard Stiffness

G.1 Ménard modulus of subgrade reaction

$$\frac{1}{k_h} = \begin{cases} \dfrac{1}{3E_m}\left[1.3R_0\left(2.65\dfrac{R}{R_0}\right)^{\alpha} + \alpha R\right] & \text{if } R \geq R_0 \\ \dfrac{2R}{E_m} \times \dfrac{4(2.65)^{\alpha} + 3\alpha}{18} & \text{if } R < R_0 \end{cases} \qquad \textbf{eq. G.1}$$

where

k_h = is the modulus of horizontal subgrade reaction [kN/m^2]
E_m = is the pressiometric modulus [kN/m^2]
R_0 = is a constant: R_0 = 0.3 [m]
R = half the diameter of the pile [m]
α = is the rheological coefficient which depends on the soil type. (See Table G.1)

Table G.1, Values of rheological coefficient α.

	Peat	Clay	Loam	Sand	Gravel
Over consolidated	-	1	2/3	1/2	1/3
Normally consolidated	1	2/3	1/2	1/3	1/4
Decomposed, weathered	-	1/2	1/2	1/3	1/4

The pressiometric modulus E_m can be obtained via correlations with the cone resistance q_c.

Peat : $E_m = 3.5\ q_c$
Clay : $E_m = 2.5\ q_c$
Loam : $E_m = 1.5\ q_c$
Sand : $E_m = 0.85\ q_c$
Gravel : $E_m = 0.6\ q_c$

G.2 Brinch Hansen ultimate soil resistance

$$K_q = \frac{K_q^0 + K_q^{\infty} \times \alpha_q \times \frac{z}{D}}{1 + \alpha_q \times \frac{z}{D}} \qquad \textbf{eq. G.2}$$

$$K_c = \frac{K_c^0 + K_c^{\infty} \times \alpha_c \times \frac{z}{D}}{1 + \alpha_c \times \frac{z}{D}} \qquad \textbf{eq. G.3}$$

where

$$K_q^0 = e^{(\frac{\pi}{2} + \varphi) \times \tan\varphi} \times \cos\varphi \times \tan\left(\frac{\pi}{4} + \frac{\varphi}{2}\right) - e^{(-\frac{\pi}{2} + \varphi) \times \tan\varphi} \times \cos\varphi \times \tan\left(\frac{\pi}{4} - \frac{\varphi}{2}\right)$$

$$K_c^0 = \left[e^{(\frac{\pi}{2} + \varphi) \times \tan\varphi} \times \cos\varphi \times \tan\left(\frac{\pi}{4} + \frac{\varphi}{2}\right) - 1 \right] \times \cot\varphi$$

$$K_q^{\infty} = K_c^{\infty} \times K_c^{\infty} \times \tan\varphi$$

$$K_c^{\infty} = N_c d_c^{\infty}$$

$$d_c^{\infty} = 1.58 + 4.09 \times \tan^4\varphi$$

$$N_c = \left[e^{\pi \times \tan\varphi} \times \tan^2\left(\frac{\pi}{4} + \frac{\varphi}{2}\right) - 1 \right] \times \cot\varphi$$

$K_0 = 1 - \sin(\varphi)$ for OCR = 1

$$\alpha_q = \frac{K_q^0}{K_q^{\infty} - K_q^0} \times \frac{K_0 \times \sin\varphi}{\sin\left(\frac{\pi}{4} + \frac{\varphi}{2}\right)}$$

$$\alpha_c = \frac{K_c^0}{K_c^{\infty} - K_c^0} \times 2\sin\left(\frac{\pi}{4} + \frac{\varphi}{2}\right)$$

Appendix H Analytical quay wall model

H.1 Coulomb earth pressure coefficients

$$K_a = \frac{\sin^2(\alpha + \varphi)}{\sin^2 \alpha \sin(\alpha - \delta)\left[1 + \sqrt{\frac{\sin(\varphi + \delta)\sin(\varphi - \beta)}{\sin(\alpha - \delta)\sin(\alpha + \beta)}}\right]^2} \quad \textbf{eq. H.1}$$

$$K_p = = \frac{\sin^2(\alpha - \varphi)}{\sin^2 \alpha \sin(\alpha - \delta)\left[1 - \sqrt{\frac{\sin(\varphi - \delta)\sin(\varphi + \beta)}{\sin(\alpha - \delta)\sin(\alpha + \beta)}}\right]^2} \quad \textbf{eq. H.2}$$

in which
φ = internal friction angle [deg]
β = upward slope of soil surface [deg]
δ = friction angle between wall and soil [deg]
a = angle of the wall with respect to the horizontal [deg]

H.2 Flamant soil model – superposition of multiple stress fields

Because of the geometric shape of the quay wall, the active soil domain is split into two parts: above the floor and below the floor. For each domain, multiple effective stress fields have been calculated and added together to obtain the total effective stress field. The total effective stress field resulting from the superposition of multiple stress fields can be seen in Figure 5.8. All the calculated stress fields are shown in Figure H.1A to Figure H.1E. The descriptions are included in the captions. As mentioned before, the final total stress field can be obtained by adding up all the fields.

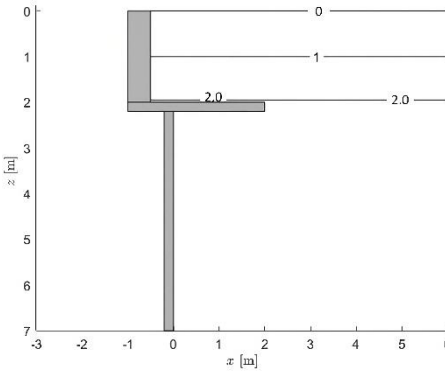

Figure H.1A, The vertical effective stress of the soil increases linearly from the surface to the bottom. This increase is caused by the weight of the soil itself.

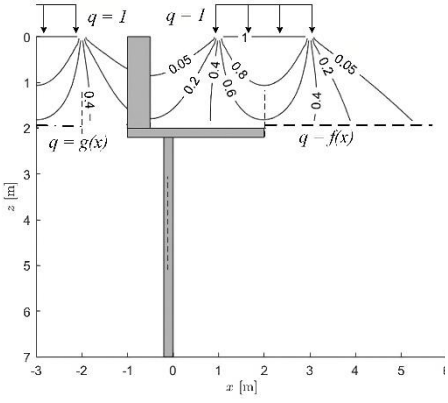

Figure H.1B, The vertical effective stresses caused by the imposed load *q* from ground level to floor level.

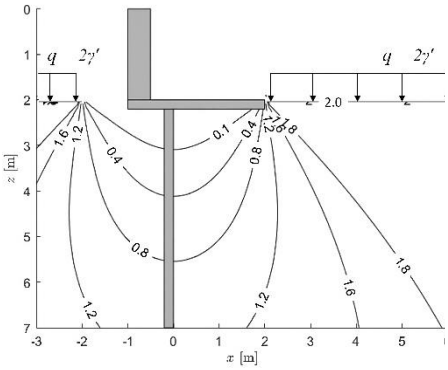

Figure H.1C, The vertical effective stresses, caused by the weight of the soil in the surface-floor domain, from floor level to from floor level to greater depths.

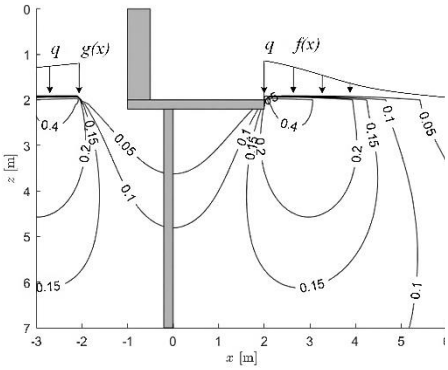

Figure H.1D, The vertical effective stresses caused by the superimposed load *q = f(x)* from ground level to greater depths.

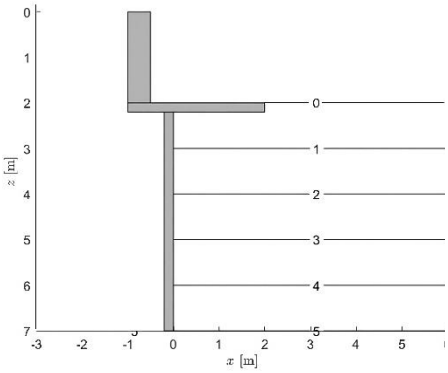

Figure H.1E, The vertical effective stress due to the weight of the soil increases linearly from the floor level to greater depths.

Figure H.1, Superposition of multiple vertical effective stress fields, according to the theory of Flamant.

H.3 Pile-headstock interface model

The total pile head moment M_{rot} as seen in eq. 5.3 is composed of an eccentric moment M_e and pin moment M_{pin}. Both components are briefly elaborated.

First, the moment that arises from eccentric stresses on the top of the pile head is explained. This process is represented in Figure H.2. There are a number of stress states that can occur on the top of the pile head, ranging from 'free', 'elastic' to 'plastic'. The compressive strength $f_{c;90}$[N/mm^2] perpendicular to the fibre direction is approximately one order of magnitude lower than the compressive strength $f_{c;0}$[N/mm^2] in the fibre direction according to EN 338 (NEN-EN 338: Wood for Structural Applications - Strength Classes). Therefore, it is assumed that the pile head will press itself into the headstock without pile damage. The same applies to the elasticity modulus, in fibre direction it is a factor 30 higher than

perpendicular to the fibre direction. As a result, the elongations in fibre direction are neglected compared to the elongations perpendicular to the fibre direction.

The five different stress states of Figure H.2 are briefly discussed. The first state is free-elastic, where the stresses remain in the linear elastic range over the surface of the pile imprint. The second state is elastic, with stresses in the headstock staying in the linear elastic range over the entire pile surface. The third state is elastic-plastic, where part of the headstock is still in the linear elastic range while the other part plastically deforms. The fourth state is free-elastic-plastic, with a portion of the headstock not affected by the pile, some in the linear elastic range and the remainder plastically deforming. Lastly, the fifth state is free-plastic, where all the headstock stresses at the location of the pile imprint exceed the compressive strength of the wood and thus plastically deform. The resultant forces F_{res}[kN] and their eccentricity e[m] with respect to the centre line of the pile are indicated in red.

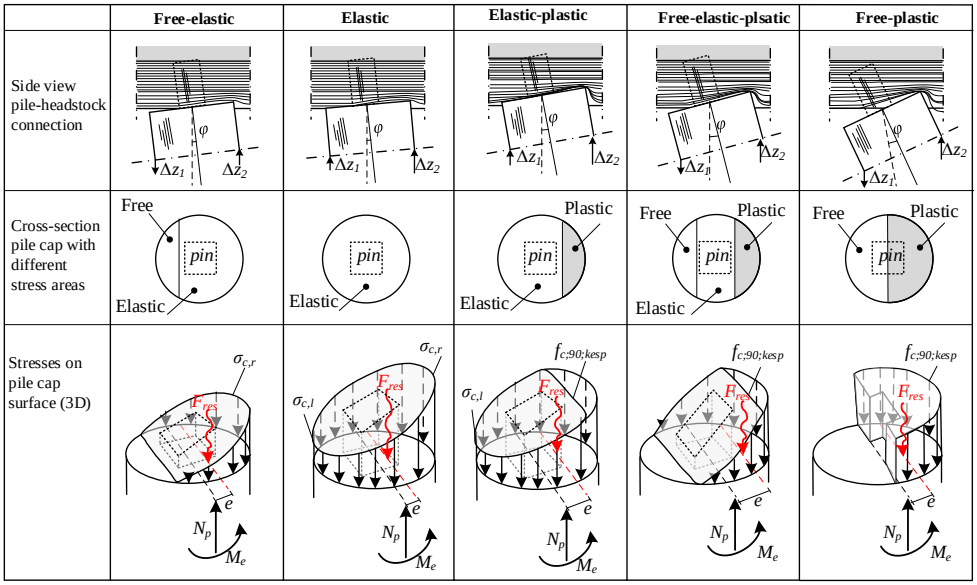

Figure H.2, Stress states that may occur at the top of the pile. In red, the resultant stress F_{res} is indicated with eccentricity e. Elastic stresses are indicated by σ_c[N/mm^2] and plastic stresses by $f_{c;90}$. The displacement direction of the pile protrusions are indicated by Δz_1[m] and Δz_2[m]

The second contribution of the pile-head moment is caused by the pin-hole. The pin-hole connection has one important difference compared to the head-headstock connection. The pin is supported laterally in two directions. The model used in this analysis assumes that the pin fits exactly into the hole and is thus perfectly locked. As with the head-headstock connection, the pin-hole connection has a number of stress states that can arise. The possible stress states are described in Figure H.3. The horizontal resultant of the stress must be equal to the transverse force absorbed by the pile. There are a number of stress states that can occur in the pin, ranging from 'elastic' to 'plastic'. A 'free' stress state, such as in the head-headstock connection, is not possible in the pin because the pin is perfectly locked in the shank's hole. Following the same analogy as for the head-headstock connection, the compressive strength and modulus of elasticity of the pin are much greater in the fibre direction than perpendicular to it. As a result, the pin will deform itself without damaging or deforming the headstock.

The stress states in Figure H.3 are briefly discussed. The first state is the double-elastic state in which the top of the pin has a positive protrusion Δx_1[m] and the bottom of the

pin has a negative protrusion Δx_2[m] with respect to the centre of the pile hole. The stresses in the pin remain within the linear elastic range. The second phase is the elastic-plastic phase in which the top of the pin has a positive protrusion and the bottom of the pin has a negative protrusion. The stresses in the top of the pin remain in the linear elastic range. The stresses in the bottom of the pin exceed the compressive strength of the wood and the pin will plastically deform there. The third phase is the double-elastic-plastic phase in which the stresses in the top and bottom of the pin exceed the compressive strength of the wood, and the pin will plastically deform there. In the 'middle' of the pin, the stresses are within the elastic range. The fourth phase is the double-plastic phase which is similar to the previous phase but without a linear elastic part middle part. The last phase is the plastic phase in which the whole pin has a negative protrusion with respect to the centre of the pile hole. The pin will exceed the tensile strength over its entire length, resulting in plastic deformation. A single sided elastic stress state is not possible in practice since this can only happen with no cap rotation.

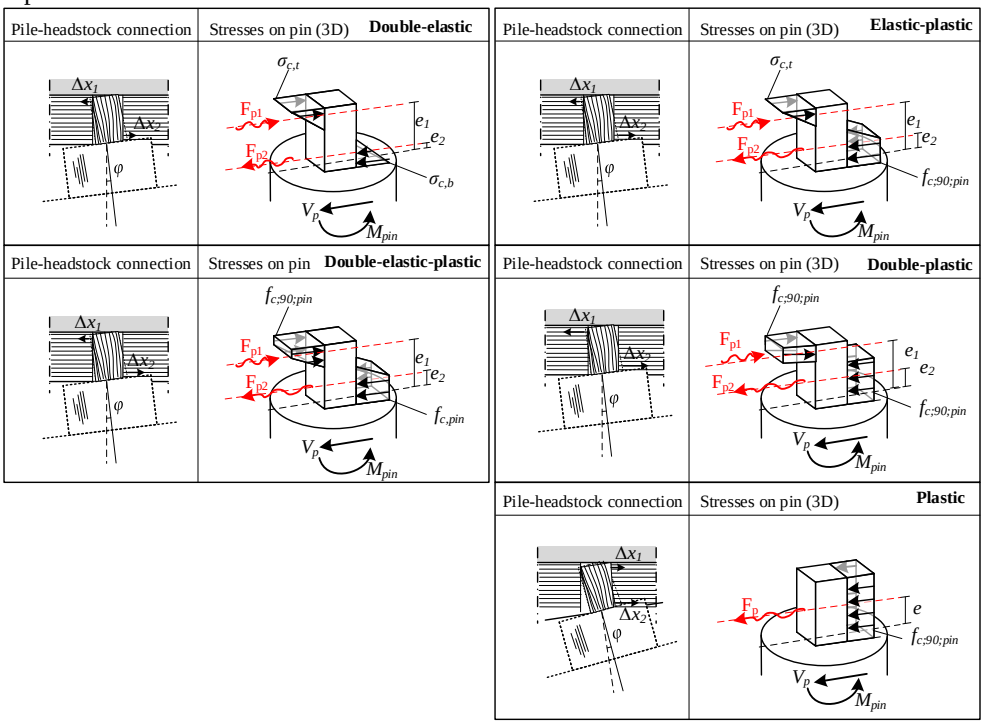

Figure H.3, Stress states that may occur in the pin-hole connection. In red, the resultants of the stresses are indicated by F_{pl}, F_{pr} and F_p[kN]. Their eccentricities with respect to the flat surface of the pile are indicated with e_1, e_2 and e. Elastic stresses are indicated by σ_c and plastic stresses by $f_{c;90}$.

H.4 Analysis of gravity wall forces

The section of the floor where the gravity wall rests is modelled as a linearly decreasing line load, $q_{d,G}(x)$, caused by the wall's self weight combined with the horizontal pressure exerted on the gravity wall. A detailed illustration of the force transfer from the gravity wall to the timber floor is shown in Figure H.4. The pressure force, F_w[kN], is determined by integrating the vertical effective soil stress and multiplying it by the active soil pressure coefficient K_a

calculated using the Coulomb earth pressure coefficients. The force F_w acts at an angle which is equal to δ + (90-α), taking into account the slope and friction of the gravity wall. Relative to the pivot point *R* (located beneath the center of gravity), the moment M_w [kNm] resulting from F_w is determined. F_v [kN] represents the vertical force of the wall on the floor, consisting of the vertical component of F_w and the weight of the wall itself, G_w [kN]. By considering M_w and F_v, the stress profile $q_{d,G}(x)$ beneath the gravity wall can be determined.

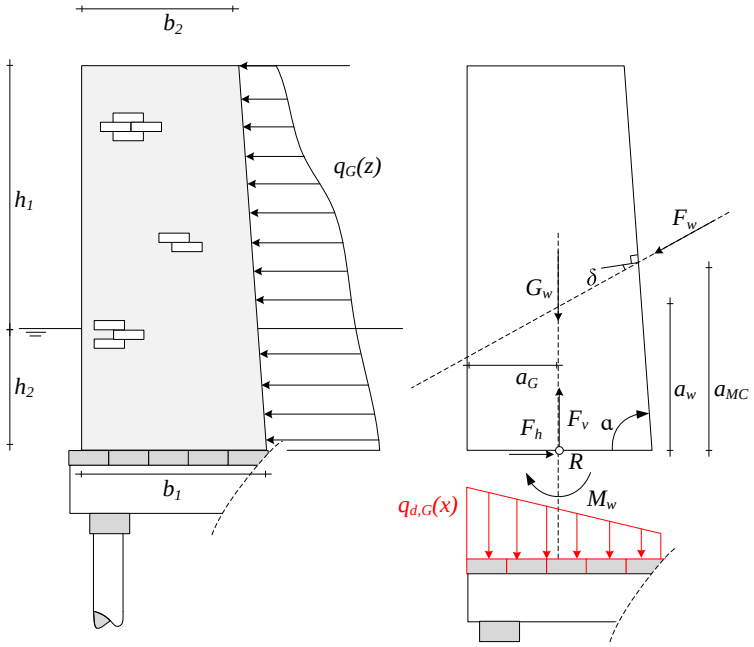

Figure H.4, The gravity wall transferring its load own weight G_w and horizontal load F_w towards the timber quay wall floor as a distributed load $q_{d,G}(x)$.

H.5 Boundary and interface conditions elastic beam framework

H.5.1 Headstock related conditions

Because the headstock is supported by vertical fixed piles, settlement at the supports is zero.

$$w_i(x_{i+1}) = 0 \qquad i = 1,2..(m+1)\,; i \neq 2 \qquad \textbf{eq. H.3}$$

$$w_{i+1}(x_{i+1}) = 0 \qquad i = 1,2..m \;;\; i \neq 2 \qquad \textbf{eq. H.4}$$

At x_1, the headstock has an 'open end' and therefore the moment and shear force is zero.

$$-EI_d \frac{d^2 w_1(x_1)}{dx^2} = 0 \qquad \textbf{eq. H.5}$$

$$-EI_d \frac{d^3 w_1(x_1)}{dx^3} = 0 \qquad \textbf{eq. H.6}$$

Because the headstock is a continues beam, there is slope continuity.

$$\frac{dw_i(x_{i+1})}{dx} = \frac{dw_{i+1}(x_{i+1})}{dx} \qquad i = 1,2..m \qquad \textbf{eq. H.7}$$

At location x_3 (which is between the first and second pile) the continuity of displacement, moment and shear force is used as interface conditions.

$$w_2(x_3) = w_3(x_3) \qquad \textbf{eq. H.8}$$

$$\frac{d^2w_2(x_3)}{dx^2} = \frac{d^2w_3(x_3)}{dx^2} \qquad \textbf{eq. H.9}$$

$$\frac{d^3w_2(x_3)}{dx^3} = \frac{d^3w_3(x_3)}{dx^3} \qquad \textbf{eq. H.10}$$

H.5.2 Pile related conditions

If the piles have a constant flexural rigidity *EI* over the full pile length, the interface conditions between the number of unique layers *n* can be written as follows in eq. H.11 - eq. H.14. The number of layers *n* can differ per pile. The interface conditions are based on the continuity of displacement, slope, moment and shear force.

$$v_{i,(j-1)}(z_{i,j}) = v_{i,j}(z_{i,j}) \qquad i = 1,2..m\ ;\ j = 2,3..n \qquad \textbf{eq. H.11}$$

$$\frac{dv_{i,(j-1)}(z_{i,j})}{dz} = \frac{dv_{i,j}(z_{i,j})}{dz} \qquad i = 1,2..m\ ;\ j = 2,3..n \qquad \textbf{eq. H.12}$$

$$\frac{d^2v_{i,(j-1)}(z_{i,j})}{dz^2} = \frac{d^2v_{i,j}(z_{i,j})}{dz^2} \qquad i = 1,2..m\ ;\ j = 2,3..n \qquad \textbf{eq. H.13}$$

$$\frac{d^3v_{i,(j-1)}(z_{i,j})}{dz^3} = \frac{d^3v_{i,j}(z_{i,j})}{dz^3} \qquad i = 1,2..m\ ;\ j = 2,3..n \qquad \textbf{eq. H.14}$$

It is assumed that the headstock has no axial deformation. Because of that assumption, the horizontal displacement of all piles is the same at $z = z_{i,1}$.

$$v_{i,1}(z_{i,1}) = v_{i+1,1}(z_{(i+1),1}) \qquad i = 1,2..(m-1) \qquad \textbf{eq. H.15}$$

At the tip of the piles, no moment and no shear force can develop, these boundary conditions are formulated in eq. H.16 and eq. H.17.

$$-EI_i \frac{d^2v_{i,n}(z_{i,(n+1)})}{dz^2} = 0 \qquad i = 1,2..m \qquad \textbf{eq. H.16}$$

$$-EI_i \frac{d^3v_{i,n}(z_{i,(n+1)})}{dz^3} = 0 \qquad i = 1,2..m \qquad \textbf{eq. H.17}$$

H.5.3 Pile-headstock connection conditions

The sum of all shear forces at the top of each pile is equal to the total horizontal soil force F_h exerted on the headstock. The vertical load on the piles cause an extra horizontal component due to the rotation of the pile caps. This needs to be considered as extra horizontal load on each pile cap which results in the following equilibrium condition given in eq. H.18.

$$\sum_{i=1}^{m} -EI_i \frac{d^3 v_{i,1}(z_{i,1})}{dz^3} = F_h + \sum_{i=1}^{m} -EI_i \frac{dv_{i,1}(z_{i,1})}{dz} N_i \qquad i = 1,2..m \qquad \textbf{eq. H.18}$$

Moment equilibrium at the pile-headstock connection is required. The sum all moments of the adjacent beams at a connection, accept for the corner connection at $x = x_{(m+2)}$, is equal to zero. This condition is formulated in eq. H.19. For the corner connection at $x = x_{(m+2)}$, there are two beam members which need to be in moment equilibrium. This condition can be found in eq. H.20.

$$-EI_d \frac{d^2 w_i(x_{i+1})}{dx^2} + EI_d \frac{d^2 w_{i+1}(x_{i+1})}{dx^2} = -EI \frac{d^2 v_{j,1}(z_{j,1})}{dz^2} \qquad \textbf{eq. H.19}$$
$$i = 1,2..m;\ i \neq 2 \qquad ;\ j = 1,2..m$$

$$-EI_d \frac{d^2 w_{(m+1)}(x_{m+2})}{dx^2} = -EI \frac{d^2 v_{m,1}(z_{m,1})}{dz^2} \qquad \textbf{eq. H.20}$$

The moment in the top of each pile is equal to pile cap moment M_{rot} and described by eq. H.21. The pile cap moments are dependent on the rotational difference $\varphi_{diff.}$ between the headstock and the piles, the horizontal component of the transverse force V_n and the normal force N in the piles.

$$-EI \frac{d^2 v_{j,1}(z_{j,1})}{dz^2} = M_{rot,j}(\varphi_{diff,j}, V_{n,j}, N_j) \qquad j = 1,2..m \qquad \textbf{eq. H.21}$$

in which:

$$\varphi_{diff,j} = \left(\frac{dw_i(x_{i+1})}{dx} - \frac{dv_{j,1}(z_{j,1})}{dz} \right) \qquad i = 1,2..(m+1);\ i \neq 2 \quad j = 1,2..m$$

$$V_{n,j} = -EI_j \frac{dv_{j,1}(z_{j,1})}{dz} N_j - EI_j \frac{d^3 v_{j,1}(z_{j,1})}{dz^3}$$

$$N_j = EI_d \frac{d^3 w_i(x_{i+1})}{dx^3} - EI_d \frac{d^3 w_{i+1}(x_{i+1})}{dx^3} \qquad i = 1,2..m;\ i \neq 2 \quad j = 1,2..m$$

$$N_m = EI_d \frac{d^3 w_{m+1}(x_{m+2})}{dx^3}$$

Appendix I CPT at Grimburgwal location

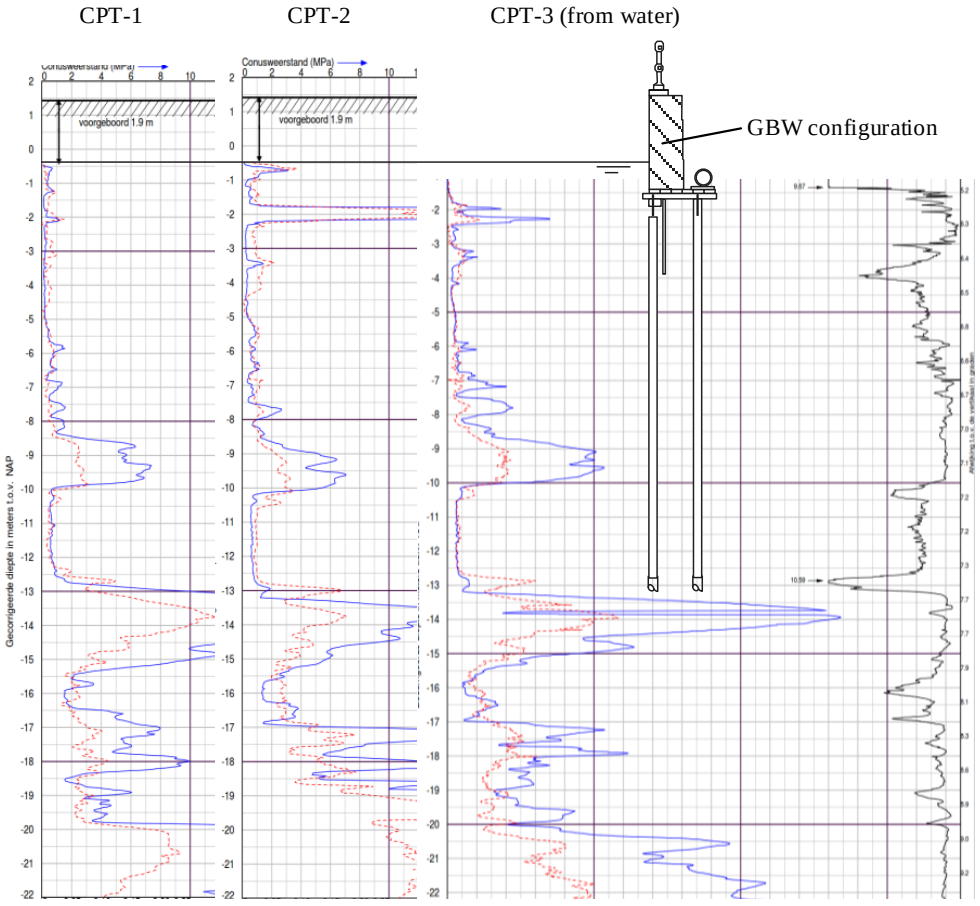

Figure I.1, Locally conducted CPT's at Grimburgwal site. CPT-1 and CPT-2 at the land and CPT-3 in the canal.

Appendix J Quay wall modelling with PLAXIS (K. Choosrithong, 2022)

J.1.1 Geotechnical and structural model input

Table J.1, CPTu based parameter input for segment A.I

Soil type/Parameters	γ_{dry}	γ_{sat}	Compression test			Triaxial tests			m	Pref	v	OCR	φ'	c'
			$E_{oed,ref}$	$E_{50,ref}$	$E_{ur,ref}$	$E_{oed,ref}$	$E_{50,ref}$	$E_{ur,ref}$						
	[kN/m3]	[kN/m3]	[kPa]	[kPa]	[kPa]	[kPa]	[kPa]	[kPa]	[-]	[kPa]	[-]	[-]	[°]	[kPa]
Ophooglaag, zand	15.0	19.0	25000	25000	100000				0.5	100	0.15	-	38	0
Geulopvulling slappe klei	14.0	16.9	3000	6000	12000				0.8	100	0.15	1.15	30	1
Hollandveen	na	10.1	500	1000	5500				0.8	100	0.12	1.15-1.24	33	3
Oude zeeklei	12.2	16.5	1500	3000	14000	6000	11750	25000	0.8	100	0.22	1.51	28	3
Wad deposit	13.3	18.5	2400	5000	13500	6000	12500	45000	0.6	100	0.20	1.82-2.17	30	3
Hydrobiaklei	9.0	14.5	1200	2500	11500	4000	7250	25000	0.8	100	0.23	1.17-2.95	27	4
Basisveen	2.0	11.7	1200	2400	12000				0.8	100	0.15	1.2	26	6
Eerste zandlaag	19.0	29.0	30000	60000	240000				0.5	100	0.2	-	33	3
Allrod	15.0	19.0	13000	13000	39000				0.5	100	0.2	-	33	0
Eemklei	11.3	16.8	4350	9000	45000				0.8	100	0.2	1.2	28	15
Second sand	19.0	19.0	35000	175000	35000				0.5	100	0.2	-	35	5

Table J.2, Structural input for timber (class 18)

Characteristic property	Unit	
Bending strength, $f_{m,k}$	[MPa]	18
Stiffness, parallel to the grain (mean value)	[MPa]	9 000

J.1.2 Construction stages included in the PLAXIS models.

1. Initial phase
2. Lowering ground water level
3. Excavation of the harbour till floor level
4. Installation of the piles and top structure
5. Second phase of excavation the harbour bed
6. Placement of the backfill (in two phases)
7. Rising of the ground water level
8. Trench excavation + struth structures
9. Trench excavation + second layer of struts
10. Wall removal from trench
11. Raking pile removal
12. Load test begins